

Sander Zakariassen

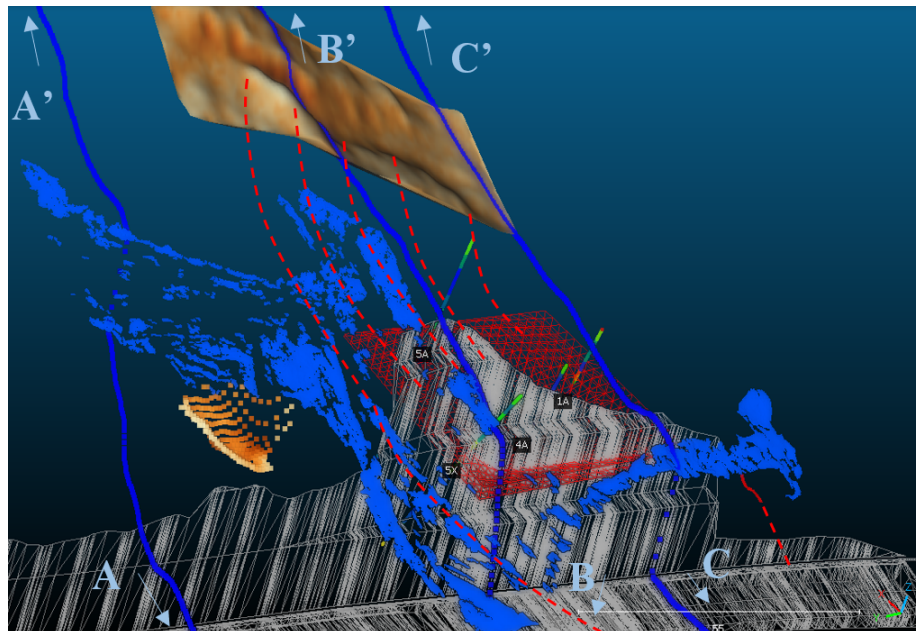
# Stability assessment of rock slope at Hommelvik along E6

Master's thesis in Geology

Supervisor: Krishna Kanta Panthi

Co-supervisor: Werner Stefanussen

June 2022





Sander Zakariassen

# **Stability assessment of rock slope at Hommelvik along E6**

Master's thesis in Geology  
Supervisor: Krishna Kanta Panthi  
Co-supervisor: Werner Stefanussen  
June 2022

Norwegian University of Science and Technology  
Faculty of Engineering  
Department of Geoscience and Petroleum





Your ref.: MS/N41T62/IGP/SZKP

Date: 06.10.2021

**GEOL3090 Master Thesis  
for  
GeoReal student Sander Zakariassen**

**Stability assessment of rock slope at Hommelvik along E6**

**Background**

Nye Veier is expanding the existing two-lane motor road to four-lane motor road for the stretch of E6 from Ranheim to Værness. The Acciona Construction is the contractor for the construction of this project and Ramboll Norge AS is working as the consultant for Acciona and is responsible for the design and construction supervision for the rock cuts. The length of this stretch of motor road is 23 km which is being built with an aim to convert the existing speed limit to 110 km/h. The construction work along this road is planned to be completed in 2025. The road expansion work is challenging which consists of the excavation of three new tube tunnels of various length, the excavation of hillside slopes which will expose many pre-existing joints in the rock mass, upgrading of the existing tunnels and filling work. It is assumed that the excavation of the hillside slope at Hommelvik may bring slope stability challenges and need investigations and stability assessment. Rock core-drillings are planned to be performed in this area to get information about the geological conditions.

**MSc thesis task**

The MSc thesis work is related to the stability assessment of the cut slope at Hommelvik area and will consist following main tasks:

- Theoretical review on the stability assessment technique and methods used in rock slopes, estimation of shear strength parameters and other engineering geological parameters required for the stability assessment of rock cut-slopes.
- Review on the importance of engineering geological investigations required for the rock slope stability assessment at Hommelvik.
- Assisting in the core logging process of the core-drilled rock, carry out field mapping and collect necessary data required for the stability assessment.
- Carry out laboratory assessment of the rock samples to find out UCS, elasticity modulus, Poisson's ration, density, tensile strength and basic friction angle.

*This MSc task must be included after the cover of the MSc thesis*

- Develop a topographic map in ArcGis or similar environments and assess both topographic and geometric condition of the potential rock-cut slope and assess the type of potential failure mode.
- Estimate and collect input variables required for the stability assessment and carry out in-depth stability assessment and assess on the use of potential stability measures against slope failure.
- Discuss and conclude the work.

### **Relevant computer software packages**

Candidate shall use relevant computer software such as ArcGis, Rocscience package etc. for the study.

### **Background information for the study**

- Relevant information about the project such as maps, information and data received from the project and collected by the candidate.
- The information provided by the professor about rock slope engineering.
- Previous MSc and PhD theses, scientific papers and books related to rock slope stability issues.
- Literatures in rock slope engineering and rock anchoring and support measures used in the stabilization of rock cut-slope.

### **Cooperating partner**

Ramboll AS, Nye Veier and Acciona Construction are the cooperating partners.

Senior engineering geologist Mr. Werner Stefanussen is the main contact person in Ramboll and co-supervisor for this MSc project.

The thesis work is to start on 1<sup>st</sup> October 2021 and to be completed by 15<sup>th</sup> June 2022.

The Norwegian University of Science and Technology (NTNU)  
Department of Geoscience and Petroleum

6<sup>th</sup> October 2021



Dr. Krishna K. Panthi  
Professor of geological engineering, main supervisor

*This MSc task must be included after the cover of the MSc thesis*

## Abstract

This MSc thesis is related to the planned road cut at Hommelvik, which is a part of the ongoing highway project E6 Ranheim – Værnes currently under construction by Nye Veier. It will likely be around 450 m long and up to 60 m tall. This thesis has been organized in cooperation with Rambøll Norge AS, which is the consultant for the project. The goal has been to perform an external stability assessment without access to their work except for basic data sets, which were deemed necessary to perform the assessment. This thesis has utilized an early road cut design by Rambøll Norge AS in the stability assessment and does not represent the final slope configuration that will be built. However, it is referred to as the planned road cut during the thesis.

The goal for this MSc thesis has been to gain an understanding of the geology of the area, and particularly the discontinuity sets (joints) there. The orientation and characteristics of the discontinuity set have been evaluated based on field mapping, core logging, and the software Discontinuity Set Extractor (DSE). Semi-automatic extraction of discontinuity sets has been achieved with DSE from high detailed point clouds mapped from the study area. The geology in the area is folded and highly complex, resulting in several local variations in the discontinuity sets. In general, four main discontinuity sets are mapped, including the heavily dominating foliation. However, DSE registered seven discontinuity sets, thus capturing some local variations in the discontinuity sets. This meant that the local best fit variation of the discontinuity set could be used during stability assessment of different sections of the road cut.

The main challenges related to the excavation phase of the road cut have been discussed, along with long-term the stability. The stability assessment has been carried out using the rock mass classification system Q-slope, kinematic analysis based on joint orientation measurements from the four core drilled boreholes at the top of the current road cut, and numerical modelling in RS2. The stability analysis in RS2 has evaluated three different cross-section profiles, set to best to fit the overall slope configuration of the planned road cut. Profile AA' with no benches (furthest north), profile BB' with three benches (tallest part), and profile BB' with two benches (furthest south).

The first part in RS2 includes sensitivity analyses of the individual parameters isolated and in combinations to evaluate their effect on the stability of the road cut. The tested parameters were groundwater, earthquake, and the different discontinuity sets. Sensitivity analysis of the rock mechanical and shear strength properties was not performed as laboratory investigations were conducted in the thesis to determine these values accurately. The second part of numerical modelling in RS2 included stability measures and a combination of the earlier tested parameters deemed the most realistic. The factor of safety was calculated to be 1.61 for profile AA', profile BB' was 1.80, and profile CC' was 2.33. A factor of safety of 1.5 is regarded as long-term stable for road cuts.

The thesis concludes that great care must be taken during the excavation phase of this project and as at least one crushed zone is located within the rock body surrounding the planned road cut. The possible curved geometry of the crushed zone makes it difficult to stabilize and secure. The first few stages of the excavation sequence will likely be the most critical in terms of the slope's overall stability.

## Sammendrag

Denne masteroppgaven omhandler den planlagte vegskjæringen ved Hommelvik som er en del av det pågående vegprosjektet E6 Ranheim – Værnes som er under bygging av Nye Veier. Den vil sannsynligvis bli rundt 450 m lang og opptil 60 m høy. Denne oppgaven er organisert i samarbeid med Rambøll Norge AS, som er rådgiver for prosjektet. Målet har vært å utføre en ekstern stabilitetsvurdering uten tilgang til arbeidet deres med unntak av grunnleggende datasett som ble ansett som nødvendige for å utføre vurderingen. Denne oppgaven har benyttet et tidligere vegskjæringsdesign av Rambøll Norge AS som utgangspunkt for stabilitetsvurderingen og representerer ikke det endelige designet av vegskjæringen som skal bygges. Den omtales likevel som den planlagte vegskjæringen gjennom hele oppgaven.

Målet for denne masteroppgaven har vært å få en forståelse av geologien for området, og spesielt diskontinuitetene (sprekkene) der. Orienteringene og egenskapene til de ulike diskontinuitetssettene har blitt evaluert basert på feltkartlegging, kjernelogging og programvaren Discontinuity Set Extractor (DSE). Halvautomatisk utvinning av diskontinuitetssett er oppnådd med DSE fra høydetaljerte punktskyer kartlagt fra studieområdet. Geologien i området er foldet og svært kompleks, noe som resulterer i flere lokale variasjoner i diskontinuitetssettene. Generelt er det fire hoveddiskontinuitetssett kartlagt, inkludert den sterkt dominerende foliasjonen. Det ble likevel registrert syv ulike diskontinuitetssett med DSE, altså noen lokale variasjoner i diskontinuitetssettene er registrert. Dette gjorde at den lokale varianten av et diskontinuitetssett kunne brukes ved stabilitetsvurdering av ulike seksjoner av vegskjæringen.

Hovedutfordringene knyttet til byggefasen av vegskjæringen har blitt diskutert sammen med dens langsiktige stabilitet. Stabilitetsvurderingen er utført ved bruk av bergmasseklassifiseringen Q-slope, kinematisk analyse basert på sprekkorienteringsmålinger fra fire kjernene hentet fra borehull på toppen av vegskjæring som eksisterer der i dag, og numerisk modellering i RS2. Stabilitetsanalysen i RS2 har evaluert tre ulike tverrsnitt som ble valgt for å passe best mulig med det totale designet til vegskjæringen. Profil AA' uten hyller (lengst nord), profil BB' med tre hyller (høyeste del), og profil BB' med to hyller (lengst sør).

Den første delen i RS2 inkluderer analyser av de enkelte parameterne isolert og i kombinasjoner, for å evaluere deres effekt på stabiliteten til vegskjæringen. Dette inkluderte parametere som grunnvann, jordskjelv og de ulike diskontinuitetssettene. Sensitivitetsanalyse av de bergmekaniske og skjærfasthetsegenskapene ble ikke utført da det ble utført laboratorieundersøkelser for å bestemme disse verdiene nøyaktig. Den andre delen i RS2 inkluderte stabilitetsanalyse med en kombinasjon av de tidligere testede parameterne som ble ansett som de mest realistiske. Sikkerhetsfaktoren ble beregnet til å være 1,61 for profil AA', 1,80 for profil BB', og 2,33 for profil CC'. Sikkerhetsfaktor over 1,5 anses som langtidsstabil for vegskjæring.

Opgaven konkluderer med at anleggsfasen av vegskjæringen må gjennomføres veldig varsomt. Det er minst en knusningssone som ligger i bergmassen som omslutter den planlagte vegskjæringen. Knusningssonen har sannsynligvis en buet form som gjør den vanskelig å stabilisere og sikre. De første palluttakene for vegskjæringen vil sannsynligvis være de mest kritiske med tanke på sikkerhet og skråningsstabilitet.



## Acknowledgments

This thesis concludes the final assignment for the Master of Science degree in Environment and Geotechnology at the Department of Geoscience and Petroleum, NTNU Trondheim.

I am greatly indebted to my supervisor Professor Krishna Kanta Panthi (NTNU), for the guidance and feedback throughout the work of this thesis. I would also like to thank my co-supervisor, Werner Stefanussen (Rambøll), for highlighting possible challenges related to the project.

I would also like to thank Acciona Construction for the opportunity to access the project site, core logs, and be a part of the project. I would also thank Nye Veier for approving my project.

Appreciation is extended to everyone in Rambøll who has helped me with fieldwork, guidance, providing data, social events, etc. Linn Døvle, Gudrun Dreiås Majala, Karsten Østerås, Sverre Paulsen Thoresen, Endre Kjernes Øen, and Inger Lise Sollie are especially highlighted for their direct contributions to my thesis in one way or another. Furthermore, I would like to emphasize my utmost gratitude for the opportunity to join the team as an engineering geologist and be able to follow up on this exciting (but challenging) project at the start of my career.

I am grateful to Jon Runar Drotninghaug at the Department of Geoscience and Petroleum at NTNU for preparing the test specimens, guidance during the rock mechanical testing, and discussion of the results.

In addition, I would like to thank my family, friends, and fellow students for all the support during my studies. I am also very grateful to Gaute Moe Fløan and Kristoffer Aurstad Dolvik for keeping me company during all the late nights at the reading hall.

Finally, I would like to Steinkubben for all the good memories as a student.

Trondheim, Norway

June 2021

Sander Zakariassen

*Sander Zakariassen*

# Contents

<b>Abstract .....</b>	<b>i</b>
<b>Sammendrag .....</b>	<b>ii</b>
<b>Acknowledgments.....</b>	<b>iii</b>
<b>1 Introduction.....</b>	<b>1</b>
1.1 Background.....	2
1.2 Research objectives .....	3
1.3 Limitations.....	4
1.4 Methodology.....	5
<b>2 Concepts of rock slope instabilities, assessment methods, and slope design .....</b>	<b>6</b>
2.1 Classification of rock slope failures and instabilities .....	9
2.2 Stability factors for rock slopes .....	11
2.2.1 Rock mass quality .....	13
2.2.1.1 Rock mass strength .....	15
2.2.1.2 Rock mass deformation.....	17
2.2.1.3 Anisotropy and inhomogeneity.....	20
2.2.1.4 Discontinuities .....	22
2.2.1.5 Susceptibility to alteration and weathering.....	25
2.2.2 Slope configuration .....	29
2.2.3 External influences .....	30
2.2.3.1 Seismic events.....	30
2.2.3.2 Hydrogeological & climatic conditions .....	32
2.2.3.3 Virgin rock stresses .....	34
2.2.3.4 Excavation technique .....	35
2.3 Rock slope stabilization and protection.....	37
2.4 Material failure theory .....	41
2.4.1 Hoek-Brown failure criterion .....	42
2.4.2 Barton-Bandis failure criterion.....	43
2.5 Assessment methods for rock slope stability.....	50
2.5.1 Q-slope .....	51
2.5.2 Kinematic analysis .....	57
2.5.3 Conventional limit equilibrium method .....	60
2.5.4 Partial factor principle limit equilibrium method.....	61

2.5.5	Numerical modelling.....	63
2.5.6	Probabilistic methods.....	65
<b>3</b>	<b>Description of the planned rock cut at Hommelvik.....</b>	<b>68</b>
3.1	Description of E6 Ranheim – Værnes.....	70
3.1.1	Road cut versus tunnel alternative.....	71
3.2	Geology.....	73
3.3	Climatic and hydrological conditions.....	76
3.3.1	Climate.....	77
3.3.2	Future climate.....	79
<b>4</b>	<b>Field and laboratory investigations.....</b>	<b>80</b>
4.1	Field mapping.....	80
4.1.1	Lithology.....	80
4.1.2	Discontinuities.....	83
4.2	Summary of core logging.....	84
4.3	Laboratory investigations.....	92
4.3.1	Rock mechanical properties.....	92
4.3.1.1	Density measurements.....	93
4.3.1.2	P-wave velocity test.....	93
4.3.1.3	Uniaxial compression test.....	94
4.3.1.4	Point load test.....	95
4.3.1.5	Brazilian test.....	96
4.3.2	Shear strength properties.....	98
4.3.2.1	Tilt test.....	98
4.3.3	Comparison of laboratory investigations.....	100
<b>5</b>	<b>Digital mapping and 3D modelling.....</b>	<b>103</b>
5.1	Point clouds.....	104
5.1.1	Structure-from-Motion photogrammetry.....	104
5.1.2	Implementation of point clouds.....	105
5.1.3	User-defined point clouds.....	106
5.1.4	Volume estimation.....	108
5.2	Selection of cross-section profiles.....	111
5.3	Extraction of discontinuity sets from point clouds.....	114
5.3.1	Discontinuity Set Extractor.....	114
5.3.2	Semi-automatic extraction of discontinuity sets.....	115

5.4	Geometry of material boundaries .....	120
5.4.1	Weakness zones.....	120
5.4.2	Rock types .....	126
<b>6</b>	<b>Analysis and results .....</b>	<b>128</b>
6.1	Stability assessment by Q-slope .....	128
6.2	Kinematic analysis.....	130
6.2.1	Kinematic sensitivity analysis .....	130
6.2.1.1	Planar sliding .....	131
6.2.1.2	Wedge sliding .....	131
6.2.1.3	Flexural toppling .....	132
6.2.1.4	Block toppling.....	133
6.3	Stability assessment by SSR-FEM in RS2 .....	135
6.3.1	Model setup .....	135
6.3.2	Material parameters .....	138
6.3.3	Discontinuity parameters.....	141
6.3.4	External influences .....	143
6.3.5	Excavation sequence .....	144
6.3.6	Sensitivity analysis.....	146
6.3.7	Stability measures .....	152
6.3.8	Results .....	156
<b>7</b>	<b>Discussions.....</b>	<b>160</b>
7.1	Evaluation of discontinuity sets.....	160
7.2	Uncertainties in the stability assessment .....	161
7.3	Stability assessments .....	162
7.4	Evaluation of used methods.....	164
<b>8</b>	<b>Conclusions and recommendations.....</b>	<b>165</b>
8.1	Main findings.....	165
8.2	Suggestions for further work .....	167
	<b>References.....</b>	<b>168</b>
<b>Appendix A</b>	<b>Ground investigations .....</b>	<b>I</b>
<b>Appendix B</b>	<b>Plan and profile drawings.....</b>	<b>III</b>
<b>Appendix C</b>	<b>Uniaxial compressive strength test results .....</b>	<b>V</b>
<b>Appendix D</b>	<b>Point load test results .....</b>	<b>XI</b>

<b>Appendix E</b>	<b>Steepness and susceptibility maps for Hommelvik.....</b>	<b>XII</b>
<b>Appendix F</b>	<b>Core logging .....</b>	<b>XIV</b>
<b>Appendix G</b>	<b>Borehole 1A .....</b>	<b>XVII</b>
<b>Appendix H</b>	<b>Borehole 4A .....</b>	<b>XXV</b>
<b>Appendix I</b>	<b>Borehole 5A .....</b>	<b>XXXIV</b>
<b>Appendix J</b>	<b>Borehole 5X .....</b>	<b>XLIII</b>
<b>Appendix K</b>	<b>GSI and disturbance factor charts.....</b>	<b>LII</b>
<b>Appendix L</b>	<b>Discontinuity sets from DSE.....</b>	<b>LV</b>
<b>Appendix M</b>	<b>Kinematic analysis .....</b>	<b>LIX</b>
<b>Appendix N</b>	<b>Sequence of excavation and installation of stability measures .....</b>	<b>LXV</b>

# 1 Introduction

This thesis will perform a stability assessment of the planned road cut at Hommelvik, which is part of the E6 Ranheim – Værnes highway project. The entire road cut will stretch from profile 16035 to 16500, as illustrated in Figure 1.1. However, the main focus will be on the section between profile 16035 to 16300, which might be deemed the most challenging in terms of stability and the overall construction processes. Depending on the slope configuration chosen by Rambøll and Acciona Construction, the slope height might be up to 56-60 m, making it possibly the tallest in Norway when finished. Construction of tall road cuts is generally avoided due to the inherent complexity and risk involved. Due to few projects of this magnitude earlier in Norway, design principles from open pit slopes should be evaluated too. This chapter will give a brief background and motivation to the thesis, research objectives, limitations, and its structure.



Figure 1.1: Overview map of the current road cut at Hommelvik, centre line for the new E6 highway (red line for planned road cut and white line for the rest), and the top of the planned road cut (red dotted line). It should be noted that the red to the left in the figure represents the tunnel portal at Helltunnelen. Modified after Multiconsult Norge AS (2019a).

## 1.1 Background

Society requires several types of excavated rock slopes. Civil engineering slopes are required for projects such as railways, highways, dam sites, tunnel portals, irrigation channels, etc. Furthermore, excavated rock slopes are also necessary for quarries and open pit mines. All types of excavated rock slopes have different design requirements and challenges related to them. However, the design of rock slopes and the associated stability assessments are often considered one of the most difficult challenges in the field of rock engineering. The design of an excavated rock slope is highly dependent on the geological conditions, and may vary from weak, heavily jointed rock masses to strong rock masses with well-defined discontinuities (Read & Stacey, 2009; Wyllie, 2018). There are five elements that are important to identify before designing and excavating a rock slope (Duncan & Goodman, 1968):

1. Identification and distribution of each rock type
1. Orientation, spacing, and character of each discontinuity set
2. Location, orientation, and character of faults and altered zones (weakness zones)
3. Depth of weathering (and degree)
4. Ground water regime and distribution

Road cut design should be based out based on Eurocode 7 (EC7) in Europe (Standard Norge, 2020). This is the basic standard for geotechnical design which also includes rock engineering designs. EC7 further states that geotechnical design can be carried out based one of four principles (Nilsen, 2017):

1. **Calculation**, which includes analytical methods, half empirical models, and numerical models.
2. **Perspective measures**, which are design based on experience (empirical). This principle can be used if calculation models are unavailable or considered unnecessary.
3. **Load testing and experimental testing**, which includes testing on physical models. This principle is not very relevant for rock engineering designs.
4. **The observational method**, which is based on assumptions and the completed design is being verified by observation and monitoring during construction.

There is a trend (particularly in Norway) to use Reliability Based Design (RBD). However, there are no demands in EC7 to use RBD (Nilsen, 2017).

A summary of the relevant governing guidelines, laws, and suggestions for construction of road cuts in Norway are:

- Eurocode 0: Basis of structural design (NS-EN 1990:2002+A1:2005+NA:2016)
- Eurocode 7: Geotechnical design (NS-EN 1997-1:2004+ A1:2013+NA:2020)
- Eurocode 8: Design of structure for earthquake resistance
- TEK 17
- NS-EN-1990
- NS-EN-1997-1
- NS-EN-1997-2

- Handbook V220 (“Geotechnics for road constructions”)
- Handbook V221 (“Ground reinforcement, embankments and slopes”)
- NVE guidance 1/2019
- Handbook V225 (“Rock cuts”)
- Handbook N200 (“Road construction”)
- Handbook R760 (“Management of road projects”)

## 1.2 Research objectives

The research objectives for this thesis are to perform a stability assessment of a planned road cut at Hommelvik. The construction of the road cut is planned to start during the summer of 2022. This thesis also aims to give a suggestion for stabilization measures at certain sections of planned road cut. Potential challenges related to the project will also be highlighted and discussed. The summary of the research objectives are as follows:

- Theory review of concepts necessary to perform rock slope stability assessments and develop rock slope designs.
- Theory review of the geology at Hommelvik.
- Theory review of the climate and the expected future climate.
- Carry out field investigations with mapping of the lithology and key features at the project area.
- Assist Rambøll with core logging of the samples retrieved from the project area.
- Carry out laboratory investigations and assess rock mechanical and shear strength properties on cores from two of the boreholes. Compare the results with the laboratory investigations done by SINTEF on the cores from the two other boreholes at the project area.
- Carry out a comprehensive assessment of the discontinuities and potential weakness zones in the project area.
- Perform slope stability assessments with empirical, analytical, and numerical methods.
- Discuss the overall versus the detailed stability for the planned road cut.
- Discuss the risk and uncertainties related to the assessment.
- Conclude the work and give further recommendations.



## 1.3 Limitations

The planned road cut at Hommelvik is in some ways unique in Norway as road cuts that tall are often avoided. A common alternative is changing the road alignment (and curvature) which means that less of road needs to intersect the terrain, thus a simpler road cut can be built. Another option is building a tunnel instead through the difficult terrain. However, in this case a tall and complex road cut was evaluated as a better option even though it involves countless of challenges. There are very few similar projects in Norway or internationally, thus the relevant literature is sparse. It will probably be the tallest road cut in Norway, and it is possible a crushed zone will intersect almost the entire second bench of the road cut at around 25 m above the trench bottom. In addition, there are possibly two more depressions which are likely weakness zones further north. Furthermore, the terrain is very steep several along the entire section and extensive protection measures will need to be implemented to avoid rock fall, icing, soil and snow avalanches. The geology in the project area is complex. It is characterized by multiple folds and faults. The discontinuities in the area are also highly localized with several variations.

There are uncertainties related to the utilized methods which were used to analyse the stability of the planned road cut. Numerical modelling requires reliable input parameters to produce any meaningful results. Detailed ground investigations have been done in the form of core logging combined with laboratory investigations to better evaluate the rock mass conditions and properties, discontinuities, and geology in general. However, there are local variations in the rock body which makes the parameterization process of the rock masses difficult. Furthermore, there are no in-situ rock stresses performed, and the distance to the nearest recorded in-situ rock stress measurements are too far away to be considered relevant. Moreover, no measurements or drillings have been done on Svartløftberga (the ridge above the planned road cut) to estimate the depth to the groundwater table.

Rock engineering problems can seldomly only be evaluated through 2D-methods. This is particularly the case for this project as the road cut will be curved along the E6 highway, and some benches will be at a slight angle. The geometry of the crushed zone would be beneficial to integrate into a 3D model along with a more precise representation of the topography as the ridge is located at an angle to the planned road cut. There are likely some topographic stresses that are not optimally introduced into the 2D models. A 3D model of the terrain has been built in Slide3, but due to time constraints stability analysis was not with it. Slide3 is also interoperable with Slide2 which was originally planned to be used but was also not done due to time constraints. The decision to use FEM with RS2 turned out to be very challenging due to the complexity (and amount) of joint sets, and the steep and curved topography of the current road cut. The main problems that occurred was high density of the discretization and mesh. This resulted in long computational time. Furthermore, small wedges and blocks created by the intersecting joints also caused the models often to not converge (even after the maximum number of convergence and iterations were adjusted). At some points during this study eight different computers were running models simultaneously.

The utilized method for extracting the discontinuity sets from the point clouds (Discontinuity Set Extractor) was also quite rigorous to use. The data sets were larger than the program could efficiently handle with the utilized computers. A non-compressed version of the main point cloud was running for four days before the analyses were aborted.

## 1.4 Methodology

The methodology and structure of the thesis can be summarized as follows:

### 1. Literature review

- I. Classification of rock slope failure and instabilities
- II. Stability factors for rock slopes
- III. Rock slope stabilization and protection measures
- IV. Material failure theory
- V. Assessment methods for rock slope stability

### 2. Description of the planned road cut at Hommelvik

- I. Introduction to the E6 Ranheim – Værnes project
- II. Short review of the decision process for why road cut was chosen over tunnel
- III. Literature study of the geology in the project area
- IV. Literature study of the climatic and hydrological conditions in the project area

### 3. Field and laboratory investigations

- I. Field mapping
- II. Core logging
- III. Laboratory testing of rock mechanical and shear strength properties
  - a. Density measurement
  - b. P-wave velocity test
  - c. Uniaxial compression test
  - d. Point load test
  - e. Brazilian test
  - f. Tilt test

### 4. Digital mapping and 3D modelling

- I. Development of 3D environments by integrating different data sources
- II. Estimation of necessary volume to excavate
- III. Extraction of discontinuity sets for the road cut from point clouds
- IV. Assessment of material boundaries

### 5. Stability assessment

- I. Empirical method: Q-slope
- II. Analytical method: Kinematic analysis
- III. Numerical methods: Finite element method in RS2 with shear strength reduction technique
  - a. Parameter sensitivity analysis
  - b. Stability analyses with stabilization measures implemented

### 6. Evaluation and assessments of the results

## 2 Concepts of rock slope instabilities, assessment methods, and slope design

Rock slopes can be divided into *natural rock slopes* and *excavated rock slopes* sometimes called artificial rock slopes or rock cuts. The prior includes valley sides and mountains, while the latter includes open pit (mine) slopes and civil (engineering) slopes (Nilsen & Palmström, 2000; Read & Stacey, 2009; Wyllie, 2018). Natural rock slopes are often relative stable in the context of the duration they have been exposed to the environment. Parts of the rock mass may be weathered or partly weathered, and many rock slopes are also covered with section of soils. Excavated rock slopes are constructed steeper than the pre-existing natural rock slope which may increase the instability. However, rock mass of lower quality (more weathered) might be removed which can improve the stability. Slope instabilities either be caused by failure along pre-existing discontinuities in stronger rocks or through weak intact rock (Cosgrove & Hudson, 2016).

Call and Savely (1990) lists three main principles to keep in mind during slope stability assessments:

- 1. Slope failures do not occur spontaneously.** One or more of the forces acting on a potentially unstable rock mass must change in order for the rock mass to become unstable.
- 2. Most slope failures tend toward equilibrium.** A slope fails because it is unstable under the existing conditions. Failure tends to bring the slope to some sort of equilibrium
- 3. A slope failure does not occur without warning.** Prior to failure, measurable movement and/or development of tension cracks will occur. These indications of failure can develop, indicating imminent slope failure, then subside for a long period of time, indicating apparent stability.

Stability assessments for natural rock slope and excavated rock slopes have some differences, as the prior tends to be stable while the latter is often easier to determine reliable input parameter for analysis. This chapter will focus on the concepts of excavated slopes with the emphasis on road cuts but with some relevant the design principles from pit slopes. Figure 2.1 shows a typical configuration for a large-scale excavated rock slope. The planned rock slope at Hommelvik will be a large-scale road cut and therefore share some design principles with open pit slopes, particularly during the excavation phase. It is stated in handbook N200 that road cuts should be constructed near vertical, meaning at a slope angle of 10:1 or steeper. It should be noted that these steep slope angle represent the final slope configuration, and intermediate benches can be constructed with lower angles. Furthermore, a slope angle of 10:1 represent the bench (face) angle, and the overall slope angle can be lower as illustrated in Figure 2.1 Ramp as a term is typically not used for road cuts but is in essence only a wider bench and often constructed with a lower angle to be more stable (NPRA, 2020; Read & Stacey, 2009; Wyllie, 2018).

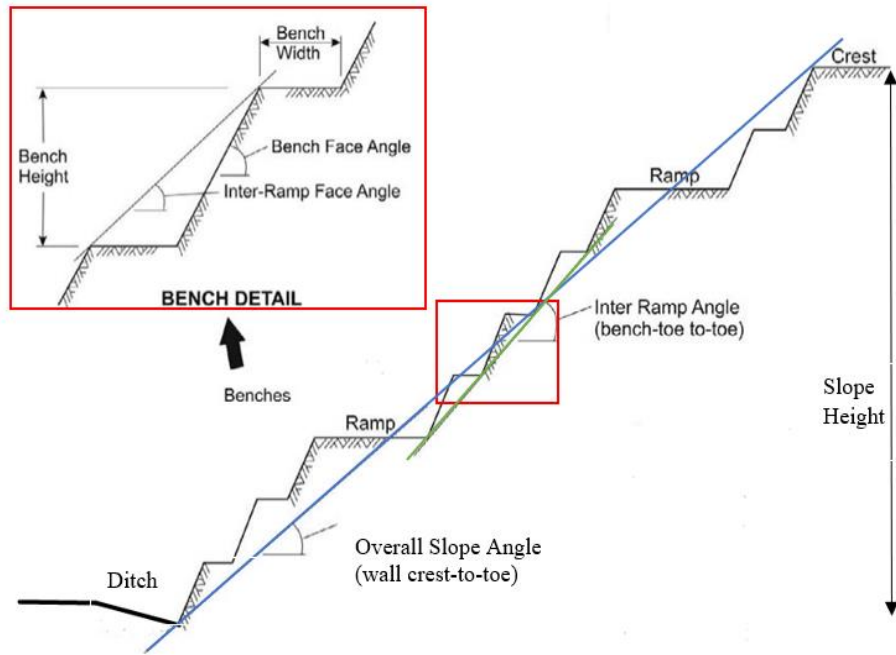


Figure 2.1: Configuration of large-scale excavated rock slope. Modified after (Read & Stacey, 2009).

The final slope configuration should be designed based on the groundwater conditions, geology, and topography according to handbook V225 (NPRA, 2020). This means that road cut can be constructed with slope angles lower than 1:10 ( $84^\circ$ ) if the rock mass quality is poor and extensive stabilization measures would be needed. The slope angle for very poor rock mass is often the designed as the same as lateral soil slopes which is often 1:2 ( $26^\circ$ ) (NPRA, 2018, 2020). Figure 2.2 illustrates a principal sketch for a standard road cut design with a catch ditch and roadway next to it.

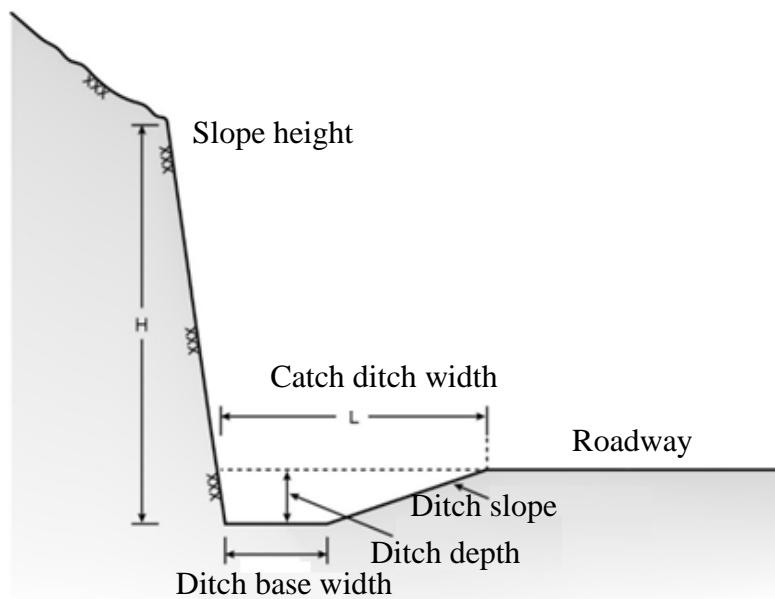


Figure 2.2: Principal sketch for the design of a road cut and ditch. Modified after NPRA (2018).

There are three main factors that need to be evaluated during the design process for excavated rock slopes according to Read and Stacey (2009). (1) Safety/social factors, (2) economic factors, and (3) environmental and regulatory factors. However, there is a big difference in how they should be evaluated for road cuts (and civil slopes) versus pit slopes. Performance and reliability of the road cuts are highly emphasised in the design process for road cuts, and the benefits should outweigh the associated costs. On the other hand, open pit slopes are designed to optimise excavation with respect to ore extraction and financial returns.

The design procedure for open pit slopes can be described as shown in the flowchart in Figure 2.3 from Read and Stacey (2009). However, it can be also implemented for large-scale road cuts too. The procedure is divided into five stages: (1) models, (2) domains, (3) design, (4) analyses, and (5) implementation. This chapter will present some of the most important elements from this flow chart. In other words, the concepts of rock slope instabilities, assessment methods, and slope design.

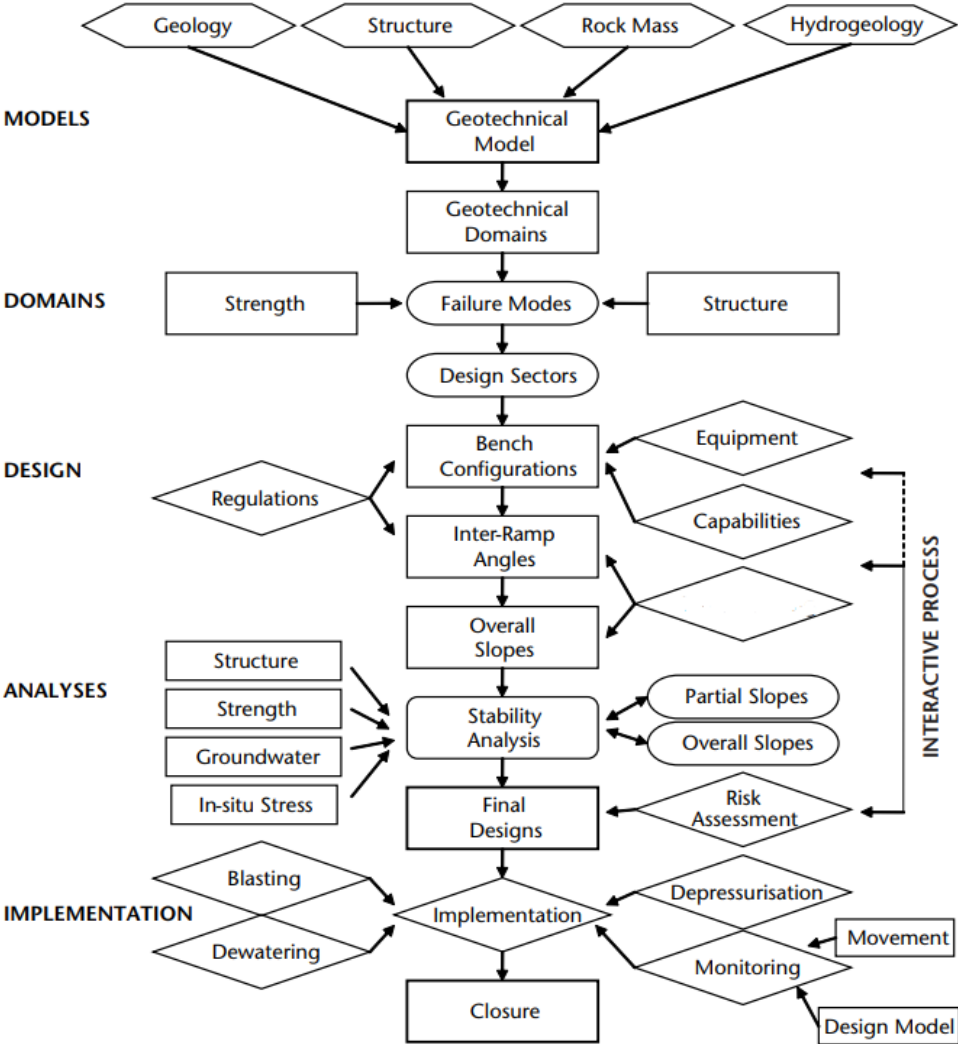


Figure 2.3: Flowchart illustrating the design procedure for open pit slopes divided into the stages: models, domains, design, analyses, and implementation. Modified after Read and Stacey (2009).

## 2.1 Classification of rock slope failures and instabilities

The time horizon in relation to the stability of the rock slope is important in when performing a stability assessment. Nilsen and Palmström (2000) divides the time horizon for the stability of rock slopes into short-term stability ranging from a few tens of years to long-term stability which can range from hundreds to thousands of years (often in context of natural rock slopes). This is relevant as certain geological factors will only have any meaningful influence on a longer time horizon such as creep and weathering.

For rock slopes, it is typical to distinguish between the scale of the stability problem in relation to the overall slope. This can be classified as total stability (or overall stability) and local stability (or detailed stability) (Nilsen & Palmström, 2000). This is illustrated in Figure 2.4. In the context of pit slopes and large-scale civil slopes failures can be divided into bench-scale failure, multibench scale failure, inter-ramp scale failures, and overall slope failure (Read & Stacey, 2009). The required stability conditions for the excavated rock slope will depend on the project type and the potential consequences of failure. For instance, road cuts located along highways with high-traffic volumes have higher priorities regarding the total and local stability, compared to a road cut with little traffic where the total stability is the most important (Wyllie, 2018).

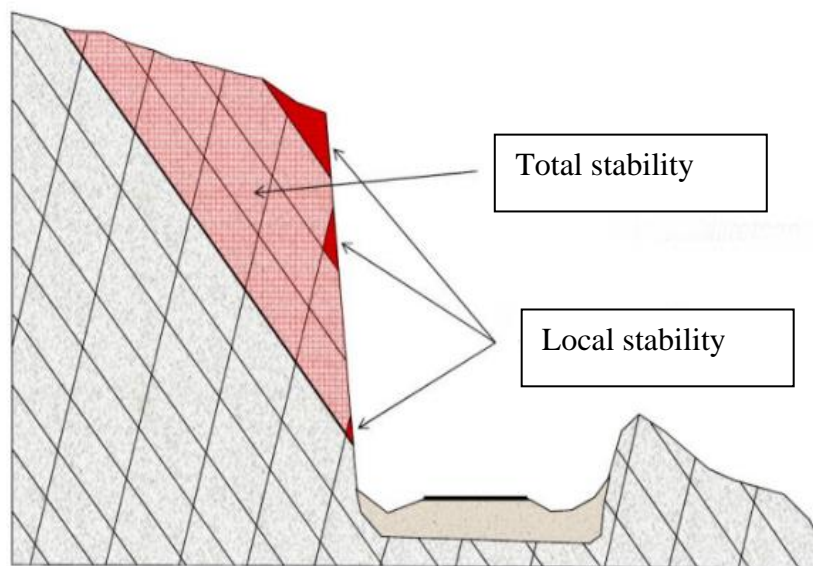


Figure 2.4: Total stability and local stability. Modified after NPRA (2020).

In Norway rock slope failures are often classified based on the runout volume. Rock fall (“steinsprang”) is classified for volumes  $< 100 \text{ m}^3$ , rock collapse (“steinskred”) has volumes between  $100 - 100\,000 \text{ m}^3$ , and rock avalanche (“fjellskred”) has volumes  $> 100\,000 \text{ m}^3$  (Hestnes, 1980).

The orientation of the discontinuities relative to the rock slope is the main governing factor for the possible failure modes (Nilsen & Palmström, 2000). There are several classification systems used for landslides or more specifically rock slope failures. The two most accepted classification systems are from Varnes (1978) and Hungr et al. (2014) proposed update to the Varnes landslide classification system. Varnes (1978) classification system is based on the failure mode/movement type (fall, topple, slide, spread, flow or complex) and the material in movement (rock, debris, or earth).

The updated version by Hungr et al. (2014) introduced the term slope deformation which replaced the term complex in Varnes system. Furthermore, the terms debris and earth were replaced with soil engineering terms for the landslide material. The summary of the updated landslide classification related to rock as material type by Hungr et al. (2014) is presented in Table 2.1.

Table 2.1: Landslide classification for rock as material type. Modified after (Hungr et al., 2014).

<b>Type of movement</b>	<b>Rock</b>
Fall	Rock fall
Topple	Rock block topple Rock flexural topple
Slide	Rock rotational slide Rock planar slide Rock wedge slide Rock compound slide Rock irregular slide
Spread	Rock slope spread
Flow	Rock avalanche
Slope deformation	Mountain slope deformation Rock slope deformation

The failure modes for rock slopes can be divided into unstructurally or structurally controlled failures. Rock slope failures usually initiate and follow already existing discontinuities rather than breaking through intact rock. For slopes with dimensions which are vastly greater than the scale of the discontinuities the effects of structural patterns will be reduced. This makes it possible for large-scale global failure mode to occur. The overall rock mass in such rock slopes is better described as an ‘equivalent continuum’. Furthermore, the discontinuities in these rock masses are typically closely spaced and with random orientation, and often with a higher degree of weathering. Structurally controlled failures occur as a result of discontinuities propagating and merging, thus creating a failure surface. These surfaces are rarely persistent continuous planes but rather a result of complex interactions between existing discontinuities and brittle failure propagation through the rock bridges (intact rock) which result in the slope failure (Pantelidis, 2009; Sullivan, 2013; Wyllie, 2018).

## 2.2 Stability factors for rock slopes

Instability processes for rock slopes are the product of local geologic, hydrologic, and geomorphic conditions. These conditions are further modified by geodynamic processes, human activities, vegetation, seismicity, and intensity and frequency of seismic events (Soeters & Van Westen, 1996). Multiple researchers over the years have proposed systems and groupings of the stability factors for rock slopes.

Nilsen and Palmström (2000) suggests that the main governing factors which influence the stability of rock slope are: (1) detailed jointing and joint surface conditions, (2) mechanical properties and rock type boundaries, (3) faults and weakness zones, (4) groundwater and climatic conditions, (5) rock stresses, (6) geometrical conditions, and (7) blast vibrations and potential earthquake activity.

Sullivan (2013) proposes only five main governing factors for rock slope stability: (1) intact rock strength, (2) rock mass character (typically described by GSI), (3) geological structure, predominately the controlling or dominant structures in the rock mass, (4) the orientation of the geological structures relative to the slope face, and (5) the groundwater conditions (and groundwater response patterns).

It should be noted that the stability effects for each of the contributing factors differs for every rock slope. However, the groundwater conditions and discontinuities (orientation and characteristics) are often the key stability factors. Nevertheless, systematic mapping and estimations of the contributing factors are important to perform a reliable stability assessment of a rock slope. Furthermore, there might be considerable local differences within a rock slope for the contributing factors (Nilsen & Palmström, 2000; Wyllie, 2018).

Figure 2.5 illustrates the major influencing factors for slope stability as suggested by Hunt (2005).

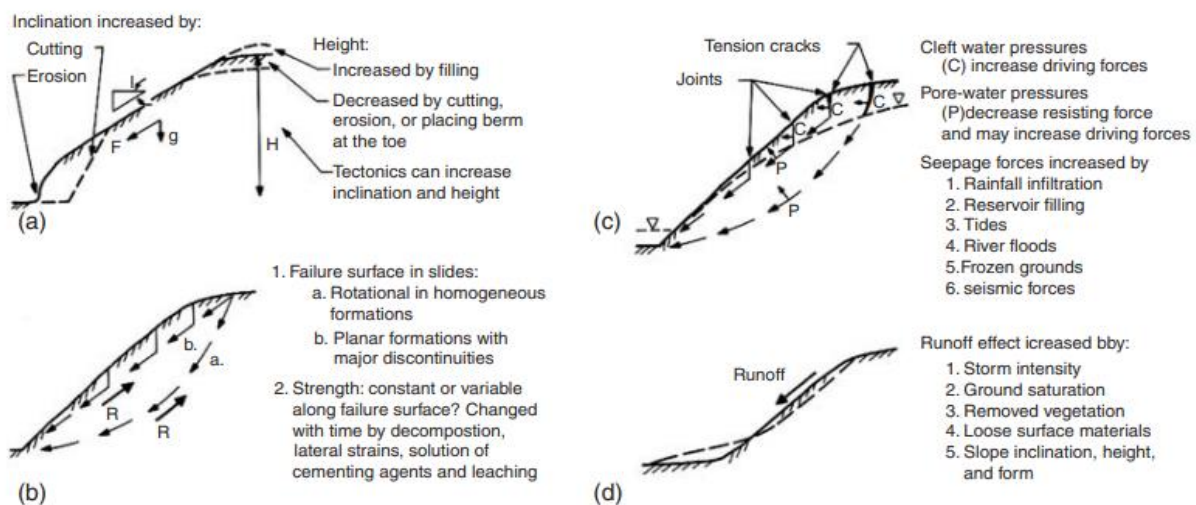


Figure 2.5: The major influencing factors for slope stability: (a) slope geometry; (b) geological structures and material strength; (c) water pressure related; (d) runoff effects (Hunt, 2005).



Figure 2.6 presents a flow chart of the stability factors for excavated rock slopes. This is a simplified illustration of how the individual factors are connected, but the reality is more complex. Several of the factors are in fact interacting with each other and correlated to some degree. Any instability or failure can also be the result of multiple factors. The task of evaluating the stability of a rock slope gets even more complex when the elements of spatial and temporal distributions are included. The factors influence each both in time and space, and to derive at reliable stability assessments simplifications and assumptions must be made (Botsialas et al., 2015).

This section will be organized around the three main components of stability of excavated rock slopes (as described in Figure 2.6): slope configuration, rock mass quality, and external influences. Effects from elements such as external loads, biological factors, heat-cool cycles do affect the stability to some degree, but the effects are often minor and will not be discussed.

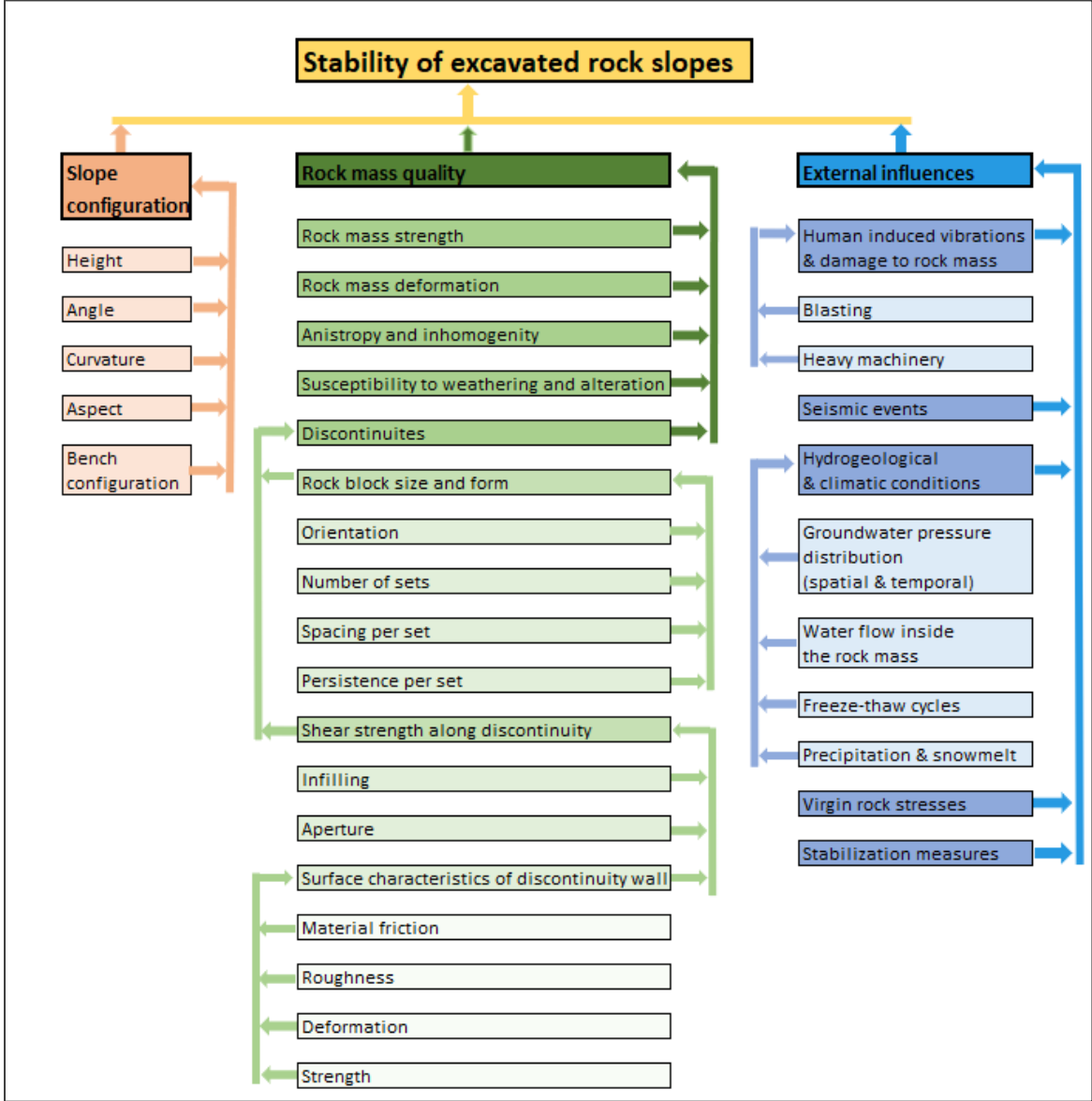


Figure 2.6: Stability factors for excavated rock slopes. Inspired after Hack (2002), Panthi (2006), Nilsen and Palmström (2000), and Botsialas et al. (2015).

## 2.2.1 Rock mass quality

Rutqvist and Stephansson (2003) defines rock mass as a composition of intact (unfractured) rock matrix and rock fractures. Intact rocks have microcracks which might have similar behaviour to macrofractures. However, it is useful to evaluate the fundamentals of rock fractures and intact rock separately. Nilsen and Palmström (2000) defines a rock mass as heterogenous and often discontinuous. The rock mass is ideally a composition of rock blocks and fragments separated by discontinuities, and this unity of elements will behave in mutual dependence, as illustrated in Figure 2.7.

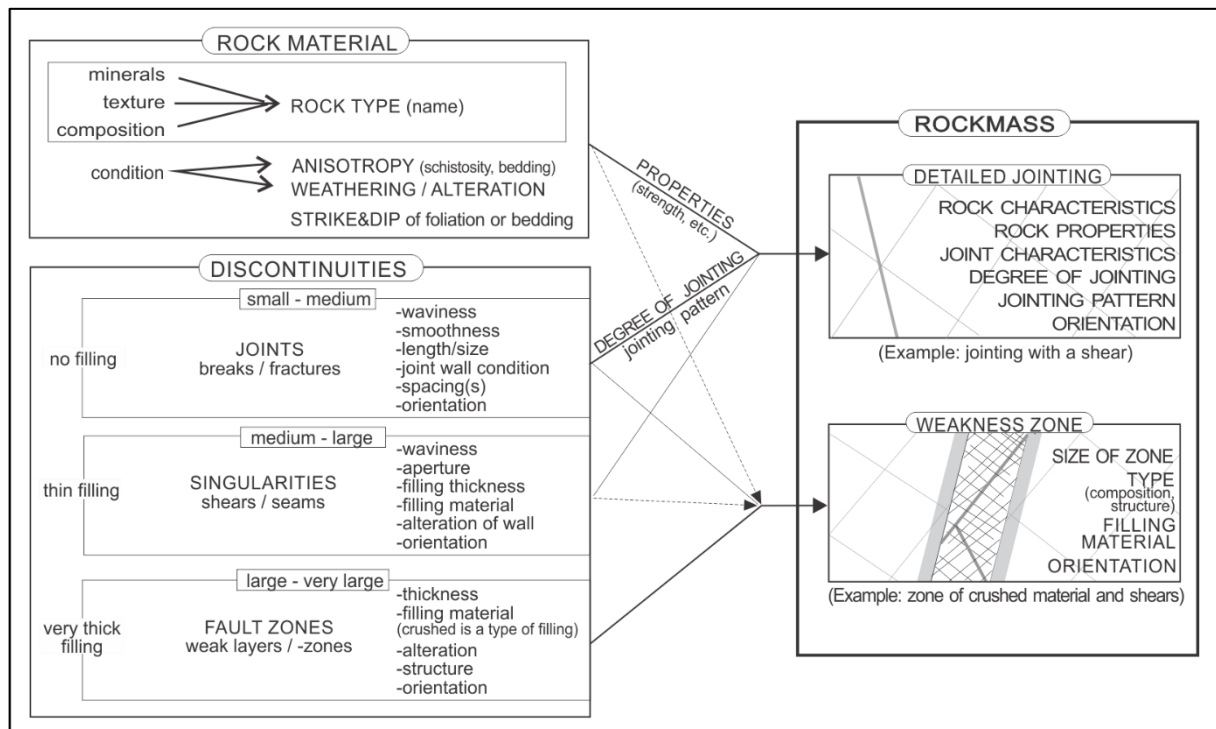


Figure 2.7: Rock mass features (Palmström, 2022).

Panthi (2006) suggest that the rock mass quality is mainly governed by rock mass strength, deformability properties, strength anisotropy, the characterises of the discontinuities (related to shear strength), and the degree of weathering. These properties will be covered later in this subsection. The rock mass can also be affected by weakness zones as illustrated in Figure 2.7.

*Weakness zones* is a body of rock mass with significantly lower mechanical properties compared to the surrounding rock mass. Furthermore, weakness zones can be thrust zones, weak mineral layers, shear zones, faults, etc. *Crushed zone* is a type of weakness zone with a core of crushed rock mass and gradual transition outwards to more intact rock (Nilsen & Palmström, 2000).

The rock mass quality is often described through rock mass classification systems which have both quantitative and qualitative elements. Hudson and Harrison (2000) describes rock mass classification systems as “[...] a comprise between the use of a complete theory and ignoring the rock properties entirely”. The use and development of these classification systems are consequence of the inability to apply the fundamental theories of rock mechanics into practical engineering circumstances, even with extensive site investigations (Hudson & Harrison, 2000).

Several rock mass classifications have been proposed over the years for different purposes. Table 2.2 shows some of the most utilized rock mass classification systems with their respective applications. Bieniawski (1989) lists the six main objectives for rock mass classifications as:

1. Identify the most significant parameters that are of influence for the behaviour of rock mass.
2. Divide rock masses of similar behaviour into rock mass classes.
3. Provide a description of the characteristics of each rock mass class.
4. Should be able to relate the rock conditions of one site to another.
5. Quantitative data and guidelines for engineering design should be provided.
6. The classification system should be understandable for both geologist and engineers.

Hoek (2007) emphasizes that considerable caution must be exercised when applying rock mass classifications to rock engineering problems that are not within the original design purpose. In Norway the conventional Q-method has often been utilized in the context of excavated rock slopes even though it was primarily designed for tunnelling and cavern. Barton and Bar (2015) introduced the Q-slope method designed for evaluating the rock mass conditions and stability for excavated rock slopes. Q-slope will be discussed in more detail in Subsection 2.5.1 and its similarities with the conventional Q-method.

Table 2.2: Classification systems for rock mass. Modified after Pantelidis (2009) Kliche (2018).

<b>Classification system</b>	<b>Abbreviation</b>	<b>Reference</b>	<b>Applications</b>
Rock loading	-	Terzaghi (1946)	Tunnels with steel support
Stand-up time	-	Lauffer (1958)	Tunneling
Intact rock strength	$\sigma_i$	Deere and Miller (1966)	Communications
Rock Quality Designation	RQD	Deere (1963); Deere et al. (1966)	General
Rock Structure Rating	RSR	Wickham et al. (1972)	Small tunnels
Rock Mass Rating	RMR	Bieniawski (1973)	Tunneling, mines, foundations, slopes
Rock Tunneling Quality Index	Q	Barton et al. (1974)	Tunneling, caverns
Geological Strength Index	GSI	Hoek (1994)	General
Rock Mass Index	RMi	Palmström (1995)	Rock design and engineering, communications

Rock Mass Strength	RMS	Selby (1980)	Excavated slopes
Slope Mass Rating	SMR	Romana (1985)	Excavated slopes
Slope Rock Mass Rating	SRMR	Robertson (1988)	Excavated slopes
Chinese Slope Mass Rating	CSMR	Chen (1995)	Excavated slopes
Rockslope Deterioration Assessment	RDA	Nicholson and Hencher (1997)	Excavated slopes
Slope Stability Probability Classification	SSPC	Hack (2002)	Excavated slopes
Fall Rock Hazzard Index	FRHI	Singh (2004)	Excavated slopes (temporary excavations)
Global Slope Performance Index	GSPI	Sullivan (2013)	Excavated slopes (temporary excavations)
Excavated rock slope stability	Q-slope	Barton and Bar (2015)	Excavated rock slope design

### 2.2.1.1 Rock mass strength

Panahi (2006) defines rock mass strength ( $\sigma_{cm}$ ) as the ability to withstand stress and deformation. The rock mass strength is difficult to estimate in in-situ or by laboratory investigations. Several authors over the years have proposed empirical estimations of rock mass strength. A common theme for most of them is the integration of the intact rock strength ( $\sigma_{ci}$ ), and the assumption of correlation between intact rock strength and rock mass strength. Table 2.3 presents a few of the most accepted estimation methods for rock mass strength. The suggested estimation by Panahi (2006) is the only of them which only integrates the intact rock strength and avoids the use of rock mass classifications (e.g., RMR, GSI, Q, and  $Q_c$ ).

Table 2.3: Approaches for estimation of rock mass strength. Modified after Panahi (2006).

Empirical model	Reference	Equation no.
$\sigma_{cm} = \sigma_{ci} \times e^{\left(\frac{RMR-100}{18.75}\right)}$	Bieniawski (1993)	(2.1)
$\sigma_{cm} = \sigma_{ci} \times s^a = \sigma_{ci} \times e^{\left[\frac{GSI-100}{9}\right]^a} = \sigma_{ci} \times e^{\left[\frac{RMR-105}{9}\right]^a}$	Hoek et al. (2002)	(2.2)
$\begin{aligned} \sigma_{cm} &= 5 \gamma \times Q_c^{1/3} = 5 \gamma \times \left[\frac{\sigma_{ci}}{100} \times Q\right]^{1/3} \\ &= 5 \gamma \times \left[\frac{\sigma_{ci}}{100} \times 10^{\frac{RMR-50}{15}}\right]^{1/3} \end{aligned}$	Barton (2002)	(2.3)
$\sigma_{cm} = \frac{\sigma_{ci}^x}{60}$	Panahi (2006)	(2.4)
$\sigma_{cm} = \sigma_{ci} \times 10^{0.013RQD-1.34}, \text{ for } RQD > 70\%$	Zhang (2010)	(2.5)

where

- $\sigma_{cm}$  = unconfined compressive strength of rock mass [MPa]  
 $\sigma_{ci}$  = uniaxial compressive strength of intact rock [MPa]  
 $s$  = Hoek-Brown failure criteria material constant (Equation 2.28)  
 $a$  = Hoek-Brown failure criteria material constant (Equation 2.29)  
 GSI = Geological Strength Index  
 RQD = Rock Quality Designation  
 $\gamma$  = rock material density [ $1000\text{kg/m}^3$ ]  
 $Q_c$  = normalized rock mass quality rating (Q-method)  
 $Q$  = rock mass quality rating (Q-method)  
 $x = 0.5$  for anisotropic rocks, and  $x = 0.6$  for isotropic, homogenous, and massive rocks

The most common practice to define the strength of rocks is through uniaxial compressive strength (UCS). The suggested classification for rock strength based on UCS by ISRM (1978d) is presented in Table 2.4. The classification system states that material with UCS < 0.25 MPa should be considered soil.

Table 2.4: Suggested classification for rock strength based on UCS (ISRM, 1978d).

Type	Classification	Uniaxial compressive strength [MPa]
Soil		<0.25
Rock	Extremely low strength	0.25 - 1
	Very low strength	1 - 5
	Lower strength	5 - 25
	Medium strength	25 - 50
	High strength	50 – 100
	Very high strength	100 - 250
	Extremely high strength	>250

Nilsen and Palmström (2000) defines a rock as a fabric of minerals and grains welded or bound together. A rock includes microscopic cracks and fissures, and with increased size it is reasonable to believe more microscopic cracks and fissures are introduced. During loading conditions close to peak-failure a smaller specimen will have to establish more crack growth and development compared to a bigger sample, thus the strength is reduced with size. Hoek and Brown (1980) suggested the correlation between the uniaxial compressive strength  $\sigma_{c(d)}$  of a specimen with diameter  $d$  [mm] and the uniaxial compressive strength of  $\sigma_{c(50)}$  of a standard 50 mm diameter sample as:

$$\sigma_{c(d)} = \sigma_{c(50)} \left( \frac{50}{d} \right)^{0.18} \quad (2.6)$$

This relationship is plotted in Figure 2.8 along the data points it is based on.

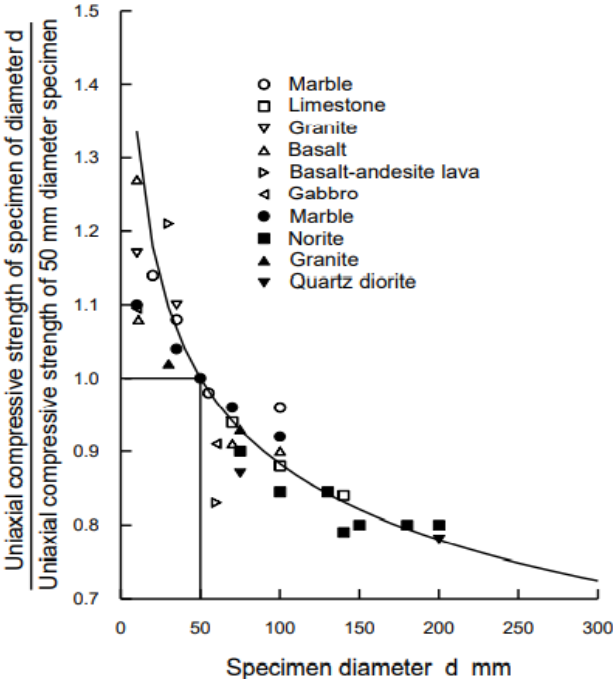


Figure 2.8: Specimen size influence on the strength of intact rock (Hoek & Brown, 1980).

**2.2.1.2 Rock mass deformation**

The rock mass deformation modulus ( $E_{rm}$ ) is an important parameter in rock mechanics and engineering. The use case ranges from building numerical models in rock engineering projects to determining rock mass responses in stressed or recently stressed conditions (Panthee et al., 2018). Gokceoglu et al. (2003) have illustrated that the deformation modulus is the most representative parameter of pre-failure mechanical behaviour of the rock mass and rock material.

In-situ testing of  $E_{rm}$  is possible through different types of hydraulic jacking tests. However, a common theme is the high expenses associated with the testing as well as being time consuming and difficult to perform. Since the determination of  $E_{rm}$  is such a difficult task several authors over the years have suggested empirical equations to estimate it. Table 2.5 presents some of the estimations for  $E_{rm}$ . A common theme for these equations is the integration of classification parameters such as RMR, Q, GSI, RMI etc. These methods are based on subjective elements in the rock mass characterization process. Panthi (2006) introduced a method that avoided this subjective element. It is based on the premises of an isotropic, homogenous, and massive rock mass. Given these conditions the ratio between rock mass strength and intact rock strength, and the ratio between deformation modulus and elasticity modulus for intact rock should be equal (in theory).

Table 2.5: Proposed estimations for rock mass deformation modulus. Modified after Panthi (2006) Nilsen and Palmström (2000).

Empirical model	Reference	Equation no.
$E_{rm} = 2 \times RMR - 100$ , for $RMR > 50$	Bieniawski (1978)	(2.7)
$E_{rm} = 10^{\left(\frac{RMR-10}{40}\right)}$ , for $30 < RMR \leq 50$	Serafim and Pereira (1983)	(2.8)
$E_{rm} = 25 \times \log_{10} Q$ , for $Q > 1$	Grimstad and Barton (1993)	(2.9)
$E_{rm} = 5.6 \times RMi^{0.375}$ , for $RMi > 0.1$	Palmström (1995)	(2.10)
$E_{rm} = \left(\frac{\sigma_{ci}}{100}\right)^{0.5} \times 10^{\left(\frac{GSI-10}{40}\right)}$ , for $\sigma_{ci} < 100$ MPa	Hoek and Brown (1997)	(2.11)
$E_{rm} = 0.1 \times \left(\frac{RMR}{10}\right)^3$ , for $RMR \leq 100$	Read et al. (1999)	(2.12)
$E_{rm} = 10 \times Q_c^{\frac{1}{3}} = 10 \times \left(\frac{Q \times \sigma_{ci}}{100}\right)^{\frac{1}{3}}$	Barton (2002)	(2.13)
$E_{rm} = E_{ci} \times 10^{0.0186RQD-1.91}$	Zhang and Einstein (2004)	(2.14)
$E_{rm} = \frac{E_{ci} \times \sigma_{ci}^x}{60}$	Panthi (2006)	(2.15)
$E_{rm} = E_{ci} \times \left(0.02 + \frac{1-\frac{D}{2}}{1+e^{\left(\frac{60+15D-GSI}{11}\right)}}\right)$	Hoek and Diederichs (2006)	(2.16)

where

$E_{rm}$  = rock mass deformation modulus [GPa]

$RMR$  = geomechanics rock mass rating

$GSI$  = Geological Strength Index

$RQD$  = Rock Quality Designation

$Q$  = Q-value

$RMi$  = Palmström's rock mass index

$E_{ci}$  = modulus of elasticity of intact rock [GPa]

$Q_c$  = Normalized Q-value

$x = 0.5$  for anisotropic rocks, and  $x = 0.6$  for isotropic, homogenous, and massive rocks

$D$  = disturbance factor

Read et al. (1999) states that the rock mass deformability should not exceed the modulus of intact rock. Thus, any empirical methods used for estimating the deformability should take the intact rock material properties into account. Figure 2.9 illustrates the inter-relationships between the methods suggested by Bieniawski (1978), Barton (2002), and Serafim and Pereira (1983). This illustrates the users of these methods should be aware of these deviations and select the equation accordingly.

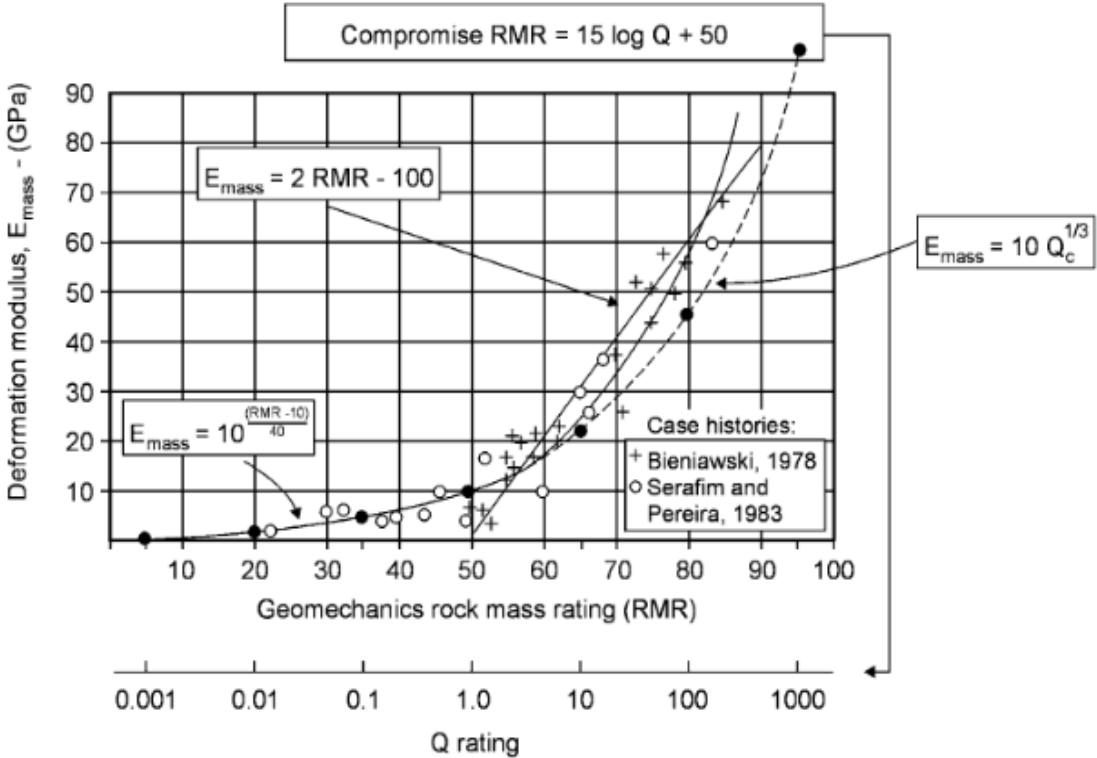


Figure 2.9: Empirical inter-relationships for Bieniawski (1978), Barton (2002), Serafim and Pereira (1983) approaches of estimating rock mass modulus  $E_m$  denoted  $E_{mass}$  on the figure (Barton, 2002).



### 2.2.1.3 Anisotropy and inhomogeneity

Hudson and Harrison (2000) defines an anisotropic rock as a rock with different properties in different directions. This can include properties such as brittleness, strength, deformability, permeability, and discontinuity frequency etc. However, an inhomogeneous rock has different properties at different locations, and refers to the mentioned properties. To characterize inhomogeneity statistical methods can be used while anisotropy is sometimes built into fundamental definition of the property itself (e.g., intact rock strength which has a compliance matrix that can contain up to 21 elastic constants and thus able to represent all possible types of elastic anisotropy).

Hudson and Harrison (2000) further emphasises that anisotropy and/or inhomogeneity can be on all scales from mineral grains to engineering structure-sized volumes of rock mass, and the variation can be gradual or sudden. The two opposites when modelling can be described through the acronyms CHILE (continuous, homogeneous, isotropic, and linearly-elastic) and DIANE (discontinuous, inhomogeneous, anisotropic, and non-elastic). CHILE was the traditional assumption for the purpose of modelling, but computational methods can now deal with deviations from these criteria. When modelling a rock mass as DIANE conditions, the likelihood for errors rises drastically. A rock with the CHILE assumptions is often not realistic, and in most scenarios the rock mass should be evaluated with criteria representing something in between.

Nilsen and Palmström (2000) states that rock anisotropy is caused by foliation, schistosity, bedding, or layering. The degree of anisotropy is a function of the amount and arrangement of certain anisotropic and elastic minerals (e.g., chlorite, mica, amphiboles, and certain pyroxenes).

The effect of anisotropy in respect to the strength of the rock can be described through several relations. One such method is the *anisotropy factor*,  $f_A$ , as described below (Nilsen & Palmström, 2000):

$$f_A = \frac{\sigma_{ci \max}}{\sigma_{ci \min}} \quad (2.17)$$

where  $\sigma_{ci \max}$  is the maximum compressive strength of intact rock, and  $\sigma_{ci \min}$  is the minimum compressive of intact rock.

An alternative method (often considered more accurate) is the *Strength Anisotropy Index*,  $I_{a(50)}$ , introduced by ISRM (1985) which is expressed as:

$$I_{a(50)} = \frac{I_{s(50)\parallel}}{I_{s(50)\perp}} \quad (2.18)$$

where  $I_{s(50)\parallel}$  is the Point Load Strength Index parallel to planes of weakness, and  $I_{s(50)\perp}$  is the Point Load Strength Index perpendicular to planes of weakness.

Figure 2.10 illustrates that the uniaxial compressive strength of intact rocks is the lowest when the loading angle ( $\beta$ ) to the planes of weakness (schistosity) are the lowest at around 30°. Furthermore, the UCS is highest when the loading angle is perpendicular to the planes of weakness. The anisotropy factor ( $f_A$ ) for the tested rocks in the figure are between 2-7. For rocks with anisotropy this important to be mindful of during testing and designing of structures on or in rock masses.

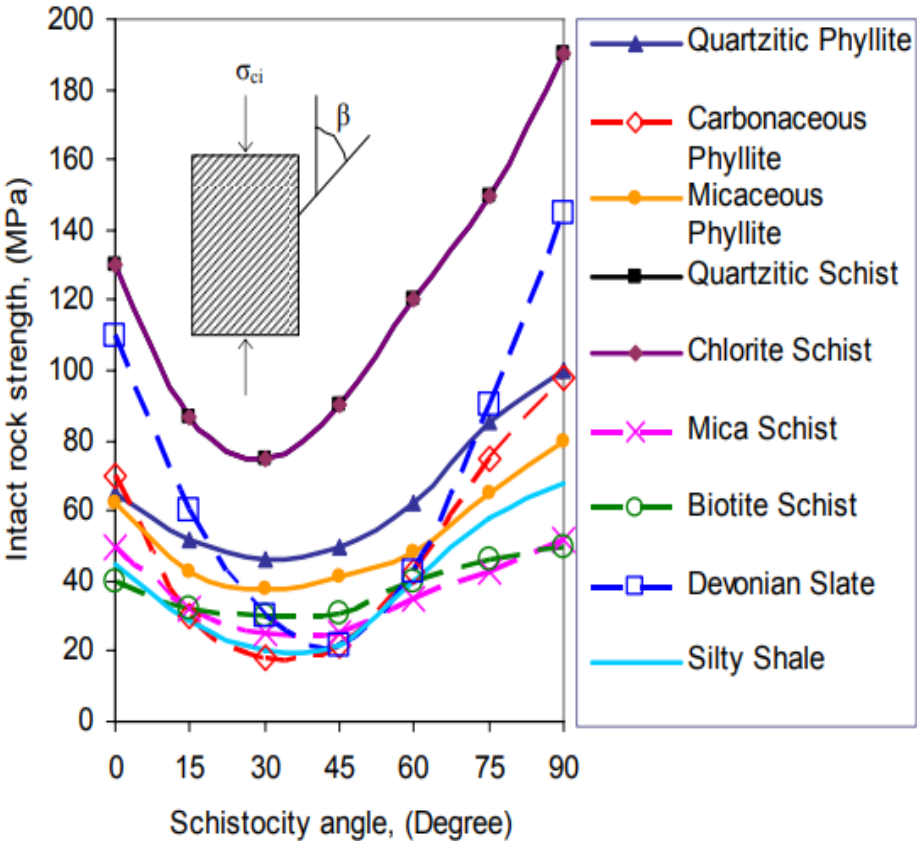


Figure 2.10: Uniaxial compressive strength at different loading angles ( $\beta$ ) to schistosity planes of selected rocks (Panthi, 2006).

Nilsen and Palmström (2000) states that the use of  $I_{a(50)}$  often is considered more reliable compared to  $f_A$ . Panthi (2006) reasons that the point load test will measure the induced tensional strength, thus resulting in a maximum strength perpendicular to the planes of weakness and a minimum parallel to the planes of weakness, which can be argued to be a more accurate method to estimate the anisotropy.

### 2.2.1.4 Discontinuities

Nilsen and Palmström (2000) defines a discontinuity as any geological or structural feature in a rock that result in changes in the homogeneity of the rock. Discontinuities have zero or close to zero tensile strength in the rock mass. Furthermore, the scale of the discontinuities varies a from a few centimetres to several kilometres in extent. Discontinuity is used a collective term, and a summary of the most important discontinuities with characteristics are listed in Table 2.6. Factors influencing the shear strength of discontinuities are: (1) the roughness characteristics, (2) nature of the contact, (3) degree (and type) of weathering, (4) type and amount of filling material, and (5) groundwater susceptibility. This is a result of different origins, age, history of development. This also means the engineering significance of the different types of discontinuities will vary (Nilsen & Palmström, 2000). Figure 2.11 illustrates possible discontinuity characteristics for a rock mass.

Discontinuities are primarily tectonically induced, and Nilsen and Palmström (2000) divides discontinuities into three main groups: rock defects, joints, and weaknesses. In the context of rock engineering the two latter are the most important.

Hudson and Harrison (2000) emphasises that discontinuities can be the most important governing factor for the strength, permeability, and deformability for rock masses. Furthermore, it is extremely rare that the spacing of the discontinuities are greater than the dimensions of the (rock engineering) project.

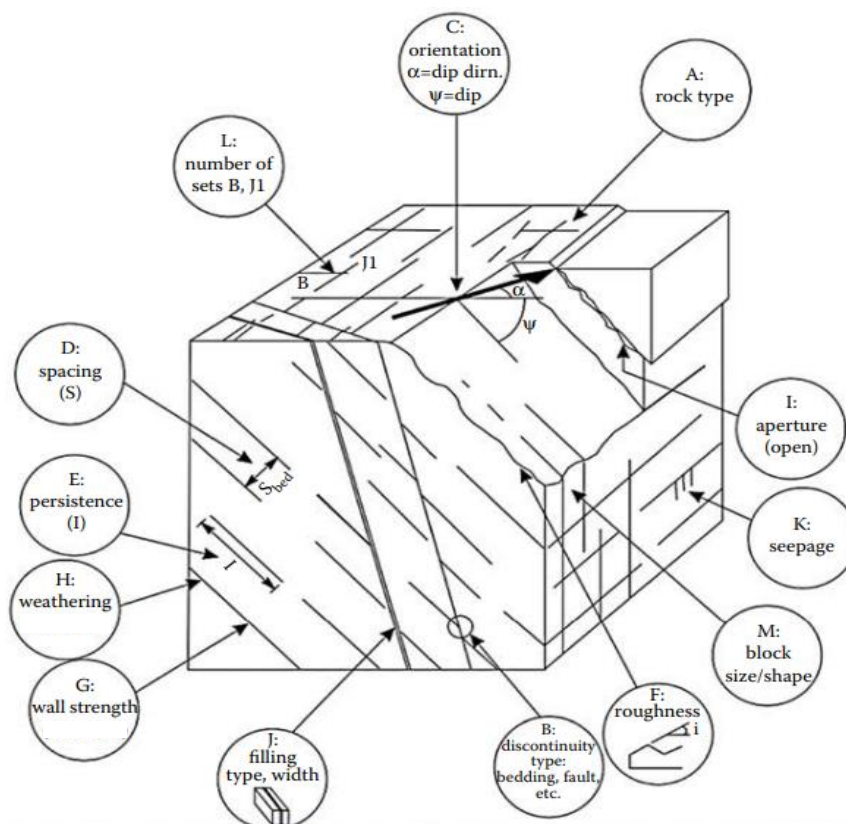


Figure 2.11 Discontinuity characteristics for a rock mass. Modified after Wyllie (2018).

There have been several discussions around the terminology around discontinuities. ISRM (1975) defines a joint as: “Joint is a discontinuity plane of natural origin along which there has been no visible displacement”. A summary of the types of discontinuities with descriptions are given in Table 2.6. The terminology is mainly divided two main groups: (1) based on composition and size or (2) based on origin (Nilsen & Palmström, 2000).

Table 2.6: Description of discontinuity types. Modified after Nilsen and Palmström (2000).

<b>Type of discontinuities</b>	<b>Description</b>	<b>Reference</b>
<b><i>Discontinuity definitions based on composition and size</i></b>		
Crack	“A small, partial or incomplete discontinuity.”	ISRM (1975)
Fracture	“A general term used in geology for all kinds of discontinuities caused by mechanical stresses in the bedrock. Fractures include joints and cracks and faults. It is suggested not to use this term in rock engineering and engineering geology.”	Palmström (2019)
Parting	“1) Small discontinuities in rock, such as foliation or bedding partings. 2) A small joint in coal or rock.”	Palmström (2019)
Rupture	“A fracture or discontinuity caused by excavation works or other human activities.”	Nilsen and Palmström (2000)
Seam	“1) a minor, often clay-filled zone with a thickness of a few centimetres. When occurring as a weak clay zone in a sedimentary sequence, a seam can be considerably thicker. Otherwise, seams may represent very minor faults or altered zones along joints, dikes, beds or foliation. 2) a plane in a coal bed at which the different layers of coal are easily separated.”	Palmström (2019)
Shear	“A discontinuity formed by shear movement, often occurring as a "seam" or "shear zone".”	Palmström (2019)
Singularity	“Small weakness zone or seam.”	Palmström (2019)
<b><i>Discontinuity definitions based on origin</i></b>		
Bedding joint/ bedding parting	“Discontinuity developed along the bedding planes in sedimentary rocks.”	Nilsen and Palmström (2000)
Cooling joints	“Joint formed by the cooling of an igneous, pyroclastic, or other heated rock body.”	Palmström (2019)
Exfoliation joint	“Discontinuity developed by a splitting off from bare rock surfaces due to the action of chemical or physical forces, such as differential expansion and contraction during heating and cooling over the daily temperature range. They also include sheeting joints.”	Nilsen and Palmström (2000)

Foliation	“Parallel orientation of platy minerals, or mineral banding in metamorphic rocks.”	Wyllie (2018)
Sheeting joint	“Joint developed more or less parallel to the surface of the ground, especially in plutonic igneous intrusions such as granite; probably as a result of the unloading of the rock mass, for example when the cover is removed from erosion.”	Nilsen and Palmström (2000)
Tectonic joint	“Discontinuities formed from the tensile stresses accompanying uplift or lateral stretching, or from the effects of regional tectonic compression.  “Commonly occur as planar, rough-surfaced sets of intersecting joints, with one or two of the sets usually dominating in persistence.”	ISRM (1975)  Nilsen and Palmström (2000)

Nilsen and Palmström (2000) states that filling in discontinuities can come from breakage of country rocks (from movements such as for breccias or crushed zones), infilling material deposited in structural planes, in-situ weathered materials (such as alteration products), and intruded materials which differs from the host rock. Nilsen and Palmström (2000) further suggest six main groups for fillings as: (1) hard and resistant minerals, (2) soft minerals, (3) soluble minerals, (4) swelling minerals, (5) swelling minerals, and (6) loose minerals.

Barton (1978) further states that the physical behaviour of the filling material mainly depends mainly on the eight factors: (1) mineralogy of the filling material, (2) grading or particle size, (3) over-consolidation ratio, (4) water content and permeability, (5) previous shear displacement, (6) wall roughness, (7) width, and (8) fracturing or crushing of wall rock.

Further discussion on topics related to the shear strength of discontinuities will be covered in Subsection [2.4.2](#).

### 2.2.1.5 Susceptibility to alteration and weathering

Weathering of rock masses a natural process near the earth's surface but can sometimes also be altered by hydrothermal processes (Palmström & Stille, 2015). In general, the weathering and/or alteration propagates through the discontinuities first and affect the discontinuity walls, and then migrates to the rest of the rock mass and its exposed minerals (Panthi, 2006). The processes can change the behaviour of the rock mass and the mechanical properties completely. The effects ranges from altered strength and deformation characteristics to changes in the physical behaviour. In practical terms, the weathering degree is often expressed as the changes in the mechanical and physical properties of the rock material. These processes are likely to significantly influence the engineering characteristics of the rock mass (except for weaker rock types), thus detailed characterisation and descriptions are important (Köken et al., 2016; Palmström & Stille, 2015).

External factors such as temperature changes, freeze-thaw cycles, biological, precipitation, and reactive components from the groundwater are some of the key contributors to these processes. Furthermore, the effects are decreasing in general as the depth increase, as illustrated in Figure 2.12.

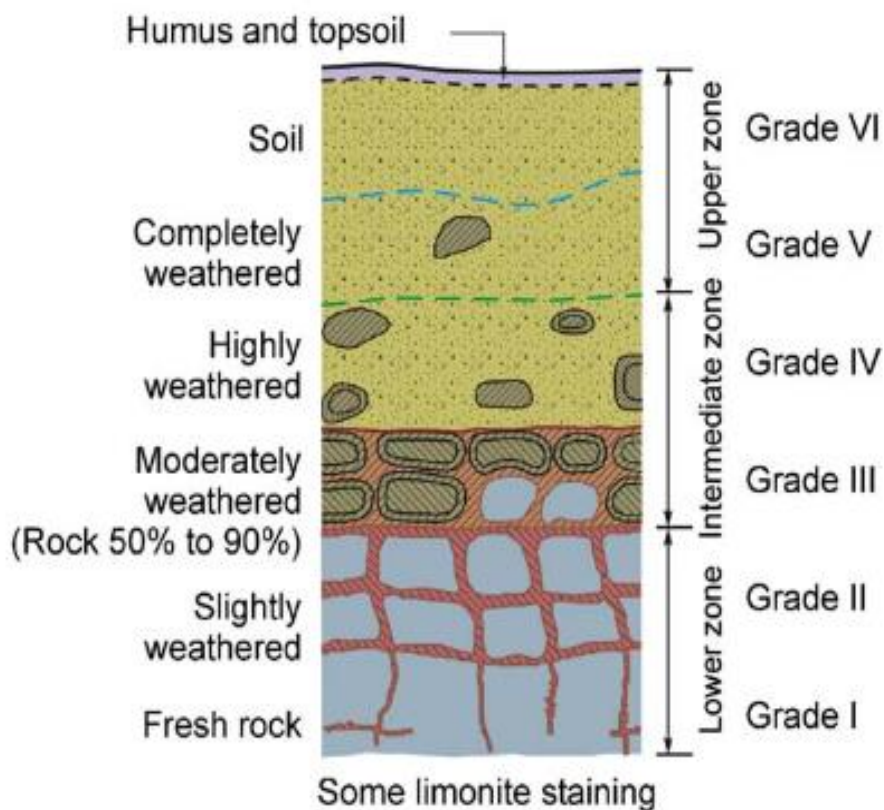


Figure 2.12: Typical weathering profile (Rahardjo et al., 2004).






The main effects from alteration and weathering of rock mass are divided into (ISRM, 1978c; Nilsen & Palmström, 2000; Palmström & Stille, 2015; Panthi, 2006):

- 1) **Mechanical disintegration** is the physical breakdown of the rock mass, and the result of frost wedging, expansion related to changes in the stress conditions, dynamic activity, or thermal expansion. It is typically located in the upper zone of weathering. The resulting effects are:
  - Increased joint openings
  - Development of new joints along grain boundaries
  - Fracturing and splitting of individual mineral grains
  
- 2) **Chemical decomposition** involves rock decay thus resulting in changes of the mineralogical and chemical composition. The resulting effects are:
  - Rock discoloration and staining
  - Leaching (or solution) of anhydrite, calcite, and salt minerals
  - Decomposition of complex silicate minerals into clay minerals (e.g., amphibole, mica, and feldspar) as the final end-products
  - Worsened discontinuity conditions such as filling material and friction
  - Worsened rock mass properties such as stiffness, sound velocity, and strength

The changes in physical and mechanical properties from weathering can be determined by P-wave velocity, point load strength, uniaxial compressive strength, changes in porosity, and Schmidt rebounding number. The weathering degree can also be determined by chemical and petrographical analysis. Determining the changes in texture and colour, discontinuity spacing, and RQD of the rock material are also helpful when determining the weathering degree (Beavis, 1985; Köken et al., 2016).

The engineering classification system for weathered rock mass as suggested by ISRM (1978d) is presented in Table 2.7 along with the corresponding alteration factor  $f_w$  proposed by Palmström (1995). It is divided into six weathering classes/grades and corresponding illustrations from ISRM (1981) are also included illustrations.

Table 2.7: Engineering classification system for weathered/altered rock mass ISRM (1978d) with corresponding suggested alteration factor ( $f_w$ ) Palmström (1995). The illustrations are from ISRM (1981).

Class/ grade	Term	Description	Rating ( $f_w$ )	Illustration
I	Unweathered	No visible sign of rock material weathering; perhaps slight discolouration on major discontinuity surfaces.	1	
II	Slightly weathered	Discoloration indicates weathering of rock material and discontinuity surfaces. All rock material may be discoloured by weathering and may be somewhat weaker externally than in its fresh condition.	1.75	
III	Moderately weathered	Less than half of the rock material is decomposed and/or disintegrated to a soil. Fresh discoloured rock is present either as a continuous framework or as corestones.	2.5	
IV	Highly weathered	More than half of the rock material is decomposed and/or disintegrated to a soil. Fresh discoloured rock is present either as a discontinuous framework or as corestones.	10	
V	Completely weathered	All rock material is decomposed and/or disintegrated to a soil. The original mass structure is still largely intact.		
VI	Residual soil	All rock material is converted to soil. The mass structure and material fabric are destroyed. There is a large change in volume, but the soil has not been significantly transported.		

The alteration reduction factor ( $f_w$ ) as shown in Table 2.7 can be used to estimate the point load strength for weathered rocks as seen below (Palmström, 1995):

$$I_{S\ 50} = \frac{I_{S\ 50\ fresh}}{f_w} \quad (2.19)$$

where  $I_{S\ 50}$  is the point load strength for a standard 50 mm thick sample of weathered rock [MPa], and  $I_{S\ 50\ fresh}$  is the point load strength for a standard 50 mm thick sample of fresh rock (unweathered) [MPa].

(Nilsen & Palmström, 2000) further discusses that the uniaxial compressive strength can be estimated by the assumption of similar reduction as for point load strength. This can be done by introducing the correlation factor  $k_{50}$  (for 50 mm thick samples) to the point load strength as seen below:

$$\sigma_c = \frac{\sigma_c\ fresh}{f_w} = k_{50} \times \frac{I_{S\ 50\ fresh}}{f_w} \quad (2.20)$$



where  $\sigma_c$  is the uniaxial compressive strength of weathered rock [MPa], and  $\sigma_{c\ fresh}$  is the uniaxial compressive strength of fresh (unweathered) rock [MPa].

Singh and Gahrooe (1989) presents another practical way to define the degree of weathering. This is called the *relative alteration factor*  $W_c$  and is expressed as the ratio between the uniaxial compressive strength of fresh rock  $\sigma_{c\ fresh}$  [MPa] and the joint wall compressive strength (strength of discontinuity surface)  $JCS$  [MPa] as described below:

$$W_c = \frac{\sigma_{c\ fresh}}{JCS} \quad (2.21)$$

It should be noted that  $W_c$  is in practice the inverse of Strength Retention Index (SRI) which is another popular method to define the degree of weathering  $\left(\frac{\sigma_{c\ weathered}}{\sigma_{c\ fresh}}\right)$  (Köken et al., 2016).

Barton and Choubey (1977) states that  $W_c$  is a useful indication for the character of joint weathering or alteration. The relative alteration is also relevant in terms of the amount of asperity damage for a respective joint roughness. In other words, a high value of  $W_c$  will result in more asperity damage due to lower strength of the discontinuity surface relative to the compressive strength of the fresh rock. This means reduced shear strength for the discontinuity surface. The opposite is true for a low value of  $W_c$ .

Possible weathering effects on rock mass can be summarized as (1) strength reduction, (2) loss of slaking durability, (3) reduced frictional resistance, (4) reduced density (in most cases), and (5) increased permeability (Barton & Choubey, 1977; Panthi, 2006). Figure 2.13 (left) displays the reduction of uniaxial compressive strength with increased weathering grades for selected rocks. The results suggest that crystalline rocks suffer from a higher degree of strength loss compared to metasedimentary and sedimentary rocks. Furthermore, Figure 2.13 (right) displays the percentage uniaxial compressive strength reduction plotted against weathering grade with the minimum, mean, and maximum curves for the plot. This plotted from the empirical formula as proposed by Panthi (2006):

$$y = 57.44 \ln(x) - 2.1114 \quad (2.22)$$

where  $y$  is strength reduction by percentage, and  $x$  is the weathering grade and only grade II to IV is valid.

Equation 2.22 can also be rearranged to calculate  $\sigma_{c\ weathered}$  directly from  $\sigma_{c\ fresh}$ :

$$\sigma_{c\ weathered} = \sigma_{c\ fresh} \times \left(1 - \frac{57.44 \ln(x) - 2.1114}{100}\right) \quad (2.23)$$

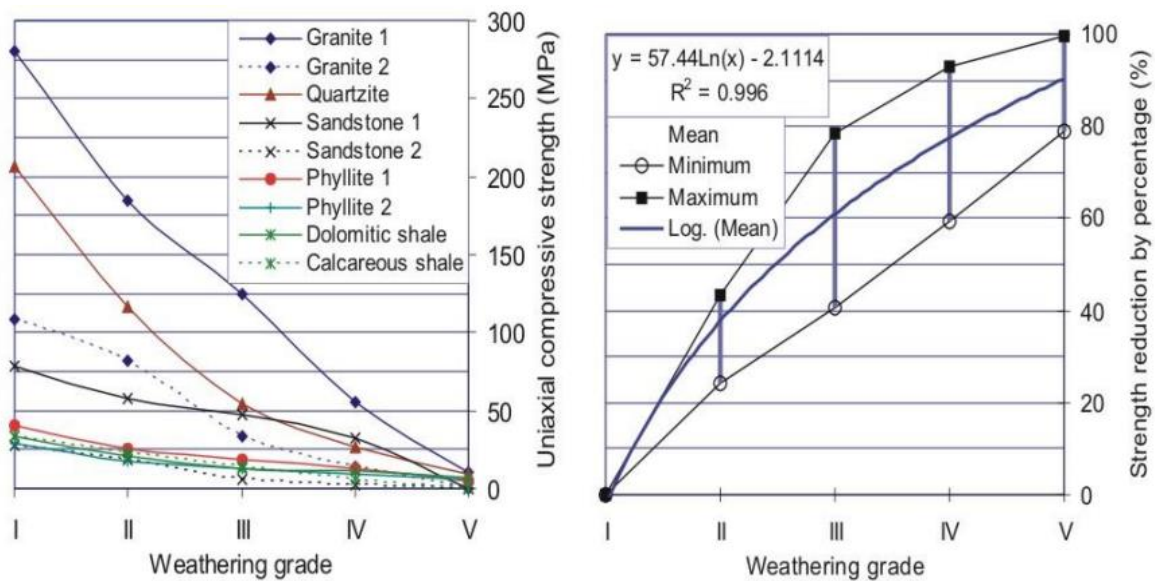


Figure 2.13: Uniaxial compressive strength for selected rocks at different weathering grades (left). Plotted reduction of uniaxial compressive strength by percentage versus weathering grade (right) (Panthi, 2006).

## 2.2.2 Slope configuration

The slope configuration is important for the stability, and the elements can be summarized as shown below (Hack, 2002):

- Height
- Angle
- Curvature
- Aspect
- Bench configuration

Reduction in height or angle will reduce the driving forces. However, it will also result in a reduction of the normal stresses, thus reducing the friction along potential sliding surfaces. Adding benches to a slope or increasing the width of benches will decrease the overall slope angle. Benches are also useful for catching or damping rock fall. It will also reduce the stress concentration in the foot of an excavated rock slope (Nilsen, 1979). Benches also makes the overall slope more accessible during and after the construction. This is beneficial in terms of the installation process of stability and protection measures, but also the maintenance and inspection later (Wyllie, 2018).

The curvature of the slope is also important for the slope stability. Concave slopes tend to have compressive horizontal tangential stresses. Rocks are stronger in compression than tension, thus a concave slope will be stabilizing. The opposite is true for convex slopes which will be acting destabilizing (Hoek et al., 2009).

The aspect (orientation) of slope dictates how discontinuities will intersect it. Furthermore, it is important in terms of the orientation relative to the in-situ rock stresses.

## 2.2.3 External influences

This subsection will give a brief introduction to what is considered the most important external influences on the rock slope stability and is based on Figure 2.6.

### 2.2.3.1 Seismic events

Risk assessment related to seismic events should be done based on (1) seismological and (2) geotechnical information (Nilsen & Palmström, 2000):

1. Seismological information:
  - Historical data for earthquake occurrence, magnitudes etc.
  - Distance to faults.
  - Historical data of movements along the faults, magnitude measurements of offset, and recurrence intervals.
2. Geotechnical information:
  - Stratigraphic section with properties for the respective layers.
  - Location of groundwater table.
  - Geophysical data such as shear wave velocity.

Seismic design is related to the design process with the potential consequences of earthquakes in mind. In general, the following terms are used (Nilsen & Palmström, 2000):

- **Maximum Design Earthquake (MDE):** is used for the earthquakes with a return period of several thousands of years. The probability of occurrence is less than 5% for the design life. MDE is used for dimensioning critical elements of public safety importance level and avoid catastrophic failures which can result in loss of life.
- **Operating Design Earthquake (ODE):** is used for earthquakes with a return period of several hundred years. In general, the likelihood of an earthquake with this magnitude to occur during the lifetime of this construction is around 40%. ODE is used for dimensioning critical elements such that as they maintain function.

The effects of seismic events on rock slope stability can be hard quantify and predict. Furthermore, the regulations for how to it should be calculated is not consistent (NPRA, 2020).

Eurocode 8 (EC8) which is using the partial factor principle (Subsection 2.5.4) is based on a pseudo-statistical principle. This means that the maximum earthquake load is considered as an equivalent horizontal load (as this is considered the most unfavourable direction). Thus, the earthquake load is decomposed similarly as any other force acting on the rock slope stability. EC8 requires seismic action to be included in slope stability assessments. The dimensioning value for seismic acceleration is selected according to the National Annex (NA) for EC 8 (CEN, 2013; Nilsen, 2017).

The *seismic acceleration* is defined as  $a_{g40Hz}$  and is based on ODE. Figure 2.14 illustrates that  $a_{g40Hz}$  varies between 0.2-1.0  $m/s^2$  in Norway and around 0.35  $m/s^2$  (or 0.0357  $g$ ) for Hommelvik). The reference peak value for the rock mass  $a_{gR}$  is set to as factor of 0.8 of  $a_{g40Hz}$ . The design ground acceleration  $a_g$  can be calculated as (NPRA, 2020):

$$a_g = \gamma_I \times a_{gR} = \gamma_I \times 0.8a_{g40Hz} \quad (2.24)$$

where  $\gamma_I$  is the partial factor for seismic acceleration (1.4 for type III construction which a tall road cut can be assumed to be). In the case for Hommelvik  $a_g$  would be 0.392  $m/s^2$  (1.4 x 0.8 x 0.35).

The dimensioning seismic horizontal force (equivalent horizontal load)  $F_a$  [kN] can be calculated as (NPRA, 2020):

$$F_a = m \times a_g = \frac{G}{g} \times a_g \quad (2.25)$$

where  $m$  is the mass of the unstable section of the rock slope [kN/m], and  $a_g$  is now described as a fraction of the gravity constant  $g$ .

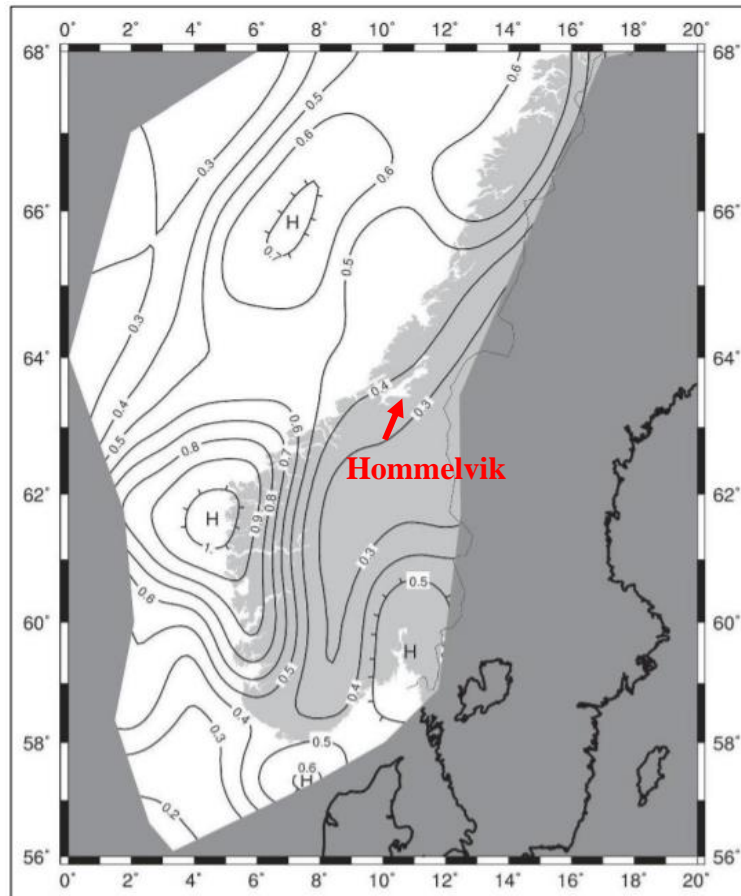


Figure 2.14: Seismic zones in Norway,  $a_{g40Hz}$  [ $m/s^2$ ]. The red arrow indicates the location of Hommelvik (StandardNorge, 2016) .

### 2.2.3.2 Hydrogeological & climatic conditions

Rocks in Norway have in general poor primary permeability, and good secondary permeability (from discontinuities). The ground water conditions are thus related to the secondary permeability combined with climatic and hydrological conditions. There are in general six factors for how water can decrease the stability of a rock slope (Grøneng, 2010; Nilsen, 2016; Wyllie, 2018).

1. Groundwater reduces the normal stress (effective stress) on the potential sliding plane.
2. Groundwater pressure in tensile cracks (or other steep discontinuities) will increase the driving forces.
3. Water will reduce the internal friction for certain filling materials in discontinuities, and active minerals will also expand given the supply of water. These active minerals will swell (expand) causing a pressure on the discontinuity walls, thus increase the driving forces.
4. Water will expand about 9% during freezing. This expansion can result in movement, detachment of blocks, and establishment of new blocks. The ice can also block the drainage in the rock mass. If the water is not able to freeze below 0°C (no room to expand), it will get sub-cooled, and will apply a stress of ca. 12 MPa per °C below 0°C on the surrounding rock mass.
5. Seepage (or flowing water) will increase the weathering which will result in a decreased strength of the rock mass.
6. Seepage (or flowing water) can also result in erosion of rock mass itself, along the discontinuities, or the removal of infillings in the discontinuities which will in most cases reduce the shear strength.

The groundwater conditions can be hard to determine and there are significant seasonal fluctuations. The triangular distribution, as seen in Figure 2.15 (a), is often used as the ‘‘worst-case’’ scenario to model the water pressure during heavy rainfall even though the values are often much lower in reality. Figure 2.15 (b) illustrates a groundwater distribution with full hydrostatic pressure. This scenario can occur if the toe of the rock slope is blocked by means such as concrete or ice, but a complete sealing of the toe rarely occurs (Nilsen & Palmström, 2000)

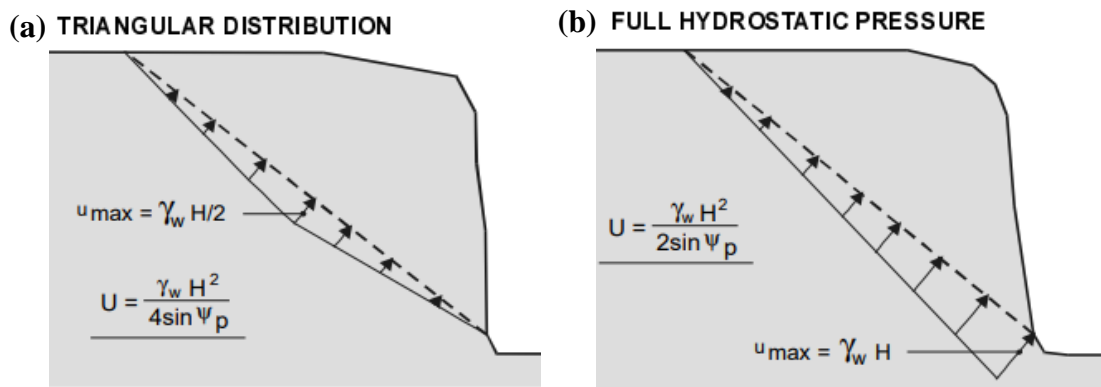


Figure 2.15: Configurations for groundwater pressure distribution along a potential sliding plane. Maximum resultant pressure is denoted  $u_{max}$  while resultant pressure is denoted  $U$ . (a) Triangular distribution; (b) full hydrostatic pressure. Modified after (Nilsen & Palmström, 2000).

Wyllie (2018) list three important factors that contribute to the ground water conditions in addition to the anisotropy and heterogeneity of the rock mass.

1. Low-persistent joints which do not intersect the slope face may result in high-transient water pressures compared persistent, as illustrated in Figure 2.16 (a). Persistent joints which intersect the slope face can drain, thus reduce the water pressure.
2. The porosity of a rock mass will dictate the transient water table during a precipitation event. A rock mass with high porosity will be able to contain the infiltrating water from the precipitation event, and there will be little changes in the ground water table. This is illustrated in Figure 2.16 (b) for a rock mass with high primary porosity. In comparison, a rock mass with low porosity, typically rock masses with wide joint spacing, will have its jointed rapidly filled with water during the precipitation event, thus rapidly increase the water pressure, as seen in Figure 2.16 (c).
3. Faults and weakness zones with high concentrations of weathered material (clays) act as a ground water barrier (Figure 2.16 (d)). The opposite is true for faults and weakness zones which contain a majority of broken or crushed rock material. The conductivity will be high for these and will act as natural drains (Figure 2.16 (e)).

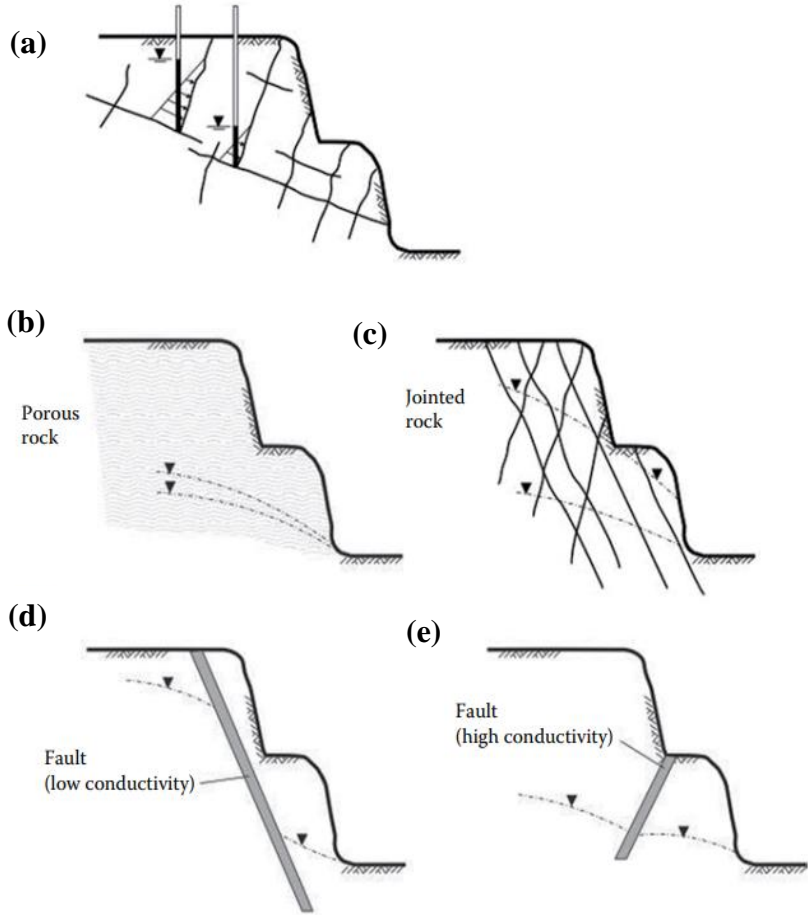


Figure 2.16: Groundwater conditions for different geological settings; (a) low-persistent joints; (b) porous rock; (c) jointed rock; (d) low conductivity fault; and (e) high conductivity fault. Modified after Wyllie (2018).

### 2.2.3.3 Virgin rock stresses

Nilsen and Palmström (2000) defines the stress prior to excavation as *virgin rock stresses* but is often referred to as in-situ rock stress. The in-situ rock stresses at the location of rock slope are important for the stability. Duncan and Goodman (1968) emphasizes that the final stress state from an excavation is sensitive to the pre-existing state of stress. While it is obvious that high stress conditions are problematic for the stability, low stress levels may be problematic too. It can cause instabilities as the normal stress is an important component of the stability of a jointed rock mass (Nilsen & Palmström, 2000).

The virgin rock stresses are the product of the following components (Nilsen & Palmström, 2000):

1. *Gravitational stresses*, result of the gravity alone (from the weight of a rock mass).
2. *Topographic stresses*, when the surface is not horizontal, the topography will affect the stress conditions. It will result in be stress concentrations in valleys while ridges will get stress relief. The principal stresses  $\sigma_1$  and  $\sigma_2$  will be rotated to become parallel with the slope surface, while  $\sigma_3$  will be reoriented perpendicular to the surface (Simonsen & Li, 2019).
3. *Tectonic stresses*, due to relative displacements between tectonic plates.
4. *Residual stresses*, remnant stresses which have been locked into the rock material during earlier geological events.

It should be noted that some authors do not include topographic stress as an induvial stress component and argues it is only gravitational stresses.

The stress conditions for an excavated rock slope can be estimated by numerical or analytical methods. In general, the excavation will result in an unloading situation, and can result in both tension and compression stress, with significant differences (Palmström & Stille, 2015).

The role of virgin rock stresses has traditionally been ignored in rock slope analysis due to (Wyllie, 2018):

- Limit equilibrium methods (Subsection 2.5.3 and 2.5.4) do not include the effect of stresses.
- Slope stability analyses were originally performed for soils which have a lower range of possible in-situ stress range, thus being easier to predict.
- Most rock slope failures are thought to be gravity driven and the assumption has been that the effects of the virgin stresses were minimal.
- In-situ rock stresses have rarely been measured for rock slopes, and their effects are unknown to some degree.

### 2.2.3.4 Excavation technique

The stability of high steep road cut during the excavation phase is one of the key difficulties for any project. A poorly conducted excavation can result in construction delays and a weakened rock mass which will reduce the stability of the slope (Deng & Chen, 2021). In general, there are two types of excavation techniques for rock slopes, mechanical and blasting. Mechanical excavation includes ripping (removal of rock) and chemical or hydraulic expanders (Caltrans, 2021). Blasting is the most common excavation technique for rock slopes but creates new fractures while expanding and opening old ones, thus decreasing the rock mass strength (Laubscher & Jakubec, 2001). Hudson and Harrison (2000) list the three primary effects on the rock mass environment from excavations.

1. **Displacements**, because of unloading (stressed rock is free to move).
2. **Stress rotation**, due to no normal and shear stress on an unsupported excavation surface. The excavation boundary must a principal stress plane which means the minor principal stress ( $\approx 0$ ) must be orientated normal to the surface. This causes a major perturbation of the virgin (pre-existing) stress fields, both in terms of magnitude and orientation.
3. **Water flow**, because the fluid pressure will be reduced to atmospheric levels in the in the rock mass at the boundary of the excavation. This will make the excavation surface acts as a sink (Bernoulli's principle) and water will tend to flow there.

These three effects are illustrated in Figure 2.17.

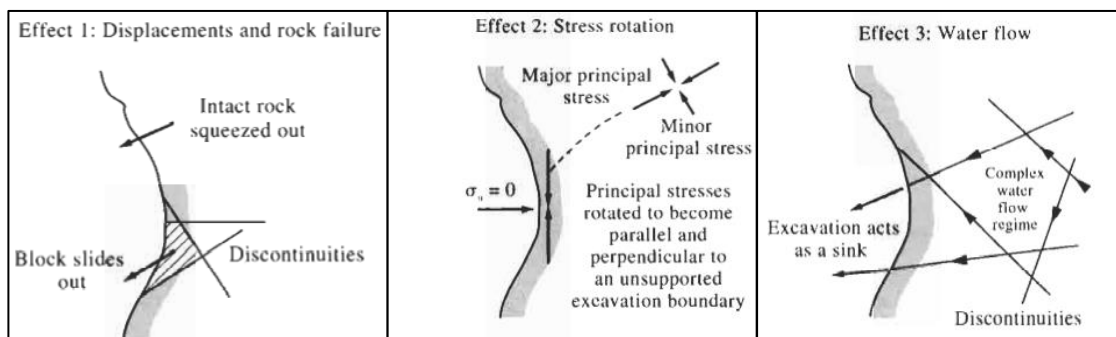


Figure 2.17: The three effects on the rock mass environment from excavation. Modified after Hudson and Harrison (2000).

The rock mass environment is also influenced by human induced vibration sources which be categorized into the three sources, transport, blasting, and heavy machinery (Sowers & Royster, 1978). If blasting is used its effects should be through a static and dynamic criterion. *Static criterion* includes indices such as factor of safety, stresses, and displacements to evaluate the potential failure modes. After blasting, unloading will result in a redistribution of stress fields, which cause stress relaxation or stress concentration (Deng & Chen, 2021). Monitoring of displacements is the simplest method of estimating rock deformations or slippage (Newcomen & Dick, 2016).



*Dynamic criterion* is mainly approached by empirical methods as dynamic load mechanisms are not fully understood yet. A strong dynamic response is generated in the surrounding rock mass resulting in reduced shear strength along structural planes and accelerated creep processes of potential sliding mass (Deng & Chen, 2021). Vibration from blasting is the main dynamic factor and has a strong correlation to peak particle velocity (PPV) (Nguyen et al., 2019). PPV is considered the most direct reflection of dynamic responses and can be monitored at the slope toe. Dynamic damage caused by blasting excavation are judged by PVV and blasting vibration frequency (Deng & Chen, 2021).

The objective for any excavated rock slope is to form a stable inclination with minimal need for maintenance (Hunt, 2005). This can be achieved by striving for clean surfaces during the excavation process (to achieve better stability). Furthermore, a reduction in the overburden will also result in less need for stabilization measures, maintenance, and longer durability (NPR, 2020). Methods such as line drilling and presplitting during excavation by blasting minimize the disturbance of the rock face (Hunt, 2005).

An indication of the relative effects on the rock mass from the excavation technique can be seen in Table 2.8 which is comprised of the disturbance factor (D) from the GSI system and the blast adjustment factor ( $A_{BLAST}$ ) in the Modified Rock Mass Rating (MRMR) system. Both systems set the base line with mechanical excavation as no disturbance/ effects on the surrounding rock mass.

Table 2.8: Effects on the surrounding rock mass by excavation techniques. Inspired after Laubscher and Jakubec (2001); Hoek and Brown (2019).

<b>Excavation technique</b>	<b>Adjustment factor (<math>A_{BLAST}</math>)</b>	<b>Disturbance factor (D)</b>
MRMR: Mechanical excavation/ boring GSI: Mechanical or hand excavation	1.00	0
MRMR: Smooth wall blasting GSI <sub>2019</sub> : Controlled presplit or smooth wall blasting	0.97	0.5
MRMR: Good conventional blasting GSI: Good blasting	0.94	0.7
MRMR: Poor blasting GSI: Poor blasting	0.80	1.0

## 2.3 Rock slope stabilization and protection

The methods used for rock slope stabilization and protection were primarily introduced in the 1970s and have been refined and developed ever since. The purpose of stabilization measures can either be to reduce or eliminate the driving forces (e.g., drainage, scaling, and trimming) or increase the resisting forces (e.g., bolts and shotcrete). Rock slope stabilization and protection measures should be evaluated based on the factors: environment, safety, stability, maintenance requirements, and cost (NPRA, 2018) (Norrish & Wyllie, 1996). Caltrans (2020) further includes the factors: aesthetics, durability, complexity, constructability, and effectiveness.

Before further discussions about this topic, the terms *prevention* and *mitigation* are important to establish. IDSR (2002) defines *prevention* as “activities to provide outright avoidance of the adverse impact of hazards and related environmental, technological and biological disasters”. *Mitigation* is defined as “structural and non-structural measures under-taken to limit the adverse impact of natural hazards, environmental degradation and technological hazards”. Caltrans (2020) lists four potential prevention and mitigation strategies that can be implemented either alone or paired together:

1. **Avoidance** measures (prevention) are based on realignment or relocation of the road to avoid the rock slope stability problems/rock fall source.
2. **Stabilization** measures (prevention) are based on changes to the slope and the use of engineered features to increase the stability of the rock slope.
3. **Protection** measures (mitigation) are based on the control of the rock fall once it destabilizes.
4. **Management** measures (mitigation) includes monitoring, warning signs, and rock patrols.

The literature does not agree on the categorization of rock slope stabilization measures. Hudson and Harrison (2000) emphasizes the use of the terms *rock reinforcement* and *rock support*. *Rock reinforcement* is the elements integrated into the rock mass so that the **rock supports itself** (by means such as rock bolts, anchors etc.) while *rock support* is external elements to the rock mass so that **the rock is supported** (with buttresses, wire mesh, shotcrete etc.). Wyllie (2018) does not make this distinction and divides instead stabilization measures instead into reinforcement and rock removal, as illustrated in Figure 2.18. Kliche (2018) on the other side, proposes the categorization of rock slope stabilization measures into the six categories: (1) grading, (2) controlled blasting, (3) mechanical stabilization, (4) structural stabilization, (5) vegetative stabilization, and (6) water control.

Stabilization measures can further be divided into temporary and permanent support (Nilsen & Palmström, 2000). Monitoring of slope movement can be useful to identify acceleration but are mostly used for large slow-moving natural rock slopes and some pit slopes. It is mainly divided into surface and sub-surface monitoring.

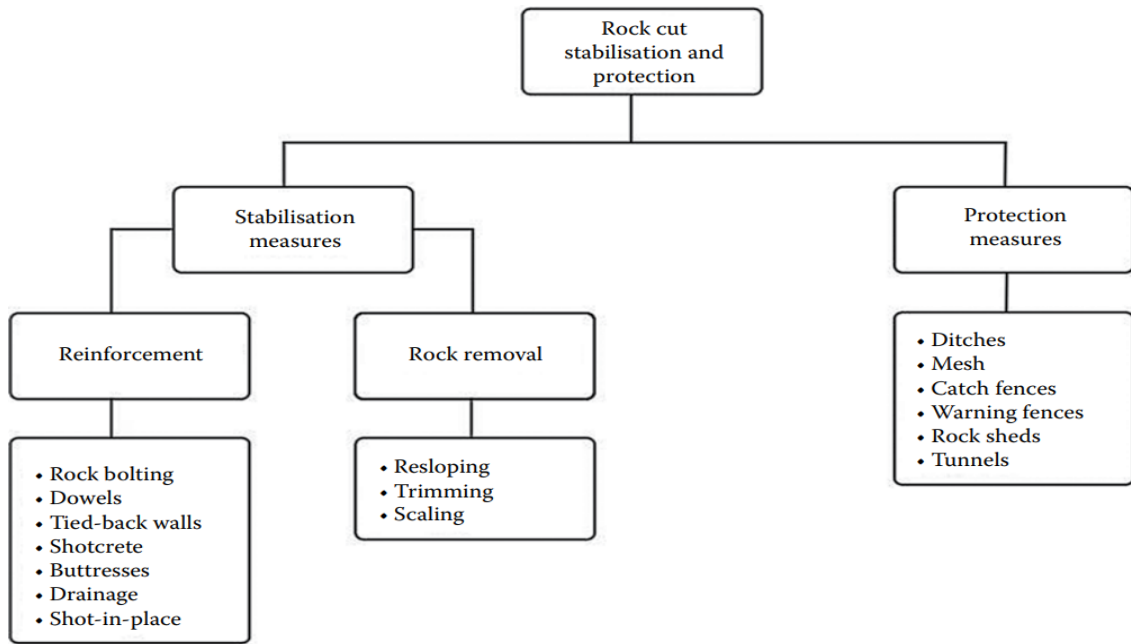


Figure 2.18: Flow chart for rock slope stabilization measures (Wyllie, 2018).

Read and Stacey (2009) emphasizes that the design of any stabilization or protection measure must consider the rock mass properties, the characteristics of the support systems, potential failure surfaces, and appropriate factor of safety. The factors to consider when designing the rock support system can be summarized as (Read & Stacey, 2009):

- The purpose of the support (e.g., prevent rockslide, slope failure or rockfall etc.)
- Geological structures within and around the slope
- Rock mass strength
- Groundwater conditions
- Groundwater chemistry
- Characteristics for the reinforcement or rock support system under loading conditions
- Rock stress conditions before, during, and after excavation of the slope
- Potential seismic events (blasting or earthquakes)

Table 2.9 presents a qualitative comparison of mitigation and prevention measures for rock slopes.

Table 2.9: Qualitative comparison of mitigation and prevention measures for rock slopes. Modified after Caltrans (2020).

MITIGATION & PREVENTATION MEASURE	CRITERIA SELECTION								
	Complexity	Effectiveness	Durability	Constructability/ special expertise	Road closure/ traffic restrictions	Environmental limitations	Aesthetical impacts	Cost	Maintenance requirements
<b>AVOIDANCE</b>									
Elevated structures	M-VH	M-H	L-H	M	P	L-H	L-M	VH	M-H
Tunnels	VH	VH	H	H	P	L-M	L-H	VH	M-H
Realignment	M-VH	M-VH	H	M	P	M-H	L-H	H-VH	M-H
<b>STABILIZATION</b>									
<i>Removal:</i>									
Scaling	L-M	L-H	L-M	M	Y	L	L	L-M	L-M
Blast scaling	M-H	L-H	M	M-H	Y	L-M	L	L	L-M
Trim blasting	M-H	M-H	M-H	M-H	Y	L-H	L-H	M	L-M
Re-sloping	L-H	M-H	H	L-M	Y	L-H	L-H	M-H	L
<i>Reinforcement:</i>									
Dowels	M	M-H	H	H	P	L	L	M-H	L
Shear pints	M	M	M	H	P	M	M	M	L
Rock bolts	M-H	M-H	H	H	P	L	L	M-H	L
Shotcrete	M-H	M-H	M-H	H	P	M-H	H	M-H	L
Buttresses	M-H	H	H	M	P	L-H	H	M-H	L
Cable lashing	M-H	L-M	L-M	M	P	L-H	M	M	L-M
Whalers/ lagging	M	M	L-M	M	P	L-H	M-H	M	L
<i>Drainage:</i>									
Weep drains	L	L-H	M	L	P	L-H	L	L	H
<b>PROTECTION</b>									
<i>Mesh/ cable nets:</i>									
Slope protection	L-M	M-H	M-H	M	Y	M-H	M-H	L	L-M
Anchored mesh	M	M	M	M	P	M	H	L-H	M-H
Suspended systems	L-M	M-H	M-H	M	Y	M-H	M-H	L-M	L-M
<i>Catchment areas/ sheds:</i>									
Ditches/ berms	L	M-H	H	L	P	L-M	L-M	L-H	H
Rockfall sheds	VH	H	M-H	H	P	H	H	H	L-M
<i>Barriers:</i>									
Rigid barriers	L	M-H	L-M	L	P	L	L	L	M-H
Flexible barriers	M	M-H	M-H	M	P	L	L	M	M-H
<b>MANGEMENT</b>									
Warning signs	L	L-M	na	na	N	L-M	L	L	L-M
Road patrols	L	L-M	na	na	N	na	na	L-H	H
Scaling	L-M	L-H	L-M	M	Y	L	L	L-M	L-M
Ditch cleaning	L	L-H	na	aa	Y	L-M	na	L-m	H
Monitoring	M-H	L	L-H	M-H	N	L	L	L-H	L-H

where: L = Low, M = medium, H = high, VH = very high, N = no, Y = yes, P = possibly, na = not applicable.

Call and Savely (1990) states that some degree of slope instability should be expected for virtually any excavated rock slope. The options available for the engineers are:

- Avoid the unstable area
- Reduce the load on the instability
- Include benches or berms in the design
- Excavate out the unstable area
- Support the unstable area
- Dewater the unstable area
- Conduct a partial clean-up

Proper drainage of the rock slope is recommended as one of the first steps in stabilizing the rock slope. Cleaning the surface along with shotcrete on the discontinuities may be useful too. The support design should be based on detailed study of the rock masses, discontinuities, and potential failure causes for the rock slope. The retaining system should be based on calculations of forces and weights (Jaeger et al., 2009). Figure 2.19 illustrates some common stabilization and protection measures for rock slopes.

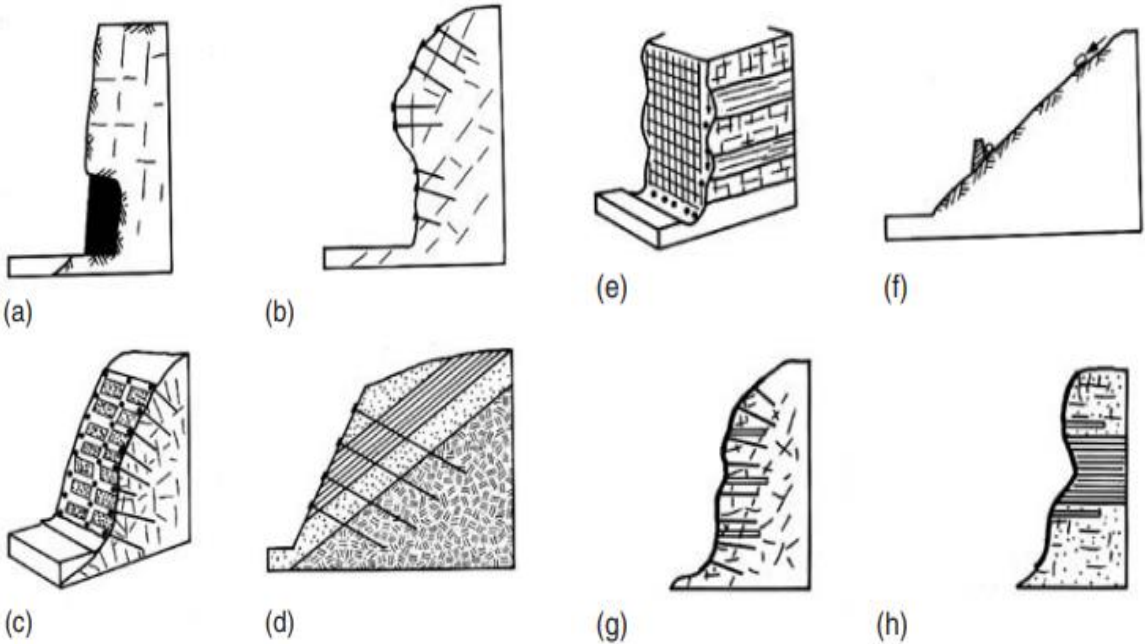


Figure 2.19: Suggested methods for stabilization and protection of rock slopes.; (a) concrete buttress for stabilizing overhang; (b) rock bolts used in jointed rock mass; (c) concrete straps and bolts for heavily jointed rock mass; (d) cabled anchors to reach stable rock; (e) wire mesh to prevent rock falls; (f) Impact walls to stop rolling blocks; (g) Drainage combined with bolting; and (h) shotcrete to retard slaking and weathering (Hunt, 2005).

## 2.4 Material failure theory

Material failure theory is the interdisciplinary field of solid mechanics and materials science. Multiple failure criteria have been proposed over the years to attempt to predict the conditions for the initiation of material failure at different loading conditions for different materials. Furthermore, material failure is defined as the loss of load carrying capacity for a unit of material. The type of failure is classified as either ductile failure (from yielding), brittle failure (from fracturing), or a combination of both (Griffith, 1921; Li, 2001).

To evaluate the strength of rock materials, which in essence is the ability to withstand failure, several failure criteria have been proposed to explain and predict the occurrence of a failure in the rock material and at which stress conditions (Wyllie, 2018).

The classical theoretical failure criteria such Mohr-Coulomb failure criterion, Tresca criterion, Griffith’s criterion, and Drucker Prager criterion are best applied to homogenous materials, and should be used with caution for heterogenous rock masses. In rock engineering, Mohr-Coulomb failure criterion is often used for joints, intact rock, or rock masses with one or two joint sets (Celada & Bieniawski, 2019). Figure 2.20 illustrates for which rock mass conditions it is beneficial to apply the Mohr-Coulomb and Hoek-Brown failure criterion for caverns and rock slopes.

This limitation has been handled by introducing empirical failure criteria which are able to predict the failure of both intact rock and rock mass. The generalized Hoek-Brown criterion one such empirical criterion and is probably the most utilized criterion within rock engineering. In this study the generalized Hoek-Brown failure criterion has been utilized for the numerical modelling of the rock mass, as well as Barton-Bandis failure criterion to describe the major discontinuities. Thus, a more thorough description of these criteria will follow in this section.

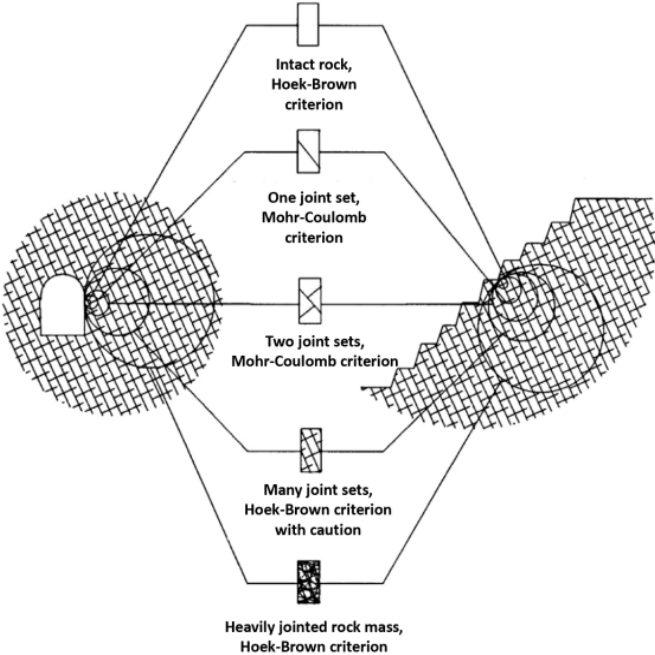


Figure 2.20: Suggested failure criterion based on the degree of jointing in the rock mass (Hoek, 2007).

### 2.4.1 Hoek-Brown failure criterion

The Hoek-Brown failure criterion was originally published by Hoek and Brown (1980) with the main purpose of providing input for designing of underground excavations (Hoek & Brown, 2019). The original criterion was limited to evaluating the shear strength of intact rock. However, the updated version published by Hoek et al. (2002), called the generalized Hoek-Brown failure criterion, incorporated both intact rock and discontinuities, resulting in a failure criterion able to describe rock mass. The addition to the criterion was derived from the geological strength index (GSI) and disturbance factor (D) estimated from the rock mass characteristics. Mechanical behaviours such as deformation and strength properties will be reduced based on the properties of the discontinuities in the rock mass (Hoek & Brown, 2019).

The Generalized Hoek-Brown criterion, is given by the following equation:

$$\sigma_1 = \sigma_3 \times \sigma_{ci} \left[ m_b \frac{\sigma_3}{\sigma_{ci}} + s \right]^a \quad (2.26)$$

where  $\sigma_1$  and  $\sigma_3$  are the major and minor principal stresses [MPa] at failure respectively,  $\sigma_{ci}$  is the intact rock strength (UCS) [MPa].  $m_b$  is Hoek-Brown constant for the rock mass,  $s$  and  $a$  are Hoek-Brown constants parameters and depended on the rock mass characteristics. GSI and D-factor are integrated through these constants, as defined by Equations 2.27, 2.28, and 2.29.

$$m_b = m_i \times e^{\left[ \frac{GSI-100}{28-14D} \right]} \quad (2.27)$$

$$s = e^{\left[ \frac{GSI-100}{9-3D} \right]} \quad (2.28)$$

$$a = \frac{1}{2} + \frac{1}{6} \left( e^{-\frac{GSI}{15}} - e^{-\frac{20}{3}} \right) \quad (2.29)$$

where  $m_i$  is the H-B material constant for intact rock.

Even though, the generalized Hoek-Brown failure criterion has become one of the most accepted criteria in the field of rock engineering, it has some limitations. Hoek (2007) states that the criterion assumes isotropic rock and rock mass behaviour. Furthermore, it should only be used on rock mass which can be classified as a Hoek-Brown material. This implies an analysed structure which is large, and a block size that is small in comparison. The rock mass should also have sufficiently spaced discontinuities with similar surface characteristics, thus meaning failure along the discontinuities can be assumed. Given a block in the same size order as the evaluated structure, the generalized Hoek-Brown failure criterion should not be used. This is also the case if a discontinuity set is drastically weaker than the rest, and failure criteria such as Mohr-Coulomb or Barton-Bandis failure criterion can be considered. The latter criterion will be discussed in the following subsection.

## 2.4.2 Barton-Bandis failure criterion

The shear strength of discontinuities is affected by multiple parameters such as normal stress, compressive strength of the joint wall, surface roughness, weathering, and infilling material (Palmström & Stille, 2015). All rock masses include discontinuities at different degrees. Furthermore, rock masses located near the surface are in a low stress environment which makes failure of the rock material itself less likely, but instead tend to happen along the discontinuities. Thus, it is paramount to evaluate the shear strength of the discontinuities governing the rock mass, to analyse the stability of the rock mass (Hoek, 2007). Several failure criteria for discontinuities have been proposed to predict the stress state at failure. One of the most accepted failure criteria for discontinuities is the Barton-Bandis failure criterion published by Barton and Bandis (1990). It has similarities to the Mohr-Coulomb failure criterion which was originally developed for soil mechanics and was later adapted to rock mechanics.

The Mohr-Coulomb failure criterion is defined as (Hoek, 2007):

$$\tau = \sigma_n \times \tan\phi + c \quad (2.30)$$

where  $\tau$  is the shear strength [MPa],  $\sigma_n$  is normal stress [MPa],  $\phi$  is the angle of friction [°], and  $c$  is the cohesive strength of the cemented surface [MPa].

The Barton-Bandis failure criterion was primarily inspired by Patton (1966) work on ‘saw-tooth’ specimens’, and derived a bi-linear approximation of the curved failure envelope for shear strength ( $\tau$ ) given as:

$$\tau = \sigma_n \times \tan(\phi + i) \quad (2.31)$$

where  $\phi$  is the basic friction angle on a smooth surface [°], and  $i$  is the angle [°] of the ‘saw-tooth’ with respect to the shearing direction.

Barton and Bandis (1990) presented the Barton-Bandis failure criterion for shear strength of discontinuities, which is non-linear and defined as:

$$\tau = \sigma_n \times \tan[JRC \times \log_{10}\left(\frac{JCS}{\sigma_n}\right) + \phi_r] \quad (2.32)$$

where  $\tau$  is the peak shear strength [MPa],  $\sigma_n$  is the effective normal stress [MPa], JRC is the Joint Roughness Coefficient, JCS is the Joint wall Compressive Strength (which is  $\approx \sigma_{ci}$  for an unweathered rock), and  $\phi_r$  is the residual friction angle [°].

The residual friction angle  $\phi_r$  can be estimated from (Barton & Choubey, 1977):

$$\phi_r = (\phi_b - 20) + 20 \times \frac{r}{R} \quad (2.33)$$

where  $\phi_b$  is basic friction angle,  $r$  is Schmidt hammer rebound value on wet and weathered fracture surfaces, and  $R$  is the Schmidt hammer rebound value on dry and unweathered surfaces.



The term *roughness* for a discontinuity surface can be divided into two scale dependent parameters which both apply for filled and unfilled joints (ISRM, 1978d):

**Large scale undulations** (*waviness*), causes dilation (increase in volume) given shear displacements (and the discontinuity walls are interlocked and in contact) as they are too big to be sheared off (given they are strong enough). Patton (1966) defines this as first order-order asperities.

Waviness ( $U$ ) appears as undulations from planarity and is defined as (Palmström & Stille, 2015):

$$U = \frac{a_{max}}{L_j} \quad (2.34)$$

where  $a_{max}$  is the maximum amplitude from planarity, and  $L_j$  is the length of joint. However, often a simplified method to estimate waviness ( $u$ ) is used, the so-called  $a/L$ -method:

$$U = \frac{a}{L} \quad (2.35)$$

where  $a$  is the measured maximum amplitude, and  $L$  is the measured length along joint. This procedure is illustrated in Figure 2.21 (a). The values for  $a$  and  $L$  be plotted in the chart in Figure 2.21 (d) to estimate the value of JRC.

**Small scale roughness** (*unevenness*), tends to be damaged/crushed given shear displacements (except for low stress levels or strong discontinuity walls which would cause dilation). Patton (1966) on the other hand defines this as second-order asperities.

Unevenness is the asperities of the discontinuity surface and can be felt by touch as the wavelength and amplitude are on the scale of tenths of a millimetre (Palmström & Stille, 2015). This is illustrated in Figure 2.21 (b). Similarly, as for large scale undulations, the  $a/L$ -method can also be used to estimate the JRC for small scale roughness. However, profile combs (profilometers) are more common to use (Figure 2.21 (c)), which can then be traced on a paper and compared visually to standard profiles such as the one published by Barton and Choubey (1977) which is often used in the field of engineering geology. It can also be correlated to standard profiles designed for the joint roughness number  $J_r$  in the Q-system. This is illustrated in Figure 2.21 (e) which shows the correlation between 20 cm scale JRC profiles and the corresponding values of  $J_r$ .

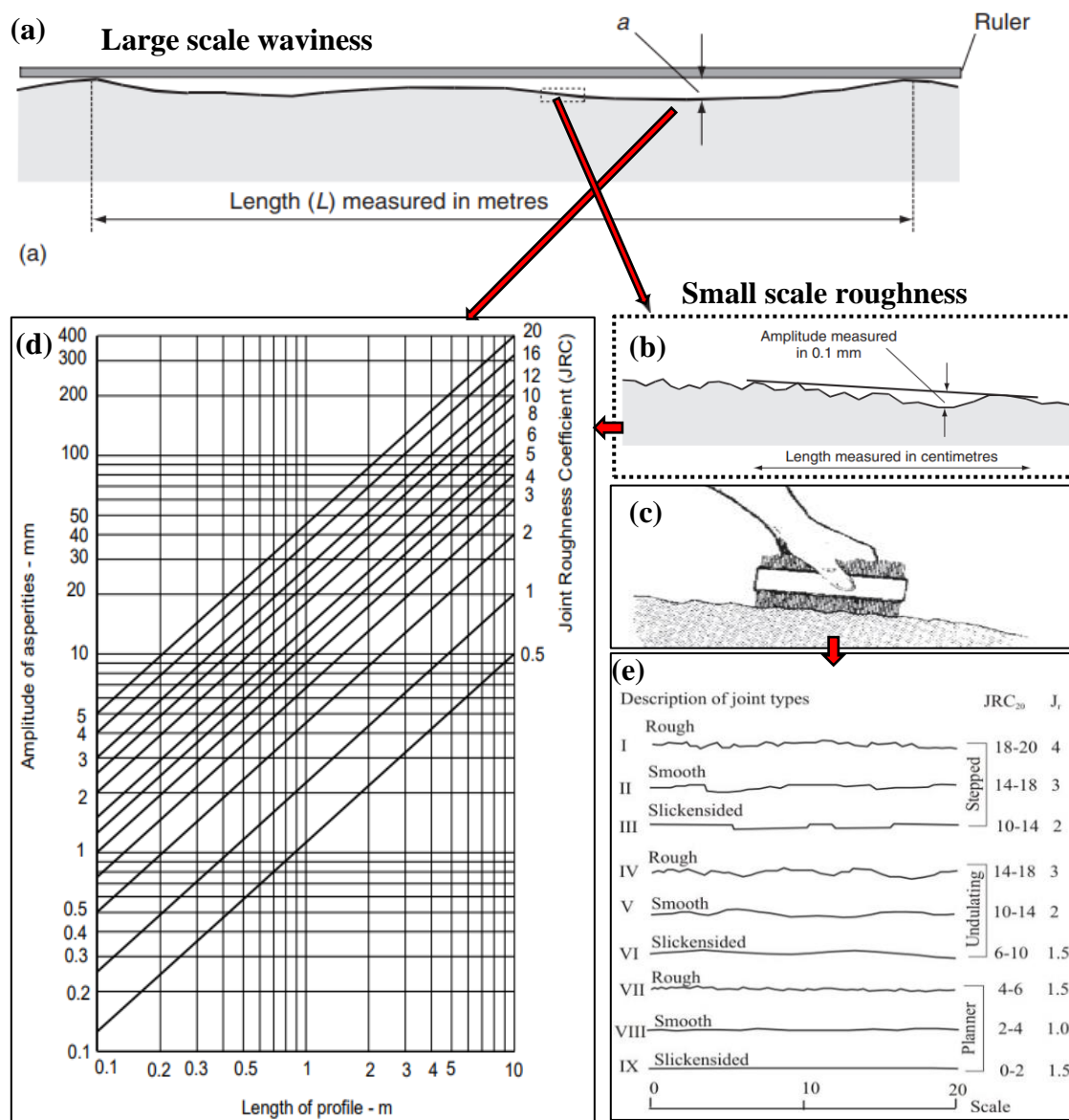


Figure 2.21: Characterization of joint roughness; (a) large scale waviness (Palmström & Stille, 2015); (b) small scale roughness (Palmström & Stille, 2015); (c) profile comb/profilometer ((Palmström & Stille, 2015); (d) chart for estimating JRC based on the a/L-method (Barton & Bandis, 1982); (e) Standard roughness profiles with corresponding JRC<sub>20</sub> (20 cm scale correlation for JRC) and J<sub>r</sub> values (Barton & Bandis, 1990).

Barton (1973) emphasizes that the friction angle of the discontinuity surface is influenced primarily of small scale roughness for low normal stresses and large scale roughness for high normal stresses. This due to dilation at low normal stress conditions and shearing of the asperities at higher normal stresses. This is illustrated in Figure 2.22. However, it should be noted that this an idealized example, and the true shear strength if also influenced by the rock strength at discontinuity surface and the amount of shear displacement that has occurred (Wyllie, 2018). ISRM (1978d) further highlights that the importance of surface roughness for the shear strength of discontinuities declines as filling thickness, aperture, or the degree of displacements increases.

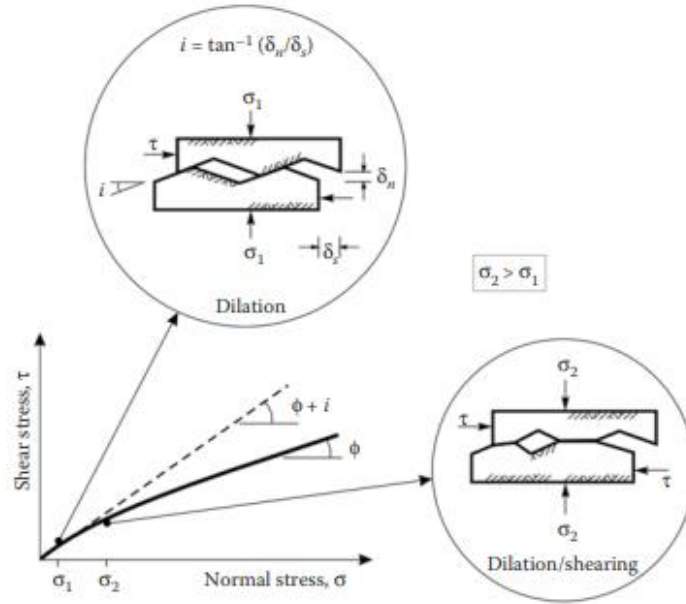


Figure 2.22: Surface roughness and normal stress effects on friction angle of discontinuity surface (Wieczorek, 1996).

Bandis et al. (1981) performed a systematic experimental study of the scaling effects of discontinuities and concluded that the peak shear strength is significantly dependent on scale. The significance of small-scale roughness decreases as the discontinuity surface size increase while large scale waviness become important. This means the values of JRC and JCS will decrease as the discontinuity surface gets larger (ISRM, 1978d; Wyllie, 2018). To compensate for this, Barton and Bandis (1982) proposed scale corrections for JRC and JCS, as seen in Equations 2.36 and 2.37.

$$JRC_n = JRC_0 \left( \frac{L_n}{L_0} \right)^{-0.02 JRC_0} \quad (2.36)$$

$$JCS_n = JCS_0 \left( \frac{L_n}{L_0} \right)^{-0.03 JRC_0} \quad (2.37)$$

where  $JRC_n$ ,  $L_n$ , and  $JCS_n$  are the dimensions of the sliding surface (in-situ) while  $JRC_0$ ,  $L_0$ , and  $JCS_0$  refer to 100 mm laboratory scale samples.

ISRM (1978d) suggests the use of Schmidt rebound hammer to estimate JCS of discontinuity surfaces in the field. There are two types of Schmidt rebound hammer: Type L and Type N. They were designed to evaluate the compressive strength of concrete, but Type L produce about 1/3 of the impact energy of Type N. Thus, being more suitable for testing of rock formations and structural elements more vulnerable to impact damage (Gilson, 2022).

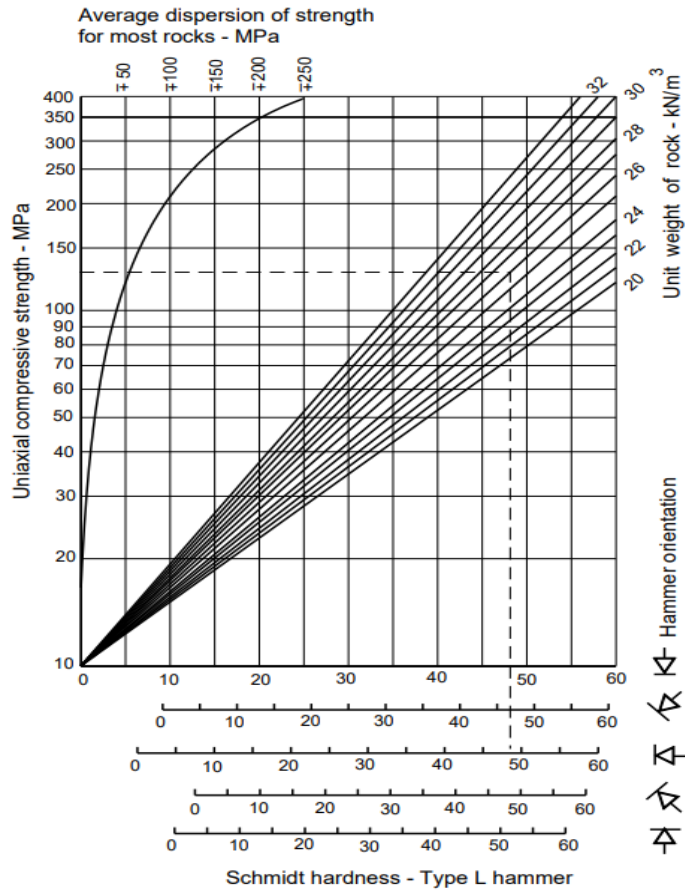


Figure 2.23: Chart for estimating JCS from Schmidt hardness with Type L hammer (Hoek, 2007).

The Barton-Bandis failure criteria is defined for shear strength of discontinuities with rock wall contact along the entire evaluated surface. However, the shear strength of the discontinuities will be significantly reduced if they are filled or partially filled (with materials such as clay or gouges). The level of roughness and/or undulation for the discontinuities are important in relation to the thickness of fill material to evaluate the shear strength reduction. For planar or low undulating discontinuities a thin layer of fill material is enough to reduce the shear strength drastically. On the other side, rough or undulating discontinuities will only have the shear strength reduced to the level of the fill material given the thickness of it exceeds the amplitude of asperities or undulation. In other words, the discontinuity surfaces are resting on the fill material and the rock-to-contact is none or limited (Hoek, 2007). Barton (1974) published an extensive review of the shear strength of common fill materials and the shear strength of filled discontinuities. Figure 2.24 presents the main findings from his study.

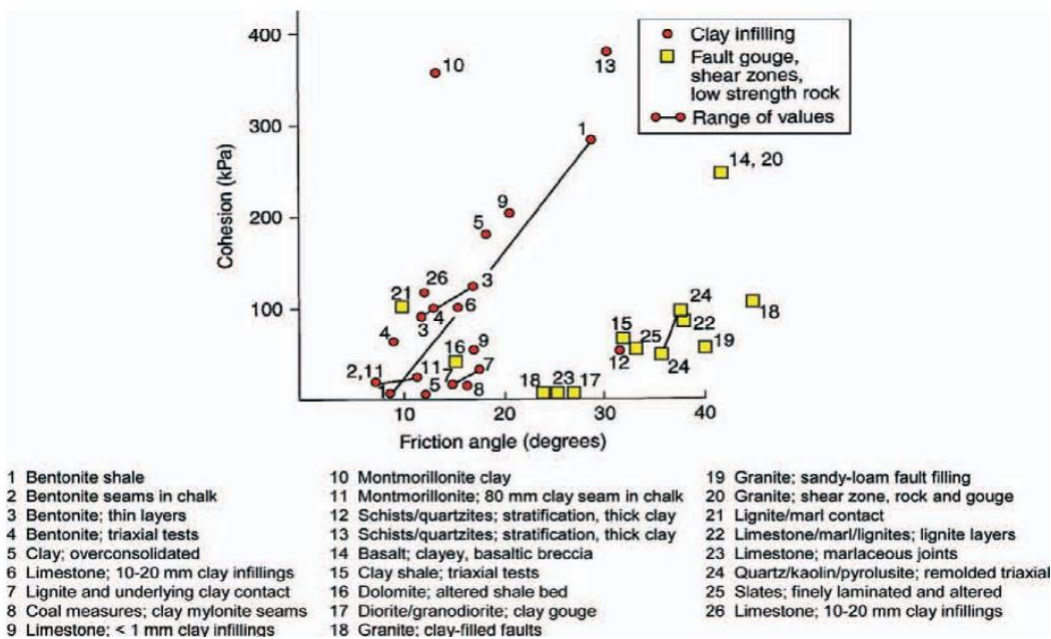


Figure 2.24: Peak shear strength for selected filling materials. Originally from Barton (1974), modified by (Wyllie, 2018).

Filled discontinuities can broadly be divided into two categories based on if there have been any prior displacements along the discontinuity. (1) Recently displaced and (2) undisplaced discontinuities can further be divided into over-consolidated (O-C) or normally consolidated materials (N-C) ((Barton, 1974; Wyllie, 2018). This is illustrated in Figure 2.25.

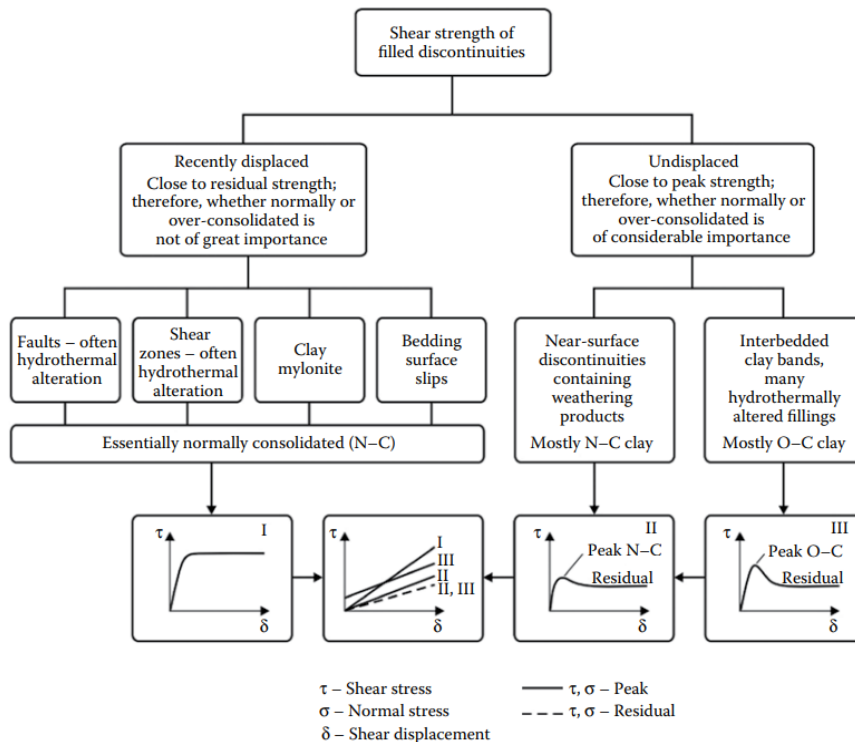


Figure 2.25: Flow chart for shear strength of filled discontinuities, divided into recently displaced and undisplaced. Originally from Barton (1974), modified by Wyllie (2018).

1. *Recently displaced discontinuities* include bedding surface slips, clay mylonite, shear zones, and faults. The infilling material in faults and shear zones has been formed during the shearing process. This material can be defined as gouge and contains both breccia which is orientation parallel to shear direction and clay particles. In comparison, bedding surface slips and mylonites were clay-bearing before any displacement occurred. The shear strength of filled discontinuities are essentially the same as the residual shear strength as any pre-existing cohesive bonds from O-C clays have been destroyed by the shearing (displacement), and can now be considered N-C (Barton, 1974; Wyllie, 2018).
  
2. *Undisplaced discontinuities* are typical for metamorphic and igneous rock where the filling material (clay) has been formed by weathering along the discontinuities. They can also be found within sedimentary formations such as sandstone interbedded with weak shales or thin beds of clay located. The infilling material in undisplaced discontinuities can also be formed by hydrothermal alteration. Furthermore, the infillings of undisplaced discontinuities can either be N-C or O-C materials. There is a significant difference in peak shear strength and residual shear strength for O-C materials, and little difference between N-C materials (Barton, 1974; Wyllie, 2018). These differences are illustrated in Figure 2.25.

The ground water pressure should also be considered for the Barton-Bandis failure criteria. Ground water within the discontinuities will apply an outward pressure against the discontinuities surfaces thus reducing the normal stress  $\sigma_n$ . Given the groundwater pressure denoted  $u$ , the effective normal stress  $\sigma_n'$  can be calculated as (Hoek, 2007):

$$\sigma_n' = \sigma_n - u \quad (2.38)$$

The groundwater pressure  $u$  can be very difficult to estimate due to factors such as the topographical conditions, degree of jointing in rock mass, precipitation, etc., as discussed in Subsubsection 2.2.3.2.

## 2.5 Assessment methods for rock slope stability

There are several approaches to classify the stability assessment methods. Bieniawski (1989) and Nilsen and Palmström (2000) categorizes the methods into three main groups: (1) empirical methods, (2) analytical methods, and (3) observational methods. Abdulai and Sharifzadeh (2019) groups slope design methods into deterministic slope stability analysis and probabilistic/reliability analysis (non-deterministic methods), as illustrated in Figure 2.26. The prior utilizes a single value per input parameter while the later considers variability in the input properties. This section will present methods from both groups such as: Q-slope (empirical classification method), kinematic analysis, both conventional and partial factor principle limit equilibrium methods (LEMs), numerical methods, and probabilistic methods.

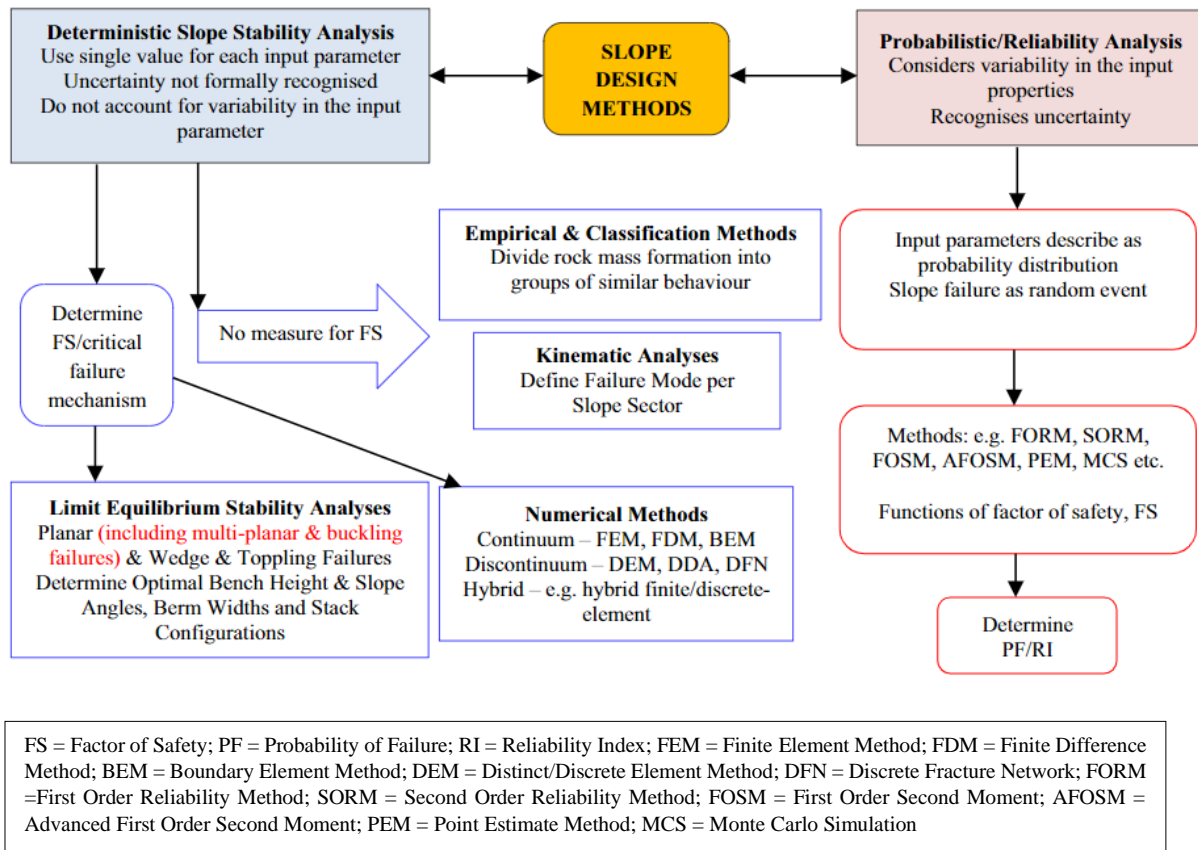


Figure 2.26: Assessment methods for rock slope stability (Abdulai & Sharifzadeh, 2019).

## 2.5.1 Q-slope

Q-slope is derived from the more commonly known Q-system introduced by Barton (1974) for rock mass characterization in tunnelling, underground mining, and underground excavations in general. Q-slope is similarly an empirical method tailored to be used in the field. However, it is applied for assessing the rock mass quality concerning the stability of excavated rock slopes. This method is used to get an indication of the maximum slope angle for long-term stability without support (or maintenance). Furthermore, it makes it possible for the geotechnical engineers to adjust the slope angles and adjust the slope design during the excavation phase as new rock mass gets exposed (Bar & Barton, 2017; Bar et al., 2016; Barton & Bar, 2015).

There exist several empirical methods for rock engineering designing (Table 2.2), empirical methods for rock slope engineering are less frequently used except for kinematic analysis. Empirical assessment methods for excavated rock slope such as SMR (Slope Mass Rating) by Romana (1985); Romana (1995) and GSPI (Global Slope Performance Index) by Sullivan (2013) were developed to predict reinforcement, support, and performance for excavated slopes. These methods do not provide any guidance for rock slope angles that are deemed long-term stable without any rock reinforcement which Q-slope does. It can further be used for both civil slopes and pit slopes (Bar & Barton, 2017; Barton & Bar, 2015). However, the Q-slope method was not meant to substitute more advanced methods such as numerical analysis but can be useful if the time is limited or the project is in the early stages (Siddique et al., 2020).

The value for Q-slope is determined by six different parameters and a discontinuity orientation factor:

$$Q_{slope} = \frac{RQD}{J_n} \times \left(\frac{J_r}{J_a}\right)_o \times \frac{J_{wice}}{SRF_{slope}} \quad (2.39)$$

where RQD is the Rock Quality Designation (degree of jointing) and the rating varies from 10 to 100,  $J_n$  is the joint set number that varies from 20 to 0.5,  $J_r$  is the joint roughness number that varies from 0.5 to 4,  $J_a$  is the joint alteration number that varies from 20 to 0.75,  $J_{wice}$  is the environmental and geological number that varies from 0.2 to 1.10,  $SRF_{slope}$  is the Strength Reduction Factor and represents the most severe case of either  $SRF_a$  (physical condition),  $SRF_b$  (stress and strength), and  $SRF_c$  (major discontinuity). The value of  $SRF_{slope}$  varies from 24 to 1. Note that installation of any stabilization measures for the excavated rock slope are adjusted for through the factor  $J_{wice}$ . It is multiplied with a factor 1.5 for drainage measures, 1.3 for reinforcement measures, and 1.95 if both are applied.

Further, the shear resistance,  $\tau$ , can also be approximated from (Bar & Barton, 2017):

$$\tau \approx \sigma_n \arctan\left(\frac{J_r}{J_a}\right) \quad (2.40)$$



RQD is defined as "[...] the percentage of intact core pieces longer than 100 mm in the total length of core" (Deere, 1963). RQD can be hard to determine, especially for a jointed rock mass with significant local difference in the degree of jointing. Palmström (2005) suggested a correlation between RQD and the *volumetric joint count*,  $J_v$  (which is the number of joints intersecting a rock mass volume of 1 m<sup>3</sup>) as:

$$\text{RQD} = 100 - 2.5 \times J_v \quad (2.41)$$

(RQD = 0 for  $J_v > 44$  and RQD = 100 for  $J_v < 4$ )

O-factor is the discontinuity orientation factor and is an orientation weight for the discontinuities in a rock slope. The Set A orientation factor is applied to the discontinuity set which is deemed the most structurally unstable while the Set B orientation is applied for the secondary discontinuity set if present and is used for wedge formations. The set A orientation factor varies from 0.25 to 2 while the set B orientation factor varies from 0.7 to 1.5. To clarify the implantation of O-factor into Q-slope two examples will be given. Equation 2.42 illustrates an example for a single discontinuity (Set A) controlling the rock slope stability while Equation 2.43 illustrates the implementation for a potential wedge formation (Set A and B).

- Set A (dominant & unfavourable):  $J_r = 1.0$ ,  $J_a = 2.0$ , and O-factor = 0.75

$$\left(\frac{J_r}{J_a}\right)_o = \left(\frac{1.0}{2.0} \times 0.75\right) = 0.375 \quad (2.42)$$

- Set A (dominant & very unfavourable):  $J_r = 1.0$ ,  $J_a = 2$ , and O-factor = 0.5
- Set B (slightly less dominant & unfavourable):  $J_r = 3.0$ ,  $J_a = 1$ , and O-factor = 0.9

$$\left(\frac{J_r}{J_a}\right)_o = \left(\frac{1.0}{2.0} \times 0.5\right) \times \left(\frac{3.0}{1.0} \times 0.9\right) = 0.675 \quad (2.43)$$

The description of the characterization process for the parameters in Q-slope is shown in Figure 2.27 and Figure 2.28.

**RQD (rock quality designation)**

Rock quality designation description		RQD (%) <sup>a</sup>
A	Very poor	0–25
B	Poor	25–50
C	Fair	50–75
D	Good	75–90
E	Excellent	90–100

<sup>a</sup> where RQD is reported or measured as  $\leq 10$  (including zero), a nominal value of 10 is used to evaluate  $Q$ -slope. RQD intervals of 5, i.e., 100, 95, 90, etc., are sufficiently accurate

**J<sub>n</sub> (joint set number)**

Joint set number description		J <sub>n</sub>
A	Massive, no or few joints	0.5–1
B	One joint set	2
C	One joint set plus random joints	3
D	Two joint sets	4
E	Two joint sets plus random joints	6
F	Three joint sets	9
G	Three joint sets plus random joints	12
H	Four or more joint sets, random, heavily jointed	15
J	Crushed rock, earthlike	20

**J<sub>r</sub> (joint roughness number)**

Joint roughness number description		J <sub>r</sub>
<i>(a) Rock-wall contact, (b) contact after shearing</i>		
A	Discontinuous joints	4
B	Rough or irregular, undulating	3
C	Smooth, undulating	2
D	Slickensided, undulating	1.5
E	Rough or irregular, planar	1.5
F	Smooth, planar	1.0
G	Slickensided, planar	0.5
<i>(c) No rock-wall contact when sheared</i>		
H	Zone containing clay minerals thick enough to prevent rock-wall contact.	1.0
J	Sandy, gravely or crushed zone thick enough to prevent rock-wall contact.	1.0

Descriptions refer to small-scale features and intermediate scale features, in that order

Add 1.0 if mean spacing of the relevant joint set is greater than 3 m

$J_r = 0.5$  can be used for planar, slickensided joints having lineations, provided the lineations are oriented for minimum strength

$J_r$  and  $J_a$  classification are applied to the discontinuity set or sets that are least favorable for stability both from the point of view of orientation and shear resistance  $\tau$ , where  $\tau \approx \sigma_n \tan^{-1}(J_r/J_a)$

**J<sub>a</sub> (joint alteration number)**

Joint alteration number description		J <sub>a</sub>
<i>(a) Rock-wall contact (no clay fillings, only coatings)</i>		
A	Tightly healed, hard non-softening, impermeable filling, i.e., quartz or epidote	0.75
B	Unaltered joint walls, surface staining only	1.0
C	Slightly altered joint walls. Non-softening mineral coatings, sandy particles, clay-free disintegrated rock, etc.	2.0
D	Silty- or sandy-clay coatings, small clay disintegrated rock, etc.	3.0
E	Softening or low friction clay mineral coatings, i.e., kaolinite or mica. Also chlorite, talc, gypsum, graphite, etc., and small quantities of swelling clays	4.0
<i>(b) Rock-wall contact after some shearing (thin clay fillings, probable thickness <math>\approx 1</math>–5 mm)</i>		
F	Sandy particles, clay-free disintegrated rock, etc.	4.0
G	Strongly over-consolidated non-softening clay mineral fillings	6.0
H	Medium or low over-consolidation, softening, clay mineral fillings	8.0
J	Swelling-clay fillings, i.e., montmorillonite. Value of $J_a$ depends on percent of swelling clay-size particles and access to water	8–12
<i>(c) No rock-wall contact when sheared (thick clay/crushed rock fillings)</i>		
M	Zones or bands of disintegrated or crushed rock and clay (see G, H, J for description of clay condition)	6, 8, or 8–12
N	Zones or bands of silty- or sandy-clay, small clay fraction (non-softening)	5.0
OPR	Thick, continuous zones or bands of clay (see G, H, J for description of clay condition)	10, 13, or 13–20

Figure 2.27: Description and classification of input values for  $Q$ -slope [1/2] (Bar & Barton, 2017).

### O-factor (discontinuity orientation factor)

O-factor description	Set A	Set B
Very favorably oriented	2.0	1.5
Quite favorable	1.0	1.0
Unfavorable	0.75	0.9
Very unfavorable	0.50	0.8
Causing failure if unsupported	0.25	0.5

### $J_{\text{wice}}$ (environmental and geological condition number)

$J_{\text{wice}}^a$	Desert environment	Wet environment	Tropical storms	Ice wedging
Stable structure; competent rock	1.0	0.7	0.5	0.9
Stable structure; incompetent rock	0.7	0.6	0.3	0.5
Unstable structure; competent rock	0.8	0.5	0.1	0.3
Unstable structure; incompetent rock	0.5	0.3	0.05	0.2

<sup>a</sup> When drainage measures are installed, apply  $J_{\text{wice}} \times 1.5$ , when slope reinforcement measures are installed, apply  $J_{\text{wice}} \times 1.3$ , and when drainage and reinforcement are installed, apply both factors  $J_{\text{wice}} \times 1.5 \times 1.3$

### SRF<sub>a</sub> (physical condition)

Description	SRF <sub>a</sub>
A Slight loosening due to surface location, disturbance from blasting or excavation	2.5
B Loose blocks, signs of tension cracks and joint shearing, susceptibility to weathering, severe disturbance from blasting	5
C As B, but strong susceptibility to weathering	10
D Slope is in advanced stage of erosion and loosening due to periodic erosion by water and/or ice-wedging effects	15
E Residual slope with significant transport of material downslope	20

### SRF<sub>b</sub> (stress and strength)

Description	$\sigma_c/\sigma_1^a$	SRF <sub>b</sub>
F Moderate stress-strength range	50–200	2.5–1
G High stress-strength range	10–50	5–2.5
H Localized intact rock failure	5–10	10–5
J Crushing or plastic yield	2.5–5	15–10
K Plastic flow of strain softened material	1–2.5	20–15

<sup>a</sup>  $\sigma_c$  = unconfined compressive strength (UCS),  $\sigma_1$  = maximum principal stress

### SRF<sub>c</sub> (major discontinuity)

SRF <sub>c</sub>	Favorable	Unfavorable	Very unfavorable	Causing failure if unsupported
L Major discontinuity with little or no clay	1	2	4	8
M Major discontinuity with RQD <sub>100</sub> = 0 <sup>a</sup> due to clay and crushed rock	2	4	8	16
N Major discontinuity with RQD <sub>300</sub> = 0 <sup>b</sup> due to clay and crushed rock	4	8	12	24

<sup>a</sup> RQD<sub>100</sub> = 1 m perpendicular sample of discontinuity, <sup>b</sup> RQD<sub>300</sub> = 3 m perpendicular sample of discontinuity

Figure 2.28: Description and classification of input values for Q-slope [2/2] (Bar & Barton, 2017).

Q-slope can also be described as three fractions which influence the rock mass quality of the artificial slope.  $\frac{RQD}{J_n}$  describes the block size or degree of joint,  $\frac{J_r}{J_a}$  describes the least favourable shear strength or average shear strength for wedges  $\left(\frac{J_r}{J_a}\right)_1 \times \left(\frac{J_r}{J_a}\right)_2$ , and  $\frac{J_{wice}}{SRF_{slope}}$  describes external factors and stress. Q-slope ranges between 0.001 (exceptionally poor rock mass) to 1000 (exceptionally good rock mass) (Bar & Barton, 2017; Barton & Bar, 2015).

High values of Q-slope indicate rock mass of high quality and the excavated rock slopes will be long-term stable at steep slope angles without any rock reinforcement. The steepest slope angle  $\beta$  (no support) was derived from over 450 cases studies of excavated slopes (stable, collapsed, and quasi-stable) at slope heights from 5-250+ m in different geological settings around the world by Bar and Barton (2017); Barton and Bar (2015).  $\beta$  can be calculated from Q-slope as shown below:

$$\beta = 20 \log_{10} Q_{slope} + 65^\circ \tag{2.44}$$

The stability chart in Figure 2.29 shows which slope angles are unstable, uncertain stability, and stable for Q-slope.

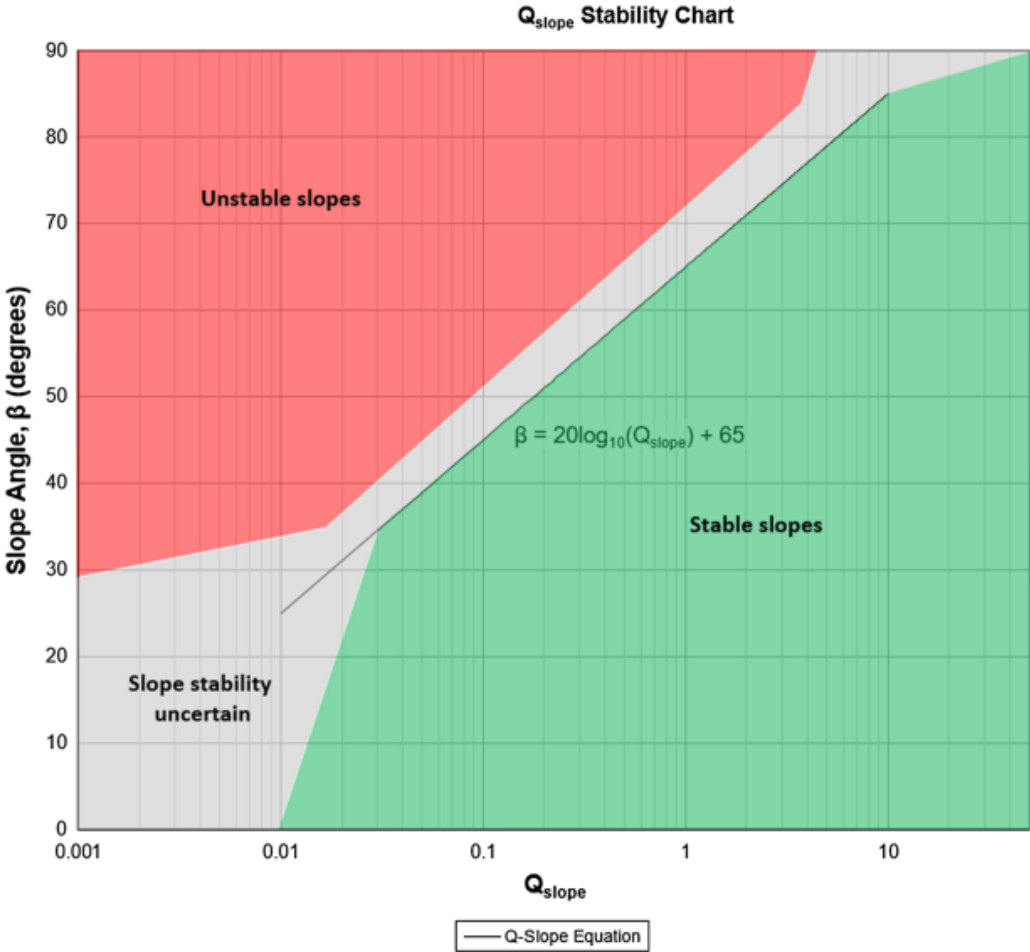


Figure 2.29: Stability chart for Q-slope (Bar & Barton, 2017).

A general relation between Q-slope, P-wave velocity, and the Q-value from the Q-system was described by Barton (2002) and Bar & Barton (2018). Normalized Q-value ( $Q_c$ ) can be derived from the relation between unconfined compressive strength ( $\sigma_c$ ) [MPa] and the Q-value given by:

$$Q_c = \frac{\sigma_c}{100} \times Q \quad (2.45)$$

P-wave velocity ( $V_p$ ) [km/s] can be estimated from  $Q_c$ :

$$V_p \approx 3.5 + \log Q_c \quad (2.46)$$

Similarly, Equation 2.46 can be rearranged and  $Q_c$  can be estimated from  $V_p$ :

$$Q_c \approx 10^{(V_p - 3.5)} \quad (2.47)$$

$Q_c$  must be corrected for by the orientation of geological structures present at the rock slope by introducing the O-factor as well as the environmental and geological conditions number  $J_{wice}$  and the strength reduction factor  $SRF_{slope}$ . The approximation of Q-slope from  $Q_c$  can thereby be calculated from:

$$Q_{slope} \approx (Q_c)_o \times \frac{J_{wice}}{SRF_{slope}} \quad (2.48)$$

## 2.5.2 Kinematic analysis

Kinematic analysis is used as an initial approach to evaluate the possibility of slope instabilities. 'Kinematics' is the study of movement without consideration of the forces that causes it (Hudson & Harrison, 2000). The kinematic analysis utilizes stereographic projections to evaluate the feasibility of translational failures due to the formations of wedges or planes (or toppling) which are daylighting. Thus, this method relies on detailed evaluation/mapping of the discontinuity sets and the rock mass structure that can contribute to the rock slope instability. The kinematic feasibility of rocks can be evaluated on physical (equal area) stereonet plots or through computer programs such as DIPS by Rocscience (Eberhardt, 2003). Figure 2.30 illustrates how (a) planar features and (b) linear features can be projected onto a 2D plane (stereonet) from the lower hemisphere of a reference sphere.

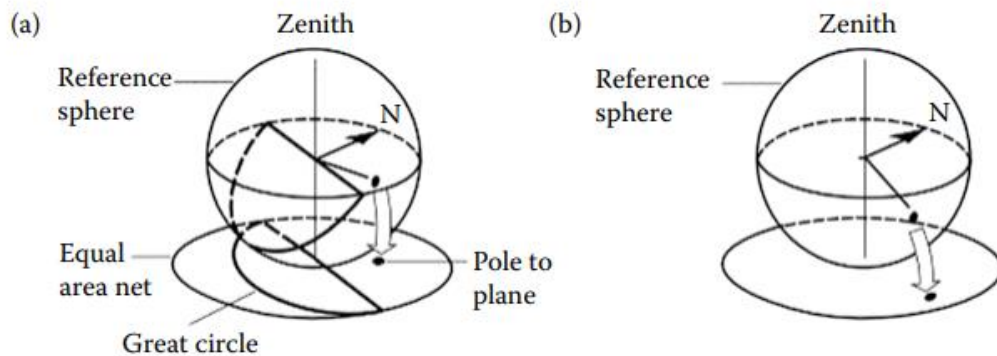


Figure 2.30: Equal area projections of (a) planar features and (b) linear features (Wyllie, 2018).

Kinematic feasibility tests include the discontinuity orientations with respect to the slope face to assess the possibilities for different failure mechanisms (Hermanns et al., 2012).

**Structural conditions for failure by planar sliding** is defined by Norrish and Wyllie (1996) as:

1. The dip direction of the planar discontinuity must be within 20 degrees of the dip direction of the slope face (the strike of the planar discontinuity must be within 20 degrees of the strike of the slope face).
2. The dip of the planar discontinuity must daylight in slope face and with a lower angle (than the slope face).
3. The dip of the planar discontinuity must exceed the angle of friction for the surface ( $20^\circ$  is often used as a conservative value (Hermanns et al., 2012)).
4. The lateral extent of the potential failure mass must be defined either by lateral release surfaces (that do not contribute to the stability of the mass) or by the presence of a convex slope shape that is intersected by the planar discontinuity.

**Structural conditions for failure by wedge sliding** is defined by Norrish and Wyllie (1996) as:

1. The trend of the line of intersection must approximate the dip direction of the slope face.
2. The plunge of the line of intersection must be less than the dip of the slope face. Under this condition, the line of intersection is said to daylight on the slope.
3. The plunge of the line of intersection must exceed the angle of friction of the surface. If the angles of friction for the two planes are markedly different, an average angle of friction is applicable

**Structural conditions for failure by toppling** is defined by Norrish and Wyllie (1996) as:

1. The strike of the layers must be approximately parallel to the slope face. Differences in these orientations of between 15 and 30 degrees have been quoted by various workers, but for consistency with other modes of failure, a value of 20 degrees seems appropriate.
2. The dip of the layers must be into the slope face. Using the dip direction convention, conditions 1 and 2 can be stated as follows: the dip direction of the layers must be between 160 and 200 degrees to the dip direction of the slope face.
3. In order for interlayer slip to occur, the normal to the toppling plane must have a plunge less than the inclination of the slope face less the friction angle of the surface.

Figure 2.31 illustrates kinematic feasibility tests for planar sliding (a), wedge sliding (b), and toppling failure (c). The attributed scores are higher in zones (at the stereo net) where the difference between the sliding direction and the slope face is lower than  $30^\circ$  and if the persistence of the discontinuities is above 20 m. This is classified as partly possible failure and is marked with a lighter grey colour in the figure (Hermanns et al., 2012).

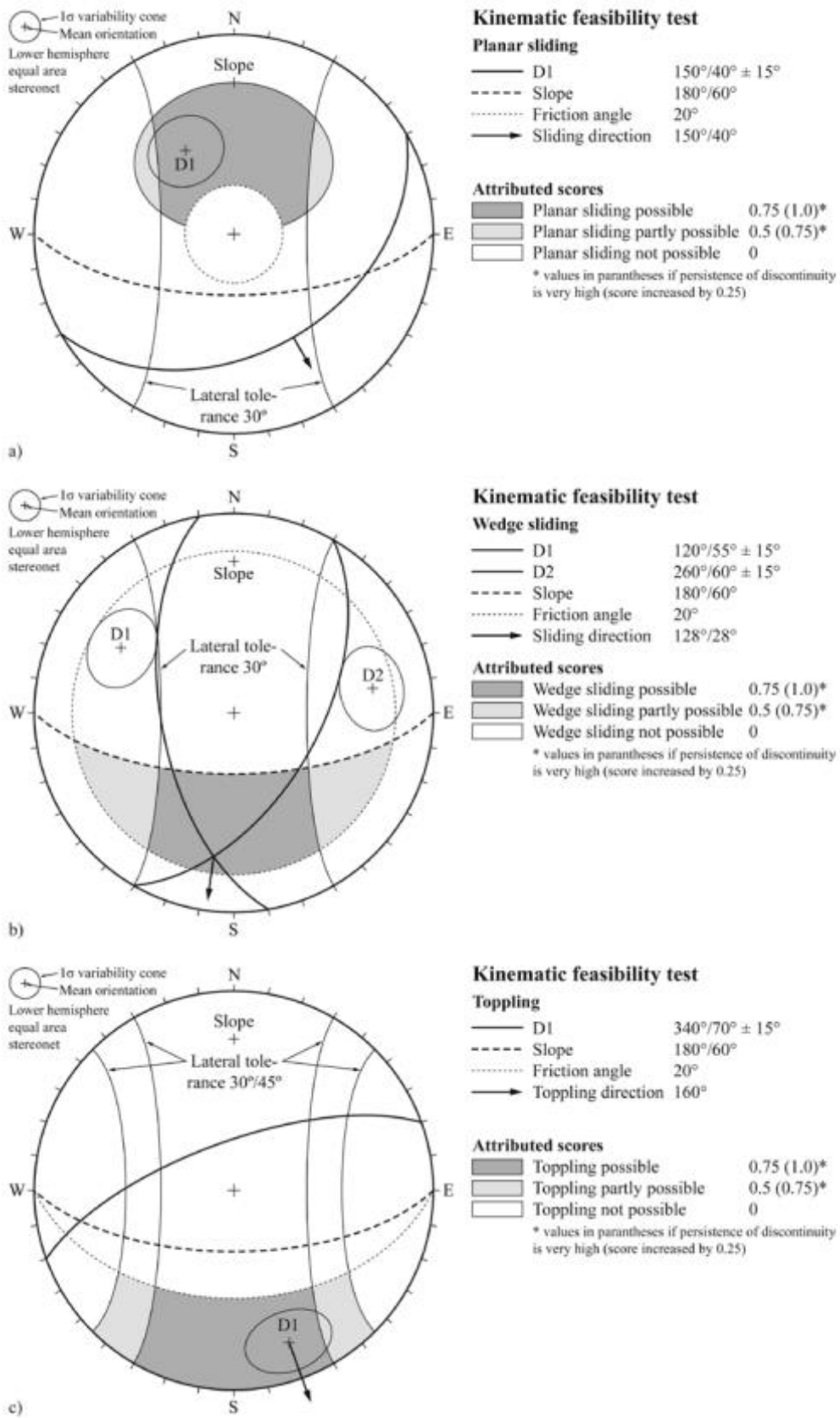


Figure 2.31: Kinematic feasibility test; (a) planar sliding; (b) wedge sliding; (c) toppling failure (Hermanns et al., 2012).



### 2.5.3 Conventional limit equilibrium method

The selection of slope analysis methods should be based on the complexity, scale, stage of the slope design, as well as the risk of failure. Limit equilibrium methods, LEM, are suited for simpler slope designs at the bench or inter-ramp scale, particularly in the early stages of a project when the information is limited. More advanced analysis methods such as numerical modelling should be used when the slope scale and the risk of the slope failure is increased (Stead & Havaej, 2016). Relevant rock slope analysis methods by numerical modelling will be presented in Subsection 2.5.5. The conventional limit equilibrium method is the most basic LEM, but more sophisticated LEM such as partial factor principle and probabilistic methods have had important developments the last years.

The traditional limit equilibrium method is deterministic in the calculation of the factor of safety ( $FS$ ) which represents the ratio between stabilizing forces ( $F_S$ ) and driving forces ( $F_D$ ). This means that the stabilizing and destabilizing forces should be at equilibrium when  $FS = 1.0$ . The factor of safety can be calculated from (Nilsen & Palmström, 2000) (Nilsen, 2017):

$$FS = \frac{F_S}{F_D} = \frac{(W \cos \psi_p - U - F_\alpha \sin \psi_p) \tan \phi_a}{W \sin \psi_p + F_\alpha \cos \psi_p} \quad (2.49)$$

$$FS = \frac{\left( \frac{\gamma_r \times H^2}{2} \left( \frac{1}{\tan \psi_p} - \frac{1}{\tan \psi_f} \right) \cos \psi_p - U - F_\alpha \times \sin \psi_p \right) \tan \left[ \text{JRC} \times \log \left( \frac{H \times \text{JCS}}{\sin \psi_p \left( \frac{\gamma_r \times H^2}{2} \left( \frac{1}{\tan \psi_p} - \frac{1}{\tan \psi_f} \right) \cos \psi_p - U - F_\alpha \times \sin \psi_p \right)} \right) + \phi_r \right]}{\frac{\gamma_r \times H^2}{2} \left( \frac{1}{\tan \psi_p} - \frac{1}{\tan \psi_f} \right) \sin \psi_p + F_\alpha \times \cos \psi_p}$$

where

$W$  = weight of the potential material in movement given a failure [kN/m]

$\psi_p$  = inclination of the sliding plane [°]

$\psi_f$  = slope angle [°]

$U$  = water pressure [kN/m]

$\phi_a$  = active or total friction angle [°].

$F_\alpha = m \times a$  = seismic action [kN/m]

$a$  = seismic acceleration as fraction of  $g$  [-]

$H$  = slope height [m]

$\gamma_r$  = specific gravity of rock mass [kN/m<sup>3</sup>]

JRC = joint roughness coefficient [-]

JCS = joint wall compressive strength [-]

$\phi_r$  = residual friction angle [°].

The slope is considered theoretically stable when  $FS > 1.0$ . However, in practice,  $FS > 1.3$  has been commonly used as the limit value for short-term stability while  $FS > 1.5$  has been used for long-term stability. This is due to uncertainties related to the input parameters (Nilsen, 2017).

LEM can also be used for a single bench for an excavated rock slope. A bench is smaller in scale and some simplifications can thereby be done. Read and Stacey (2009) states that the FS for a planar failure for a bench, given  $U = 0$ , can be calculated from:

$$FS = \frac{\tan \phi}{\tan \theta} + \frac{2c \times \sin \beta}{\gamma \times H \times \sin (\beta - \theta)} \quad (2.50)$$

where

$\phi$  = angle of friction [ $^{\circ}$ ]

$c$  = cohesion of sliding plane [Pa]

$\gamma$  = unit weight of rock mass [N]

$H$  = bench height [m]

$\beta$  = effective bench face angle [ $^{\circ}$ ]

$\theta$  = joint dip angle [ $^{\circ}$ ].

## 2.5.4 Partial factor principle limit equilibrium method

The partial factor principle is to be used instead of the conventional limit equilibrium method after Eurocode 7 (NS-EN 1997-1:2004+NA:2008) replaced the National standard NS3480 in 2010 as the governing standard for rock engineering designs. For rock stability assessments and designing of excavated rock slopes, the partial factor principle is the most used method (Nilsen, 2017).

In the traditional deterministic limit equilibrium method, the overall safety factor (FS) is calculated in comparison to the partial factor principle for limit equilibrium analysis where partial factors are assigned to acting forces/loads, and material strength/resistance. Acting forces/loads include components such as gravitational forces, water pressure, and seismic load while material strength includes cohesion, friction, and support elements (Nilsen, 2000) (Nilsen, 2017).

Eurocode 7 lists three design approaches to characterize the partial factors (Nilsen, 2017). In the Norwegian guideline for Eurocode 7, it is stated that design approach 3 should be used for geotechnical designs with the exception for piles based on the National Annex (NA) given at the end of the Eurocode (NBG, 2011). This means that the limit state of rupture or excessive deformation should be verified such that the combination of partial factors do not occur (StandardNorge, 2020):

$$Combination = (A1^* \text{ or } A2^{**}) + M2 + R3 \quad (2.51)$$

where A indicates partial factors on action ( $\gamma_F$ ) or the effects of actions ( $\gamma_E$ ), \* indicates on structural actions, \*\* indicates on geotechnical actions, M indicates partial factors for the ground/soil conditions ( $\gamma_M$ ), and R indicates partial factors for resistance ( $\gamma_R$ ).

Furthermore, it is stated that the geotechnical (GEO) limit state verification should use: A2 + M2 + R3, while the structural (STR) limit state verification should use: A1 + M2 + R3 (NBG, 2011) (StandardNorge, 2020).

The design is considered satisfactory if the sum of dimensioning load (stabilizing forces) is greater than characteristic load (driving forces) as given by (Nilsen, 2000) (Nilsen, 2017):

$$\sum R_d > \sum F_d \quad (2.52)$$

Dimensioning load  $F_d$  and dimensioning strength/resistance (action)  $R_d$  is defined by Equation 2.53 and 2.54 respectively.

$$F_d = F_c \times \gamma_f \quad (2.53)$$

$$R_d = \frac{R_c}{\gamma_m} \quad (2.54)$$

where  $F_c$  is characteristic load (action),  $\gamma_f$  is the load (action) factor,  $R_c$  is the characteristic strength, and  $\gamma_m$  is the material factor.

Given the parameters used for the conventional limit equilibrium method as described by Equation 2.49. The resultant forces for  $M_d$  and  $F_d$  can be calculated as seen below:

$$\sum R_d = (W \times \gamma_f \times \cos \psi_p - U \times \gamma_f - F_\alpha \times \gamma_f \times \sin \psi_p) \times \frac{\tan \phi_a}{\gamma_m} \quad (2.55)$$

$$\sum F_d = W \times \gamma_f \times \sin \psi_p + F_\alpha \times \gamma_f \times \cos \psi_p \quad (2.56)$$

Nilsen (2017) mentions several limitations to the partial factor principle when it is used for rock slope limit equilibrium stability analysis. The main problem that arises is the difficulty and uncertainty of quantifying the input parameters and partial factors for the stability analysis with the appliance to Eurocode 7. Nilsen (2017) concludes that the partial factor principle is also slightly more conservative (safe) compared to the conventional limit equilibrium method.

## 2.5.5 Numerical modelling

Numerical modelling is primarily used for the analysis of rock deformations and stresses, but also can be used to predict and describe other physical behaviours of rock masses (Nilsen & Palmström, 2000; Palmström & Stille, 2015). *Numerical modelling* is used as a term for all calculation types that involve numerical solutions for complex differential equations used to describe the rock mechanics. In most of the methods this also involves the *discretization* of the rock mass into (small and individual) elements. The solutions are based on iterative calculations (Palmström & Stille, 2015).

Rock masses are complex in nature, often with DIANE features (see Subsection 2.2.1), and to do any analysis or modelling of them simplifications and assumptions must be made. Several numerical methods have been developed to describe the rock mass. The numerical methods are commonly categorized into three categories (Barla, 2016; Jing, 2003).

### 1. Continuum methods

- Finite Difference Method (FDM)
- Finite Element Method (FEM)
- Boundary Element Method (BEM)

### 2. Discontinuum methods

- Discrete Element Method (DEM)
- Discontinuous Deformation Analysis (DDA)
- Discrete Fracture Network (DFN) methods
- Particle Flow Method (PFC)

### 3. Hybrid continuum/ discontinuum methods

- Hybrid FEM/ BEM
- Hybrid DEM/ BEM
- Hybrid FEM/ DEM
- Other methods

The continuum methods (differential models) are based on modelling the rock mass as a continuous medium, except for the introduction of a few discontinuities. Discontinuum methods (block models) represent the rock mass as a system of blocks which are interacting along their boundaries (Nilsen & Palmström, 2000). Hybrid methods can be used to provide adequate representations of the most significant processes or features in rock masses which a single continuum or discontinuum method is not able to provide alone (Jing, 2003). It is important for that the user is familiar with the limitation of the methods (Bjordal et al., 2011). Figure 2.32 illustrates different numerical methods of representing a rock mass.

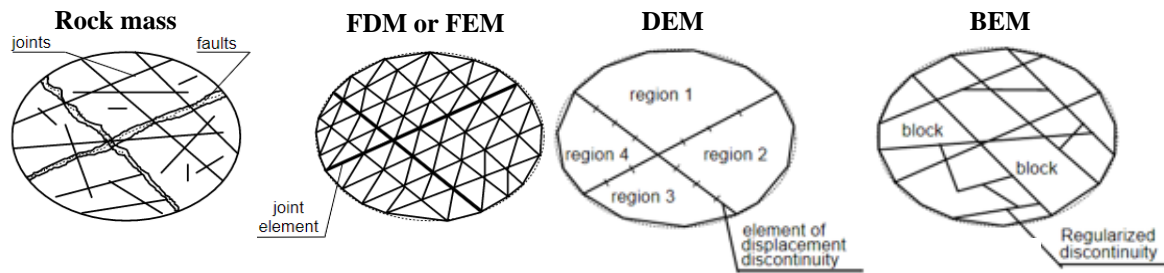


Figure 2.32: Different numerical methods to represent a rock mass. Modified after (Jing, 2003).

Wyllie (2018) lists four main benefits with numerical modelling for rock slope stability assessments:

1. Numerical models can achieve sufficient results without defining an exact failure mechanism (which empirical methods needs)
2. Numerical analysis gives a more realistic approaches to the rock mass response from geological such as weakness zones or ground water conditions)
3. Numerical modelling can be used to explain observed physical behaviour (such as deformations).
4. Numerical modelling can be used to construct geological models, evaluate potential failure modes, and choose appropriate design options.

Numerical analysis for rock slopes evaluates the stresses and strains developed in the slope. The stability is estimated based on comparing the rock strength and stresses developed in the slope (Wyllie, 2018). FEM has emerged as one of the most utilized methods for simulation of rock engineering problems. It is particularly useful for its flexibility in handling elements such complex boundary conditions, material anisotropy, and dynamic problems (Singh et al., 2013). Shear strength reduction (SSR) technique enables finite element methods (DEM) or finite difference methods (FDM) to calculate factors of safety for slopes, thus provide an alternative to limit equilibrium methods (Diederichs et al., 2007). DEM/FDM searches systematically for a stress reduction factor which brings the slope to the brink of failure, a so-called trial factor of safety (Hammah et al., 2007). The shear strength properties of the model are reduced until the stability limit of the model is reached (Diederichs et al., 2007). The stability limit between actual strength and model strength (at the brink of failure) is defined as the *critical shear strength factor* (CSR<sub>F</sub>) which is equal to factor of safety (Diederichs et al., 2007; Wyllie & Mah, 2004). Deformations will increase rapidly when the slope starts to fail, and FEM will not be able to converge anymore. The point of non-converge defines the CRSF (Mohammed Al-Bared et al., 2015).

SSR is also more accurate for analysis of slopes with strain-softening, heterogeneous stiffness, and passive structure-ground interaction compared to LEM. The technique can also be utilized for other non-linear problems such as multiblock discrete element simulations (Diederichs et al., 2007).

## 2.5.6 Probabilistic methods

Stability analyses of rock slopes require reliable geomechanical input parameters like friction angle, rock mass strength, groundwater pressure, and shear strength of the potential gliding surfaces. These parameters are inherently uncertain, and their exact values cannot be known. Deterministic approaches such as kinematic analysis, limit equilibrium methods, and numerical methods do not evaluate the variability of the input parameters (Abdulai & Sharifzadeh, 2019). Figure 2.33 illustrates the types of uncertainty.

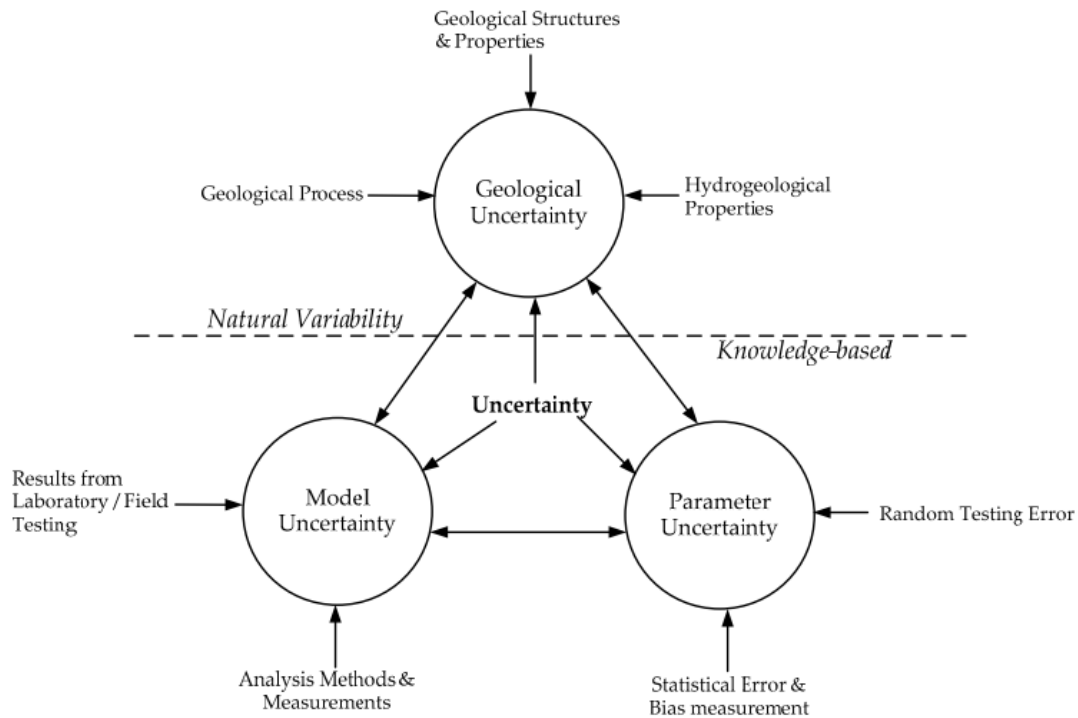


Figure 2.33: Types of uncertainty (Abdulai & Sharifzadeh, 2021).

The nature of uncertainties and the approaches for dealing with them have been discussed by many researchers over the years. The mathematical frameworks to assess uncertainties can be categorized into reliability analysis and non-deterministic methods. Non-deterministic methods can further be categorized into probabilistic and non-probabilistic methods. It should be noted that the non-deterministic approaches are combined with deterministic slope stability assessment methods. Thus, non-deterministic methods should be classified as an extension of the deterministic slope stability assessment methods, and not an entirely new slope stability assessment method (Abdulai & Sharifzadeh, 2019). Figure 2.34 shows different probabilistic and non-probabilistic methods for uncertainty quantification.

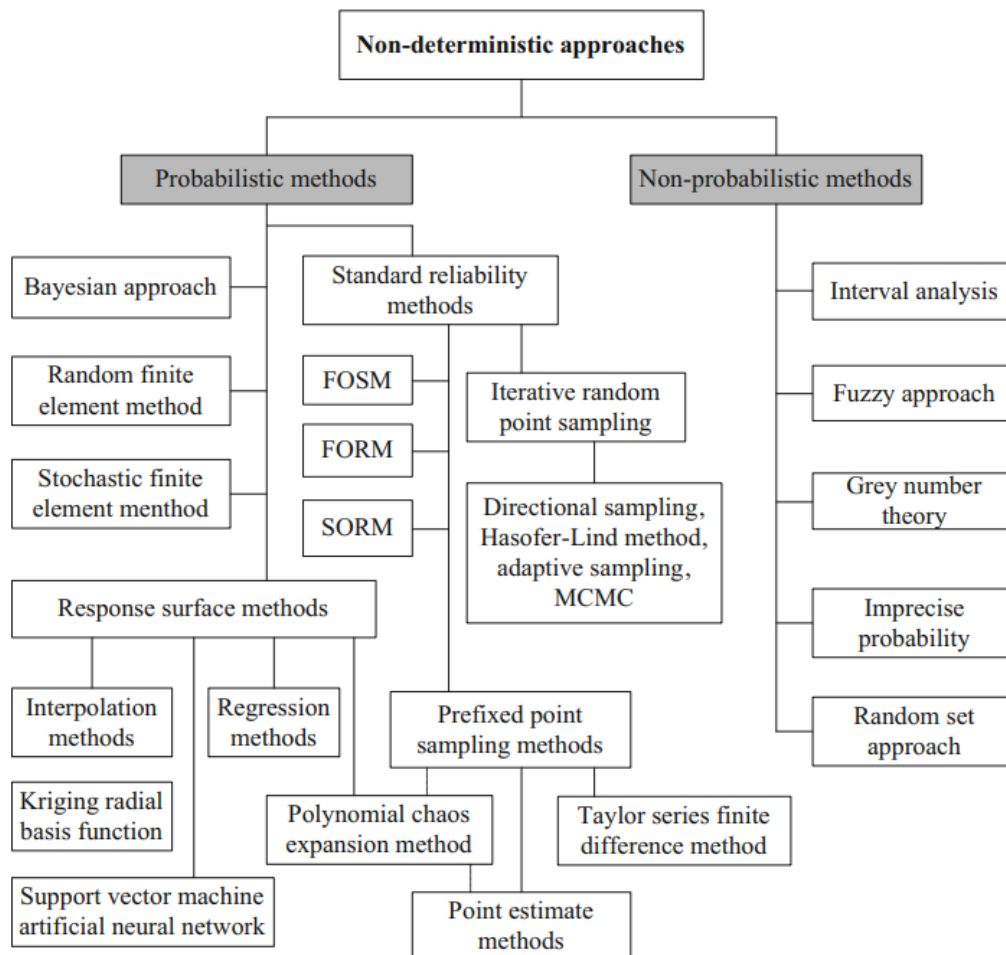


Figure 2.34: Non-deterministic approaches for uncertainty quantification (Huber, 2013).

Probabilistic methods utilities probability distributions to examine the effect of the variability of input parameters instead of deterministic values to assess the stability (Bjordal et al., 2011). By including the same set of parameters as the limit equilibrium methods a probability distribution for the factor of safety can be calculated and thereby achieve a probability of failure (PF) for the slope described by  $P(FS < 1.0)$ . The two most common methods for calculating the probability of failure are the Monte Carlo method, and the margin of safety method, but the first is considered more versatile (Nilsen, 2000; Nilsen, 2017; Wyllie, 2018).

Figure 2.35 presents a case example from Nilsen (2017) where the probability of failure is displayed both with an exponential and a cumulative probability distribution for the factor of safety. The probability of failure can also be divided by the total period if it was calculated. By doing this the yearly nominal probability of failure can be calculated which is useful as many countries use safety classes based on maximum yearly probability of slides, like Norway's TEK 17. The engineering geologist can thereby control if the slope is within the respective safety class.

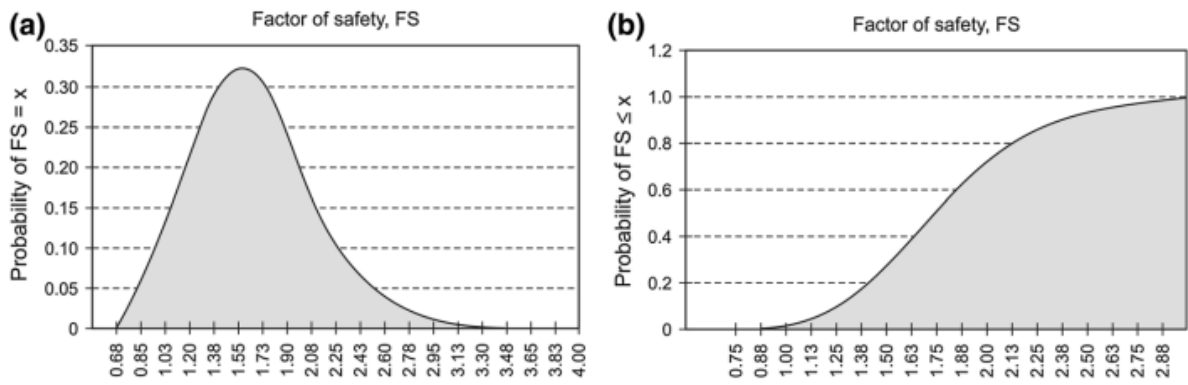


Figure 2.35: Results from slope stability assessments by probabilistic methods given in a case example from Nilsen (2017). This case example was for probability distribution over 50 years, and the probability of failure during this period was 4.6% given by  $P_{total}(sliding) = P(FS < 1.0) = 0.046$ ; (a) exponential probability distribution for the safety of factor; b) cumulative distribution for factor of safety.



### 3 Description of the planned rock cut at Hommelvik

This chapter will briefly introduce the highway road project E6 Ranheim – Værnes, and more specifically the challenging planned road cut at Hommelvik which is a part of the project. In addition, a brief introduction to why it was decided to be built a road cut (day zone) instead of tunnel for that part of the highway. Furthermore, the geology around the planned road cut will be described based on previous studies by other authors. This chapter will also present the climatic and hydrologic conditions for the area. Figure 3.1 shows photorealistic models of the planned E6 highway at Hommelvik with an early slope configuration of the road cut design. It has 20 m benches for the tallest part of the road cut while the newer version of the slope configuration has 15 m benches. However, they are otherwise very similar, and the figure still gives a good indication of it will look when it is finished. The relevant plan and profile drawings for this section can be found in Appendix B. The terrain is steep to extremely steep for most of the ridge (Svartløftberga) the planned road cut will be constructed into, as illustrated by the morphometry map in Figure 3.3. Figure 3.2 shows a 3D model of the terrain which highlights the steepness as brighter colour.

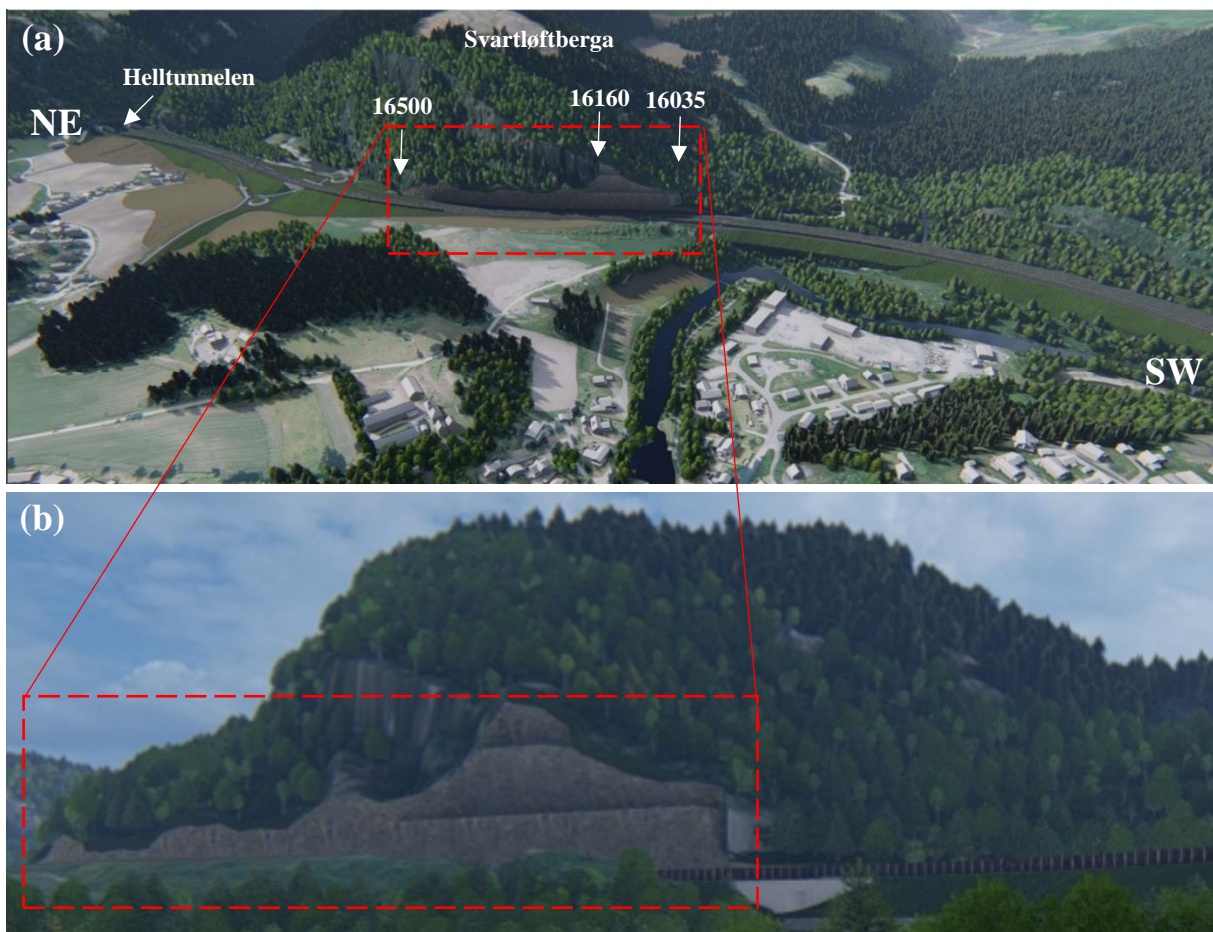


Figure 3.1: Photorealistic models of the planned E6 highway with an early-stage slope configuration (20 m tall and 10 m wide benches) which will not be used. Profile numbers at the start, end, and the tallest part of the road cut are included too. Modified after Gullikstad and Rønberg (2019).

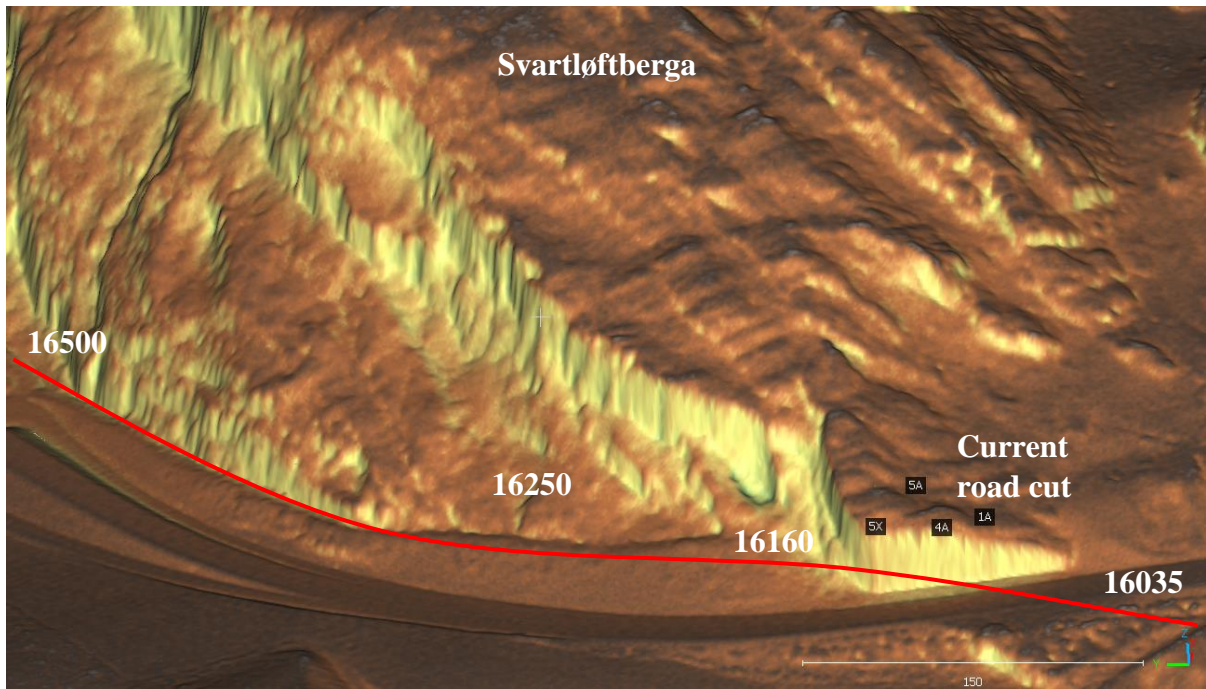


Figure 3.2: Terrain model of Svartløftberget in CloudCompare. Bright colour indicates steeper terrain. The red line illustrates roughly the centre line of the planned E6 highway. The four IDs above the current road cut indicates the drilled boreholes which will be presented in more detail in Chapter 4.

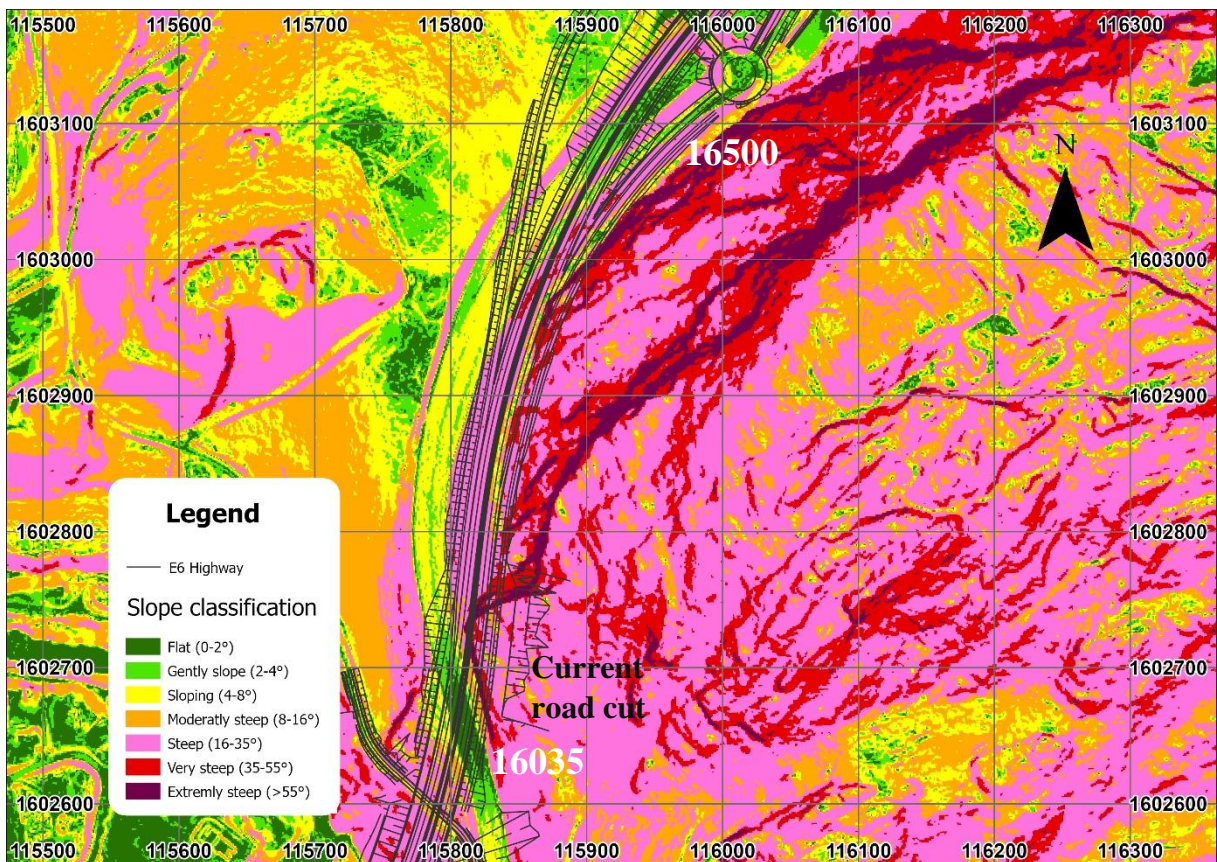


Figure 3.3: Morphometry map at the planned road cut along the new E6 highway. Slope classification after Zuidam (1986).

### 3.1 Description of E6 Ranheim – Værnes

The project E6 Ranheim-Værnes is planned to replace the current E6 highway road section (built in 1988-1995) located in the municipalities of Trondheim, Malvik, and Stjørdal by 2025/2026. Nye Veier AS signed the construction contract with the Spanish contractor Acciona Construcción for 4.3 billion NOK (VAT excluded) in 2018 and the construction work started in 2020. It is planned to be CEEQUAL-certified (sustainability certification) to the level of *very good* or *excellent* for the whole project (Multiconsult Norge AS, 2019a) (Nye Veier, 2021).

The new road section will be a four-lane highway designed for the speed limit of 110 km/h and stretching over 23 km reducing the travelling time with up to 5 minutes (from 18 to 13 min). The road standard will be H3 and AADT (annual average daily traffic) for 2045 is estimated to be ca. 35 000. The project will also include three double tube, double lane tunnels with the expansion of the existing tubes to profile T9,5 while the new tubes will be built with profile T10,5. Furthermore, the project will establish new road cuts as the curvature requirements are quite strict. The most challenging road cut is located at Hommelvik, as seen in Figure 3.4, and will be the focus for this thesis. The old E6 highway will be operative during the entire construction process of E6 Ranheim – Værnes (Multiconsult Norge AS, 2019a) (Nye Veier, 2021).

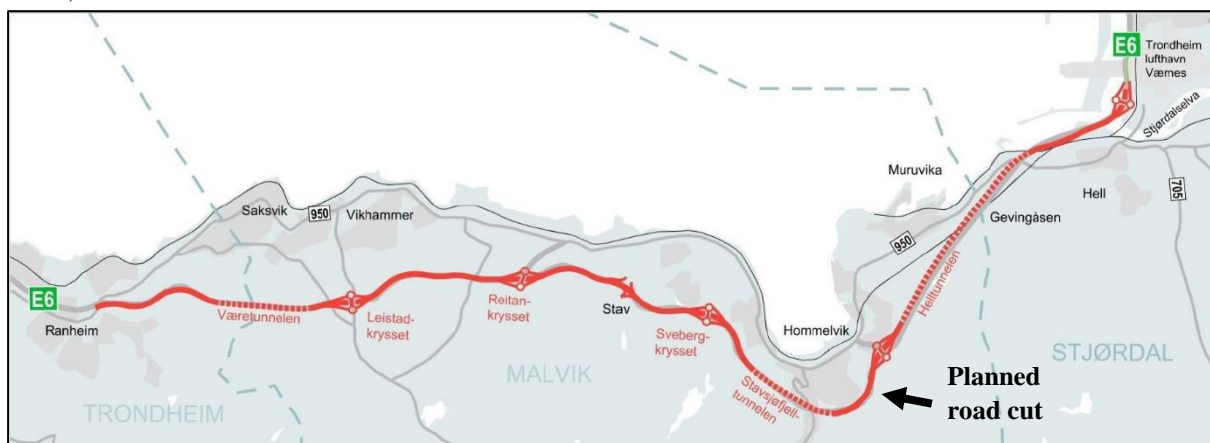


Figure 3.4: E6 Ranheim – Værnes. Modified after (Nye Veier, 2021).

Nye Veier has listed its five project goals as follows (DFØ, 2022):

- Realize the goal of an injury- and accident-free construction and operating period, as well as a health-promoting and fair working life.
- Minimize construction and lifetime costs through collaboration and digitization.
- Minimize inconveniences for all road user groups during the construction and operation period.
- Minimize greenhouse gas emissions and other impacts on the environment.
- Minimize temporary and permanent agricultural seizures.

### 3.1.1 Road cut versus tunnel alternative

In earlier stages of the planning an alternative with tunnel instead was evaluated too. NPRA (2018, 2020) suggests a maximum height of 20-30 m for road cuts. The reasoning for this is safety during excavation, and accessibility during operation and maintenance. However, the planned road cut at Hommelvik will be around 58 m tall at the maximum. In summary, both alternatives had to deviate from the regular standards and guidelines and had get approval from the Road Agency. A day zone with road cut was evaluated as the better alternative. The reader is referred to report E6RV-MUL-GE-MEM-CA#00-0006 for the rock engineering evaluation (Multiconsult Norge AS, 2020).

However, the main deciding factors for a road cut instead of tunnel were:

- More accidents in highway tunnels than highways in day zones.
- A tunnel in Hommelvik would create two very short day zones between Stavsjøfjelltunnelen and Helltunnelen. The statistics for accidents in the zone entering and exiting tunnels are particularly high (due to rapid changes in light conditions and weather factors such as misting on the window and icing on the road), but also changes in
- The distance requirements from a tunnel exit to an intersection (or ramps) would not be met with a tunnel there.

Risk analysis performed by emergency departments, NLF (Norwegian Truck Owners Association), Road Forum Trøndelag, NPRAs emergency department and road sign authority also concluded with road cut as better alternative compared to tunnel (NyeVeier, 2021).

Multiconsult Norge AS (2019c) evaluated 16 different categories regarding the five project goals for Nye Veier in report E6RV-MUL-ZP-RPT-CA#00-0013. It concludes that the alternative with a day zone scores better than the alternative with a tunnel in six of the categories for the Hommelvik parcel. The suggested tunnel alternative scores better in four categories, and the alternatives are about equal for six of the categories. Figure 3.5 illustrates locations of the suggested tunnel alternatives and day zone alternative. Figure 3.6 shows a more detailed map how the new E6 highway will cut into the current terrain and where the road cut will be.

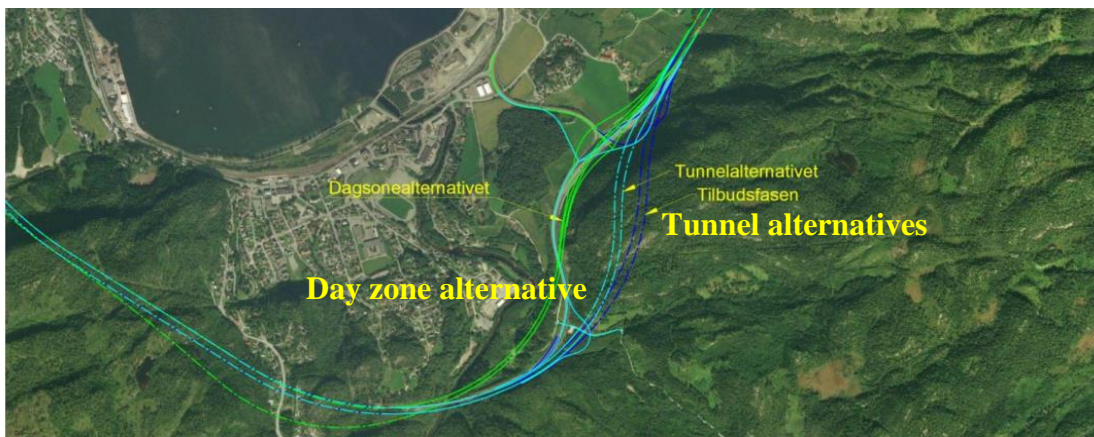


Figure 3.5: Overview of the daylight alternative (green line), the original tunnel alternative (blue), and the revised tunnel alternative approved by the NPRA (Norwegian Public Road Administration) (cyan) (MulticonsultNorgeAS, 2019c).

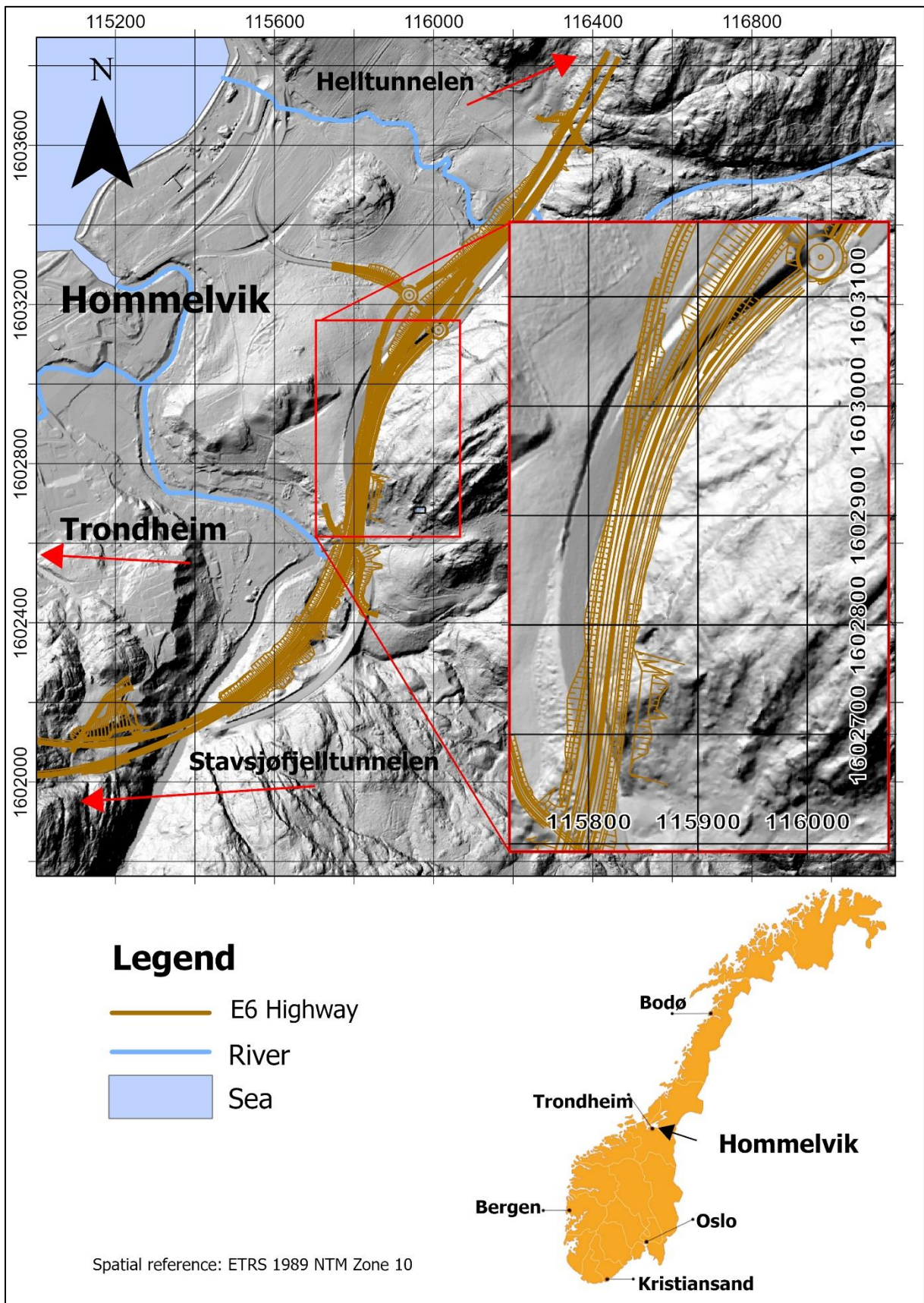


Figure 3.6: Location of the planned road cut at Hommelvik.

## 3.2 Geology

The Trondheim region are one of the main provinces in the Caledonian Orogeny in Norway. The rock types from the Hommelvik area and south to Mostadmarka are predominately from the Ordovician to Silurian age, and consists of metamorphic volcanic, intrusive, epiclastic rocks, and sedimentary rocks. All the rocks can be classified to be within the Greenschist Facies. Furthermore, the nappes have enjoyed several phases of thrusting, thus resulting in a complex geology (Torske, 1965). The main features of the stratigraphic column in the region are presented in Table 3.1.

Table 3.1: Main features of the stratigraphic column in the Trondheim region (Torske, 1965).

Period	Group	Prominent rock types
Silurian	Horg	Shale and sandstone Conglomerate (Lyngestein cgl.)
	Upper Hovin	Rhyolite and rhyolite tuff Sandstone Conglomerate (Volla cgl.)
	Lower Hovin	Shale Rhyolite tuff Sandstone, shale, limestone Conglomerate (Stockvola, exl. Venna cgl.)
Ordovician	Støren	Greenstones: Lavas, pyroclastic rocks, minor amounts of sedimentary rocks
	Røros	Mainly phyllites and mica schists

Aagaard (1981) proposes that the rock types around the study area are likely deposited in an early phase of the Caledonian Orogeny. Pyroclastic rocks and basalts were likely formed first then sedimentary rocks were deposited. Later phases of the Caledonian Orogeny resulted in regional metamorphoses. The processes can be summarized as folding, recrystallization, and uplifting. The rocks were folded around an axis parallel to the Caledonian Mountain Chain, NNE-SSW. They were later tilted from lateral compressions resulting in large-scale deflections and undulations from the main trend of the Caledonian Orogeny (Torske, 1965).

The area around the planned road cut consists predominately of low-metamorphic sedimentary rocks with some igneous rocks. The deposition of the rocks happened within a similar time frame and thus have undergone similar metamorphose. This resulted in intricate patterns of folding and irregular distribution of rock types, making the rock boundaries blurry occasionally (Torske, 1965).

The bedrock map N50 (1:50 0000) from NGU (Geological Survey of Norway) is displayed in Figure 3.7. All the dominant rock types there are part of Støren Nappe and the Ekne Group, and of sedimentary origin (Lutro, 2005).

The summary of the expected rock types in the study area is listed below:

**Tuffite:** The tuffite in the area has rhyolitic composition (Lutro, 2005). Tuffite consist of rounded and/or angular fragments. Tuffite is a type of tuff (rock made of volcanic ash) but consists of both detrital material and pyroclastic material (minimum 25 %). The rock is fine-grained and light brownish in colour. The possibly present minerals are albite, quartz, calcite, muscovite, chlorite, sphene, zircon, rutile, and ore minerals. Torske (1965) preferred the descriptive term calcareous arkose over tuffite in his work in the area. Based on the N50 bedrock map in Figure 3.7 the layer of tuffite should be located about 300 meter south of the planned road cut and will likely not be intersected even if the layer was sub-horizontal.

**Polymictic conglomerate:** The polymictic conglomerate in the study area can be some places be classified as conglomeratic greywacke. Conglomerates in general are defined as a sedimentary rock consisting of clasts with minimum 30% rounded particles that are coarser than 2 mm. Furthermore, the matrix consists of detrital sediments from clay to sand size or siliceous cement (Goodman, 1993). Polymictic conglomerate consist of a minimum of two types of minerals or rock types (or a combination). These types of rock have a tendency of high permeability, thus susceptible to weathering and erosion.

**Metagreywacke:** The metagreywacke has similarities to metasandstone, and distinction between them is not always clear. In the N50 bedrock map for the area it is called metasandstone (metagreywacke). Multiconsult Norge AS (2019a) suggests it is metagreywacke there based on their field observations.

The varieties of metagreywacke in the area are for the most part fine-grained and angular. The colour varies from light grey-green, dark grey to brownish grey. The mineral composition varies a lot and can contain minerals such as: quartz, muscovite, chlorite, rutile, sphene, tourmaline, zircon, ore minerals, albite, limonite, apatite ± biotite (Torske, 1965).

Thin bands of laminated clayshale and phyllite are also interchanging with some of the metagreywacke. The banded phyllites is grey to brown in colour, and fine- to medium-grained. It consists of chlorite, muscovite, albite, quartz schist, with some variation in carbonate content (Torske, 1965).

The brownish varieties of metagreywacke have the highest content of carbonate minerals. This colouration is a result of the formation of limonite which is a weathering product of carbonates (Torske, 1965).

Some variations of metagreywacke have cm-thick quartzitic layers which are alternating with mm-thick pelitic layers. Furthermore, some of the metagreywackes are interbedded with white to light grey coloured quartz schist. Along this boundary with quartz schist, 1-2 mm thick quartz veins dissect the rocks (Torske, 1965). There metagreywacke have graded bedding with no crossbedding which is typical for deep marine sediments (Goodman, 1993). Given a higher degree of metamorphoses the metagreywacke would turn into mica gneiss or mica shale (Løset, 2006).

Torske (1965) introduced a subdivision of nomenclature for the metagreywacke due to its complex nature and big span of variation. It was divided into greywacke, calcareous greywacke, calcareous felspathic quartzite, calcareous arkose, and subgreywacke. For simplistic reasons only the term metagreywacke will be used further.

The reader is referred to the studies of Torske (1965) for a more comprehensive review of the general geology of the study area.

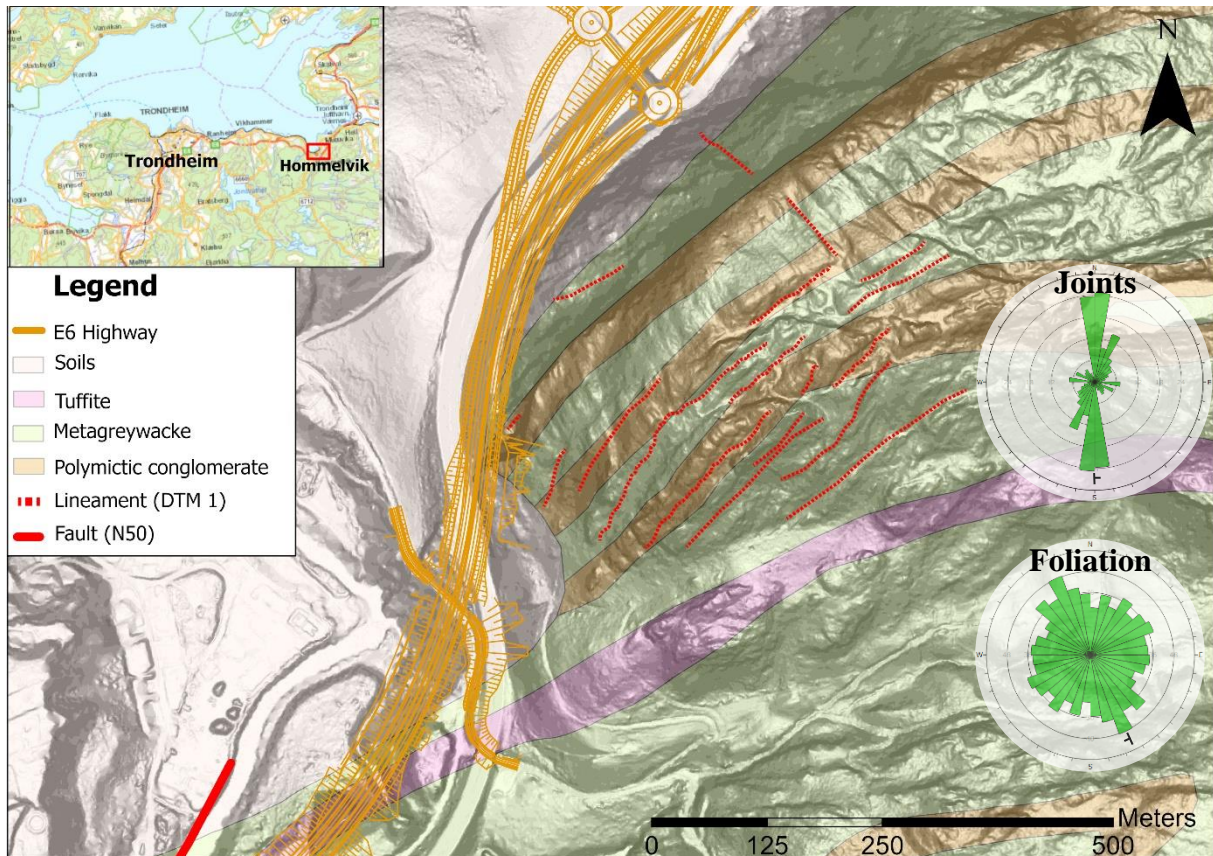


Figure 3.7: Overview of the different bedrocks and soils at Hommelvik. Lineaments from DTM 1 and fault from N50 are added too. Data from NGU's Bedrock N50. Lineament (DTM1) is determined visually from the shadow relief from DTM 1 (terrain model with 1 m resolution). The rosette plots are from the core logging which will be discussed further in Section 4.2.

The specific soils in the study area will not be discussed in a separate section as the overburden is assumed to not affect the excavation process too much. Ground investigations were done along the planned E6 highway in 2018, and that included cone penetration testing (CPT) (Multiconsult Norge AS, 2019b). Relevant CPT tests near the planned rock cut with depth to bedrock can be found in Appendix A. Based on these tests it seems like the depth to bedrock is between 6-13 m for the area around the planned E6 highway and road cut, some sections further away seems to be deeper, and one CPT test showed 21 m depth (MC-1046).



### 3.3 Climatic and hydrological conditions

Climatic and hydrological conditions are important to consider as slope failures are often closely related. Slope instabilities or failure often occur in periods with heavy precipitation, particularly combined with snowmelt in colder climates. There are no direct studies on the percentages of the triggering mechanics for landslides in Norway. However, Pantelidis (2009) states that 92% of landslide movements are related to heavy rainfall in Greece. On highways in California rainfall was the trigger mechanics for rock fall in 30% of the cases while freeze-thaw processes were 21%. In Yosemite National Park (California), 51.0% of the registered rock falls had rainfall as the trigger while 11.8% was from freeze-thaw processes (Turner & Schuster, 2012). This gives an indication of the importance of climatic and hydrological conditions for rock slope stability.

The introduction of moisture for rocks may reduce the strength drastically. Nilsen and Palmström (2000) states that sandstones and shales can get a strength reduction of 40% and 60% in a saturated state compared to dry, respectively for the two rocks. The planned excavated rock slope at Hommelvik will be located in metagreywacke and polymictic conglomerate, thus the same range is probably applicable. Figure 3.8 illustrates the hydrological conditions at Hommelvik.

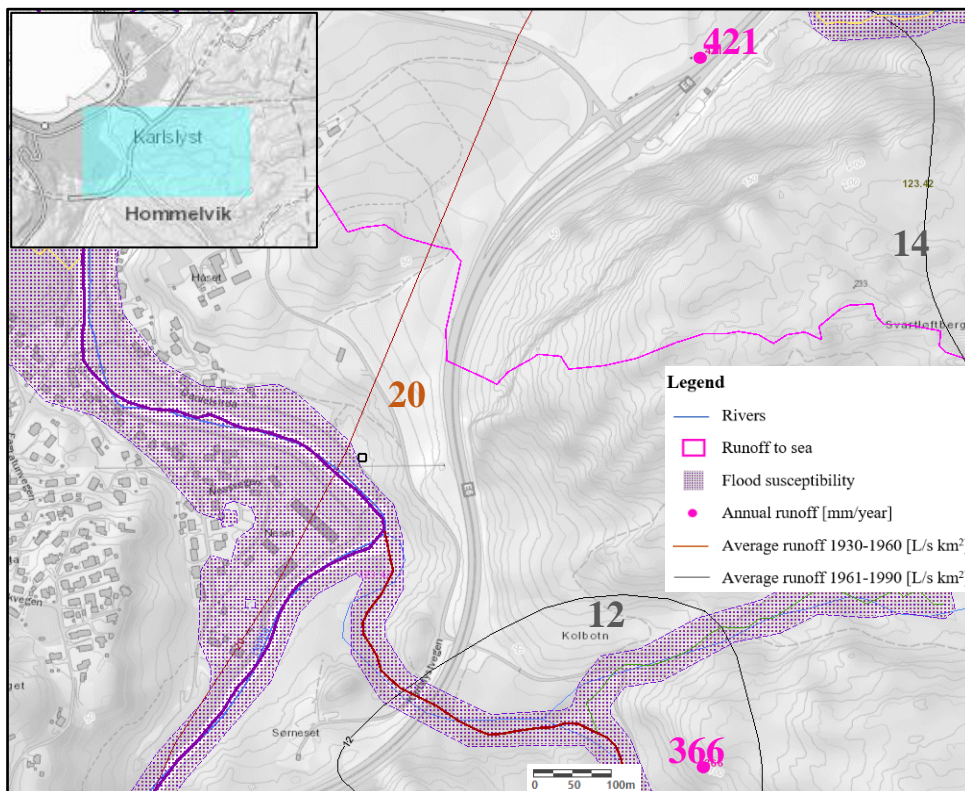


Figure 3.8: Hydrological conditions at Hommelvik. The pink line indicates the division between two precipitation fields (NVE, 2022).

### 3.3.1 Climate

Hommelvik is located within the Trondheim Fjord and thereby affected by the coastal climate, represented by warmer winters and cooler summers. However, it is less exposed compared to other coastal areas closer to the Norwegian sea. This results in less annual precipitation as seen in Figure 3.9. The normal annual precipitation is 832 mm in Hommelvik and is defined from the standard 30-year period 1991-2020 (MET, 2021). Furthermore, the total precipitation for 2021 was 974.5 mm (MET, 2022). There was 144 days with precipitation in 2021, as seen in Figure 3.10. The fall and spring seasons had the highest representation, which is expected for regular years. It is further evident from the figure that the monthly precipitation from 2021 deviates significantly from the normal, with some months such as October and November with over double the normal precipitation. On the other hand, January, February, and July had less than half the normal precipitation for 2021. This emphasises that the climate for an area is evaluated over a longer period as yearly deviations are expected. However, it could also indicate more extreme weather which fits with the projected future climate which will be further discussed in Subsection 3.3.2.

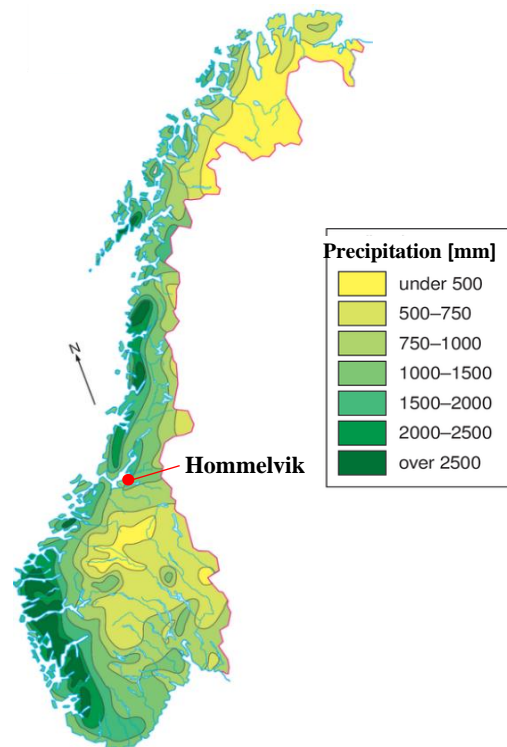


Figure 3.9: Approximate annual precipitation in Norway. Modified after Dannevig and Harstveit (2021).

It should be noted that these measurements are based on the closest weather station (measuring both temperature and precipitation), which is located at Værnes, id SN69100. There is a weather station at E6 Malvik, id 69035, which is a little bit closer (6.7 km) than the one at Værnes (8.7 km), but only temperature is measured there. It was established October 2016 and thus lack the necessary historical data (MET, 2022). Furthermore, several days are missing data. Data from this station will thereby not be included.

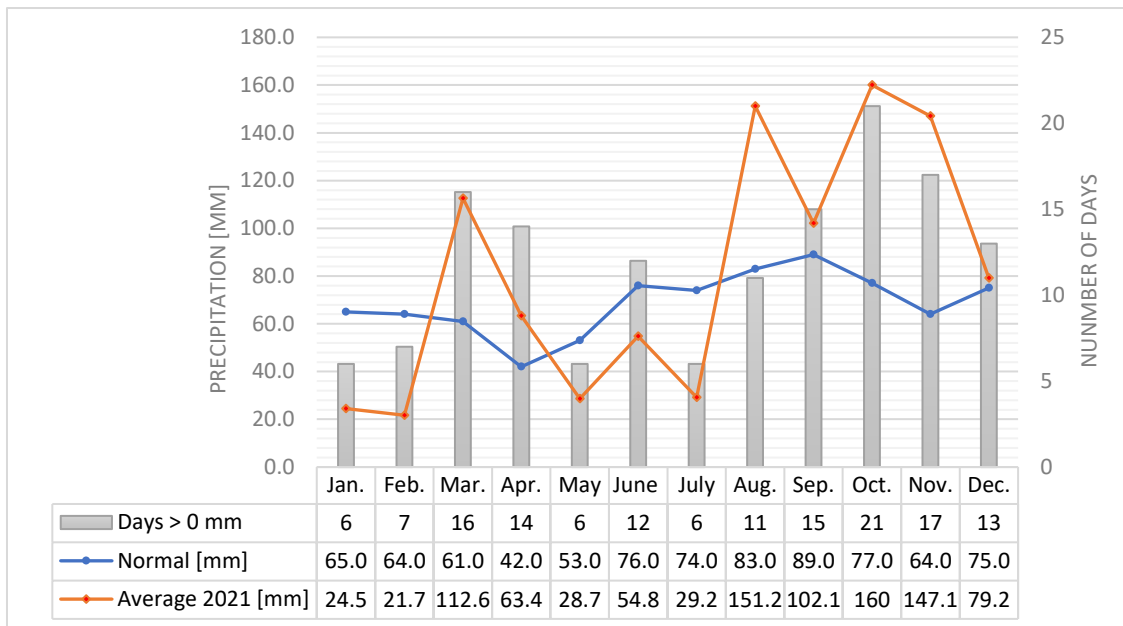


Figure 3.10: Monthly precipitation measured at the Værnes weather station (SN69100). The blue line indicates the normal precipitation from the period 1991-2020, the red line indicates average precipitation from 2021, and the grey columns indicate the number of days in the respective months with some precipitation.

Figure 3.11 shows that the temperature went below the freezing point for 118 days in 2021 at Hommelvik with January and December being the peak months with 30 and 25 days respectively. Furthermore, January, February, March, November, and December, have normal and average temperature from 2021 close to or below 0°C. This is problematic in terms of the freeze-thaw processes which is an important factor for the development of joints and blocks, thus resulting in block fall, rockslides, and rock slope stability problems in general (Bjordal et al., 2011).

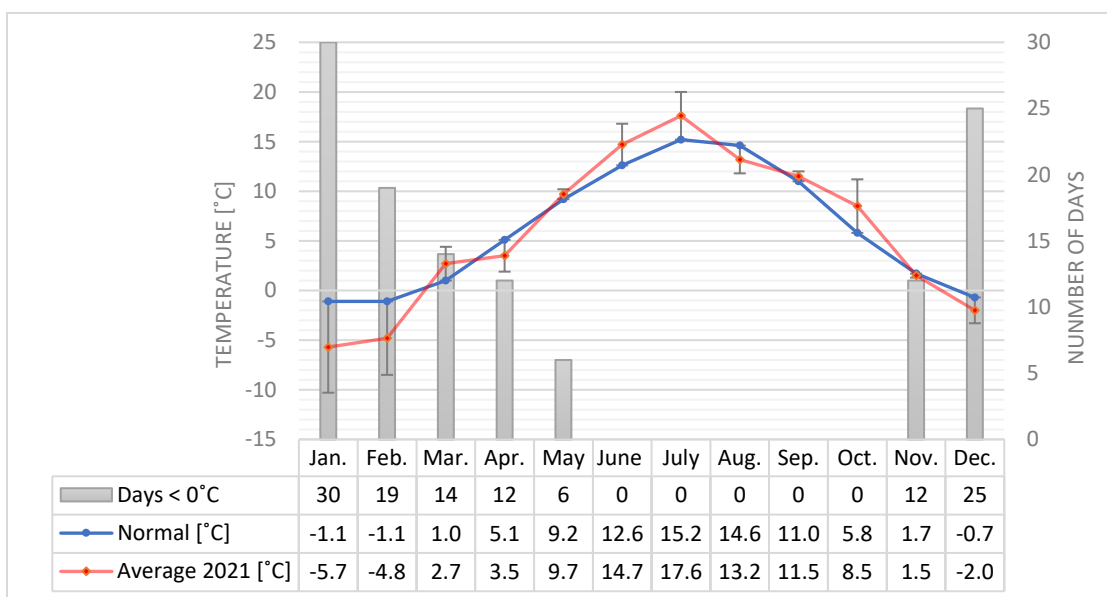


Figure 3.11: Monthly temperatures measured at the Værnes weather station (SN69100). The blue line indicates the normal temperature from the period 1991-2020, the red line indicates average temperatures from 2021, and the grey columns indicate the number of days in the respective months of 2021 when the temperature dropped below the freezing point. Average 2021 also includes error bars for standard deviation.

### 3.3.2 Future climate

Projections of future climate changes are not deterministic and definitive like short-term weather forecasts are. Furthermore, there are several elements of uncertainties involved in the projections and models of climate changes. These can be summarized as three main factors, (1) anthropogenic and natural forcings that are uncertain in terms of the climatic scenarios that unfold from them in the future, (2) imprecise models and lack of understanding of the climate, and (3) internal climate variability (Stocker et al., 2013).

The change of block fall and rockslide activity, and thereby rock slope stability due to the climate changes are hard to quantify. Even though this is the case, Bjordal et al. (2011) suggests that it is reasonable to assume that there will be a gradual increase of block fall and rockslides events the next 50 years.

Bjordal et al. (2011) lists the following factors as the main contributing factors:

- More extreme precipitation events with local variations
- Increase in annual precipitation
- More snow accumulation in the mountains during the winter season
- Larger areas without snow in the lowlands during the winter season
- More and extended freeze-thaw cycles due to warmer winters

The western part of Norway is expected to get the greatest increase in annual precipitation, and the part of the country which are expected to get the greatest increase of block fall and rockslide activity particularly during the fall and summer. Furthermore, roads along steep terrain and rock slopes are expected to be the most exposed. Bjordal et al. (2011) emphasizes it hard to predict the percentage increase of block fall and rockslides events, but 5-10% is a reasonable expectation of the increase on a national level over the next 50 years.

## 4 Field and laboratory investigations

During this thesis field and laboratory investigations have been done with the purpose of establishing reliable and representative input parameters for later stability assessments. This includes estimating input parameters for determining the shear strength of discontinuities with Barton-Bandis failure criteria, evaluate the rock mass quality with Q-slope, and establishing rock mechanical properties for later numerical modelling. In the first sections the main findings from the field mapping will be presented. Following this, a summary of the core logging, then the laboratory investigations, and at last a comparison of the laboratory results performed by SINTEF (2022). The author did tests on cores from two of boreholes while SINTEF did tests on the two others.

### 4.1 Field mapping

This section will include the results from the field mapping which was done at 25.11.2021. The field mapping was primarily done from profile 16150 to 16300 (north of the current road cut). Multiconsult AS mapped the entire stretch for the planned road cut in 2019, and their observations particularly of the southern side of the current road cut will be supplemented into this section and discussed. Potential sliding planes and weakness zones observed in the field will not be discussed explicitly in this section but will rather be supplemented into Subsection 5.4.1 for an easier and more meaningful comparison with the other data sources (core logs and point clouds).

#### 4.1.1 Lithology

The dominating rock type observed in study area is metagreywacke. As discussed in Section 3.2 the metagreywacke in the area is expected to have several variations, which was confirmed during the field mapping (and later the core logging as seen in Section 4.2, Appendix G, H, I, and J). The metagreywacke was occasionally folded and with small scale folding some places, as seen in Figure 4.2 (a) and Figure 4.2 (b). Figure 4.2 (c) also shows evidence of parasitic s-folds and fault lines. Several faults were also observed in the later core logging. At some locations the metagreywacke was also interbedded with cm-thick quartzitic layers, as seen in Figure 4.2 (b).

Furthermore, small sections of phyllites and greywacke interbedded with phyllite were also observed. Torske (1965) used the term greywacke-phyllite to cover this transitional rock type. The darker parts in the phyllite and greywacke are hemipelagic mud which is silt and clay-sized grains with some biogenic material.

Further, the rock type was polymictic conglomerate was observed. It should be noted that only smaller outcrops (which were hard to distinguish) were observed west for the current rock cut (which the author mapped). However, east for the current rock cut polymictic conglomerate was more prominent as documented by Multiconsult Norge AS (2019a). An outcrop of polymictic conglomerate is shown in Figure 4.1 (b).

In the middle of the current rock cut, at profile 16120, two diabase dikes are observed, as shown in Figure 4.1 (a). Borehole 1A and 4A (which will be described further in Section 4.2) were drilled about 30 m behind the road cut wall which the diabase dikes were observed, but there were no signs of the diabase dikes.

The observed rock types are in general unweathered to slightly weathered (weathering class I-II, Table 2.7). However, there are smaller sections of what is assumed to be metagreywacke (greywacke-phyllite) with moderate weathering (class III) and more distinct bedding. The phyllite layers are more susceptible to weathering compared to the surrounding phyllite.

There were no signs of pyrites in the field which occurred regularly in the core logging. The rock types were not tested for carbonate minerals, however the testing by Multiconsult AS showed that the metagreywacke contained occasionally carbonates (Multiconsult Norge AS, 2019a). Figure 4.2 (d) shows a brown variant of metagreywacke which often contains more carbonates as discussed by Torske (1965).

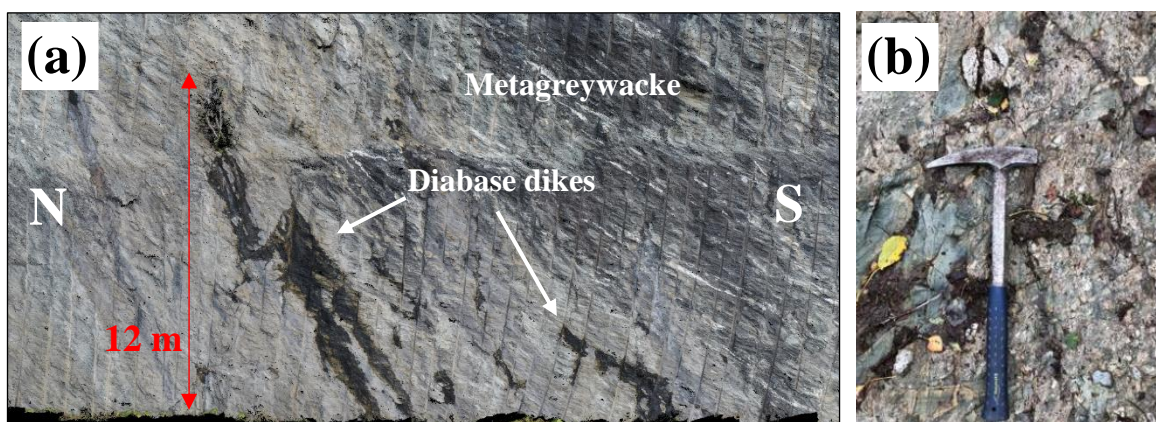


Figure 4.1: (a) Diabase dikes surrounded by metagreywacke at profile 16120 (from point cloud). (b) Polymictic conglomerate observed 100 m east from the current road cut by Multiconsult Norge AS (2019a) .

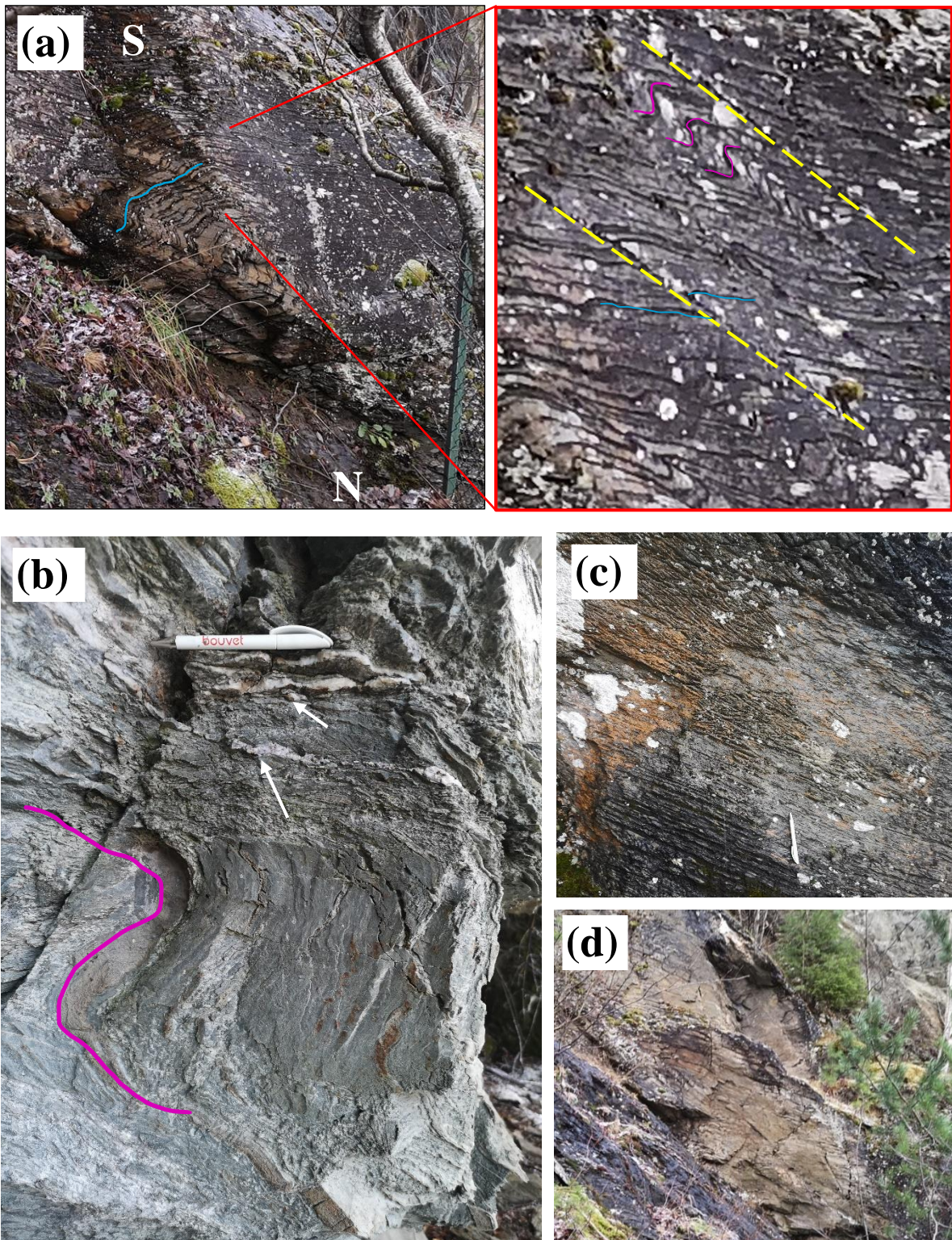


Figure 4.2: (a) Metagreywacke with small scale folding (blue), fault lines (yellow), and parasitic s-folds (pink) at profile 16160. (b) Folded metagreywacke interbedded with cm-thick quartzitic layers. (c) Metagreywacke (greywacke-phyllite) interbedded with mm-thick pelitic layers (shale) which are more susceptible to weathering compared to the rest of the rock body which has bigger grains. There is also distinct staining on the surface (dark brown). (d) Brownish variant of metagreywacke at profile 16230, possibly from limonite (weathering product of carbonates).

## 4.1.2 Discontinuities

Mapping of the discontinuity orientations were not prioritized during the limited time in field by the author as Multiconsult Norge AS (2019a) had already mapped the entire stretch (profile 16100-16600) in detail. Furthermore, point clouds and orientated core logs would be used by the author to determine the discontinuity sets and their orientation more precisely later and be the basis for later stability assessments. A general assessment of the joint characteristics was done in field, and the results are added in Table 5.3 along with supplementations from Multiconsult Norge AS (2019a) observations.

The summary of the discontinuity mapping from Multiconsult Norge AS (2019a) is given in Table 4.1 and rosette plots in Figure 4.3. Only the foliation (L) was observed in the entire study of the mapped discontinuities. These defined discontinuity sets, and their orientations will be evaluated and compared against the other data sources in Subsection 7.1.

Table 4.1: Joint characteristics from the current road cut for profile 16100 – 16500. Values in brackets indicate the dominating values if ranges are used. Modified after (Multiconsult Norge AS, 2019a).

Parameter	Foliation (L)	Joint set A	Joint set B	Joint set C
Dip direction [°]	160-240	300-330	100-140	265
Dip [°]	25-55	60-85	55-80	40-70
Spacing [m]	0.5	1-2	<0.1-2 (1-2)	0.5
Persistence [m]	<5–100 (<5)	5-20+	20+	20+
Jr*	1.0-1.5	0.5-3.0	1.0	1.5

\*Interpreted based on joint roughness description in the report.

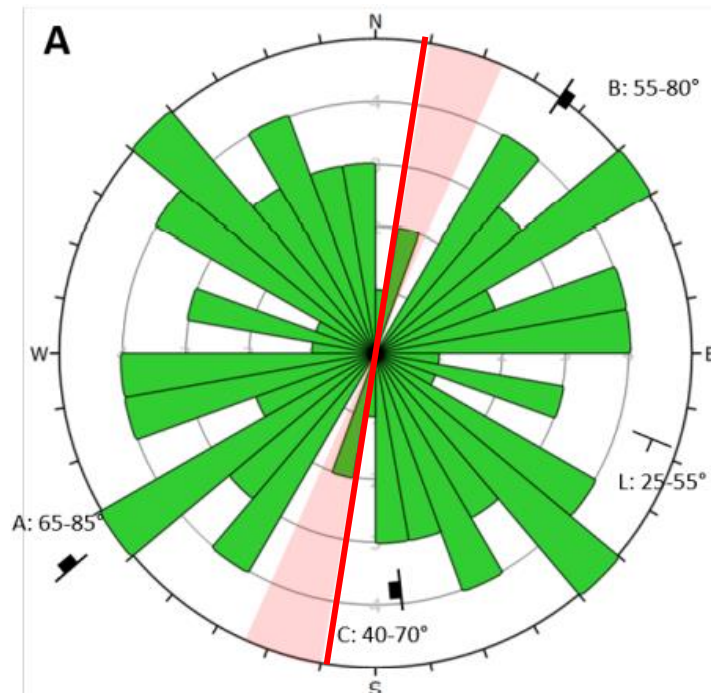


Figure 4.3: Rosette from the current road cut, profile 16100 – 166500. Red line indicates the orientation of planned road cut in southern to centre parts while the red hatching indicates the variation in orientation for the entire road cut. Modified after (Multiconsult Norge AS, 2019a).



## 4.2 Summary of core logging

Simplified core logging was performed by the author and personnel from Rambøll (Linn Døvle, Karsten Østerås, and Endre Kjærnes Øen) at 09.12.2021, 14.12.2021, 20.12.2021, and 12.01.2022. The boreholes were drilled at different locations (and angles) along the planned road cut. The cores of the boreholes were oriented during drilling, thus making it possible to evaluate the orientation of the discontinuities later.

The summary of geographical information and orientation of the boreholes are listed in Table 4.2. Furthermore, the locations of the boreholes (both top and bottom points) are displayed in Figure 4.4. The surface conditions at the borehole sites and the used equipment for drilling are shown in Appendix F.

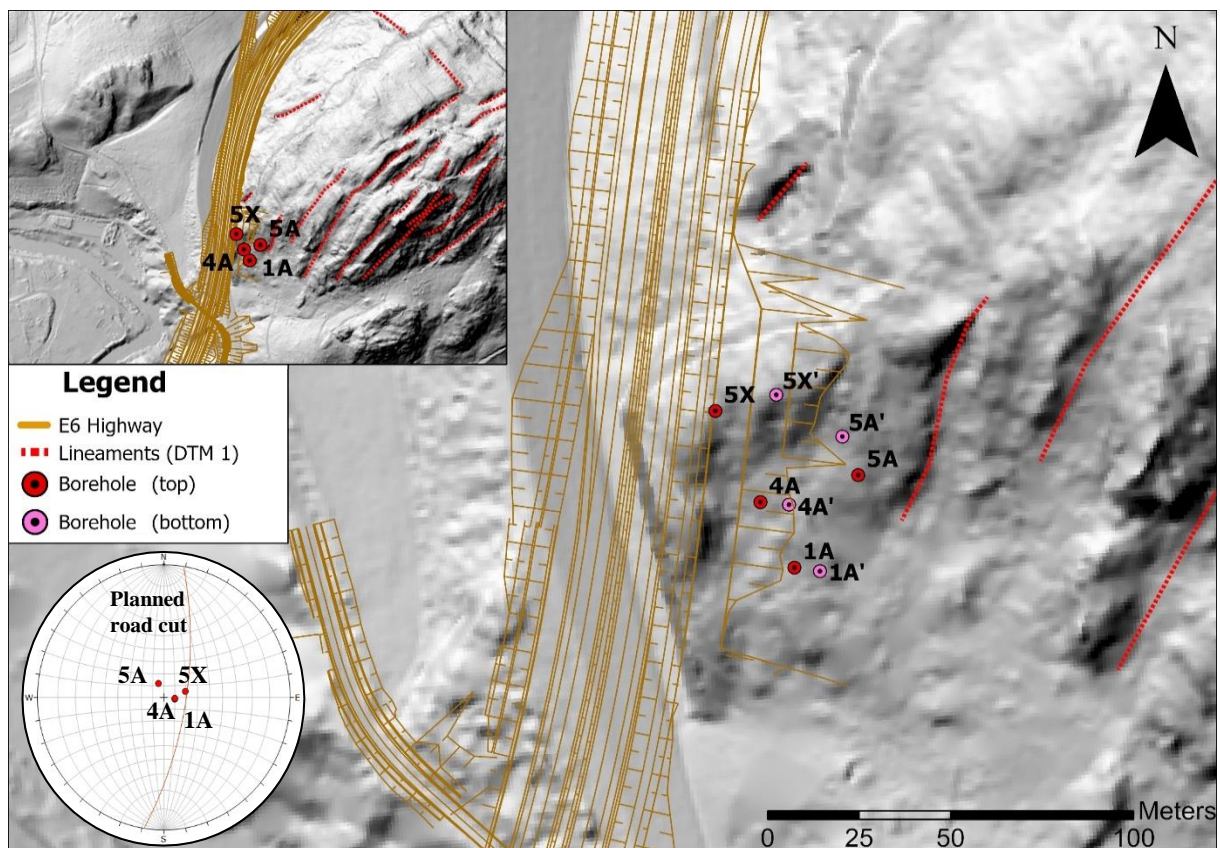


Figure 4.4: Location of drilled boreholes at Hommelvik and the planned E6 highway (brown). Red points indicate the surface locations of the boreholes while the pink points indicate the bottom locations in the ground.

The purpose of the core logging was to get an overview of the rock mass quality, detect discontinuities with properties and orientations, retrieve core samples for testing of rock mechanical (Subsection 4.3.1) and shear strength properties (Subsection 4.3.2), and evaluate which rock types were present, as illustrated in Figure 4.5 (a). Furthermore, zones with core loss or broken rock were mapped, and JRC was measured in particular sections included all sections with low rock mass quality (RQD and NI), marked with orange to red colours in Figure 4.5 (b) and (c). Section of the cores with rust, staining or fillings were also logged.

The discontinuities present in the boreholes can be correlated with discontinuities sets estimated from the point cloud and fields measurements. Thus, check if the discontinuities intersect the boreholes as expected (and with the same orientation). Deviations in orientations can be used to calibrate the models for the discontinuity sets. This can further be used to evaluate the spacing and persistence of the discontinuity sets, which is relevant for the numerical models in RS2.

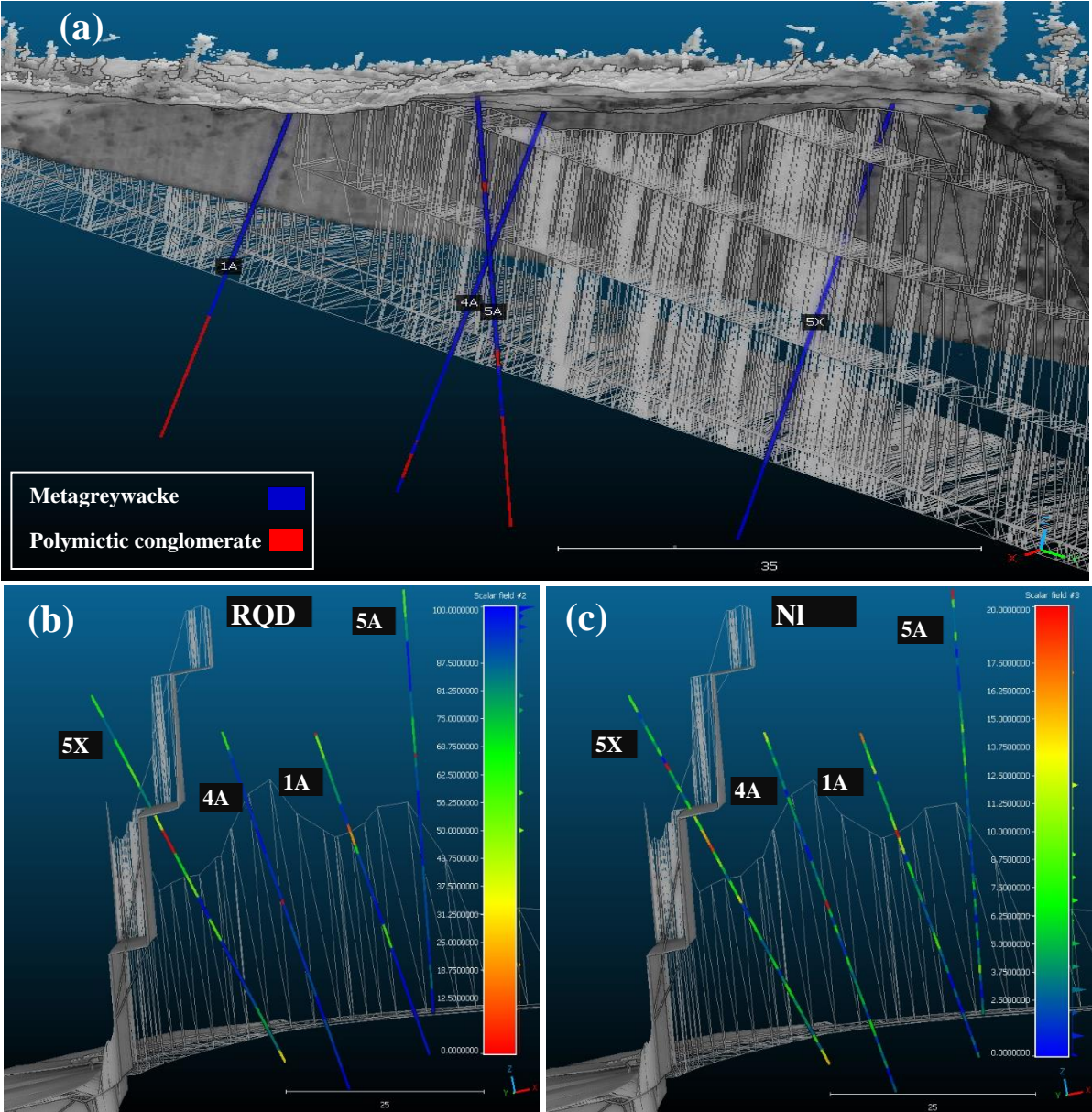


Figure 4.5: Drilled boreholes at Hommelvik plotted in CloudCompare. They are assumed straight with no curving. Polyline mesh indicates the planned deep blasting surface for the E6 highway and the suggested road cut (by Multiconsult). (a) Blue colour indicates metagreywacke while red indicates polymictic conglomerate; (b) RQD for the boreholes; and (c) joint frequency per meter (NI) for the boreholes.

Table 4.2: Geographical information and orientation of the boreholes given in ETRS89 / NTM zone 10 + NN2000 height (EPSG:5950). The core diameters were approximately 50 mm.

Parameter	Borehole 1A	Borehole 4A	Borehole 5A	Borehole 5X
X-coordinate	115857.690	115848.413	115875.117	115836.099
Y-coordinate	1602686.302	1602704.455	1602711.973	1602729.767
Z-coordinate (masl.)	74.853	76.953	89.108	84.035
Drillhole trend [°]	098	095	338	075
Drillhole plunge [°]	80	80	77	70
Total length borehole [m]	40.65	45.15	51.2	50.35
Offset X-direction (from top to bottom) [m]	6.990	7.810	-4.315	16.634
Offset Y-direction (from top to bottom) [m]	-0.982	-0.683	10.679	4.457
Offset Z-direction (from top to bottom) [m]	-40.032	-44.464	-49.888	-47.314

The cores were orientated during drilling and marked with scribe marks to identify what direction is up. The cores were placed (and assembled) on two steel pipes during logging and reference points were aligned with them. By using photogrammetry, Karsten Østerås from Rambøll was able to create 3D models of the cores in Plaxis3D. A measuring tool in excel which was also developed by Karsten Østerås integrated these orientated cores. The individual discontinuities could then be measured individually as illustrated in Figure F.3 in Appendix F. The orientation of 692 joints were measured by the author in total by this tool, while 1010 joints were registered during the physical core logging (the sum of joints registered for the joint frequency per meter, NI). The measured joint orientations compared to the registered joints for the respective core logs were:

- Borehole 1A:  $190/214 = 88.8\%$
- Borehole 4A:  $166/173 = 96.0\%$
- Borehole 5A:  $162/262 = 61.8\%$
- Borehole 5X:  $174/361 = 48.2\%$

The orientation of the joints was not measured if the respective joint was heavily weathered and with no distinctive joint orientation, or if there was crushed (or rotated) segments between the respective joint and the orientated part of the core (with scribe marks). The majority of the joints was concentrated along the crushed zones (resulting in low values of RQD and NI) as illustrated in Figure 4.5 (b) and (c), Figure G.1, Figure H.1, Figure I.1, and Figure J.1. This means the measurements for borehole 5A and 5X are still representative even though the percentage of measured joints are lower compared to 1A and 4A.

The orientations of the joints are presented in Figure 4.7 and Figure 4.8 as rosette and pole plots. Furthermore, the orientations of boreholes for the current and planned road cut are included in the figure too. It is evident that the bedding (foliation) is the dominated joint set. Furthermore, all the boreholes were drilled at a steep or sub-vertical (70-80°) angle which makes sub-horizontal joints (e.g., bedding in this case) more prone to intersect. Joints parallel or sub-parallel to the boreholes are within the blind zone (shadow zone) and are not likely to intersect. To compensate for joints are less likely to intersect the boreholes as the angle interval (between joint and boreholes),  $\delta$ , decreases Palmström (1995) introduced a weighting factor  $f_i$ . The original intention for this was to be able to calculate weighted jointed density per m<sup>3</sup> ( $wJd$ ) as illustrated in Figure 4.6 but can be used for weighting in pole plots and rosette plots, similarly to Terzaghi weighting (Terzaghi, 1965). The suggested angle intervals for  $f_i$  are presented in Table 4.3. The measured joint orientations (both true dip./dip dir. and relative) with corresponding  $f_i$ -factor for the boreholes can be found in Appendix G , H, I, and J.

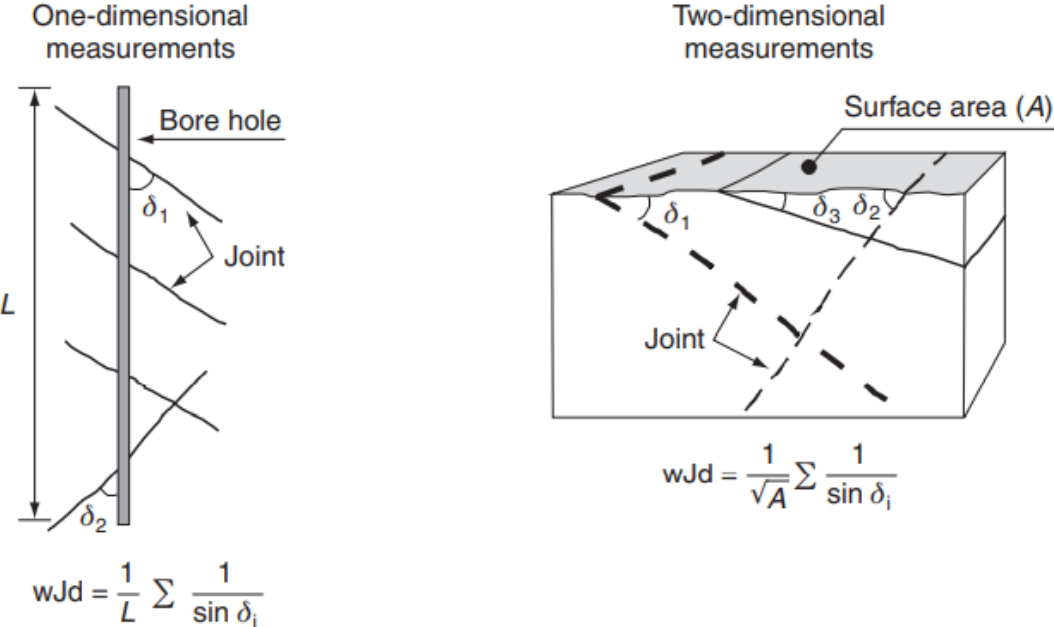


Figure 4.6: Illustration of one-dimensional and two-dimensional measurement of angle interval ( $\delta$ ), and the formula for  $wJd$  (Palmström, 1995).

Table 4.3: Angle interval and ratings for factor  $f_i$ . Modified after (Palmström, 1995).

Angle interval (between joint and borehole)	Rating for factor $f_i$
$\delta > 60^\circ$	1
$\delta = 30-60^\circ$	1.5
$\delta = 15-30^\circ$	3.5
$\delta < 15^\circ$	6

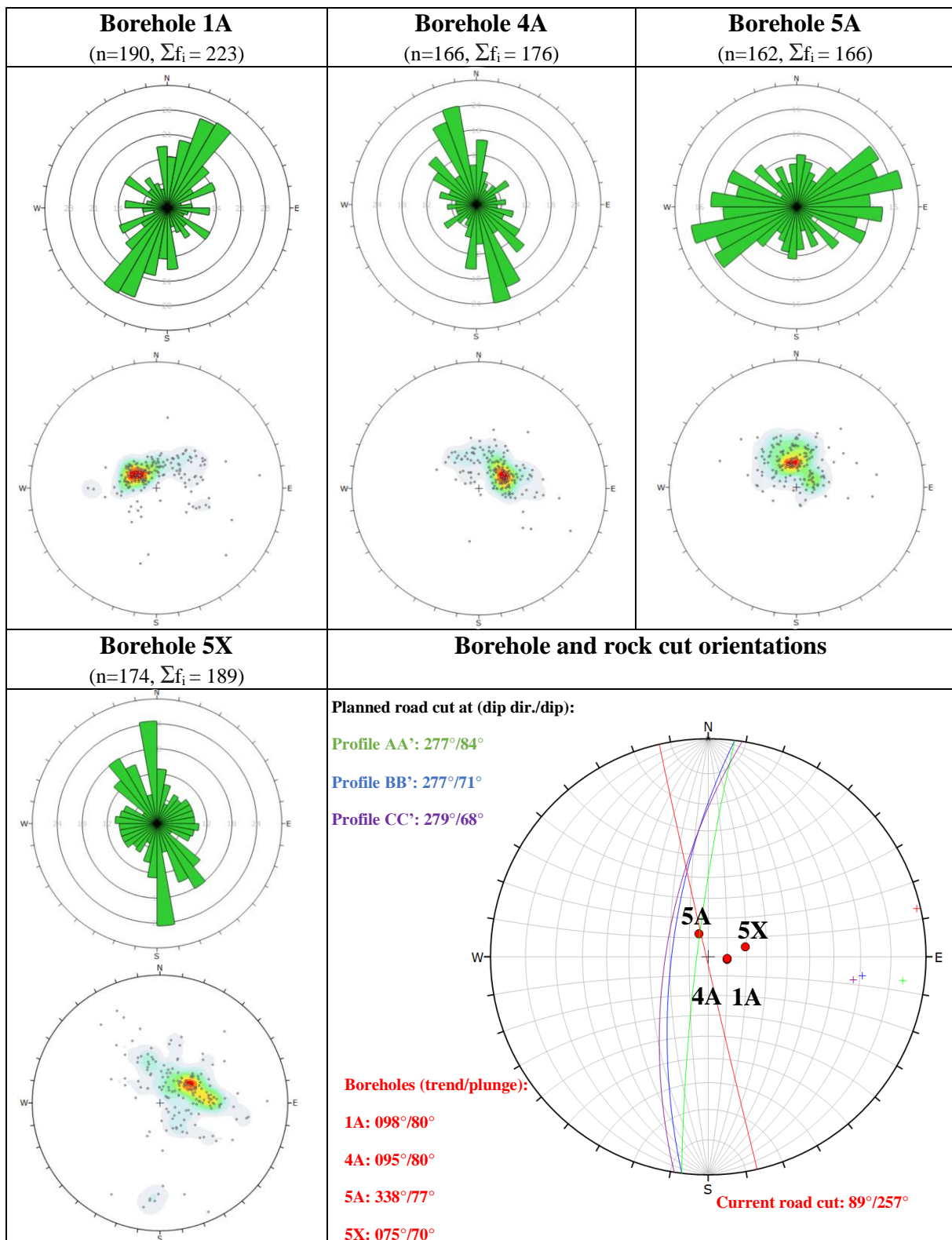


Figure 4.7: Rosette and pole plots for the boreholes weighted with factor  $f_i$ .

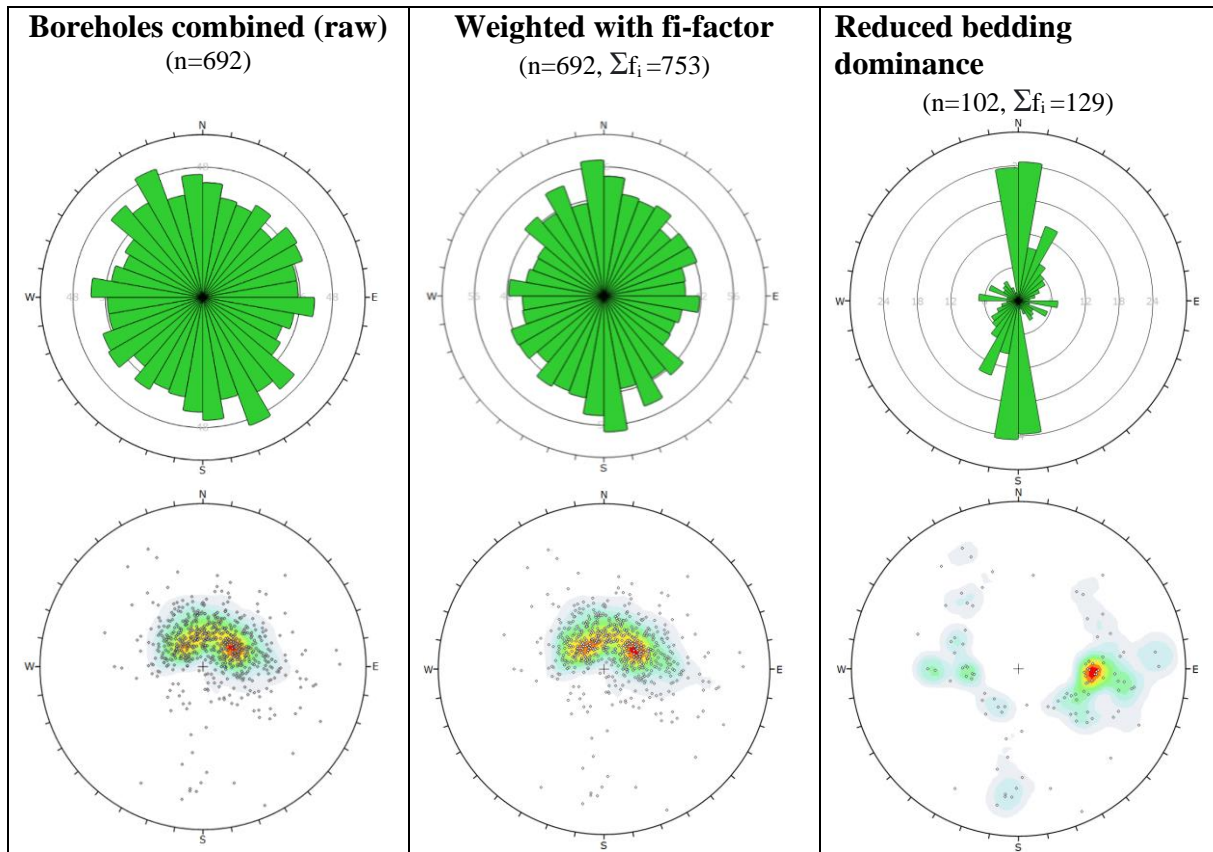


Figure 4.8: Rosette and pole plots for the combined measurements of the boreholes. (Left) raw data; (middle) joints are weighted with a factor  $f_i$  which was introduced by Palmström (1995) for joints intersecting the cores at a steeper angle; (right) filter to reduce bedding dominance and the use of the factor  $f_i$ .

The sub horizontal foliation is the dominating discontinuity for all boreholes. This is most evident for 1A, 4A, and 5A with only a few other joints sets intersecting the cores. However, 5X shows more variation in present joint sets, as illustrated in Figure 4.7. The main orientation for the measured joints in 1A is NNE-SSW, 4A is NNW-SSE, 5A is ENE-WSW, and 5X is N-S and NW-SE. The rosette plot for the boreholes combined raw show no dominant joint direction and is distributed in all directions, as seen in Figure 4.8. When the  $f_i$ -factor is introduced the N-S become more prominent for the joints, but the bins are still orientated in all directions. Li (2021) suggests the use of filter in Dips to reduce the bedding (foliation) dominance to easier interpret other joint sets. The cluster cone was set to a maximum angle of  $35^\circ$  around the main concentration of the foliation which was filtered out. The other joint sets became more visible to evaluate. The determination of discontinuity sets will be made in Subsection 6.3.3 with the comparison of orientation measurements from the field and point cloud models.

The RQD mapped for the boreholes shows that above 78% of the rock mass is good to excellent based on groups used in the Q-method and Q-slope, as seen in Table 4.4. Figure 4.9 illustrates the RQD distribution for the boreholes combined in 10 percent increments. Mapped RQD values below 30 represents the identified crushed zone. Thus, Table 4.5 show the percentiles for the three groups RQD < 30 (crushed zone), RQD > 30 (rock mass excluded crushed zone), and RQD between 0-100 (all values included). This was done such that the evaluated rock masses in later analysis are assigned a more accurate RQD value, as the geometry of the crushed zone has been evaluated thoroughly (Subsection 5.4.1). For sections with higher uncertainty of the geometry of the crushed zone or potential weakness zones, the RQD group between 0-100 will be used. 25. percentiles (1st quartile, Q1) will be used in later analysis, as it is a conservative estimate of the RQD, but not too conservative.

Table 4.4: RQD classes for the boreholes in percent. The top 0.2 m of borehole 1A is ignored to get a representative evaluation of the crushed zone (which is also within RQD class E).

Description	RQD	Borehole 1A	Borehole 4A	Borehole 5A	Borehole 5X	Boreholes combined
	[%]	[%]	[%]	[%]	[%]	[%]
<b>Excellent</b>	(90-100]	62.3	71.8	46.9	23.6	49.9
<b>Good</b>	(75-90]	14.1	22.4	37.5	36.4	28.5
<b>Fair</b>	(50-75]	9.9	4.7	14.6	33.7	16.4
<b>Poor</b>	(25-50]	7.2	0.0	0.0	6.3	3.3
<b>Very poor</b>	(0-25]	6.5	1.1	1.0	0.0	1.9

\*RQD classes used in Q-slope and Q-method

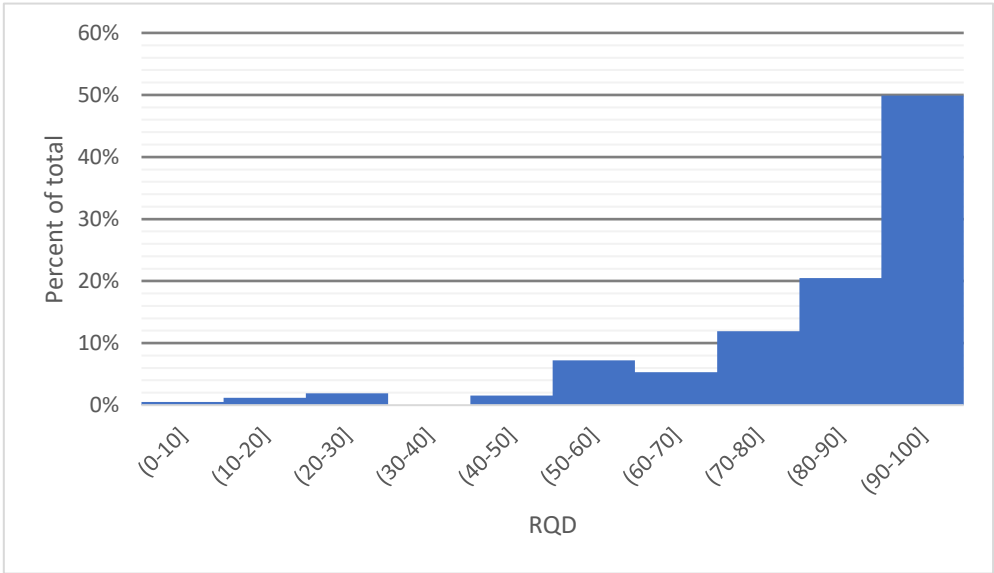


Figure 4.9: Column chart for the RQD-values for the boreholes combined.

Table 4.5: Percentiles for the RQD-values. RQD > 30 represents the crushed zone and will be evaluated as its own material in later analysis in RS2, thus excluding it from the rest of the rock mass. The top 0.2 m of borehole 1A is ignored.

Percentile	RQD < 30	RQD > 30	RQD (0-100)
10.	0	65	58
25. (Q1)	12	79	77
50. (Q2)	25	92	90
75. (Q3)	28	97	97

There were some deviations between the measured joint frequency per meter (NI) for the four boreholes, but their interquartile ranges (ICR) mostly overlap with each other (Q1 for 5X barely does not overlap with Q3 for 4A), as seen in Figure 4.10. ICR measures statistical dispersion and includes the spread of the middle half of the population (borehole meters). There seems to be some trends and possible correlations with the measurements of RQD for the boreholes. The NI ICR for 4A is the lowest among the boreholes but has the highest RQD values with 94.2% between 75-100 as seen in Table 4.4. Furthermore, Q3 are the highest for 1A and 5X, and the RQD values in the groups 75-100 are the lowest for them (among the boreholes), respectively 76.4% and 84.4%. One disadvantage with RQD is that only segments above 10 cm contribute positive to the overall score. Nine segments with 1 cm spacing between each other and one segment with 9 cm are both classified as 0 for RQD. However, NI per definition measures all the joints. Given the trend of higher RQD values for lower values of NI it seems like the RQD represent the joint density in the rock mass well in this case, and the representation of RQD is fair in comparison to the joint frequency per meter.

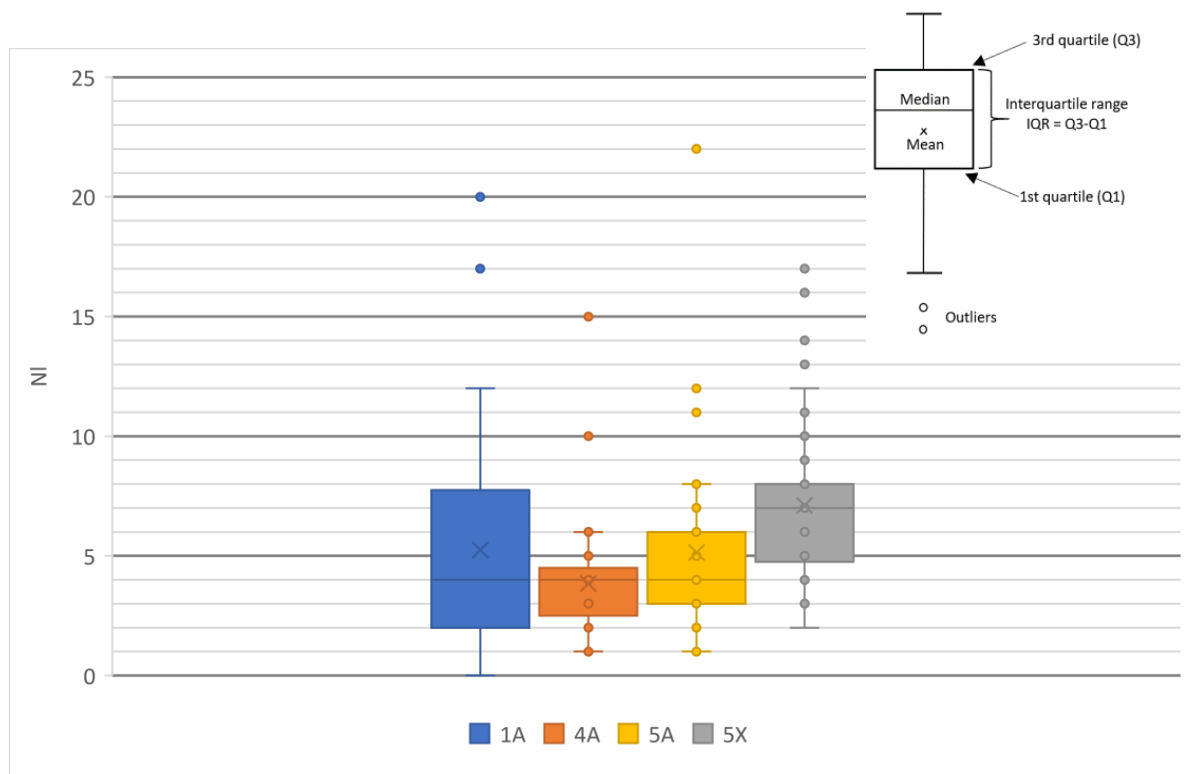


Figure 4.10: Box plot of the NI for the boreholes. Outliers are defined as measurements with values greater than 1.5 times the interquartile range (IQR). IQR is defined as the difference between Q3 and Q1.



### 4.3 Laboratory investigations

Different laboratory investigations have been carried out for the core samples retrieved from the boreholes at the current Hommelvik road cut, with the purpose of establishing representative rock mechanical and shear strength properties for the metagreywacke and polymictic conglomerate. The tests have been carried on core samples from borehole 1A and 5X by the author with assistance from Jon Runar Drotninghaug in February 2022 at the rock mechanical laboratory at the Department of Geoscience and Petroleum at NTNU, Trondheim. Laboratory investigations from core samples from the two other boreholes, 4A and 5A, were carried out by SINTEF in January 2022. It should be further noted that the author only performed tests on metagreywacke while SINTEF (2022) performed on both rock types in question.

The list of carried out tests with respective obtained parameters and applicable test standards are displayed in Table 4.6. This section will only give a brief introduction to the key principles of the test standards while also mentioning any deviations from the standards. Furthermore, the tests results will be presented consecutively and discussed. A summary of the laboratory investigations will be presented in Subsection 4.3.3 along with a comparison of the results from SINTEF (2022) done on the two neighbouring boreholes (4A and 5A). In later analysis, laboratory test results from both, the author and SINTEF will be used, but establishment of input parameters will be presented in Subsection 6.3.2 and 6.3.3.

Table 4.6: Overview of test types, investigated parameters, and reference of standards.

Test type	Parameter	Test standard
Density measurements	Density ( $\rho$ )	-
P-wave velocity test	P-wave velocity ( $v_p$ )	ISRM (1978a)
Uniaxial compression test	UCS ( $\sigma_c$ ), E-modulus (E), Poisson's Ratio ( $\nu$ )	Bieniawski and Bernede (1979)
Point load test	Point load strength	ISRM (1985)
Brazilian test	Tensile strength <sup>1</sup> ( $\sigma_t$ )	ISRM (1978b)
Tilt test	Basic friction angle ( $\phi_b$ )	Stimpson (1981)

<sup>1</sup> Indirect

All following tables presenting test results will include sample standard deviation, denoted SD, and coefficient of variation (relative standard deviation), denoted CV. Sample standard deviation has been used instead of pooled standard deviation, as the tests are only a subsample of the reality (and possible values) and do not represent the entire range of possible values.

#### 4.3.1 Rock mechanical properties

This subsection will present the test methods and results relevant for establishing the necessary rock mechanical and shear strength properties which will be us in later stability analysis of the planned road cut by numerical modelling in RS2 (Section 6.3).

### 4.3.1.1 Density measurements

The six core samples prepared for UCS testing were used for the density measurements. The density  $\rho$  for the samples was calculated based on the ratio between mass  $m$  and the volume  $V$  as shown below:

$$\rho = \frac{m}{V} \quad (4.1)$$

### 4.3.1.2 P-wave velocity test

P-wave velocity  $v_p$  can give an indication of the strength and rock mass conditions, but there are several limitations. Barton (2007) suggests numerous factors influence the seismic velocity, and can be summarized as porosity, joint frequency, rock (and joint wall) strength, depth, stress, degree of saturation, saturation fluid, and anisotropy.

The P-wave velocity  $v_p$  was measured by sending a 54 kHz ultrasonic pulse through each of the six UCS cores in axial direction by an apparatus called Pundit PL-200.  $v_p$  was derived calculated from the travel time  $t_p$  it took for the elastic waves to propagate through the length of the core  $d$  from the transmitter to the receiver transducer, as shown below:

$$v_p = \frac{d}{t_p} \quad (4.2)$$

The results from the density measurements and P-wave velocity test are given in Table 4.7 along with mean values, (sample) standard deviation, and coefficient of variation. All core samples were tested dry (unsaturated), but the specific water content is not measured.

Table 4.7: Results from density measurements and P-wave velocity test. All core samples were tested dry (unsaturated).

Sample ID	Borehole	Length [mm]	Diameter [mm]	Density [g/cm <sup>3</sup> ]	Sampling time [μs]	P-wave velocity [m/s]
UCS-1	5X	129.45	49.89	2.77	22.9	5653
UCS-2	5X	129.45	49.92	2.76	23.3	5556
UCS-3	5X	129.44	49.89	2.76	22.4	5779
UCS-4	5X	124.64	49.87	2.77	20.9	5964
UCS-5	1A	129.82	50.47	2.75	28.1	4620
UCS-6	1A	129.83	50.46	2.75	27.7	4687
Mean		128.77	50.08	2.76	24.2	5376
SD		2.03	0.30	0.01	3.0	577
CV		1.6%	0.6%	0.4%	12.3%	10.7%

Several empirical formulas have been proposed over the years linking P-wave velocity to rock quality descriptors such as rock mechanical properties or rock mass classifications. One such example is the relation between normalized Q-value ( $Q_c$ ) and P-wave velocity as described earlier in Subsection 2.5.1. Barton (2007) emphasizes the limitations and short coming of such relations. A massive chalk marl with  $v_p$  of 2500 m/s will have different engineering consequences compare to a fault zone with the same  $v_p$ .

### 4.3.1.3 Uniaxial compression test

UCS tests were performed to determine strength, elastic, and deformability parameters for the rock samples (Bieniawski & Bernede, 1979). Golodkovskaia et al. (1975) lists the four groups of factors which control the strength of solid rocks as: (1) texture, structure, and mineral composition, (2) anisotropy, jointing, and bedding, (3) water content, and (4) state of stress in rock mass.

Tests for investigating uniaxial compressive strength (UCS) for the metagreywacke were performed using the machine GCSTS RTR-4000 rock press with a load rate of 0.2 MPa/s. Originally it was planned to perform five UCS tests, but due to the high anisotropy it was decided after consultations with J. R. Drotninghaug to perform six tests. Figure 4.14 shows which section of the cores the UCS samples were extracted from.

Table 4.8 presents the ratio between length to diameter for the samples, uniaxial compressive strength (UCS,  $\sigma_{ci}$ ), tangent E-modulus at 50% of UCS ( $E_{t,50\%}$ ,  $E_{ci}$ ), Poissons' ratio ( $\nu$ ), angle to foliation, fracture angle ( $\theta$ ), and failure mode. Stress-strain curves for every sample along with post-failure pictures can be found in Appendix C. Furthermore, a comparison of the stress-strain curves without post yielding can be found in Figure C.1.

Table 4.8: Results from uniaxial compression test.

Sample ID	Length/diameter	UCS [MPa]	E-modulus [GPa]	Poisson's ratio [-]	Angle to foliation [°]	Fracture angle, $\theta$ [°]	Failure mode
UCS-1	2.59	121.9	53.79	0.31	75	30	Simple shear
UCS-2	2.59	138.1	58.14	0.37	75	13	Partial axial splitting (spalling) Simple shear
UCS-3	2.59	184.1	55.02	0.36	75	36	Simple shear
UCS-4	2.50	180.4	60.18	0.33	50	22	Partial axial splitting (spalling)
UCS-5	2.57	73.5	45.15	0.26	60	50	Along foliation
UCS-6	2.57	71.5	48.95	0.25	60	60	Along foliation
Mean		128.3	53.54	0.31	66	35	
SD		49.4	5.64	0.05	11	17	
CV		38.5%	10.5%	16%	16%	50%	

In the classification by ISRM (1978d) samples with UCS between 50-100 MPa are classified as strong rocks (grade R5) while samples between 100-250 MPa are classified as very strong rocks (grade R6). This would indicate that sample UCS-5 and UCS-6 would be classified as grade R5 while the rest are grade R6. The lower strength is likely due to the failure along foliation. UCS-5 and UCS-6 were also from borehole 1A compared to the others that were from 5X. The angle of foliation was less ideal for strength, and foliations were also more distinct and thicker compares to the tested samples from borehole 5X. The effect of the angle of foliation/schistosity for UCS was illustrated in Figure 2.10. Similarly, E-modulus and Poissons' ratio were also lower for sample UCS-5 and UCS-6 compared to the rest. Hard and brittle rocks may get failure mode of axial splitting during UCS testing which is indicated by axial extension fractures (Li, 2018). The post-failure samples from the UCS tests are shown in Figure 4.11.

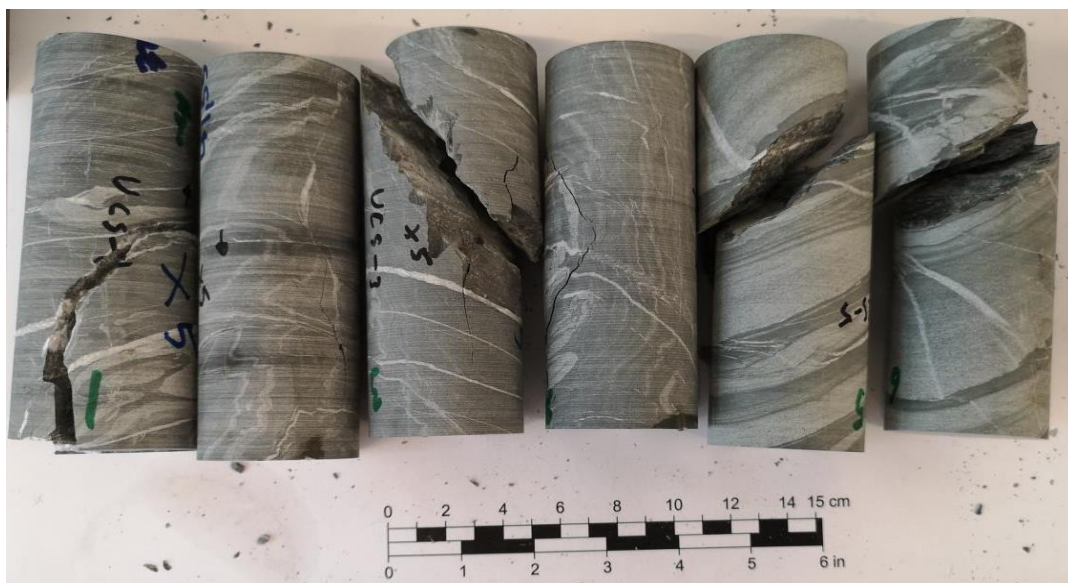


Figure 4.11: Core samples after uniaxial compression tests. From left to right: UCS-1, UCS-2, UCS-3, UCS-4, UCS-5, and UCS-6.

#### 4.3.1.4 Point load test

Point load tests are useful to determine the (point load) strength in the field of rocks. This test type is also very beneficial to determine the rock strength anisotropy. The point load strength ( $I_s$ ) is defined as:

$$I_s = \frac{P}{D_e^2} \quad (4.3)$$

where  $P$  is the peak load at failure [kN], and  $D_e$  is the equivalent sample diameter [mm].  $D_e$  is equal to the core diameter for diametrical cores axial cores tests, and  $D_e = 4A/\pi$  for block or lump tests as well as axial core tests.

The Point Load Strength Index,  $I_{s(50)}$ , and Strength Anisotropy Index,  $I_a(50)$ , for the tested metagreywacke is presented in Table 4.9. The material is classified as medium strength perpendicular to planes of weakness and high to very high strength parallel to planes of weakness. Furthermore, it classifies as *highly anisotropic*, as  $I_a(50) \in [2.5, 4.0]$  (Palmström, 1995). The complete results from the point loads tests can be found in Appendix D.

Table 4.9: Results from point load tests.

Parameter	$I_{s(50)\parallel}$	$I_{s(50)\perp}$	$I_a(50)$
Mean	8.51 MPa	2.74 MPa	3.109
SD	2.02 MPa	1.41 MPa	-
CV	23.7%	51.4%	-
Point load strength classification (Deere et al., 1966)	High strength	Medium strength	-
Point load strength classification (Bieniawski, 1984)	Very high strength	Medium strength	-

$\parallel$  = parallel to planes of weakness,  $\perp$  = perpendicular to planes of weakness

(ISRM, 1985) states that there should preferably be at least 10 tests per sample for anisotropic rocks. However, only 5 tests of axial type were performed (perpendicular to the planes of weakness). The author in conjunction with J. R. Drotninghaug decided to prioritise a sixth UCS test due to the highly heterogenous nature of the test material instead of getting enough test material for 10+ tests of axial type. The cores differ a lot in physical appearance and the anisotropy differs likely a lot too.

#### 4.3.1.5 Brazilian test

The Brazilian test is used to measure the tensile strength ( $\sigma_t$ ) indirectly for the rock specimens. The tests were conducted with a GCTS Point Load Tester (Enerpac PLT-1000) by placing disc-formed test samples in the apparatus. The diameter of the samples was about 50 mm, and the thickness was about half of the diameter. The samples were placed between two curved steel claws, and then loaded diametrically to induce a tensile fracture. The loading rate of 0.2 kN/s was strived for manually.  $\sigma_t$  was calculated by Equation 4.4.

$$\sigma_t = \frac{2}{\pi} \times \frac{P}{D \times t} \quad (4.4)$$

where  $P$  represents peak load before failure,  $D$  is sample diameter, and  $t$  is thickness.

11 samples of the greywacke were tested and four of them had an invalid failure. The core samples had strong foliations and several distinct microstructures as expected for turbidites. The samples were oriented such that the load direction was perpendicular to the structure or foliation that was perceived as most dominant. For the four invalid tests, the strength of the structures was lower than the tensile strength which resulted in fracturing along these structures as seen in Figure 4.12. It is expected that cores bored perpendicular to the foliation would result in higher tensile strength.

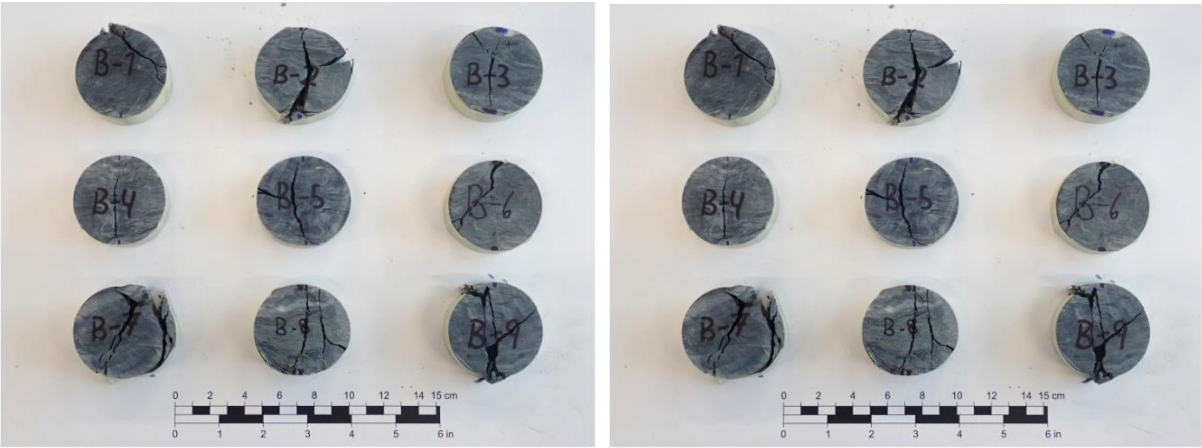


Figure 4.12: Samples B-1 to B-11 after failure from the Brazilian test. Red dots indicate load direction from the apparatus and are marked on both sides of the samples.

After removing the two highest and two lowest values of tensile strength (invalid failures are also excluded) from the pool of test samples, the mean value for tensile strength is calculated to be 15.27 MPa. This is similar to the mean value of all valid results which is 15.62 MPa, as seen in Table 4.10.

Table 4.10: Results from the Brazilian test. Rows with grey backgrounds indicate invalid mode of failure (B-4, B-6, B-7, and B-11). Calculations of mean values and standard deviation exclude samples with invalid failure.

Sample ID	Borehole	Diameter (D)	Thickness (t)	Peak load (P)	Tensile strength ( $\sigma_t$ )
		[mm]	[mm]	[kN]	[MPa]
B-1	1A	50.42	24.61	28.39	14.57
B-2	1A	50.46	23.40	28.01	15.10
B-3	5X	49.82	24.70	31.15	16.12
B-4	5X	49.94	25.42	37.89	19.00
B-5	5X	49.91	25.27	38.29	19.33
B-6	5X	49.90	25.21	32.54	16.47
B-7	5X	49.88	25.16	32.54	16.51
B-8	5X	49.95	24.96	32.10	16.39
B-9	5X	49.95	25.21	26.24	13.27
B-10	5X	49.97	25.24	28.93	14.60
B-11	5X	49.90	25.11	29.45	14.96
Mean					15.62
SD					1.94
CV					11.5%

## 4.3.2 Shear strength properties

This subsection will present the tilt test used for determining the basic friction angle  $\phi_b$ .

### 4.3.2.1 Tilt test

Basic friction angle  $\phi_b$  was determined from tilt tests with a three-core setup (also called the Stimpson method) with linear contact between them as described from Stimpson (1981). Tilt test for samples UCS-1, UCS-2, UCS-3, UCS-5, and UCS-6 were performed.

The setup was done by locking the two bottom cores in place while the third core on the top was free to slide. In total 5 test series ( $j = 1, \dots, 6$ ) were performed with 5 tests ( $i = 1, \dots, 5$ ) for each series. The tilt board was raised at a constant rate of  $2^\circ/\text{s}$  until sliding was initiated, and the angle of failure  $\beta_i$  was measured. The basic friction angle  $\phi_{b,j}$  for each series was then calculated from Equation 4.5, and  $\phi_b$  was derived from the average of  $\phi_{b,j}$  (Alejano et al., 2018).

$$\phi_{b,j} = \text{median} \left[ \arctan \left( \frac{\sqrt{3}}{2} \tan \beta_{i=1, \dots, 5} \right) \right] \quad (4.5)$$

Each core sample was divided into four sections A, B, C, and D, as seen in Figure 4.13. The samples were rotated such that each quarter were only in contact with the gliding surfaces for only one test series, and the amount of polishing along the sides would be reduced to a minimum.

Core samples UCS-1, UCS-2, and UCS-3 were tested against each other, all from borehole 1A. However, UCS-5 and UCS-6 from borehole 5X were tested against an extra core sample (used for point load tests from the same borehole) denoted X. in Figure 4.13. This was done as UCS-4 was from borehole 1A and was hence not tested.

As the core samples were recovered from boreholes and there were indications of bore marks that could affect the angle of friction, most likely increase it. Furthermore, the cores were assembled on steel pipes during the core logging process which could have caused some sliding along the pipes and caused a polishing effect that would reduce the measured angle of friction. These effects should cancel out each other to some extent.

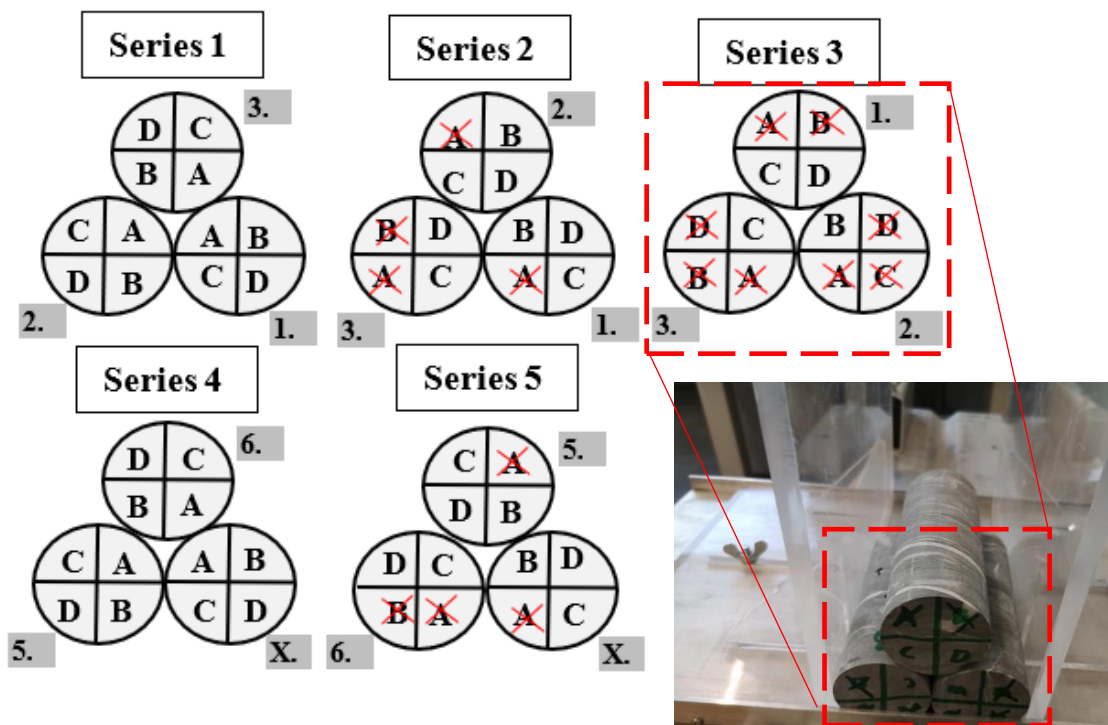


Figure 4.13: Setup for tilt test. Red crosses indicate sides used in previous tests.

The results from the tilt test are presented in Table 4.11, and  $\phi_b$  was calculated to be 31.1°.

Table 4.11: Results from tilt test.

Test arrangement: Linear contact between three cores						
Date: 10.02.2022				Tilting rate: 120°/min		
Rock type: Metagreywacke				Specimen identification: UCS-(1,2,3,5,6)		
Series j	$\beta_1$ [°]	$\beta_2$ [°]	$\beta_3$ [°]	$\beta_4$ [°]	$\beta_5$ [°]	$\phi_{b,j}$ [°]
Series 1	36.4	36.0	36.3	36.4	36.6	32.5
Series 2	36.7	35.9	36.2	35.4	35.6	32.1
Series 3	35.5	36.5	35.3	34.9	36.3	31.9
Series 4	34.8	33.1	32.1	31.2	31.8	29.0
Series 5	35.4	34.0	33.0	32.8	33.1	30.0
$\phi_b$						31.9
SD $\phi_b$						1.5
CV $\phi_b$						4.8%



### 4.3.3 Comparison of laboratory investigations

This subsection will compare the laboratory investigations performed by the author of the metagreywacke from borehole 1A and 5X with the polymictic conglomerate and metagreywacke from borehole 4A and 5A tested by (SINTEF, 2022). The tested material is shown in Figure 4.14. It is evident that rock types are anisotropic and heterogeneous with lots of differences between the cores and within the same cores. Different type of folding, faults, and sections of with phyllites and metasandstone characteristics the specimens. Torske (1965) divided the metagreywacke into subgroup for the area (as presented in Section 3.2). However, such nuanced classification does not make sense in an engineering geological perspective as it would be too difficult to create a reliable and accurate model of the area. Furthermore, it would likely introduce more uncertainty when parameterizing the input parameters of the materials for later analysis. The broad categories of metagreywacke and polymictic conglomerate have been used to describe the rock types.

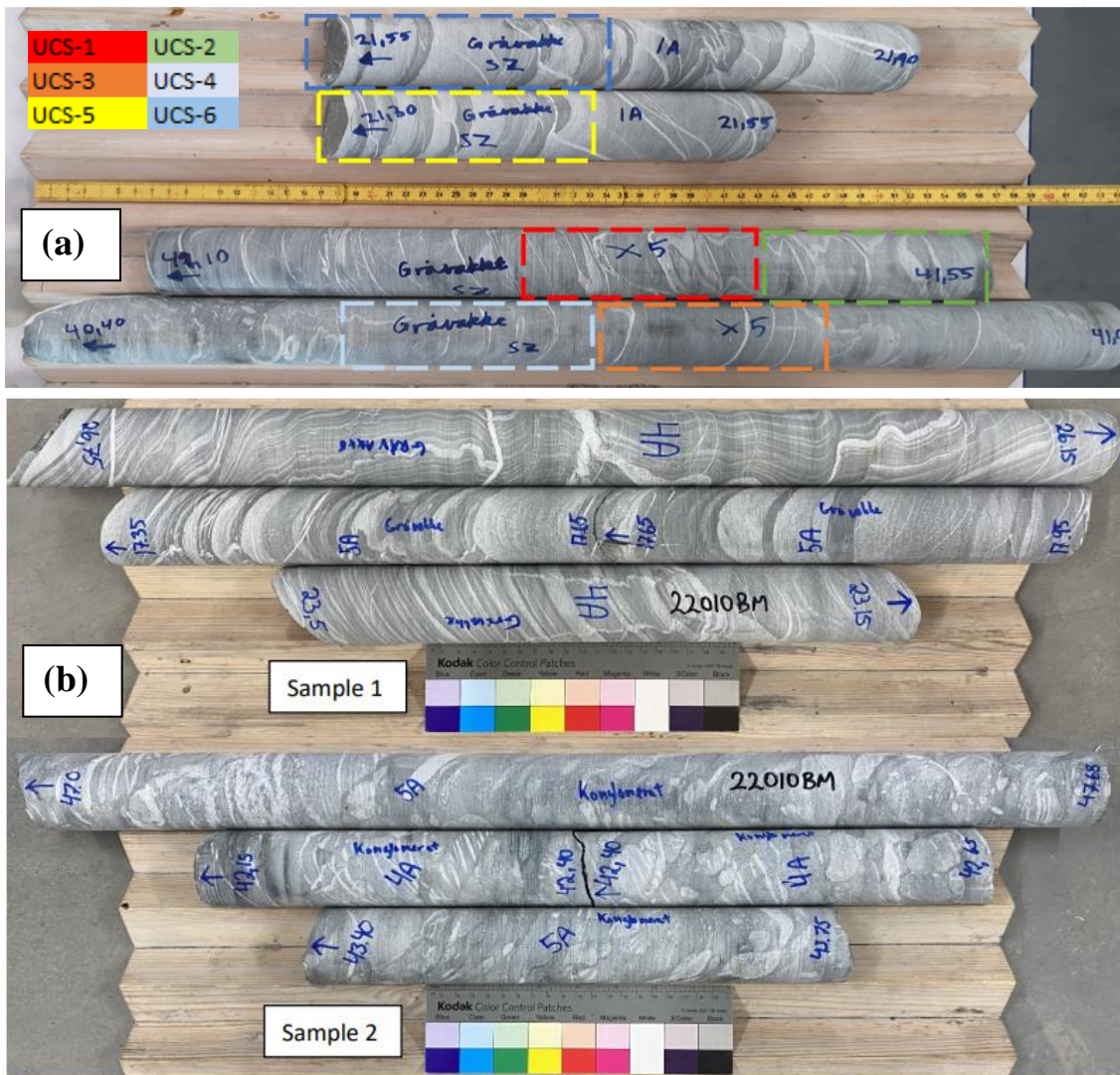


Figure 4.14: (a) Core samples of metagreywacke from borehole 1A and 5X tested by the author. (b) Core samples of metagreywacke (sample 1) and polymictic conglomerate (sample 2) from borehole 4A and 5A tested by SINTEF (2022).

The summary of the laboratory investigations is displayed in Table 4.12 along with the results for metagreywacke and polymictic conglomerate from borehole 4A and 5A tested by SINTEF (2022) 18.01.2022. A brief discussion of the key properties will be presented below.

Table 4.12: Summary of laboratory investigations for the rock core samples. Samples from borehole 4A and 5A were tested by SINTEF (2022) while the author did tests for samples from borehole 1A and 5X with the assistance from J. R. Drotninghaug.

Property	Unit	Polymictic conglomerate	Metagreywacke	Metagreywacke
		Borehole: 4A & 5A	Borehole: 4A & 5A	Borehole: 1A & 5X
Mean values $\pm$ Standard deviation				
Density	g/cm <sup>3</sup>	2.749 $\pm$ 0.012	2.761 $\pm$ 0.009	2.758 $\pm$ 0.010
UCS <sup>2</sup>	MPa	89.3 $\pm$ 7.7	66.4 $\pm$ 19.7	128.3 $\pm$ 49.4
E-modulus <sup>1,2</sup>	GPa	54.1 $\pm$ 3.9	47.8 $\pm$ 8.5	53.5 $\pm$ 5.6
Poisson's Ratio <sup>3</sup>	-	0.212 $\pm$ 0.036	0.240 $\pm$ 0.027	0.313 $\pm$ 0.050
Fracture angle, $\theta$	°	25 $\pm$ 1	39 $\pm$ 15	35 $\pm$ 17
Basic friction angle <sup>3</sup>	°	31.3 $\pm$ 1.6	31.9 $\pm$ 0.6	31.9 $\pm$ 1.5
P-wave velocity	m/s	-	-	5376 $\pm$ 577
Tensile strength	MPa	-	-	15.62 $\pm$ 1.79
Point Load Strength	-	-	-	8.51 $\pm$ 2.02
Index (parallel to planes of weakness), $I_s(50)$	-	-	-	2.74 $\pm$ 1.41
Point Load Strength Index (perpendicular to planes of weakness), $I_s(50)\perp$	-	-	-	3.109
Strength Anisotropy Index, $I_a(50)$	-	-	-	

1. Tangent E-modulus at 50% of UCS.
2. SINTEF used a load speed of 0.5 MPa/s while the author used 0.2 MPa/s.
3. Standard deviation is calculated from all valid results while the mean value is calculated without the two highest and the lowest values.

The results shows that there is significant difference in measured UCS values for the metagreywacke tested for 4A and 5A compared to 1A and 5X. The mean UCS value for 4A and 5A was 66.6 MPa as mean borehole. All of them had failure along foliation. In comparison, the mean UCS for 1A and 5X was 128.3 MPa. For these boreholes only two of the six samples had failure along foliation. While it is likely that the strength of the metagreywacke varies for different sections of the rock body, the strength difference of almost 100% between 1A and 5X compared to 4A and 5A seems unreasonable.

The strength of the tested specimen is dependent on the loading angle to the foliation planes and is generally at its lowest between 30-45°, as illustrated earlier in Figure 2.10. The UCS is logically the highest when the foliation is perpendicular to the loading angle. The core samples were retrieved from boreholes with foliation and folding at different angles, which often not optimal for strength and more prone failure along foliation. Read and Stacey (2009) suggests a range for UCS between 75-220 MPa for greywacke. The test results from the author (1A and 5X) were between 71.5-184.1 MPa which fits well within the reference range. However, the test results from SINTEF (4A and 5A) were on the lower side between 38.0-92.7 MPa, and only 2 of 5 tests were inside the suggested reference range.

The difference in E-modulus between the samples seems reasonable, and the metagreywacke and polymictic conglomerate have similar values. Hansen (1988) research on Scandinavian rocks suggests expected an E-modulus for greywacke between 68-82 GPa and 22-78 GPa for conglomerate. This means that the Hommelvik conglomerate lies close to the average of the expected value while the E-modulus for the tested greywacke is below the expected range for that type of rock. The samples cores are highly heterogenous as mentioned earlier with foliation and folds at different degrees. It is possible that Hansen (1988) samples were quite homogenous as Read and Stacey (2009) suggests an expected range of E-modulus between 20-60 GPa as for greywacke, which matches the tested metagreywacke.

Read and Stacey (2009) lists Poisson's Ratio of 0.05 to 0.15 for greywacke which is significantly lower than both sets of the tested metagreywacke. Lower values of Poisson's ratio indicates that the rock fractures easier (Belyadi et al., 2019).

Barton and Choubey (1977) suggests a basic friction angle between 31-33° for (dry) siltstone and 35° for (dry) conglomerate). The prior matches well with the tested metagreywacke even though it is not entirely the same rock type. The latter is higher compared to the tested polymictic conglomerate but is expected as the surface characterises varies a lot for conglomerates.

## 5 Digital mapping and 3D modelling

Digital mapping and 3D modelling are beneficial to use for any rock engineering project. However, it was especially beneficial for the planned rock cut at Hommelvik due to:

- The geology is highly complex (e.g., folds, several localized discontinuity sets, rock types with several variations).
- The rock cut has three main design configurations and is curved along the alignment of the planned highway.
- There is a minimum of one crushed zone which will daylight the planned rock cut. Important to be able to evaluate in 3D.
- Possible smaller wedges that can affect the detail stability of the slope and can easier be detected compared to conventional methods.
- Integrate data from the core logging into the models of the planned road cut and highway.
- Select and place representative cross section for further 2D modelling in RS2.

The programs CloudCompare, Maptek Pointstudio 8, Slide3, and Discontinuity Set Extractor (DSE) have been used to solve and visualize the mentioned problems. The focus for this chapter will be presenting the utilized methods and results, and how they have been integrated into the rest of the stability assessments for the planned rock cut. Furthermore, important theory will also be briefly presented.

An important part of digital mapping and 3D modelling is to manipulate, convert, and combine different sources of data. Figure 5.1 illustrates the point clouds of the existing rock slope and the construction road north of it in the current terrain. The point cloud for the construction road has primarily been used for calibration purposes (as this thesis mainly focus on the central parts).

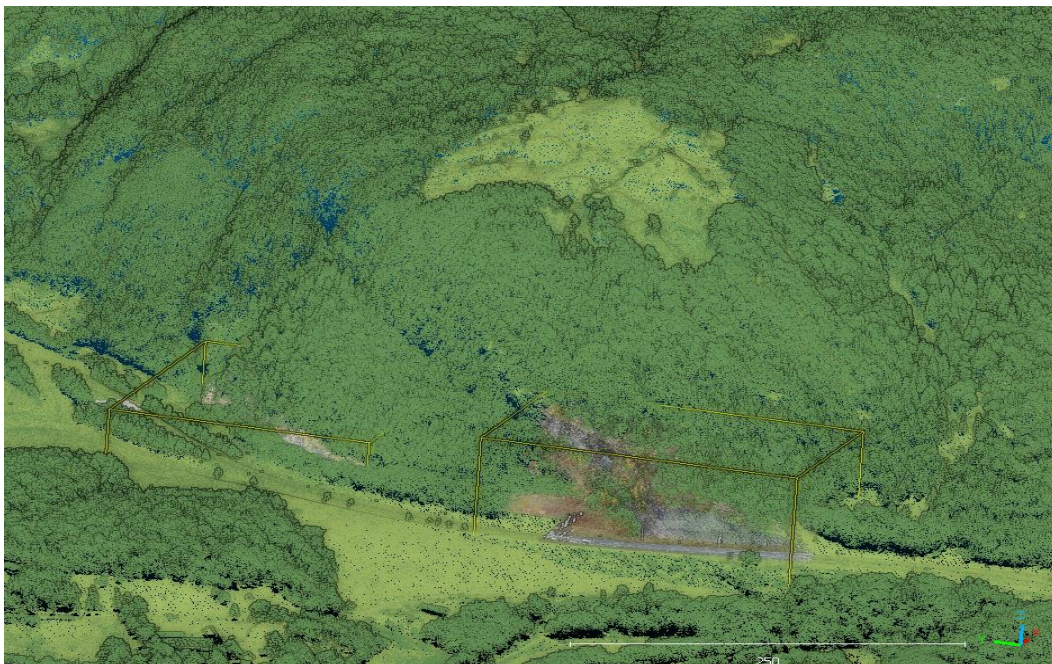


Figure 5.1: Overview of the project area at Hommelvik. The yellow octrees indicate the mapped point clouds of the construction road (left) and the existing road cut (right) from Rambøll by drone. The surrounding point cloud (NDH Malvik-Stjørdal 2pkt 2016) is from Georange (2016).

## 5.1 Point clouds

This section will briefly present the theory behind Structure-from-Motion photogrammetry (SfM) which is the method used to create the point clouds of the current road cut and the exposed rock at the construction road ca. 100 m north by Rambøll. Then use cases for point clouds will be discussed and how it was implemented and utilized for this project. Finally, the topic of manipulation of point clouds and how they were manipulated in this project will be introduced.

### 5.1.1 Structure-from-Motion photogrammetry

*Structure-from-Motion photogrammetry* (SfM) which is a low-cost, user-friendly photogrammetric technique which overlaps 2D-images through a method called Scale Invariant Feature Transform (SIFT) to produce a large high-resolution 3D-datasets as point clouds (Westoby et al., 2012). SfM is particularly useful for mapping of remote and hard to get to places in the terrain as drone can be used.

The point cloud model is produced by calculating the 3D-location (X,Y,Z-coordinates) for shared points in the overlapping 2D images by analysing for similar surfaces features, as illustrated in Figure 5.2. The matching points are used to automatically calculate the camera orientations and positions as well as the 3D-position for the matching points. The resulting point clouds can provide information about the colour and texture too. Furthermore, it can be used to construct digital elevation models (DEM) (Bemis et al., 2014). For a more detailed description of SfM the reader is referred to the studies of Westoby et al. (2012) and Bemis et al. (2014).

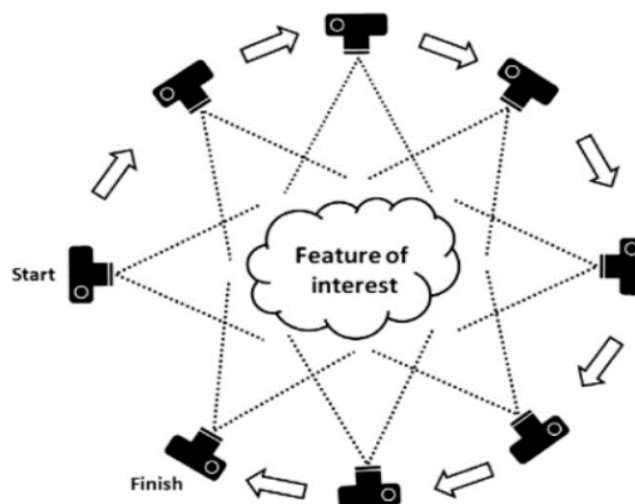


Figure 5.2: Basic principles of photogrammetry to overlap 2D-images to recognise features of interest (Westoby et al., 2012).

## 5.1.2 Implementation of point clouds

High resolution SfM point clouds of the topography and rock faces can be useful in any rock engineering project. In this project it was used for the extraction of discontinuity sets (Section 5.3), volume estimations of mass removal for the planned road cut (Subsection 5.1.4), comparison with photos from the field investigations and terrain models in ArcGIS Pro, evaluation of potential weakness zones (Subsection 5.4.1), and to evaluate potential failure modes.

The point clouds were implemented into a 3D environment in CloudCompare which allowed them to be evaluated and visualized with other 3D file formats such as shape. This was particularly useful as the deep blasting surface, trench bottom, and the planned road cut surface could be evaluated alongside with the point clouds, as seen in Figure 5.3. This was also used to check how the discontinuity sets would intersect the planned road and road cut (Section 7.3) and how they would propagate into the terrain. Furthermore, the chosen profiles (Section 5.2) could be georeferenced for all the elements in the 3D environment and be exported to a chosen 2D stability analysis program (which was RS2 for this project).

CloudCompare utilizes a local reference system which the user defines, but the centre of the local reference system should be close to origin (0,0,0) to avoid stretching effects (gaps) within the point clouds which occurs for very high numbers. This means point clouds with different coordinate systems can be converted to the same local coordinate system by defining a conversion rule for each dataset of the respective coordinate system. In the case for this project the SfM point cloud for the construction road was while the current road cut was ETRS89 / UTM zone 32 + NN2000 height (EPSG:5972) while the current road cut was ETRS89 / NTM zone 10 + NN2000 height (EPSG:5950). The same principle was applied to the shapefiles which were EPSG:5950.

The original points size of the SfM point cloud for the construction road was 15 863 141 points but was reduced to 8 672 809 points after removing vegetation and none exposed rock. The cleaned version is shown in Figure 5.3 (left). The original point size for the SfM point cloud from the current road cut was 74 377 311 points, and the cleaned version was 44 307 004 points and is shown in Figure 5.3 (right). For some analysis a subsampled version with maximum 0.02 cm spacing between points was utilised (Subsection 5.3.2), and it had 14 265 216 points.

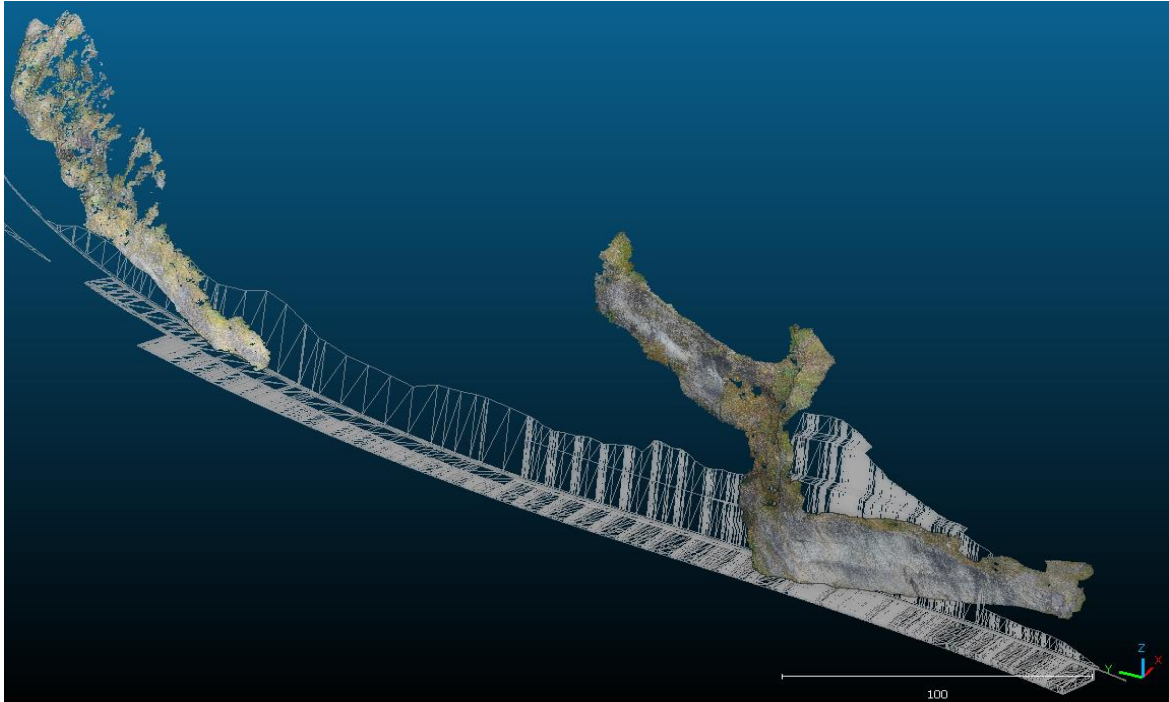


Figure 5.3: The point clouds of the current road cut (EPSG: 5950) and the exposed rock along the construction road (EPSG: 5972) in CloudCompare. The shapefiles are the planned road cut, deep blasting surface, and the trench bottom. The average point density for the point cloud of the current rock cut is 1.2 cm and is calculated by PointStudio 8.

### 5.1.3 User-defined point clouds

Point clouds are in essence a collection of points defined by coordinates which can contain information represented as scalars (real numbers). They may can represent an object or 3D surface and is often considered the simplest form of 3D models. This means user-defined point cloud can easily be made from scratch in program such as excel or be converted from other data sources. An example of the latter is the conversion of DTM1 in raster format to a point cloud, and then mesh the points to create a terrain model in CloudCompare (and Slide3), as illustrated in Figure 5.4.

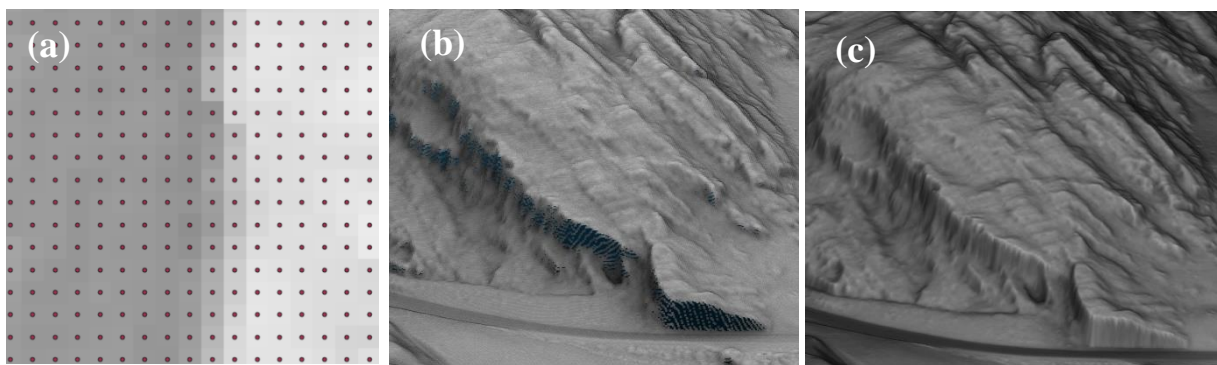


Figure 5.4: (a) DTM1 raster with 1 point per cell ("Raster to Point" toolbox in ArcGIS Pro) and assigned coordinate information to each point (see stage 3. and 4. described in Section 5.2 ). (b) Points exported into CloudCompare as point cloud. (c) Mesh triangulation of the point cloud to create a detailed terrain surface.

Figure 5.5 illustrates another use case from this project. The boreholes were plotted as points forming discs stacked on top of each other in excel and were assigned information as scalars (rock type, RQN and NI). The (global) coordinates for each point were calculated based on the local coordinates within the disc, the adjusted coordinates dependent on the orientation of the boreholes and the length to the top of the borehole from the respective point, and the coordinates at the top of the borehole. The boreholes were represented as 109 980 points in total, and the individual points were assigned information based on simple scripts in excel and the information retrieved from the core logging.

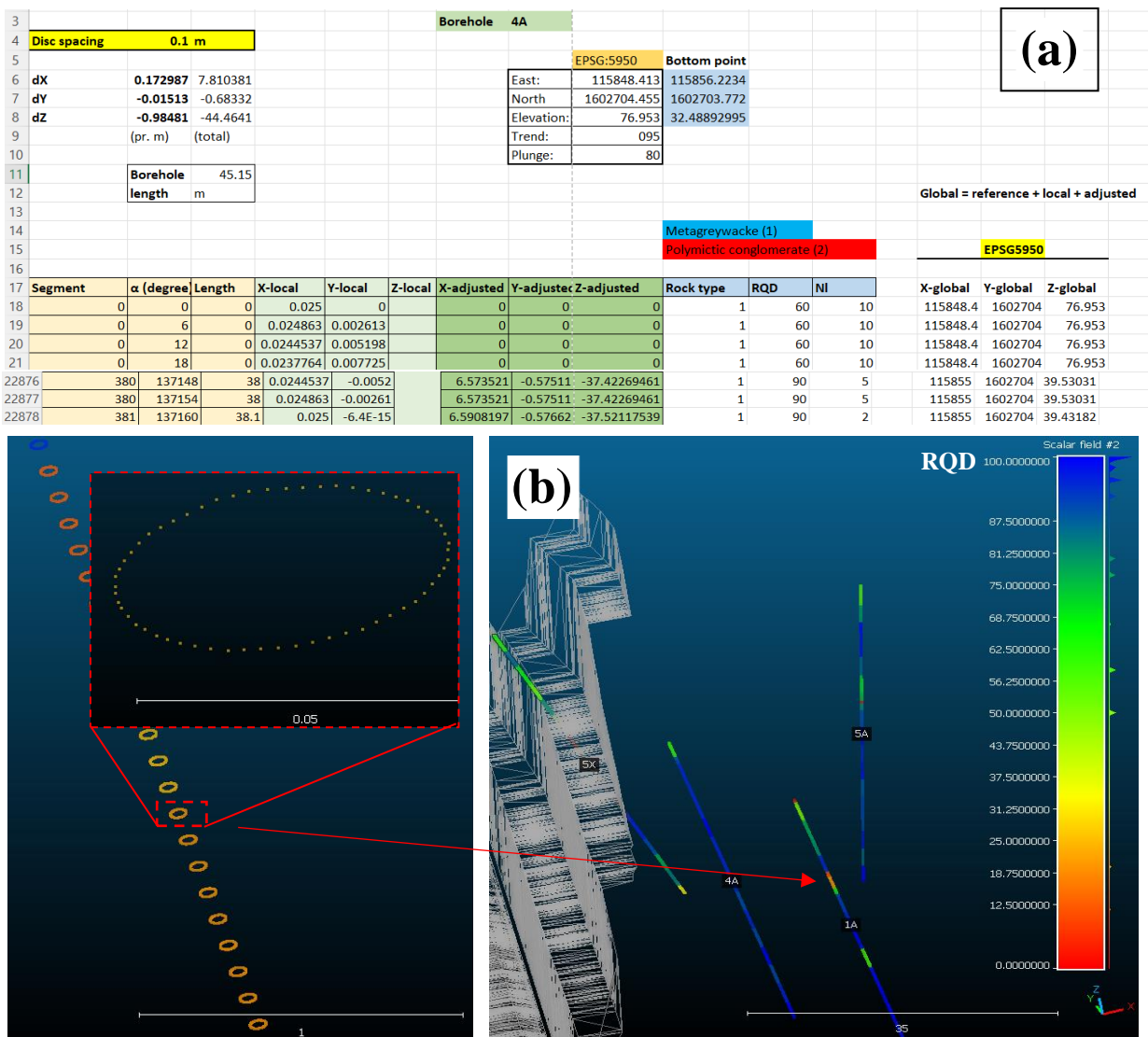


Figure 5.5: (a) The set up in excel for defining the information to the points. (b) The point cloud for the boreholes in CloudCompare.



### 5.1.4 Volume estimation

The projected solid mass for the entire road cut, deep blasting surface, and trench bottom is estimated to be 163 255 psm<sup>3</sup> (“pfm<sup>3</sup>”) in CloudCompare. The side terrain will also contribute to the overall mass but is mostly dominated by soils. This is also possible to calculate but will not be done in this case.

Figure 5.6 illustrates the volume calculation toolbox in CloudCompare used to calculate the removed volume (excavated) between two surfaces represented as point clouds. The output from this process is both added and removed volume, but the prior can be ignored as it is a by-product of the interpolation conditions for the surfaces. The added volume represents the positive changes in relative height as seen in Figure 5.6. The two surfaces are compared cell for cell (grid), and the cell size is set to 1 m (step). The total grid size is 65 698 m<sup>2</sup> (152 m x 434 m).

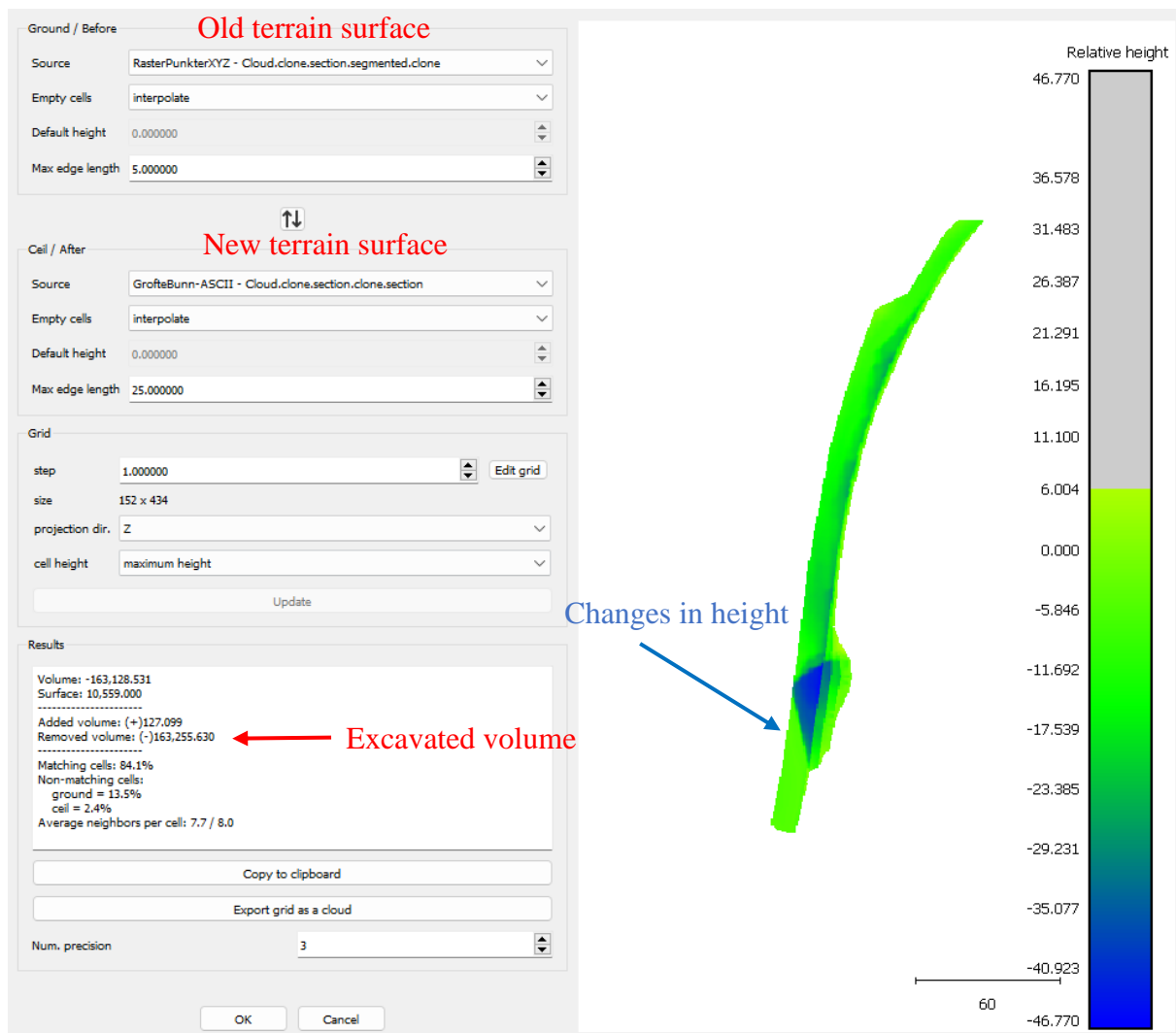


Figure 5.6: Volume calculation in CloudCompare.

The ground surface used for these calculations is the DTM1 (raster) converted to point clouds as described in Subsection 5.1.3. To represent the deep blasting surface, trench bottom, and road cut as point clouds, a five-step process was used:

1. Define projection for DWG-file
2. Export as shapefile
3. Convert to points with the toolbox ‘‘Feature Vertices To Points’’ in ArcGIS Pro
4. Export the table for the points and convert the DBF-file to XLSX (or CSV)
5. Convert to text-file (Unicode)

The ground surface should roughly match the excavation surface. In this case the ground surface had to be cut (with the segmentation tool in CloudCompare), as shown in Figure 5.7 (a) and (b). Furthermore, both data sources have empty cells set to be interpolate based on the neighbouring points. The max length conditions define the maximum distance to neighbouring points an empty cell can use data for interpolation of elevation and geometry. Maximum length for DTM1 (with 1 m spacing between points) was set to 5 m while 25 m was set for the excavation surfaces (bigger gaps some places in the point clouds). Different values were tested but these gave good fit with the constructed geometry in Figure 5.6, the relative height difference model in Figure 5.8 (a), and the original geometries of the point clouds. The most dominant height difference between the two models is -6 m, but there also two dominant peaks at -9 m and -20 m as seen in Figure 5.8 (a) and (b).

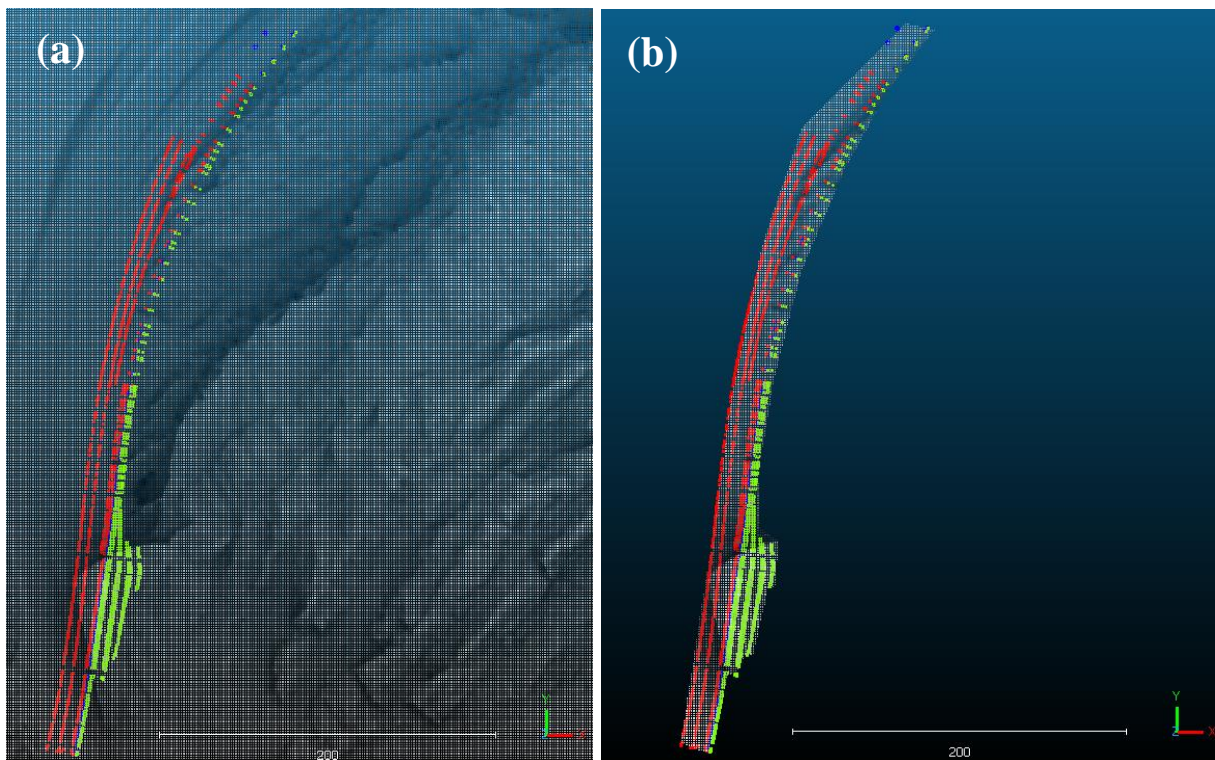


Figure 5.7: The point clouds the terrain surface (grey), deep blasting surface (red), trench bottom (blue), and planned road cut (green). (a) Before clipping; (b) after clipping.

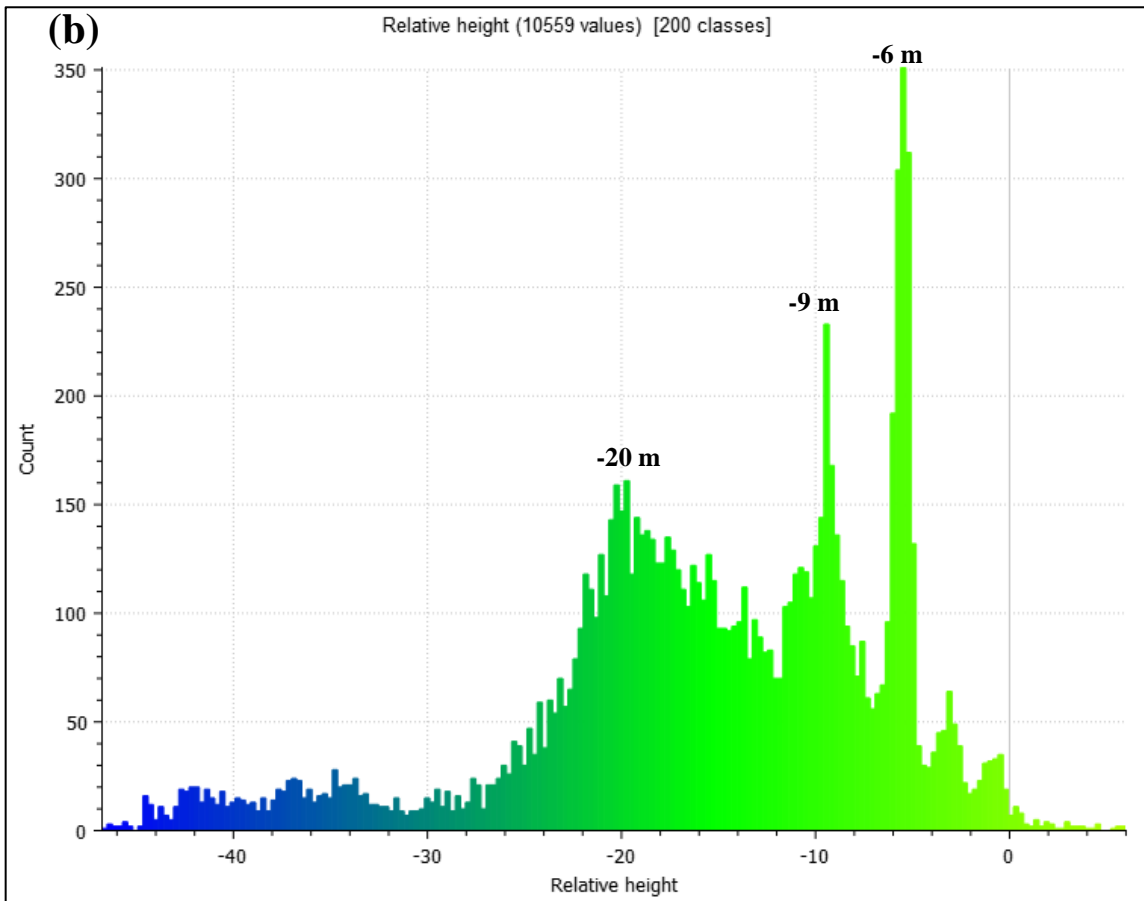
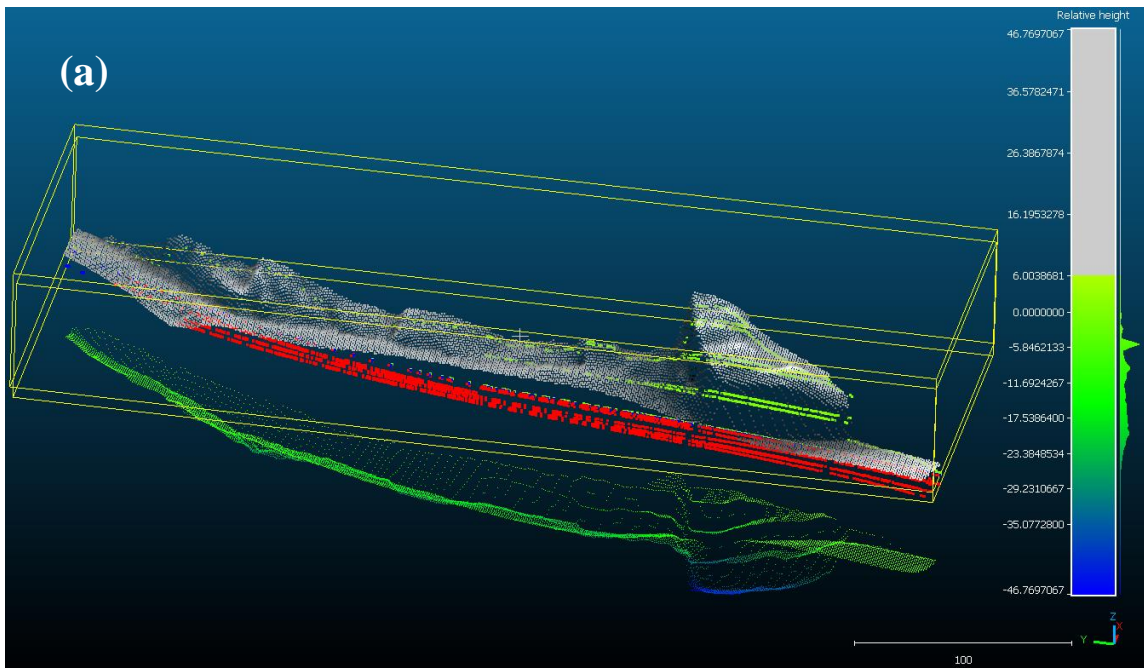


Figure 5.8: (a) Point clouds representing the terrain surface before and after excavation. The point cloud beneath represents the relative height difference and there is one point per  $m^2$ . (b) The relative height distribution between the two surfaces. Values above 0 should be ignored.

## 5.2 Selection of cross-section profiles

Numerical modelling in RS2 requires 2D-profiles (cross-sections) to evaluate the rock slope stability. To represent the surrounding topography and the planed slope configuration optimally three profiles were selected: AA', BB', and CC' (Figure 5.11). Profile AA' represent the no-bench configuration, profile BB' represents the 3-bench configuration, and profile CC' represents the 2-bench configuration, as seen in Figure 5.11 (b). They were placed roughly orthogonally to the planned road cut to achieve a more realistic representation of stresses and stabilization measures. It should be noted that the planned road cut will be parallel to most of the road section except for the part with the 3-bench configuration (at profile BB') which is at slight angle. Profile BB' is angled such that it intersects the two top benches roughly orthogonally while the lower angle is at slight angle. This was done as the crushed zone will likely intersect at the second bench (which will be discussed in more detail in Subsection 5.4.1) and the stresses and displacements there are likely the best most important to capture as accurate as possible.

The orientations (vector space) of the cross sections are listed in Table 5.1.

Table 5.1: Orientations (vector space) for evaluated cross sections

Profile	Centre (EPSG:5950)	Orientation			Strike °
		X	Y	Z	
AA'	x = 116045.03125	0.99737942	0.07234357	0	094.2
	y = 1602801.75	-0.07234357	0.99737942	0	
	z = 121.29501343	0	0	1	
BB'	x = 115933.0859375	0.99987435	-0.01585258	0	089.1
	y = 1602743.5	0.01585258	0.99987435	0	
	z = 118.70831299	0	0	1	
CC'	x = 115912.125	0.99999756	0.00266189	0	090.0
	y = 1602694.25	-0.00266189	0.99999756	0	
	z = 97.50579834	0	0	1	

The profiles were created in ArcGIS Pro with a five step process:

1. Create a 2D line (polyline) with the chosen orientation.
2. Insert points along the line with a fix distance of 0.5 m per point ("Generate Points Along Lines"-toolbox).
3. Add elevation data (Z-coordinates) to the points from the data source DTM1 ("Add Surface Information"-toolbox). The dataset has 1 m resoultion (raster) but since the profiles are not parallell to it, 0.5 m spacing was chosen to capture the steep terrain in detail.
4. Add latitude and longitude (X-, Y-coordinates) to the points ("Add XY Coordinates"-toolbox).
5. Export the table informations for the points and then convert to text-file (unicode).

To implement the profiles into RS2 they have to be projected into a 2D-plane. The Z-coordinate for the points in the profiles are equal to y-coordinate (secondary axis) in RS2. The distance along the XY-line from the start point to each individual point was calculated by pythagoras. This represents the primary axis in RS2 and any points in RS2 can be easily compared to a map with the profiles or a 3D-environment. The described process is illustrated in Figure 5.9.

3D				2D	
XY	X	Y	Z	X	Y
0	115628.16	1602657.50	4.64	0.00	4.64
0.67	115628.77	1602657.75	4.58	0.67	4.58
1.60	115629.63	1602658.13	4.64	1.60	4.64
1.84	115629.89	1602658.13	4.58	1.84	4.58
2.74	115630.71	1602658.50	4.63	2.74	4.63

Figure 5.9: Part of a spreadsheet to convert a 3D profile into 2D. Orange fields) the length along the XY-line; yellow fields) original coordinates for points; green fields) new 2D coordinates used for RS2.

The implementation of the road cut geometry into RS2 at the respective profiles used a similar method to the one described above. The geometry of the road cut was in shapefiles which in essence is points connected by lines. To convert the shapefiles to points, the toolbox ‘‘Feature Vertices To Points’’ in ArcGIS Pro was used. The points were exported to CloudCompare and cross sections with orientations given in Table 5.1. Furthermore, the cross sections in CloudCompare are technically boxes and the thickness (normal to the profile lines) was set to 0.5 m (arbitrary number with good fit after visual inspection) as there is some spacing between the points, as illustrated by the red points in Figure 5.10. These points within the boxes (cross sections) were imported to excel and sorted for overlapping points (and points in proximity). Then the process of projection from 3D to 2D was done as described above, but the starting points of the profiles for the terrain were used to get the correct XY-distance (primary axis in RS2).

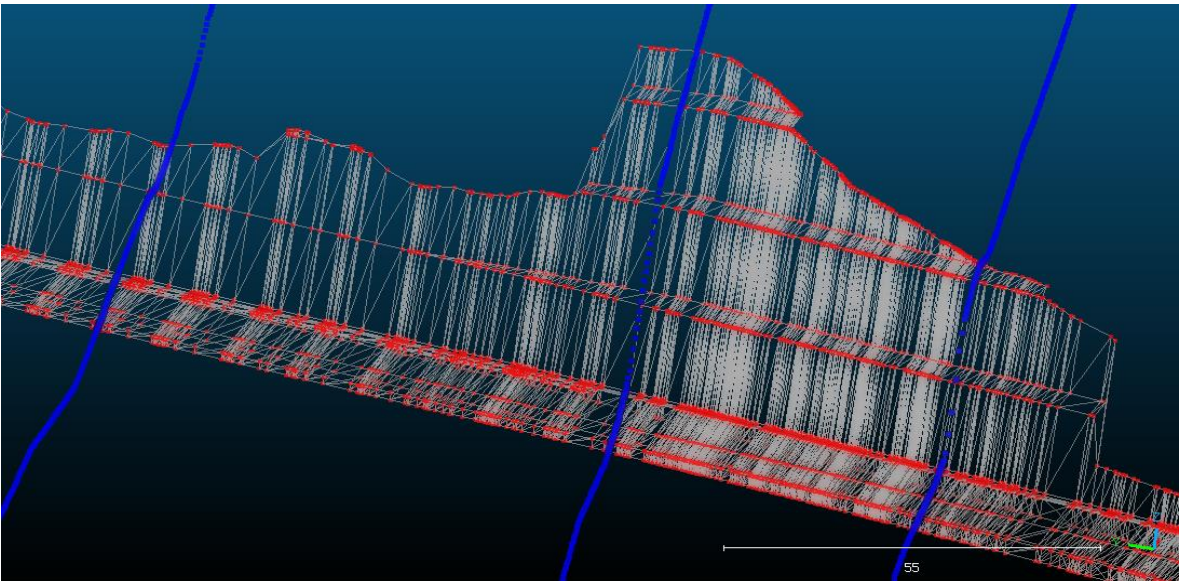


Figure 5.10: Geometry of road cut, deep blasting surface, and trench bottom (grey) as shapefiles. Red points are the vertices representing the geometry, and the blue lines are the profiles.

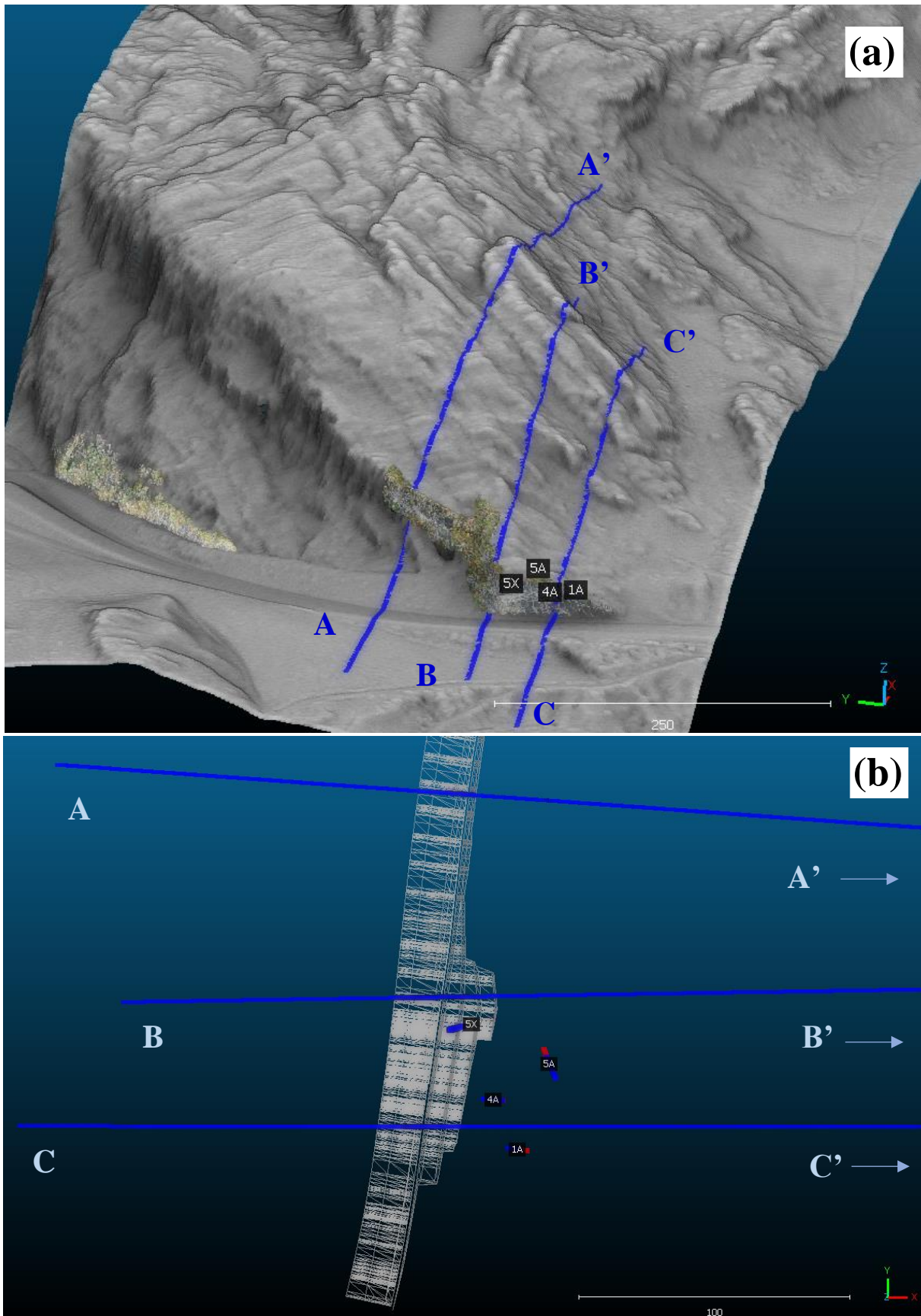


Figure 5.11: (a) Location of the profiles in the current terrain. The terrain model is from DTM1 converted to a point cloud and exposed to the shading filter PCV in CloudCompare. (b) The profiles relative to the planned road cut and boreholes.

## 5.3 Extraction of discontinuity sets from point clouds

Remote sensing techniques such as photogrammetry and Light Detection and Ranging (LiDAR) are increasingly being used for discontinuity characterization. Conventional measuring techniques in the fields are prone to human bias and only give a rough description of the discontinuity network which the new 3D data acquisition techniques can reduce or eliminate (Buyer & Schubert, 2016; Riquelme et al., 2015). The remote sensing techniques provide high spatial resolution and high accuracy of the terrain. Different approaches for developing orientations of discontinuities from point clouds have been proposed in recent years (Riquelme et al., 2014). Some of these approaches are the least square method from a subset of points, calculation of normal vectors to 2.5D interpolated surfaces, and calculation of the normal vectors to a subset of point clouds (Riquelme et al., 2014). Once the discontinuities in the point clouds are classified, information such spacing, persistence, and roughness are also possible to analyse (Riquelme et al., 2015).

This thesis has utilized an open-source program called Discontinuity Set Extractor (DSE) to analyse the point cloud and detect the discontinuity sets around the current road cut at Hommelvik. This method was especially suited for this location due to the variations within each discontinuity set and sometimes the slight curving from folding.

### 5.3.1 Discontinuity Set Extractor

Discontinuity Set Extractor (DSE) analysis every single point in the dataset (point cloud) and evaluates them to their neighbouring points. Best fit planes are calculated for each subset of neighbouring points from the evaluated point. A coplanarity test is performed of the subset of points and given high enough degree of planarity, the normal vector for the plane is calculated. The density of poles is analysed after coplanarity tests have been performed for the entire dataset. The kernel density estimation technique is used to calculate the density function of the planar features in the dataset and evaluate their orientations. The user can then evaluate the preliminary discontinuity sets and make changes to it such as removal of discontinuity sets or rename them. After the user is satisfied, every point in the dataset is assigned to its matching discontinuity set. This early classification can now be exported to a point cloud program such as CloudCompare (Riquelme et al., 2016).

To find the group of point in the same exposed plane (cluster) for each discontinuity set the so called DBSCAN algorithm is used to perform the cluster analysis. These clusters are planar or sub-planar based on the method they were assigned. Thus, it possible to describe them through the equation of a plane as described below (Riquelme et al., 2016):

$$A \times x + B \times y + C \times z + D = 0 \quad (5.1)$$

Normal vectors (A, B, C) are assigned to each cluster in a discontinuity set and are assigned based on the mean orientation of the corresponding discontinuity set. This means that only the parameter D will be different for the clusters of a discontinuity set and will in essence represent the discontinuity spacing. Each point in the dataset is assigned information about its discontinuity set, its cluster number, and the equation representing the cluster (Riquelme et al., 2016).

### 5.3.2 Semi-automatic extraction of discontinuity sets

DSE version 3.01 was used for semi-automatic extraction of discontinuity sets of the SfM point cloud of the current road cut. Multiple iterations of analysis were performed to extract the discontinuity set to compare the results. The first few iterations struggled to run the cluster analysis (DBSSCAN algorithm) due to big file sizes (4 GB). Noise in the point clouds such as vegetation was removed in CloudCompare with the plugin CEA Virtual broom. The point cloud was further subsampled to 2 cm maximum spacing between points. The original point cloud had an average point density of 1.2 cm as mentioned earlier.

The main problem was the current road cut which was very dominating in the dataset, and was evacuated as a joint set. Furthermore, the steep dipping joint set J2 (orange in Figure 5.15) had similar orientation as the current road cut and was evaluated as the same joint set. Unwanted joint sets can be removed in DSE as mentioned earlier, but this would in this case also mean the removal of J2. The orientation of the points in a cluster is also assigned based on the mean orientation of the discontinuity set, thus overweighting the current road cut, and misrepresenting the orientation of J2. Due to the big data set with lots of variation, curvature, and folding, smaller joint sets were not identified. The number of bins for the kernel density estimation could be adjusted, which could affect the number of discontinuity sets identified. When the number of bins were increased discontinuity sets were split into multiple discontinuity sets. This was especially the apparent for the foliation (J1) which had the most variation and could easily be recognised as multiple discontinuities.

The solution to the mentioned problems was to split the dataset into two: one for the current road cut wall, one and for the rest. J2 was not located on the current road cut wall. Thus, the entire discontinuity set which the road cut wall was assigned to could be removed in DSE during the semi-automatic extraction of discontinuity sets process. After the discontinuity sets for both data sets had been extracted as point clouds, they were then merged in CloudCompare. This new point cloud which only represented discontinuity surfaces was then analysed in DSE again. This was done to find common discontinuities set in the merged data set and their mean orientation. This dataset contained less noise (points which are not discontinuities), and the less dominant discontinuity sets were preserved.

The input parameters used in all stages of the analysis in DSE are listed in Table 5.2. Figure 5.12 (a) shows the interface in DSE with the current road cut wall without the foliation analysed. Figure 5.12 (b) shows the corresponding density plot of poles in 3D. However, in other parts of the thesis the 2D projection of the density plots (from DSE) will be used for an easier comparison with regular pole plots. Figure 5.12 (c) shows one of the formats the point clouds are exported as after the analysis.



Table 5.2: Input parameters for semi-automatic extraction of discontinuity sets in DSE. Values are set based on suggested values from Riquelme et al. (2014) and Riquelme et al. (2017).

Parameter	Value	Description
<b>Normal vector calculation</b>		
knn	30	Number of nearest neighbours
$\eta$	0.2	Tolerance parameter for the coplanarity test
<b>Principal poles calculation</b>		
nbins	64	Number of bins for the kernel density estimation
$\gamma$	30	Minimum angle between normal vectors of the assigned discontinuity sets
<b>Assignment of a discontinuity set to each point</b>		
$\gamma_1$	30	Maximum angle between the normal vector of a joint and of the discontinuity set
$\kappa$	2	Cluster distribution threshold for cluster alignment (parameter to check if two clusters should merge)

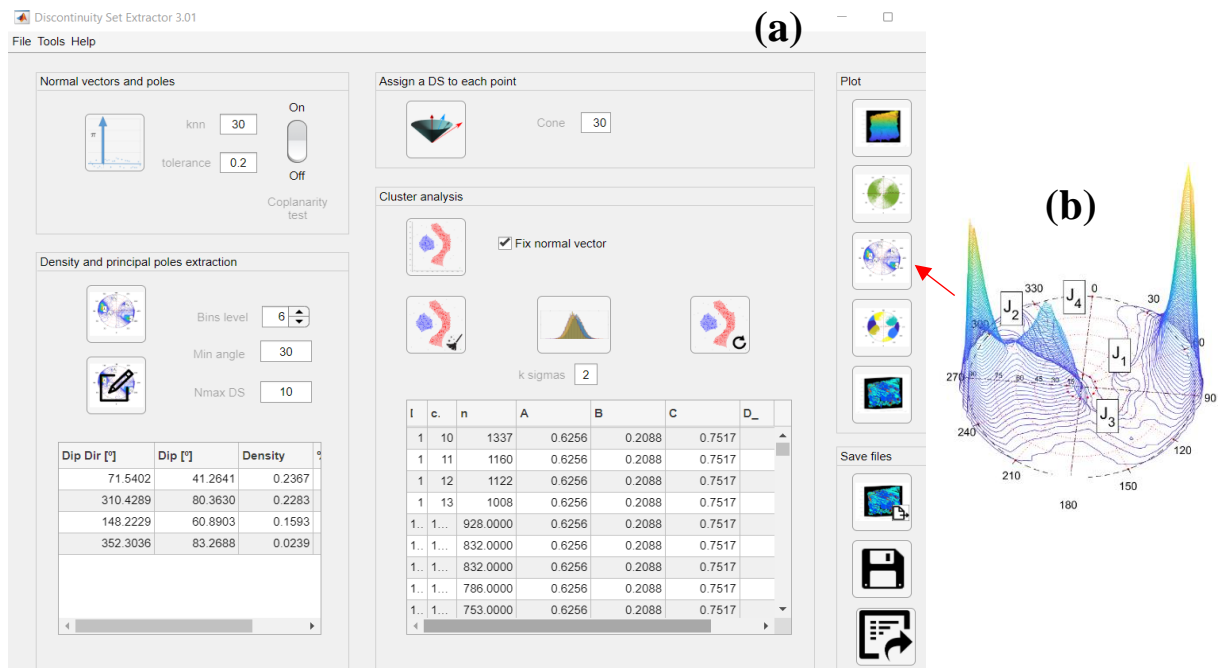


Figure 5.12: (a) The point cloud of the road cut wall without the foliation analysed in DSE 3.01 (b) Density plot of the poles. (c) One of the formats it is saved as after the analysis in DSE is done.

The clusters within the discontinuity sets can be edited or removed after the cluster analysis is done. They can be edited directly in DSE by choosing a minimum number of points the clusters must contain. The other option is to export the point clouds to a program such as CloudCompare, and sort it based on the cluster number. The cluster number is sorted from low to high, which means cluster 1 is the biggest cluster within the discontinuity set. Both options were tested out, but for the point clouds at Hommelvik the latter worked best and is also a more qualitative approach. The point clouds were split into one file (in CloudCompare) per discontinuity set. The individual discontinuity sets were then sorted based on the cluster number (size of the clusters) by adjusting the display parameters as illustrated in Figure 5.13 (a). When a sufficiently number of small clusters were deselected (grey in Figure 5.13 (a)), the discontinuity could be split into small and big cluster for the corresponding discontinuity set.

The point clouds for the different discontinuity sets also contained parameter D which was used to determine the spacing between the clusters in the respective discontinuity sets, as illustrated in Figure 5.13 (b). The complete process from SfM point cloud to analysis in DSE and extraction of discontinuity sets is illustrated in Figure 5.14.

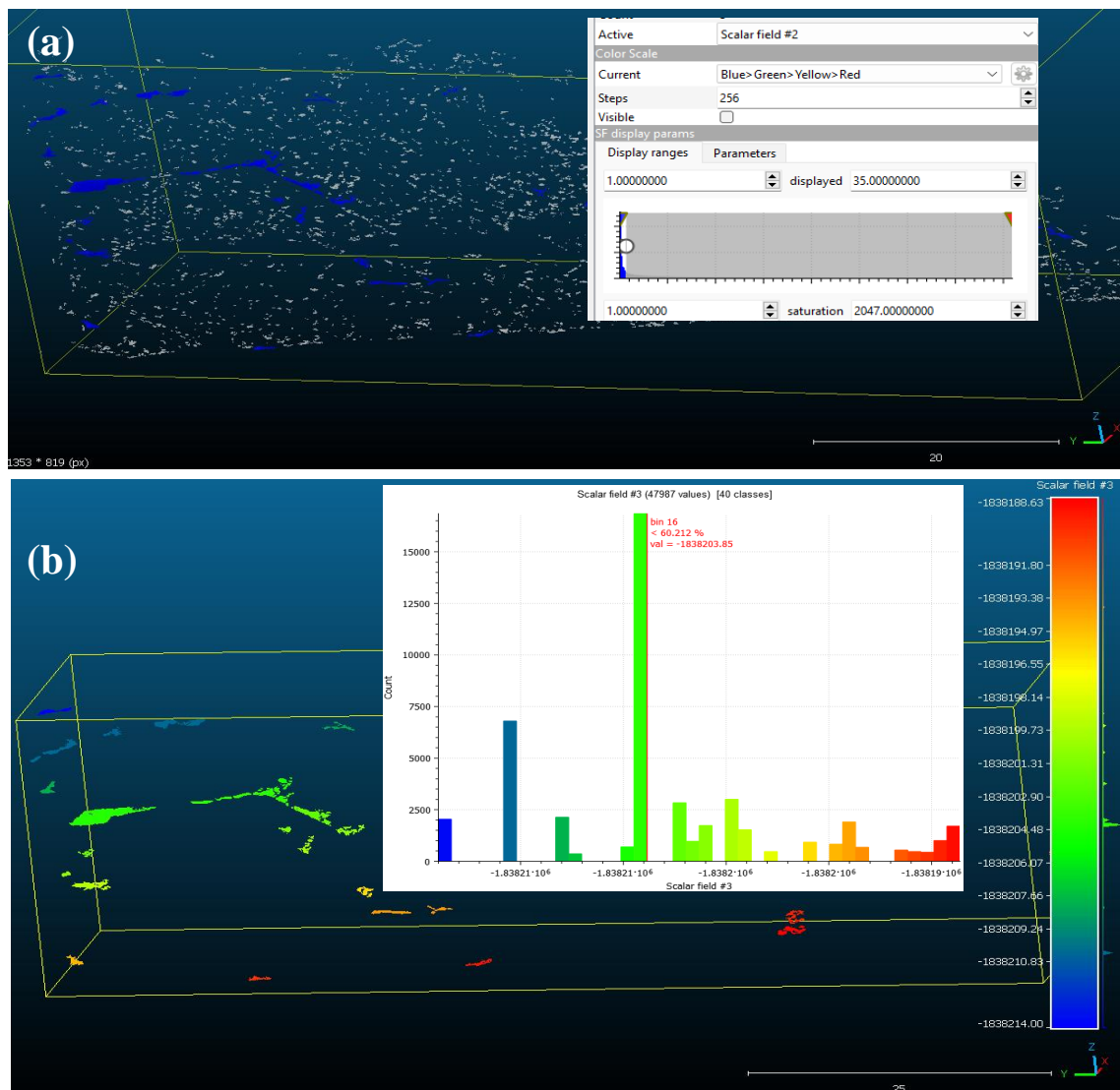


Figure 5.13: (a) Qualitative approach for removal of small clusters for discontinuity set J6 in CloudCompare. (b) Sorting of discontinuity set J6 by parameter D (spacing) and the corresponding histogram for the clusters.

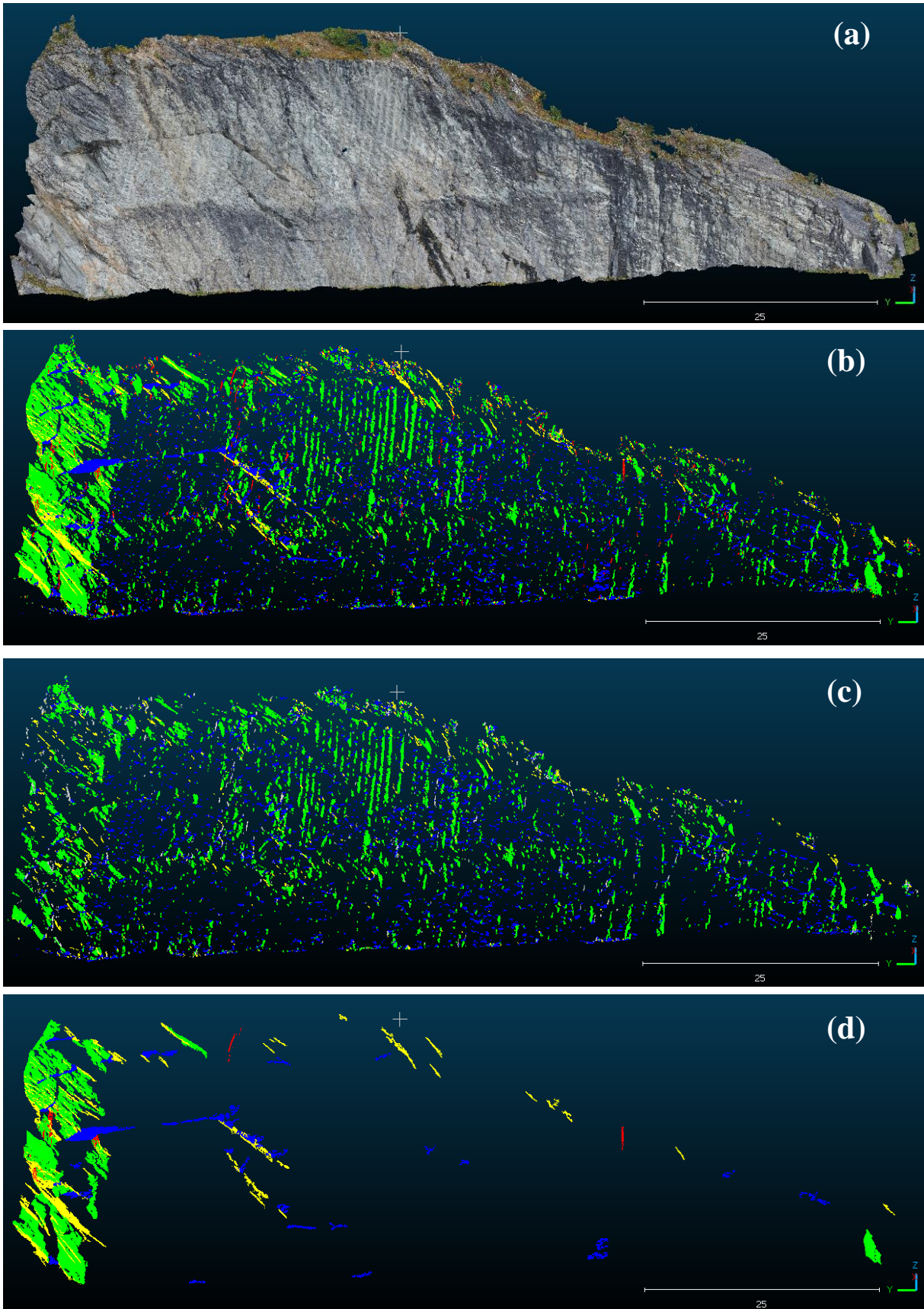


Figure 5.14: (a) SfM point cloud of the current road cut wall. (b) Early classification of discontinuity sets (before cluster analysis). (c) Small clusters removed (split into its own dataset) after the cluster analysis. (d) Big clusters which represents the discontinuities at the road cut wall which are of interest.

The finalized discontinuity sets for the current road cut is illustrated in Figure 5.15. The discontinuity sets are visualized individually in Appendix L. Table 5.3 shows the characteristics of the discontinuity sets and includes some information gathered from the core logging and field mapping. An evaluation of the discontinuity sets will be done in Section 7.1 along with a comparison with the other data sources.

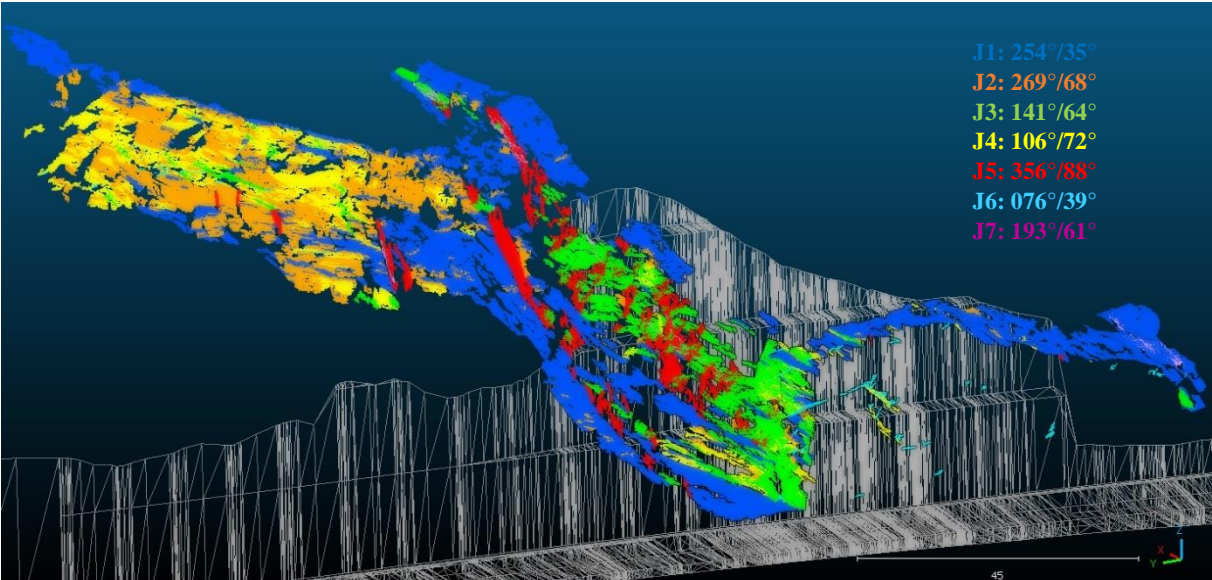


Figure 5.15: Finalized discontinuity sets for the SfM point cloud of the current road cut analysed with DSE.

Table 5.3: Characteristics of the mapped discontinuities. The values are based on field observations, core logging, and the point clouds. The values in brackets represent the mean or the most representative value and will be used in later analysis. The orientation of the discontinuities is obtained from DSE, but the foliation measurements (J1) from the core logging is considered the most representative for profile BB' and CC'.

Discontinuity set	J1	J2	J3	J4	J5	J6	J7
Type	Foliation	Joint	Joint	Joint	Joint	Joint	Joint
Dominance [%]	47.0	20.3	10.0	10.0	9.2	0.85	1.89
Dip direction [°]	254 (198)	269	141	106	356	076	193
Dip angle [°]	35 (17)	68	64	72	88	39	61
Spacing [m]	0.2-2 (0.5)	0.5-5 (2)	0.5-4 (2)	1-15 (2)	3-15 (4)	3-6 (5)	25-75 (25)
Persistence [m]	50	10	10	10	20	15	10
Surface roughness* (Jr)	1.0-1.5 (1.0)	1.5	1.0	1.0	0.5-3.0 (1.0)	2.0	1.0-1.5 (1.5)
Infilling material*	Silty-clay coatings	None or sandy particles	None or sandy particles	None or sandy particles	Sandy particles or silty- clay coatings	None or sandy particles	None or sandy particles
Weathering grade*	II	I-II (1.5)	I-II (1.5)	I-II (1.5)	I-II (1.5)	I	I

\*Determined from core logging and/or field mapping.

## 5.4 Geometry of material boundaries

The geometry of the material boundaries between metagreywacke, polymictic conglomerate, and weakness zones were evaluated in CloudCompare along with Slide3. An overall prediction of the orientation for all geometry elements will be presented. The intersection of the material boundaries at profile AA', BB', and CC' will also be evaluated, and is important to establish for later analysis in RS2 and as seen in Section 6.3.

### 5.4.1 Weakness zones

There are likely two weakness zones in the section of the planned road cut located near the current road cut. A crushed zone confirmed by core logging (Section 4.2) likely stretching behind the entire current road cut and a depression at profile 16200. Both are also observed during the field mapping and from the SfM point clouds. Figure 5.16, 5.17, 5.18, 5.19, and 5.20 illustrates the geometry them, visualized in Slide3 and CloudCompare. Furthermore, there is possibly a depression at profile 16400 based on the lineaments mapped from DTM1 as shown in Figure 3.7 earlier and the terrain model in Figure 5.17. There was observed plenty of water spilling out of the rock mass around this section during the field mapping.

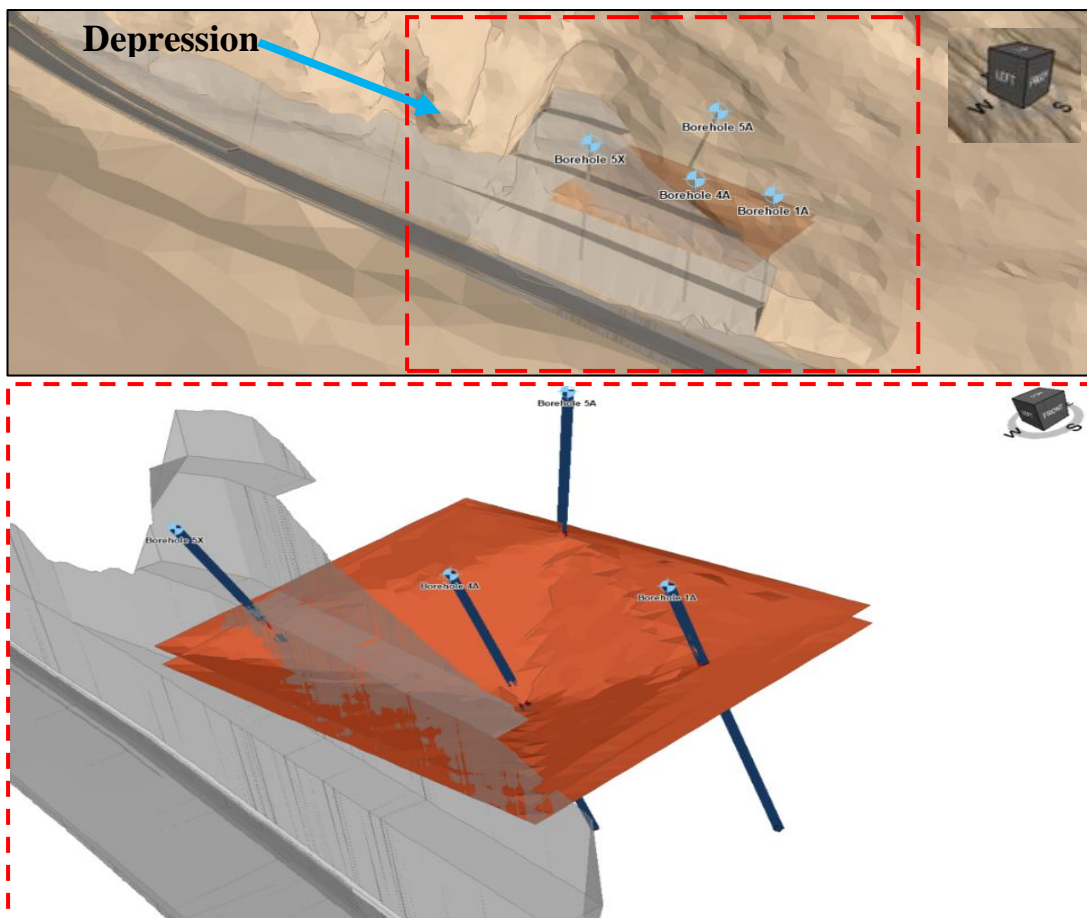


Figure 5.16: The suggested geometry for the crushed zone by Slide3. It is likely it will intersect the planned road cut along the entire 2nd bench.

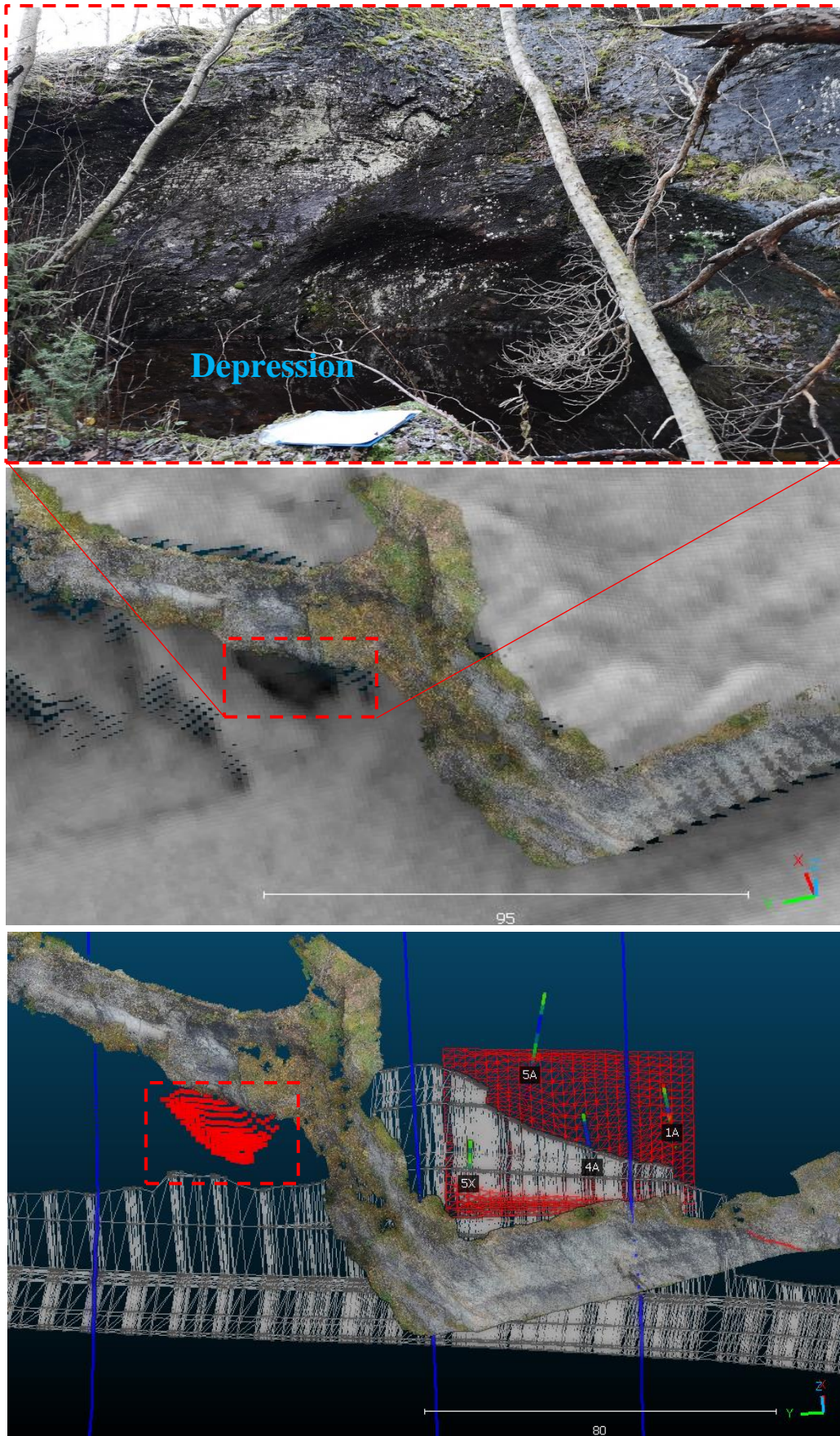


Figure 5.17: (a) Depression observed in the field and in the terrain model (DTM 1). The depression is located above the planned road cut.

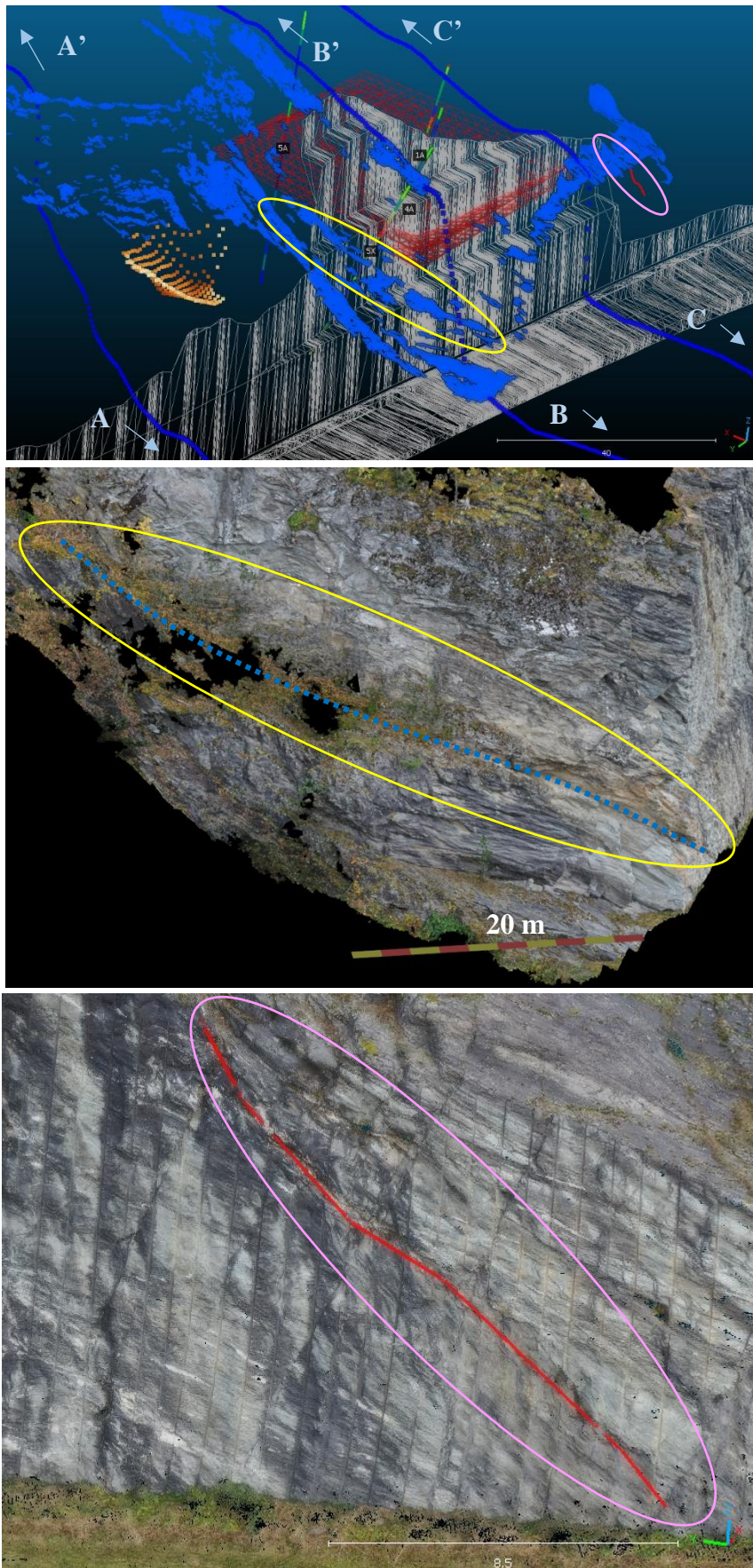


Figure 5.18: The crushed zone is likely connected to the foliation (J1) plane surrounded with a yellow oval. The red line (with pink overall surrounding it) represents a discontinuity with damaged/crushed material along it and is likely connected to the crushed zone.

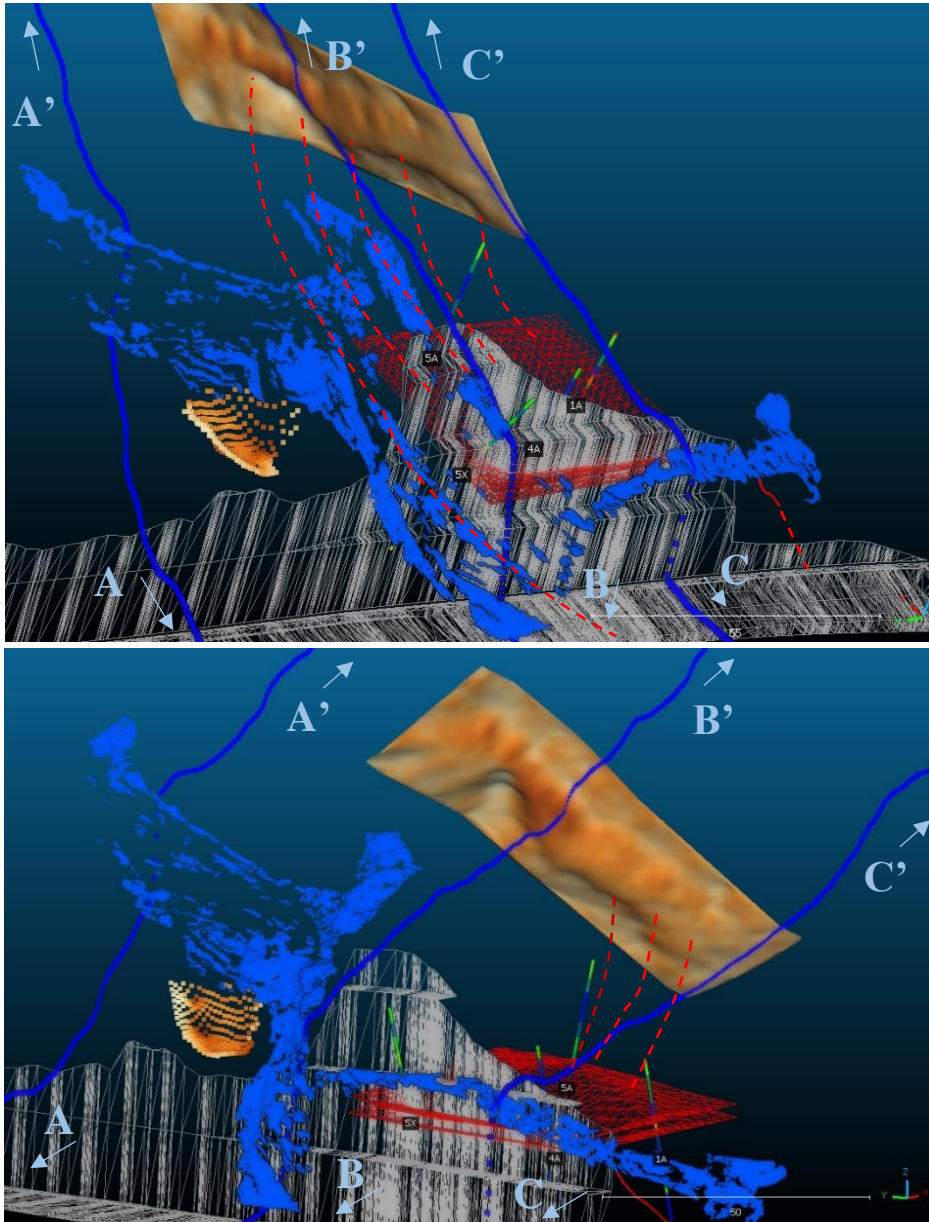


Figure 5.19: Illustration of the possible connection (red dotted lines) between the crushed zone, the depression located 80-100 m behind (east) the current road cut, the foliation (J1) plane (blue surfaces), and the discontinuity with crushed material surrounding it (red line). Profile AA', BB', and CC' are indicated with blue lines.

Figure 5.19 illustrates a possibility how the crushed zone could be connected to the depression (lineament) in the terrain 80-100 m behind the face of current road cut (and 50 m behind the current road cut). This may be an overidealized approach to the reality but can only be confirmed with drilling at an angle eastwards and intersecting the dotted lines representing the continuation of the crushed zone as illustrated in Figure 5.19. It is also possible that it is better represented several intact rock bridges leading up to the depression at the surface and only some sections have similar characteristics to the crushed zone (discontinuous rock mass). There is also a possibility that there are multiple crushed zones with similar orientations intersecting the boreholes. It is also possible the crushed zone(s) is more deep seated and not directly connected to the surface depression. This would probably be a better scenario in the context of the overall stability for the planned road cut.



Given the scenario of a connection between the crushed zone and the depression (lineament) a total rock mass of roughly 150 000 m<sup>3</sup> would be encapsled by this zone and a surface area of 5800 m<sup>2</sup>. This is almost the same magnitude of volume as the entire excavation for the planned road cut, deep blasting surface, and trench bottom which was presented in Subsection 5.1.4. This would classify as a rock rotational slide given a complete failure. The potential extent of of is illustrated in Figure 5.20. The red dashed lines is located relatively close to borehole 1A. However, it is likely the crushed zone is likely located behind the entire current road cut, thus stretching further south from 1A.

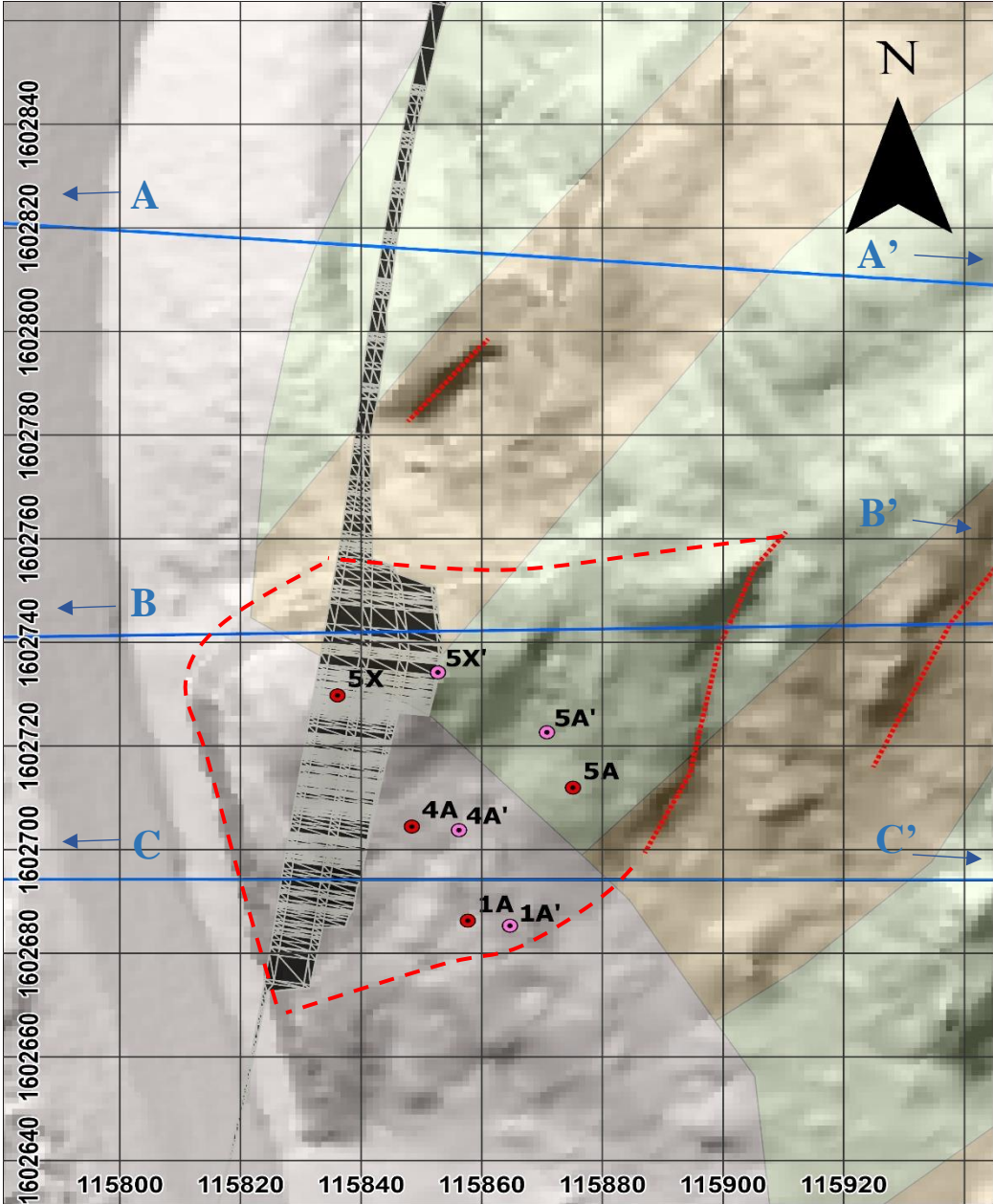


Figure 5.20: Possible outer boundary of the rock mass likely enclosed by the crushed zone (red dashed lines). The surface area is calculated to be 5800 m<sup>2</sup> in ArcGIS Pro. The map also includes the locations of the boreholes (red = top, pink = bottom), NGUS' bedrock map (metagreywacke = green, polymictic conglomerate = brown), surface of the planned road cut (black), and lineaments (depressions) mapped from DTM1 (red dotted lines). Blue indicates the location of profile AA', BB', and CC'.

The crushed zone is likely to be isolated to behind the current road cut, thus only be relevant for profile BB' and CC'. Figure 5.21 illustrates of the geomtry of the crushed zone is in those two cross-sections based on the suggested boundaries from Slide3 plotted from the four boreholes. The crushed zone is observed at 62 masl for profile BB' in CloudCompare and corresponds to the foliation plane (J1) as shown in Figure 5.18. Profile CC' intersects directly with the suggested crushed zone geometry which means Slide3 provide a profie drawing as seen in Figure 5.21 (c). It should be noted that the depressions are not that prominent in Slide3 compared to CloudCompare due to the triguagulation process used by the program smooths (simplifies) the surfaces.

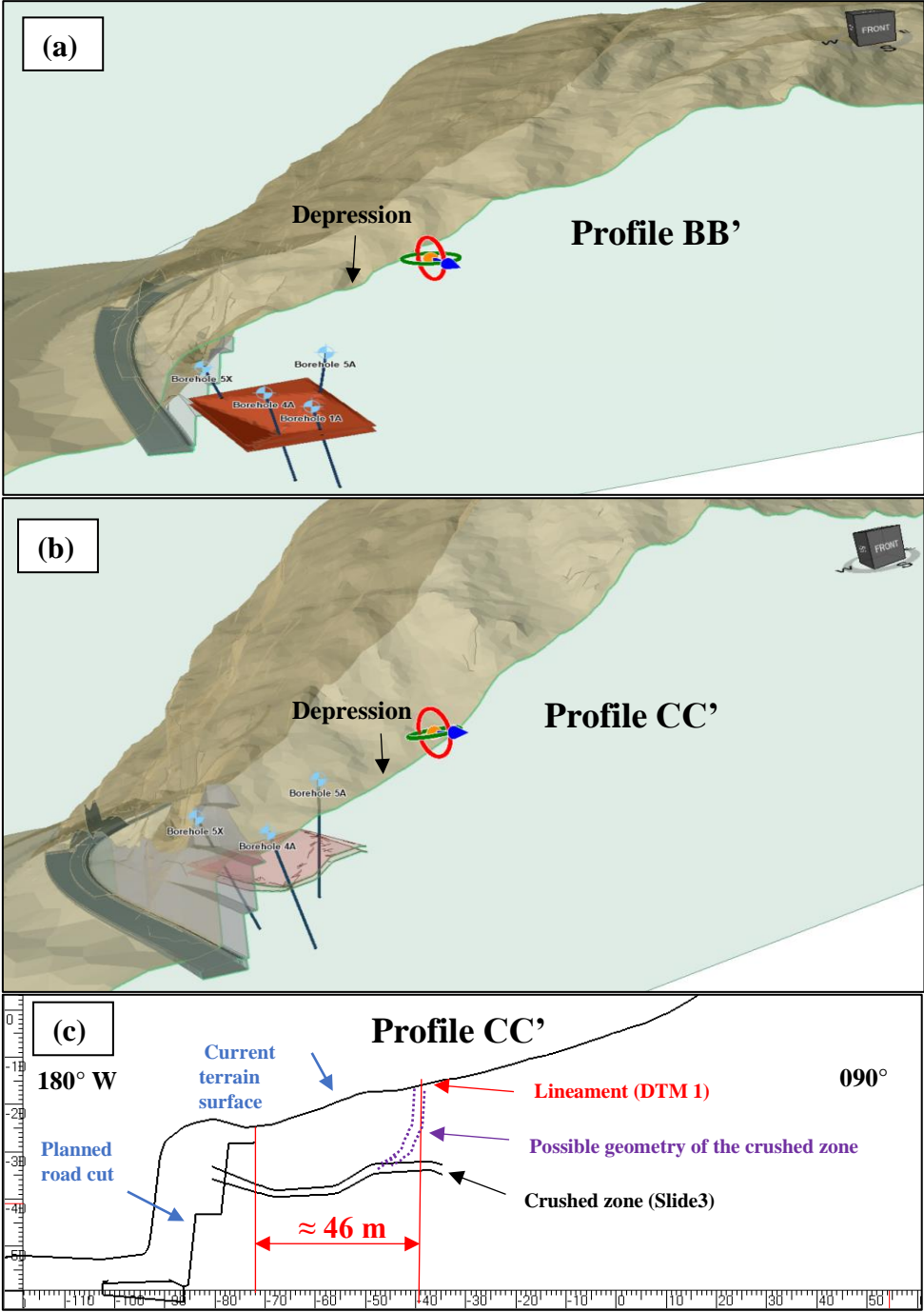


Figure 5.21: Cross-sections in Slide3. (a) profile bb'; (b) profile CC'; (c) Profile drawing in Slide3 with the geometry of the planned road cut and crushed zone.

## 5.4.2 Rock types

The material boundary between metagreywacke and polymictic conglomerate is quite complex. The bottom layer is quite prominent as polymictic conglomerate and is assumed to be located from the deep blasting surface and below for profile AA', BB', and CC'. However, there are some sections of the core logs with abrupt changes between the two rock types, as seen in Figure 5.22. It should be further noted that there are a few sections with 10 cm layers of polymictic conglomerate for 4A and 5A that are not included in Figure 5.22 but set to metagreywacke to simplify the model and the material boundaries.

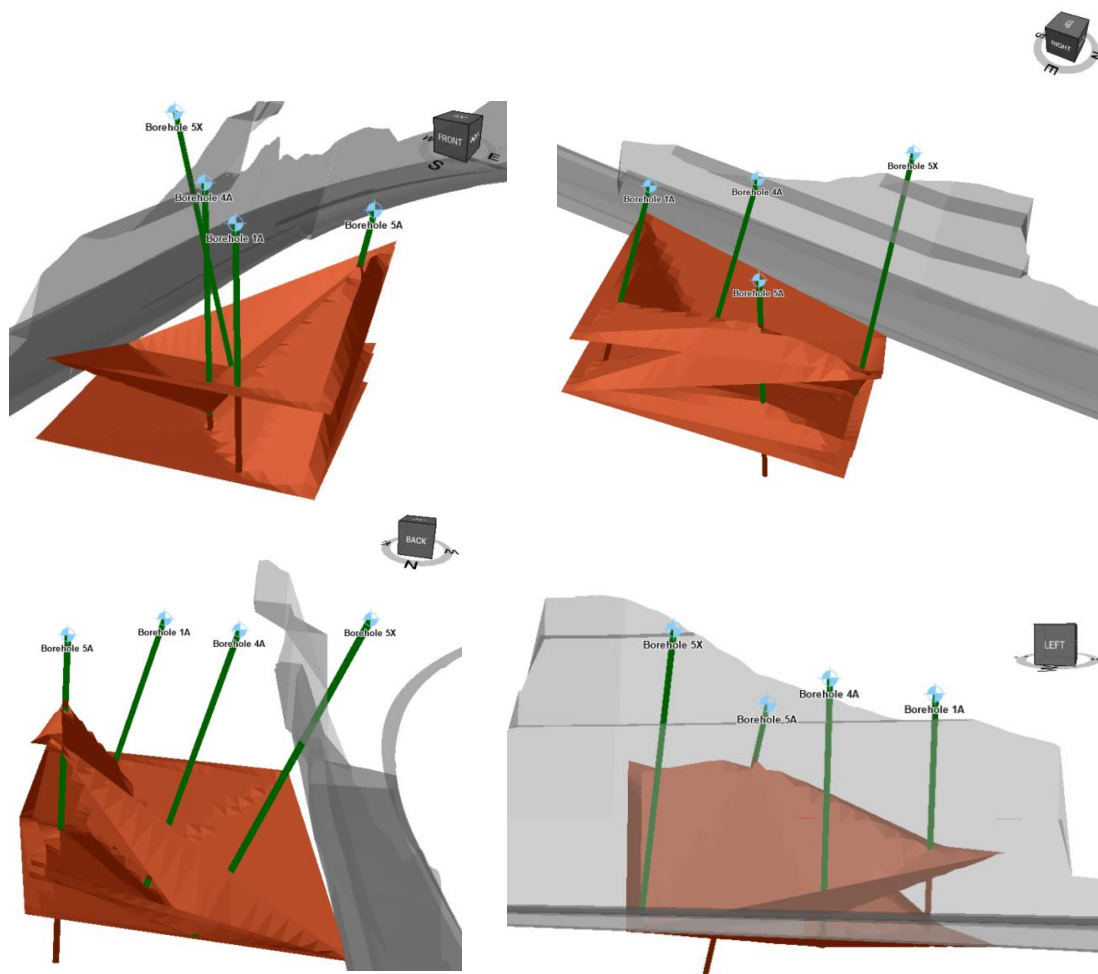


Figure 5.22: Geometry of material boundaries between metagreywacke (green) and polymictic conglomerate (brown).

Figure 5.23 and Figure 5.24 shows the cross-sections of profile CC' and BB'. Borehole 5X is the closest to profile BB' and was mapped entirely as metagreywacke but based on the models it is likely that polymictic conglomerate would occur a couple meters deeper. There are uncertainties for the material boundaries for profile AA'. The polymictic conglomerate is assumed to be located a little bit further up than for profile BB', based on Figure 3.7.

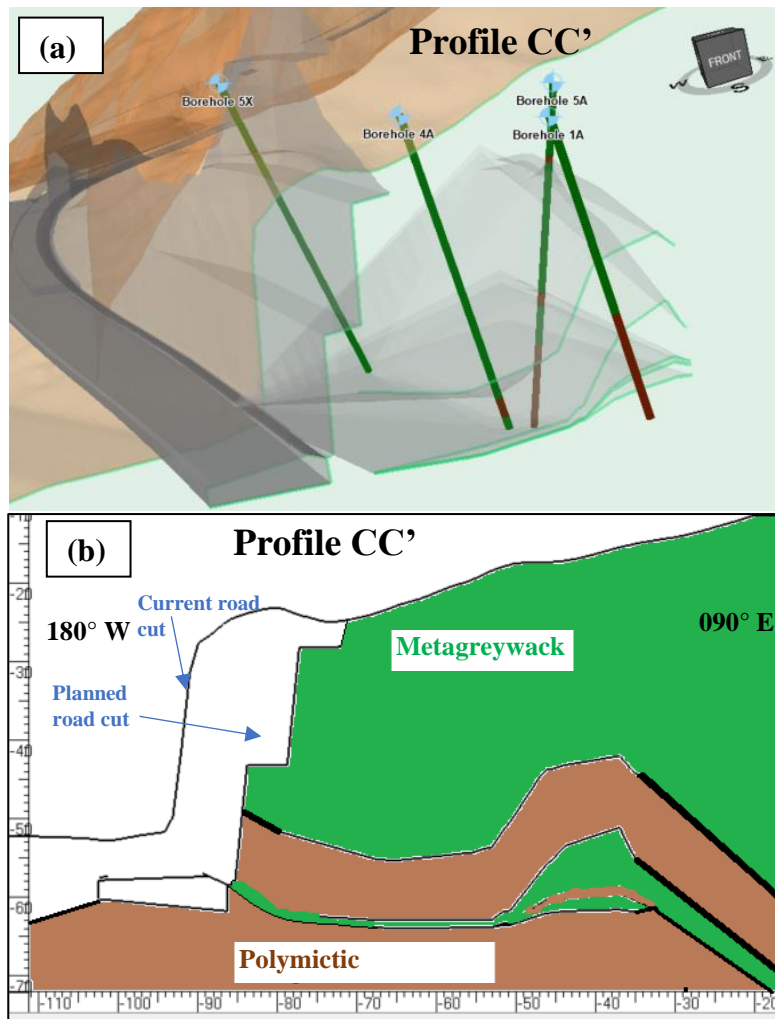


Figure 5.23: Profile CC'. (a) Boundaries between metagreywacke and polymictic conglomerate. (b) The thin black lines with white dots on the sides represent the boundaries created by Slide3 while the rest is assumed.

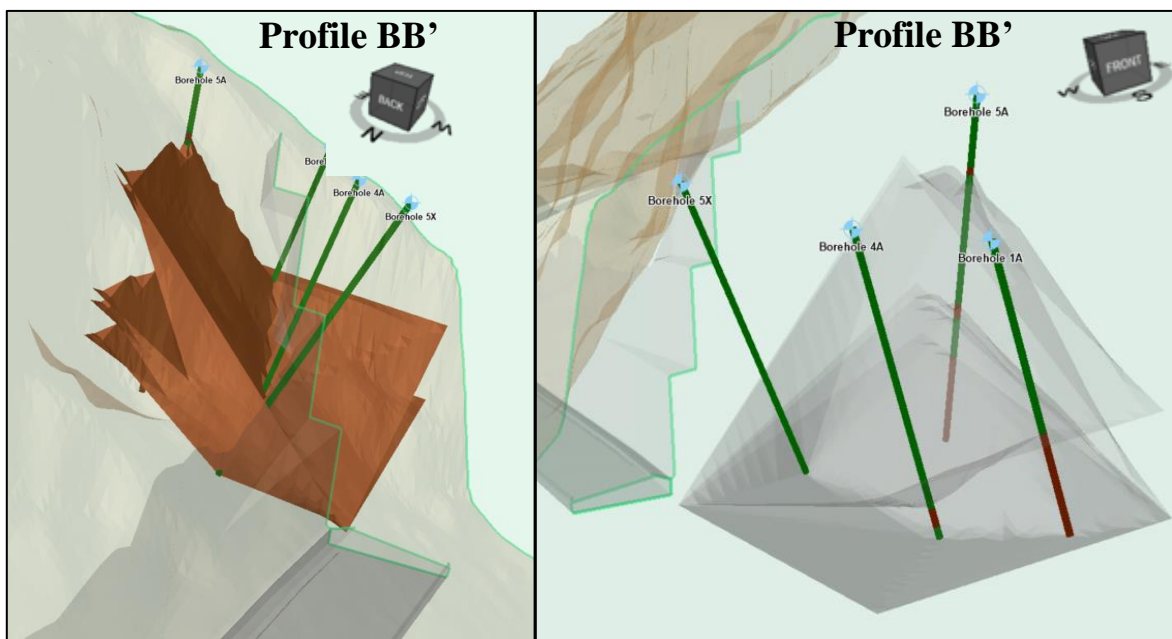


Figure 5.24: Material boundary between metagreywacke and polymictic conglomerate at profile BB'.

## 6 Analysis and results

This chapter will present the analysis and results related to the stability assessment of the planned road cut at Hommelvik. This includes the Q-slope method, kinematic analysis, and numerical modelling by SSR-FEM in RS2.

### 6.1 Stability assessment by Q-slope

Mapping of Q-slope was done at the potential sliding surface (parallel to the foliation) at profile 16140 as shown in Figure 6.1. This represents the overall slope stability for the section of the planned road cut with multibench slope configuration. It was evaluated for planar sliding, but it is technically rock rotational failure which is the potential failure mode.

The measurements for the Q-slope mapping are shown in Table 6.1. The final road cut will probably include both drainage measures and slope reinforcement (stabilization) measures.  $J_{\text{wice}}$  (environmental and geological condition number) are multiplied with 1.5 when drainage measures are installed, 1.3 when slope reinforcement measures are installed, and 1.95 when both are installed. Q-slope was also used to determine the reinforcement free angle for the intermediate benches that will be constructed during the excavation phase of profile BB' and CC' (Table 6.1).  $J_n$  of 12 indicates three joints plus random joints. There are technically more than three joints set there but the orientation of some of them are quite similar, thus  $J_n$  of 12 seems appropriate.

The overall slope and the 10 m intermediate bench utilised the RQD group between 0-100 as shown in Table 4.5 while the 5 m intermediate benches utilise the RQD>30 group. This is done as 5 m intermediate benches with high certainty will not intersect the crushed zone. However, it will be located within the 10 m intermediate bench and the overall slope. The RQD values representing the 10<sup>th</sup> and 25<sup>th</sup> (Q1) percentile for the respective RQD groups.

The steepest stable slope angle  $\beta$  for the overall slope of the planned road cut is calculated to be 66.0-67.4° from the Q-slope method. This is representative for profile BB' and CC'. The steepest reinforcement free angle ( $\beta$ ) for the 5 m intermediate benches for profile BB' and CC' is calculated to be 60.5-61.8°.  $\beta$  for the 10 m intermediate bench at profile BB' is calculated to be 57.8-60.2°.

Table 6.1: Classification of Q-slope in the field at the Hommelvik.

	Overall slope (profile BB' and CC')	Intermediate benches (5 m) (profile BB' and CC')	Intermediate bench (10 m) (profile BB')
Value	Set A	Set A	Set A
RQD	77-90	79-92	58-77
$J_n$	12	12	12
$J_r$	1.0	1.0	1.0
$J_a$	3	3	3
O-factor	0.75	0.75	0.75
$J_{wice}$	1.755	0.9	0.9
$SRF_a$	2.5	2.5	2.5
$SRF_b$	2.5	2.5	2.5
$SRF_c$	2	n/a	2
Q-slope	1.126-1.316	0.593-0.690	0.435-0.578
$\beta$	66.0-67.4°	60.5-61.8°	57.8-60.2°

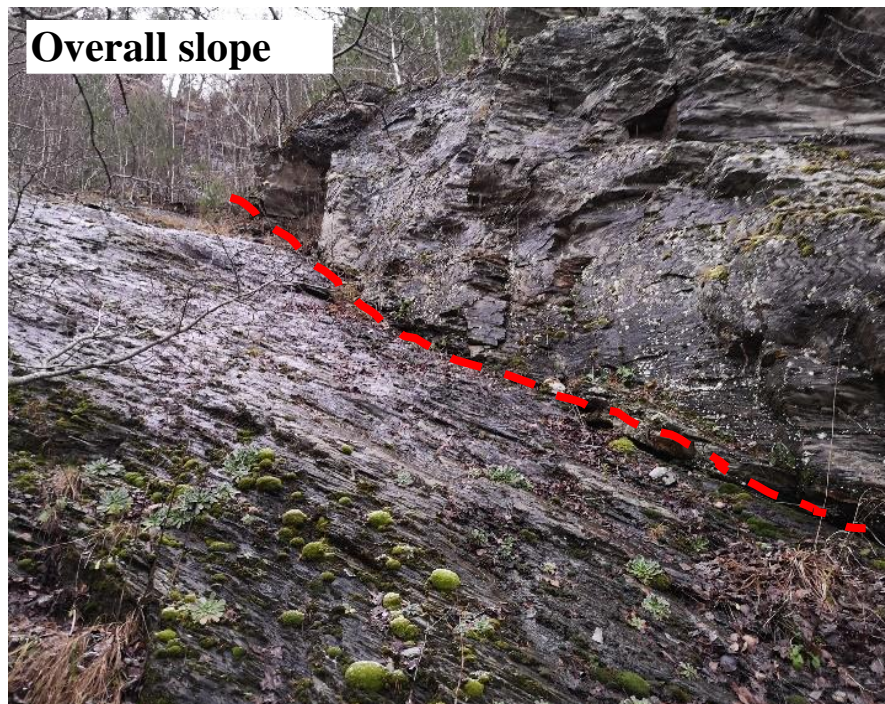


Figure 6.1: Outcrop representing the conditions indicative for the overall slope which will be representative for profile BB' and CC'. The red dashed line represents the potential sliding plane and it parallel with the foliation (J1). It is likely an extension of the crushed zone observed (from the core logging) within the rock mass behind the current road cut.

## 6.2 Kinematic analysis

Kinematic analysis has been performed on each of the three selected profiles (AA', BB', CC') with the planned slope configurations. This analysis was performed in Dips 8.013 with data from the core logging which is weighted with the factor  $f_i$  as described in Section 4.2. The summary of the results is presented in Table 6.2. The values represent the percentage of critical intersections for the poles. It is evident from the table that block toppling from the base plane is the most critical failure mechanism for all the three profiles with values between 38.1-40.6% of the intersections being critical. The possibility of wedge sliding is also high with 12.0-17.0% critical intersections while planar sliding has 9.0-10.7%.

Table 6.2: Summary of kinematic analysis. The values for the failure mechanisms represents the percentage of critical intersections. The orientation is given in dip direction/dip [°].

Profile	Orientation of rock cut	Planar sliding	Wedge sliding	Flexural toppling	Block toppling		
					Direct toppling	Oblique toppling	Base plane
AA'	277/84	10.70%	17.06%	1.99%	5.67%	0.01%	40.60%
BB'	277/71	9.83%	14.51%	1.06%	2.36%	0.01%	39.73%
CC'	279/68	8.97%	12.03%	0.60%	1.71%	0.01%	38.07%

The kinematic analysis for each of the profiles with the respective failure can be found Appendix M.

### 6.2.1 Kinematic sensitivity analysis

Kinematic sensitivity analysis for the parameters slope dip, slope dip direction, and friction angle have been done. This is useful to evaluate the sensitivity to each parameter for the respective failure mechanism, or possibly make adjustments to the slope design (or establish stabilization measures to counteract the failure mechanism). Furthermore, this can be useful if there are uncertainties in respect to input parameters. The four boreholes were drilled closer to profile BB' and CC' compared to AA', thus making it likely that any input parameters are more representative for those profiles.

The slope orientations (dip and dip direction) at each profile are quite similar. Thus, the kinematic sensitivity analysis for each failure mechanism can be presented in the same chart for all profiles. The slope dip is defined from 60-90°, slope dip direction from 270-290°, and friction angle from 25-35°. Table 6.3 represents the parameter values used in the kinematic analysis for each profile and where they are plotted in the following figures (percent of defined range).

Table 6.3: Kinematic sensitivity analysis with percent of the defined range in brackets for each respective parameter.

Profile	Slope dip	Slope dip direction	Friction angle
AA'	84° (80.0%)	277 (35.0%)	31.9 (69.0%)
BB'	71° (36.7%)	277 (35.0%)	31.9 (69.0%)
CC'	68° (26.7%)	279 (45.0%)	31.9 (69.0%)

### 6.2.1.1 Planar sliding

The sensitivity analysis for planar sliding is shown in Figure 6.2. The maximum critical percentage for slope dip top up at 81° and do not increase anymore to 90°. Furthermore, the critical percentage is almost identical between 71-77° slope dip. The general trend for slope dip direction is a decrease in the critical percentage when the slope dip direction increases. If turned out the measured friction angle from the laboratory investigations overestimated the real value of the rock mass by 2° (and the real friction angle was 30°), the increase in critical percentage would only be about 0.3%.

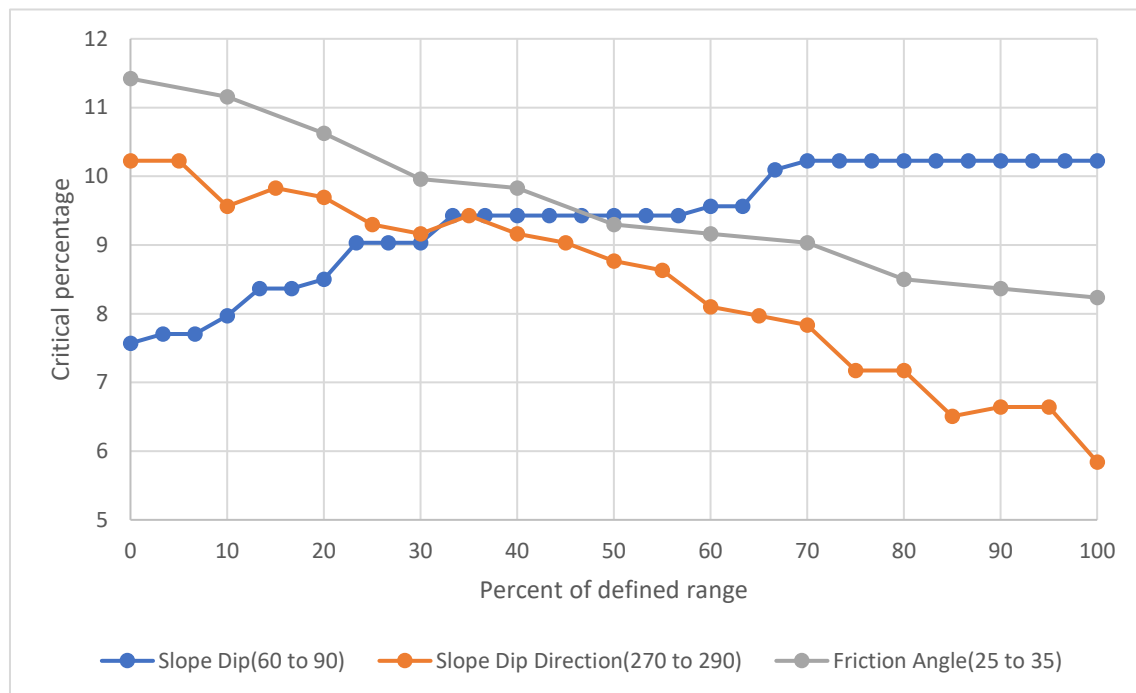


Figure 6.2: Sensitivity analysis for planar sliding.

### 6.2.1.2 Wedge sliding

The sensitivity analysis for wedge sliding is presented in Figure 6.3. The critical percentage for slope dip increases gradually when the slope dip increases (9.1% for 60° to 17.3% for 90°). Slope dip direction and friction angle have very similar trends lines, with a gradual decrease in the critical percentage for the respective parameter as the percent of defined range increases.



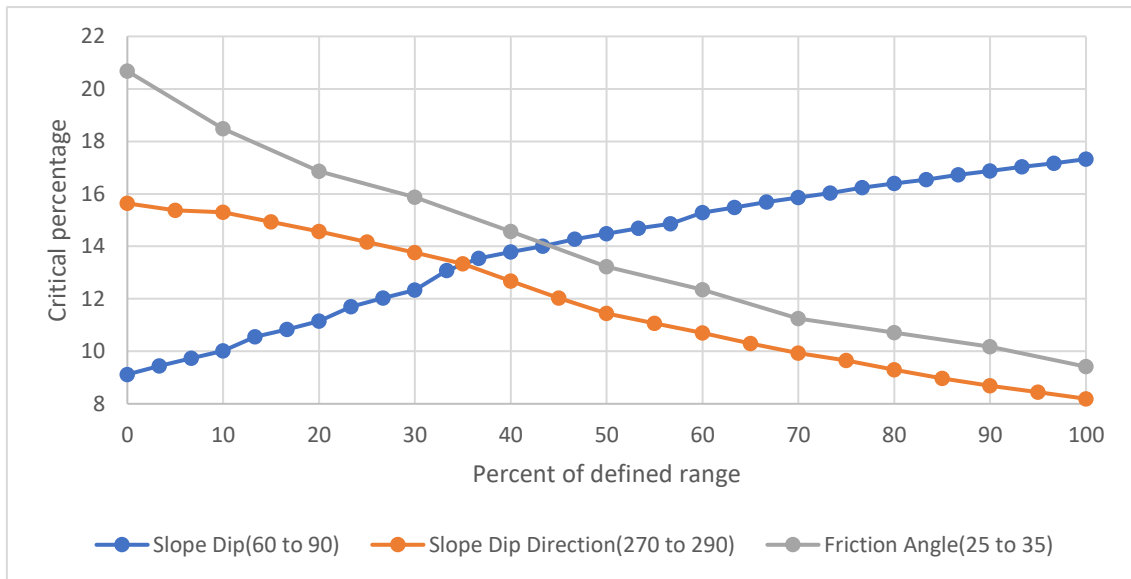


Figure 6.3: Sensitivity analysis for wedge sliding

### 6.2.1.3 Flexural toppling

The sensitivity analysis for flexural toppling is shown in Figure 6.4. It is evident from the figure that the critical percentage is constant at 0.66% for the slope dip direction. Furthermore, the critical percentage is constant at 1.06% for friction angle between 25-30° and 0.66% between 31-34°. The critical percentage increases step wise from slope dip 60-65°, 66-69°, to 70-75°, and then increases gradually to 85° before a steep spike to 90°.

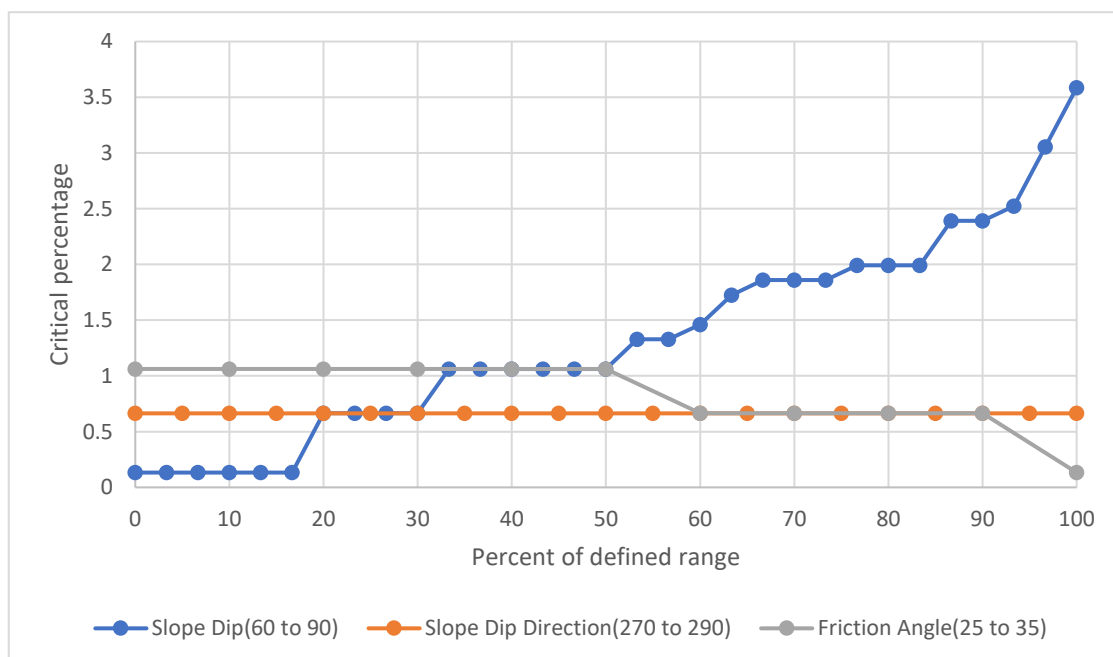


Figure 6.4: Sensitivity analysis for flexural toppling.

### 6.2.1.4 Block toppling

The sensitivity analysis for block toppling in terms of changes in slope dip is illustrated in Figure 6.5. The critical percentage for failure from the base plane increases slowly as the slope dip increases and flattens out at 84°.

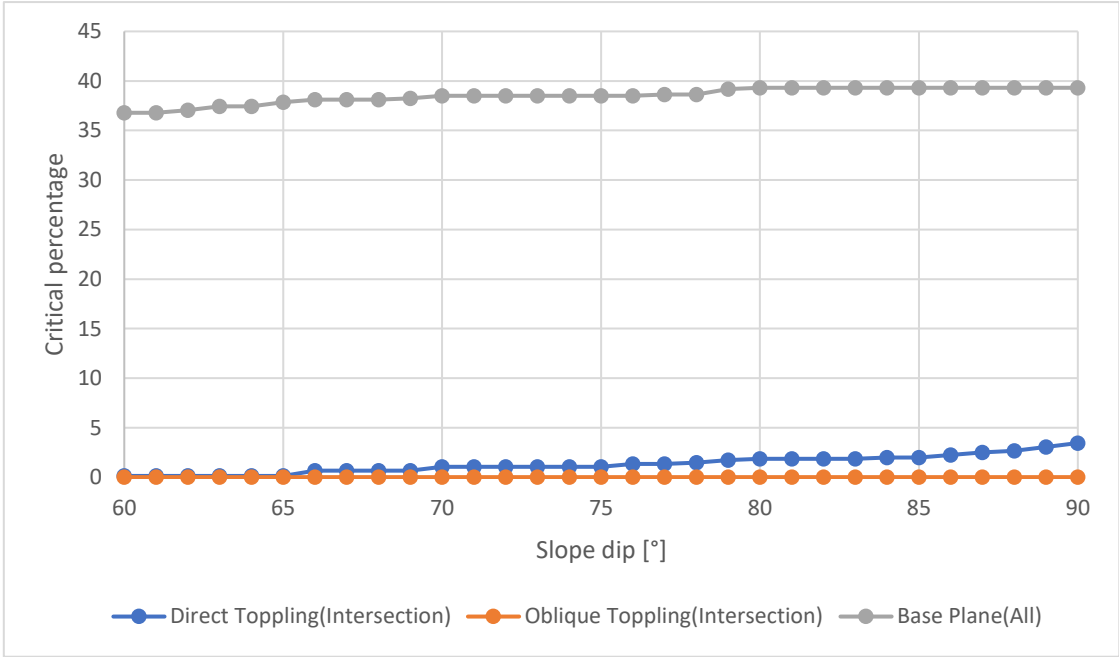


Figure 6.5: Sensitivity analysis for block toppling evaluated against slope dip.

The sensitivity analysis for block toppling in respect to changes in the slope dip direction shows that the critical percentage from the base plane decreases gradually as the slope dip direction increases, as seen in Figure 6.6. The opposite is true for block toppling evaluated against friction angle (for failure from the base plane), as seen in Figure 6.7. Increased friction angle causes a steady increase in critical percentage, which is counterintuitive compared to the other failure mechanisms. Higher friction angle is expected to increase the stability, but it turns out this is true for all failure mechanisms except for block toppling.

This is the opposite to the other failure mechanism where higher friction angle decreased the critical percentage.

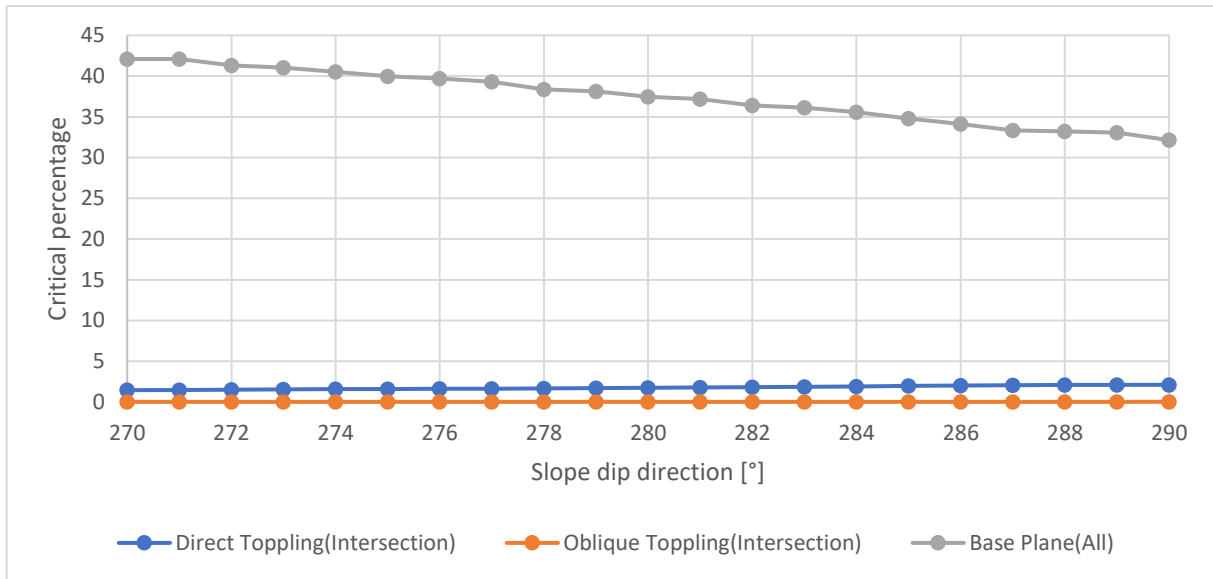


Figure 6.6: Sensitivity analysis for block toppling evaluated against dip direction.

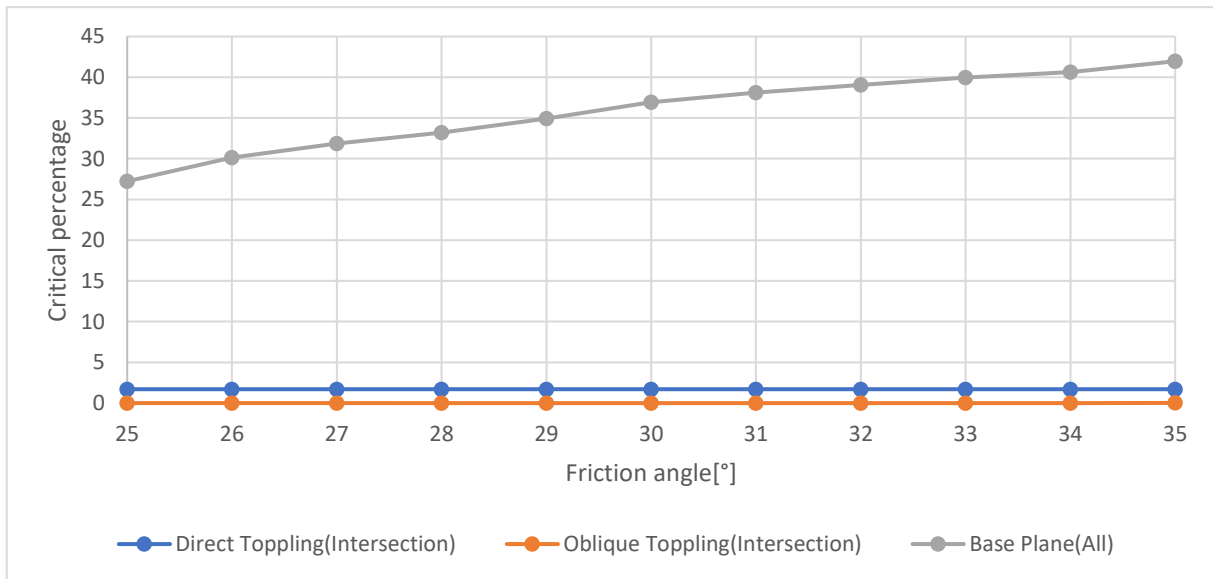


Figure 6.7: Sensitivity analysis for block toppling evaluated against friction angle.

### 6.3 Stability assessment by SSR-FEM in RS2

Numerical modelling with the use of shear strength reduction (SSR) technique with finite element method (FEM) in RS2 from Rocscience Inc have been used to evaluate the stability of the planned road cut at Hommelvik. Numerical modelling of the three profile AA', BB', and CC' along the planned road cut was done in two parts. In the first part, the slopes sensitivity to different parameters such as groundwater, earthquake, and the individual discontinuity sets were analyzed. This was done by evaluating and comparing the critical shear strength reduction factor (CSRF) and the total displacement. The second stage of the numerical modelling integrates stability measures and a combination of the earlier tested parameters which seems the most reasonable. In this part CSRF and total displacement is also evaluated, and potential critical sections of the road cut is highlighted.

#### 6.3.1 Model setup

The geometry for the three profiles in RS2 corresponds to the profiles created in CloudCompare. Thus, 0 along the X-axis in RS2 can be correlated to the start of the profiles in the 3D models. The distance between points along the topography was 0.5 m when the profiles were imported into RS2. However, to simplify the models, points along the topography was removed with the "simplify boundary"-tool in RS2. The preservation rate was set to between 60-70% based on visual inspection of the results. The geometry and setup for profile AA', BB', and CC' are in shown in Figure 6.8, Figure 6.9, and Figure 6.10 respectively.

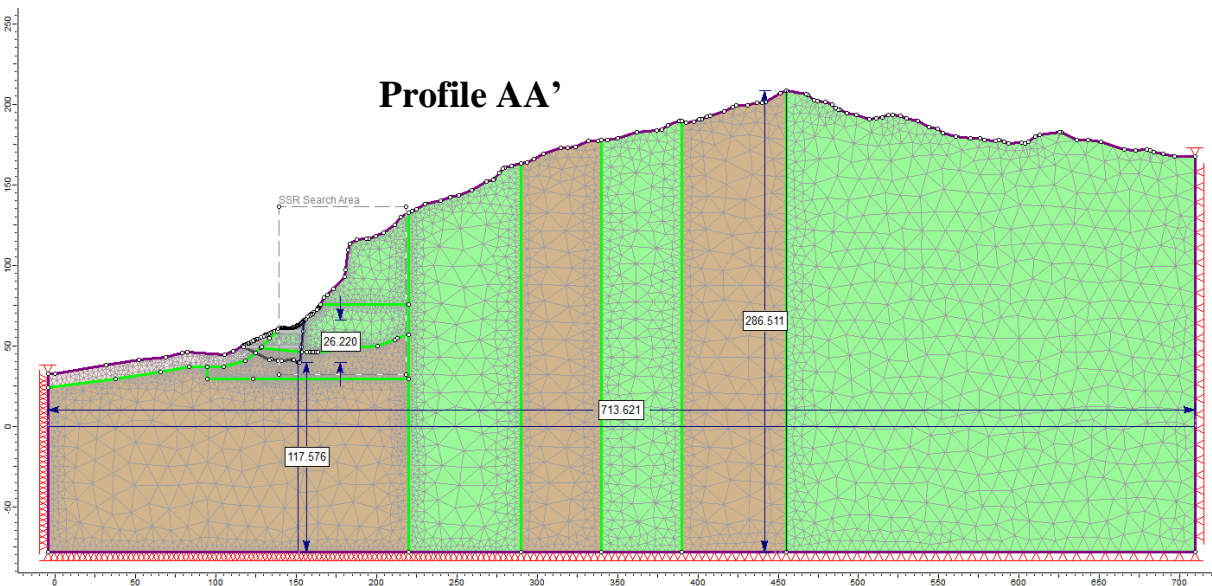
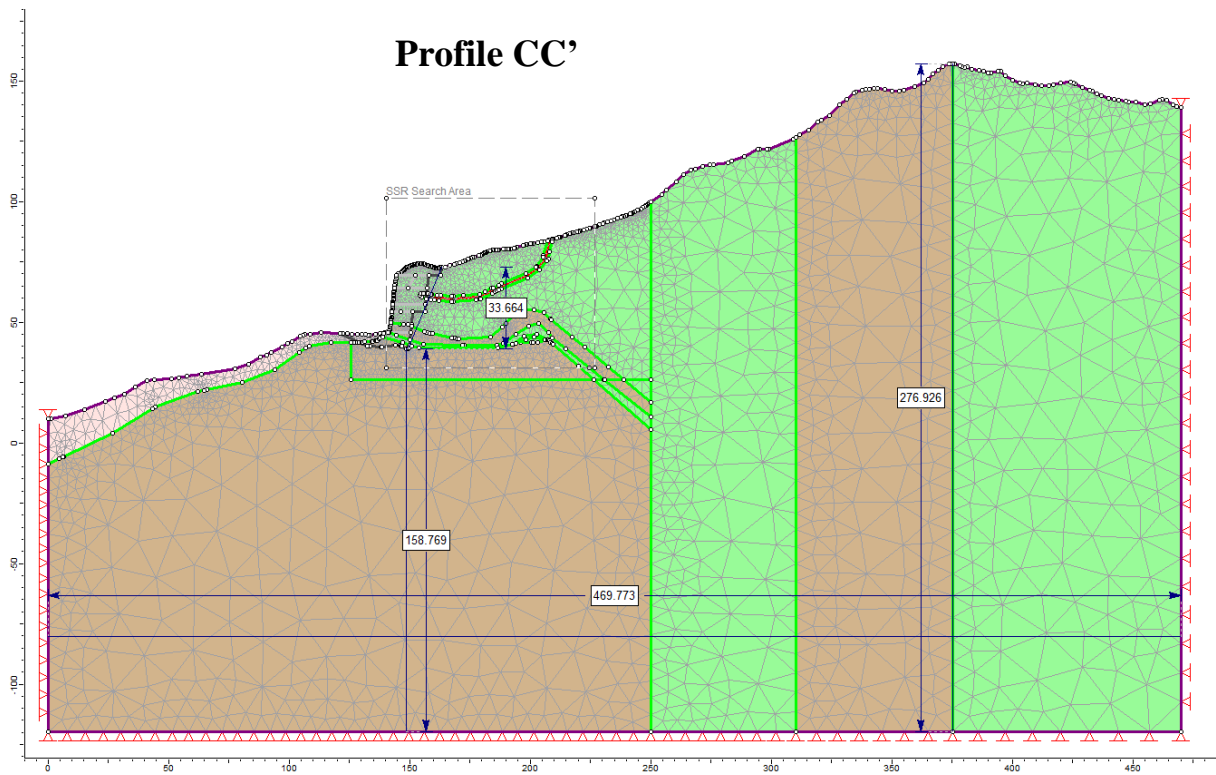
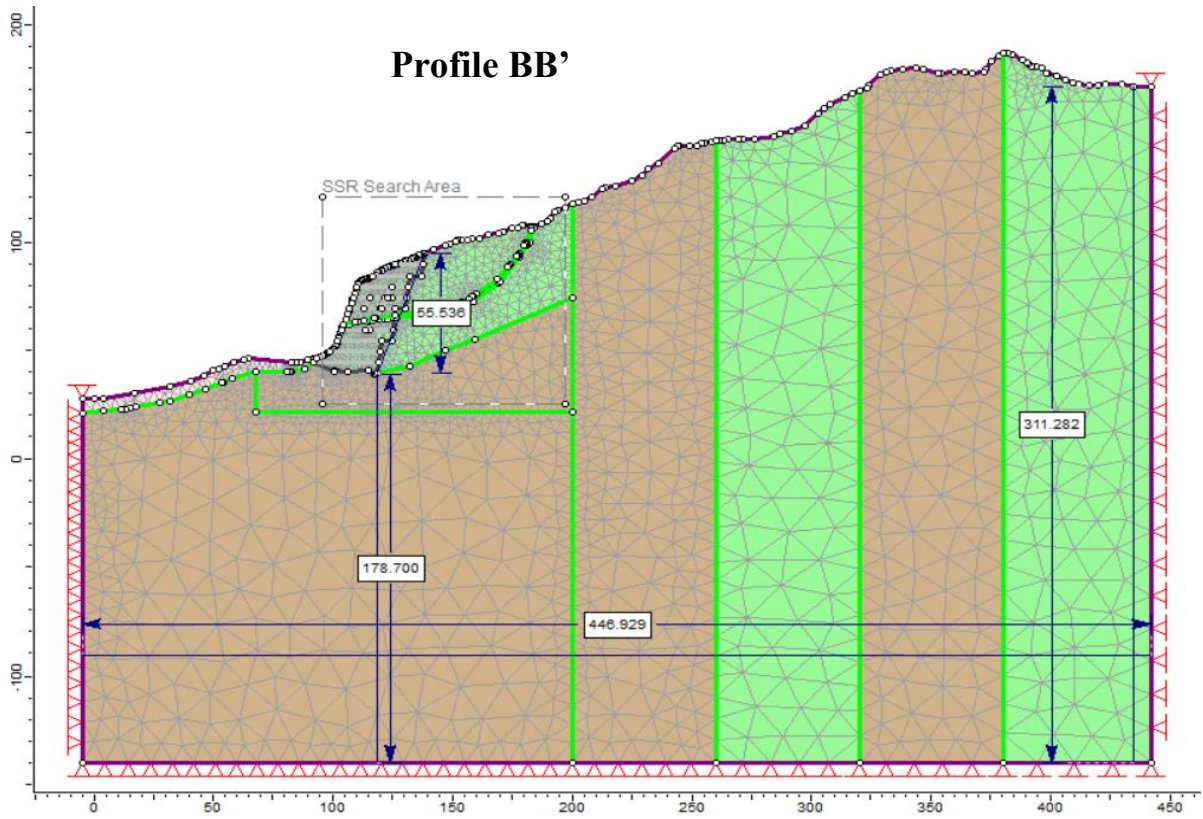


Figure 6.8: Geometry for profile AA' in RS2.



The external boundaries in the models are set to avoid any boundary effects and is done in accordance with the recommendations by Wyllie (2018) given that only small part of the overall rock slope include the road cut which will be evaluated for shear strength reduction. The suggested boundary dimensions for slope stability analysis are shown in Figure 6.11. Panthi (2022) further recommends the depth from the trench bottom to the bottom of the model to be roughly three times the height of the road cut.

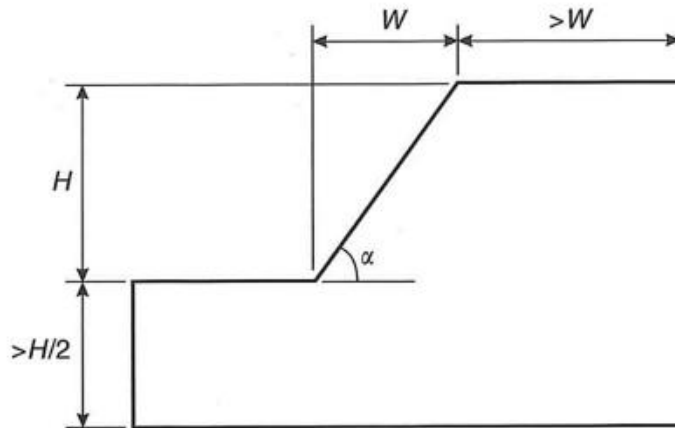


Figure 6.11: Recommended boundary dimensions for slope stability analysis by numerical modelling (Wyllie, 2018).

The displacement boundary along the surface of the models is set to rollers (free to move in all directions). The rest of the boundaries are locked in both horizontal (x) and vertical (y) directions, included the utter node on each side of the ground surface (Liu et al., 2015). Some authors prefer to only restrain the corners in both horizontal and vertical direction while the sides are free to move vertically, and the bottom move horizontally. Due to the size of the models compared to the evaluated parts of the rock slope, it was considered to be a minimal difference between the two approaches. The mesh type for the models is set to graded and 3-noded elements are used. Furthermore, the gradation factor is set to 0.1 and the default number of nodes on all excavations are set to 110 (Rocscience, 2022).

The models are defined with a SSR (shear strength reduction) search area to avoid that a critical failure zone occur anywhere unwanted such as the sections with sand (soils). It would also result in reduced computational time for the models. The geometry of the rock boundaries close to the SSR search areas are estimated based on field mapping, core logging, and the estimated boundaries by Slide3 (Subsection 5.4.2). The material boundaries further away are based on the N50 geological map (Figure 3.7), and for simplistic reasons set to have vertical boundaries. The difference in density between metagreywacke and polymictic conglomerate was small, thus making it unlikely that some uncertainties in the border there having much effect on the overall stability and stress distribution. The geometry of the soils (sand) and depth to bedrock is based on the ground investigations which can be found in Appendix A. A squared material boundary is also created just outside the SSR search areas. This is the area the discontinuities will be assigned for (and not the whole model). This was done to reduce the complexity and processing time for the models.

### 6.3.2 Material parameters

From the laboratory investigations, it was found that the metagreywacke can be classified as highly anisotropic. Due to the folding nature of the rock type and its different variants, this anisotropic behaviour is hard to quantify in any meaningful in RS2. However, from the core logging and DSE it was confirmed that the joints were heavily foliation dominated. Thus, it is assumed that this anisotropic behaviour (strength and stiffness) of the rock mass can be represented by the introduction of the foliation (and the other joint) sets into the models.

The generalized Hoek-Brown failure criterion will be utilized in RS2. The Hoek-Brown material constant  $m_i$  is set to 18 for the metagreywacke (and weak metagreywacke) and 21 for the polymictic conglomerate based on the studies of Marinos and Hoek (2001).

The values for GSI are set based on the equation published by Hoek et al. (2013) which utilizes parameters from the Q-method (and Q-slope), and is given by:

$$GSI = \frac{52(J_r/J_a)}{(1 + J_r/J_a)} + \frac{RQD}{2} \quad (6.1)$$

GSI can also be set based on charts as seen in Appendix K. However, it was decided to use Equation 6.1 which is a more quantitative approach and reduces subjectivity which qualitative methods are prone to which the traditional GSI charts are prone to.

The RQD values in Equation 6.1 is set based on Table 4.5. The RQD is set for metagreywacke and polymictic conglomerate combined as there were transitional zones between the rock types and their rock mechanical properties were quite similar. The possible geometry of the crushed zone (weak metagreywacke) was presented in Subsection 5.4.1. Based on the clear distinction between the crushed zone and the rest of the rock mass, the RQD values were grouped into RQD<30 (crushed zone), RQD>30 (crushed zone excluded), and RQD between 0-100 (all values included) as discussed in Section 4.2. The RQD is set to Q1 for the group RQD>30 for metagreywacke and polymictic conglomerate, and RQD<30 for the weak metagreywacke (crushed zone), as seen in Table 6.4. This seems conservative but this still reasonable for the overall rock mass. The values for  $J_a$  were set based on core logging, and the most representative values for the respective rock types were used in the calculation. The same principle was done for  $J_r$ . However, JRC was measured for the cores. The correlation between the two parameters, which was proposed by Barton and Bandis (1990), was used and was shown in Figure 2.21 (e) The summary of the used input values to calculate GSI is shown in Table 6.4.

Table 6.4: Input values for the calculation of GSI ( $GSI_{2013}$ ).

Rock type	RQD	$J_a$	JRC	$J_{r1990}$	$GSI_{2013}$
Crushed zone (weak metagreywacke)	12	4.0	2-4	1.0	16
Metagreywacke	79	3.0	10-12	2.0	67
Conglomerate	92	2.0	14-16	3.0	77

Materials have to be defined as plastic to perform stability analysis with SSR. The post-failure characteristics of the rock masses is important to define accurately for the results from RS2 to be realistic. The most recognised post-failure characterization of plastic materials was published by Hoek and Brown (1997). Three models for post-failure behaviour were suggested: elastic-brittle, strain-softening, and elastic-plastic, as illustrated in Figure 6.12. Elastic-brittle is indicative for very good quality hard rock masses. Strain softening is typical for average quality rock masses, and elastic-plastic behaviour for very poor quality rock masses. The metagreywacke and polymictic conglomerate are likely best represented as elastic-brittle models.

The crushed zone which is represented as continuum of weak metagreywacke could maybe be presented with elastic-plastic behaviour, but elastic-brittle behaviour is instead used. This was done to keep the material models consistent, and there are very small differences between elastic-brittle and elastic-plastic behaviour for poor rock masses as shown in Table 6.5 for the weak metagreywacke. The values in brackets in the table indicates residual values (e.g., elastic-brittle behaviour), and if the rock masses were modelled with elastic-plastic behaviour the residual values would be the same as peak values. It should be noted that RS2 can only model elastic-brittle or elastic-plastic behaviour as the residual characteristics of materials are assigned immediately after yielding.

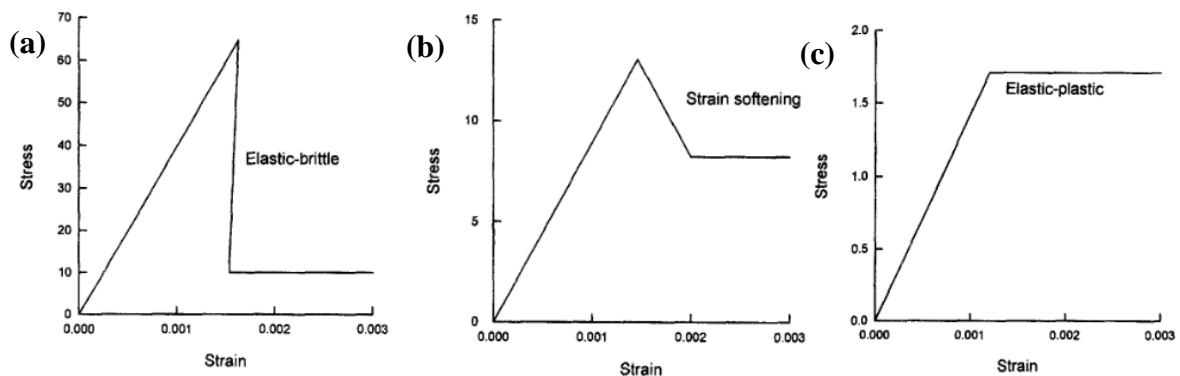


Figure 6.12: Post-failure characteristics for different quality rock masses; (a) very good quality hard rock mass; (b) average quality rock mass; (c) very poor quality soft rock mass (Hoek & Brown, 1997).

The residual GSI,  $GSI_r$ , which characterizes the broken rock mass, is calculated from (Cai et al., 2007):

$$GSI_r = GSI \times e^{-0.0134 \times GSI} \quad (6.2)$$

$\gamma$ ,  $\sigma_{ci}$ ,  $E_i$ , and  $\nu$  were assigned based on the laboratory investigations (Section 4.3). It should be noted that  $\sigma_{ci}$  and  $E_i$  is reduced by 61.0% for weak meta greywacke (crushed zone) compared to metagreywacke. This was done as the metagreywacke in crushed zone were assigned weathering grade III during the core logging. The compressive strength reduction was determined from Equation 2.22.  $E_{rm}$  was calculated with Equation 2.16.

The disturbance factor D was set to 0.5 based on the disturbance factor chart found in Appendix K. This was done as controlled presplit or smooth wall blasting will likely be used during the excavation phase of the road cut.



The Hoek-Brown constants  $s$ ,  $a$ , and  $m_b$  were calculated automatically in RS2, but were verified with Equation 2.27, 2.28, and 2.29. The summary of the input data for the rock types in RS2 are given in Table 6.5.

There will be a section with sand (soils) west (downside) for the planned road cut. The Mohr-Coulomb parameters used for the sand is presented in Table 6.6.

Table 6.5: Input data for rock types in RS2. Residual values are in brackets.

Parameter	Symbol	Value			Unit	Remarks
		Weak meta-greywacke	Meta-greywacke	Polymictic conglomerate		
<i>Estimated based on laboratory investigations</i>						
Specific weight	$\gamma$	27.61	27.61	27.58	kN/m <sup>3</sup>	Subsection 4.3.1
Intact rock strength (UCS)	$\sigma_{ci}$	50.0	128.3	89.3	MPa	Subsection 4.3.1
Young's modulus (intact rock)	$E_i$	20780	53500	54100	MPa	Subsection 4.3.1
Young's modulus (rock mass)	$E_{rm}$	559 (525)	20677 (2055)	29623 (2079)	MPa	Equation 2.16
Poisson's ratio	$\nu$	0.313	0.313	0.212	-	Subsection 4.3.1
<i>Estimated based on Generalized Hoek-Brown failure criterion</i>						
Geological strength index	GSI	16 (13)	67 (27)	77 (27)	-	Equation 6.1 (Equation 6.2)
Disturbance factor	D	0.5	0.5	0.5	-	Appendix K
H-B material constant (intact rock)	$m_i$	18	18	21	-	
H-B constant (s)	$s$	0.000014 (0.000009)	0.012277 (0.000059)	0.046576 (0.000059)	-	Equation 2.28
H-B constant (a)	$a$	0.557147 (0.569846)	0.501702 (0.527338)	0.500771 (0.527338)	-	Equation 2.29
H-B material constant	$m_b$	0.32968 (0.28579)	3.73947 (0.55665)	7.02366 (0.64942)	-	Equation 2.27

Table 6.6: Mohr-Coulomb parameters for sand (Sadoglu, 2015).

Parameter	Symbol	Value	Unit
Dry unit density	$\gamma_d$	15.81	kN/m <sup>3</sup>
Poisson's ratio	$\nu_s$	0.3	-
Youngs' modulus	$E_s$	24	MPa
Cohesion	$C$	5	kPa
Friction angle	$\phi_p$	41	°
Dilation angle	$\psi$	20.5	°

### 6.3.3 Discontinuity parameters

The discontinuity parameters are modelled by Barton-Bandis failure criterion in RS2. Based on the core logging it seems like polymictic conglomerate is mostly located towards the bottom part of road cut while the rest is dominated by metagreywacke. Since metagreywacke is the dominating rock type, it is utilized as the host rock when the properties of the joints are assigned.

The residual friction angle ( $\phi_r$ ) for the joint is assumed to be equal to the basic friction angle ( $\phi_b$ ) (for the metagreywacke) due to no visible displacements along the joint walls for any of the mapped joint sets (Wyllie, 2018).

The Joint wall Compressive Strength (JCS) for the joint sets are estimated based on  $\sigma_{ci}$  as measurement of JCS were not done in the field. JCS should be in theory be equal to  $\sigma_{ci}$  for unweathered joint walls. Barton and Choubey (1977) suggests JCS to be set equal to 25 % of  $\sigma_{ci}$  for weathered joints as a conservative estimate. This is very similar to weathering grade IV which is equal to 22.5% of  $\sigma_{ci}$  from Equation 2.22. It was therefore decided to use the respective weathering grades for discontinuity sets given in Table 5.3 to estimate the values for JCS.

Normal stiffness ( $k_n$ ) and shear stiffness ( $k_s$ ) for joints are often considered some of the most difficult parameters to quantify precisely. The joint stiffness can be described through the stress-deformation characteristics of the joints.  $k_n$  and  $k_s$  are defined based on commonly used approach given by the following equations (Barton, 1972):

$$k_n = \frac{E_i \times E_{rm}}{L(E_i - E_{rm})} \quad (6.3)$$

$$k_s = \frac{G_i \times G_{rm}}{L(G_i - G_{rm})} \quad (6.4)$$

where

$E_i$  and  $G_i$  = intact rock modulus and intact rock shear modulus

$E_{rm}$  and  $G_{rm}$  = rock mass modulus and rock mass shear modulus

L = mean joint spacing

Shear modulus for intact rock ( $G_i$ ) and rock mass ( $G_{rm}$ ) are defined as (Barton, 1972):

$$G_i = \frac{E_i}{2(1 + \nu)} \quad (6.5)$$

$$G_{rm} = \frac{E_{rm}}{2(1 + \nu)} \quad (6.6)$$

where  $\nu$  is the Poisson's ratio.

The spacing of the joints set for Equation 6.3 and 6.4 are given in Table 5.3 and derived from DSE and CloudCompare.

The discontinuities are integrated into the RS2 as a joint network. The individual discontinuities can either be defined as infinite or with persistence and a length. The definition of persistence in RS2 differs from the traditional description for the term, which is the absolute distance of a discontinuity propagating through the rock mass and this description fit to the term “length” used in RS2. Persistence on the other side is the ratio between the “length” of the discontinuity (L1) and total length along the joint plane (“length” of discontinuity + rock bridge between adjacent discontinuities) (L2), as illustrated in Figure 6.13. Thus, persistence is described as a ratio between 0 and 1 (Rocscience, 2022). Persistence and length for discontinuities are estimated in CloudCompare (visual comparison and dominance factor) but there are some uncertainties to the values.

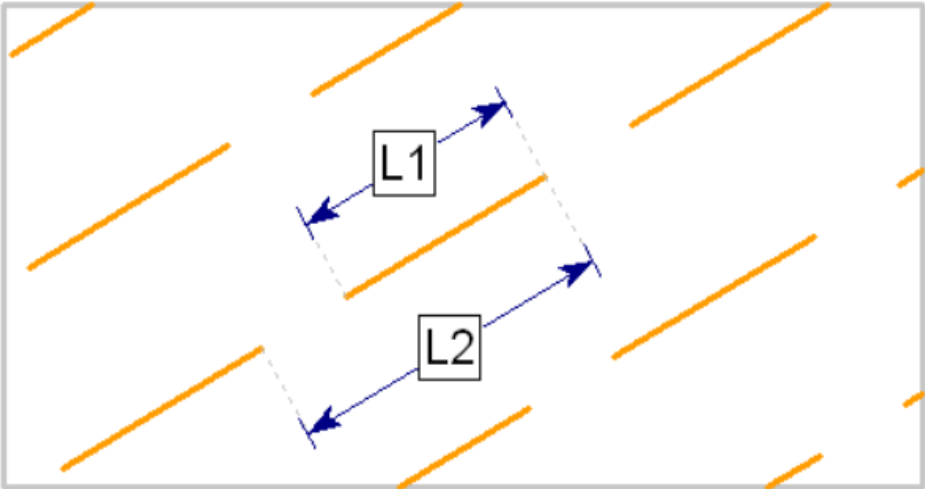


Figure 6.13: Definition of joint length (L1) and persistence (L1/L2) in RS2 (Rocscience, 2022).

Joint end conditions are set to open any only at the excavation surfaces. This allows relative movement (slide or open) to occur at the joint ends as it is represented by two nodes which can move with respect to each other compared to closed joint ends which are only represented by one node (Rocscience, 2022). This also means that the joint ends are closed within the rock mass, which is recommended by Rocscience (2022). Joint intersecting the rest of the slope was still set to be closed to avoid any unwanted displacement from blocks or wedges along the surface, thus resulting in a model which is not able to converge. These conditions were set for all the joints.

The summary of the joint parameters is given in Table 6.7.

Table 6.7: Joint parameters used for FEM analysis. Apparent dips for the joints are integrated as trace planes in RS2.

Parameter	Value							Unit	Remarks
	J1	J2	J3	J4	J5	J6	J7		
Domain (profile)	AA'	AA'	BB'	AA'	AA'	BB'	BB'	-	Figure 5.15
	BB'	BB'	CC'		BB'	CC'	CC'		
	CC'	CC'			CC'				
Dip direction	198	269	141	106	356	076	193	°	Table 5.3
Dip	17	68	64	72	88	39	61	°	
Spacing ( <i>S</i> )	0.5	2 (3*)	2	2	4	5	25	m	Table 5.3
Length	50	10	10	10	20	15	10	m	Table 5.3
Persistence <sup>1</sup>	0.8	0.6	0.5	0.5	0.5	0.2	0.2	-	
Residual friction angle ( $\phi_r$ )	31.9	31.9	31.9	31.9	31.9	31.9	31.9	°	
Joint Roughness Coefficient (JRC)	4	6	4	4	4	12	8	-	Table 5.3
Joint wall Compressive Strength (JCS)	38.8	52.6	52.6	52.6	52.6	66.4	66.4	MPa	Table 5.3 and Equation 2.23
Joint normal stiffness ( $k_n$ )	67405	33703	33703	16851	8426	6741	1348	MPa/m	Equation 6.3
Joint shear stiffness ( $k_s$ )	25668	12834	12834	6417	3209	2567	513	MPa/m	Equation 6.4

\*Spacing for J2 is set to 3 m for profile AA' to avoid unrealistic failure ( $CRSF \leq 1.0$ ).

### 6.3.4 External influences

Seismic events were incorporated into the RS2 models. The design ground acceleration

$a_g = 0.392 \text{ m/s}^2 = 0.04 \text{ g}$  (Subsubsection 2.2.3.1). In RS2 the seismic loading is defined as:

$$\text{Seismic force} = \text{Seismic coefficient} \times \text{Body force} \quad (6.5)$$

Thus, the seismic coefficient is set to -0.04 which is the seismic acceleration as a fraction of *g* for the horizontal load direction (right to left loading direction) and applied in the last stage (representing the final slope configuration). Seismic loading in the vertical direction is ignored as it is typically considered insignificant for rock slopes (Rocscience, 2022).

In-situ rock stresses are not integrated into the models as no measurements have been done there or anywhere near which are of relevance. Wyllie (2018) states that most slope failures are gravity driven and the general consensus is that the in-situ stresses are thought to be minimal. However, it is emphasized that their effects are largely unknown, and they are rarely measured for slopes. In Norway the in-situ horizontal stresses tend to be higher than the vertical stresses to relatively high residual stresses (Nilsen & Palmström, 2000). However, Wyllie (2018) states

that slightly higher horizontal stresses compared to vertical stresses are likely to improve the stability as the normal stress will increase for joint and/or shearing surface within slope. Thus, it possible that the models in RS2 are slightly more conservative than the reality.

The groundwater conditions and the depth to groundwater table is highly uncertain as no measurements have been done. However, it is likely that the crushed zone has affected it. Multiconsult Norge AS (2019a) states little icing was observed on the current road cut during the winter of 2018 but there was more accumulation of icing north of it. The drawn piezometric lines in RS2 represents the groundwater table. They were drawn based on the assumed groundwater table after excavation and the influence of the crushed zone. The groundwater table for profile AA' is set closer to the surface compared to profile BB' and CC' as this profile was closer to the area with more icing seen during the winter.

### 6.3.5 Excavation sequence

The excavation sequence for the planned road cut at the different profiles are set to be excavated from the top down. This is done optimize the stabilization phase of the final road cut face and easier accessible to the walls. The bench excavation will mostly be done in 5-10 m increments to optimize safety and efficiency but also be able to install the necessary stabilization measures. For profile BB' and CC' some intermediate benches are suggested in the excavation stages close to the crushed zone. This is done such that temporary rock bolts and anchors can be in installed in the floor beneath to secure the slope and crushed zone. The bench angle for these intermediate benches is based on Q-slope, as seen in Table 6.1. Intermediate benches which will likely intersect the crushed zone and are set to have reinforcement free angle ( $\beta$ ) of  $55^\circ$ . This is set a little bit lower than the calculate range which is  $57.8-60.2^\circ$ . This was done to be a little more conservative. The 5 m intermediate benches are set to  $60^\circ$  and do not intersect the crushed zone.

The excavation sequences used for all the models in RS2 are presented in Figure 6.14, 6.15, and 6.16.

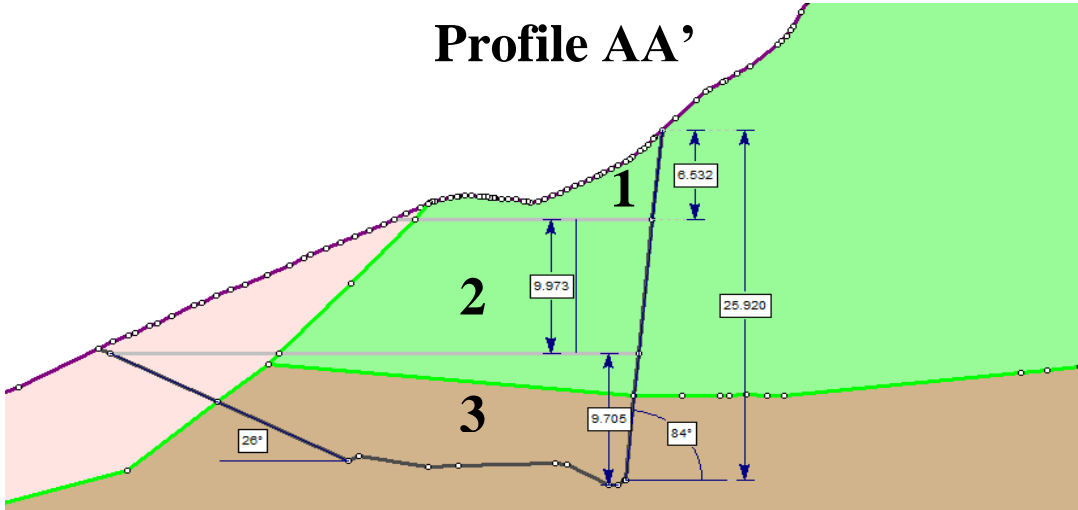


Figure 6.14: Excavation sequence for profile BB'. The excavation area is 543 m<sup>2</sup> and the excavation perimeter is 107 m.

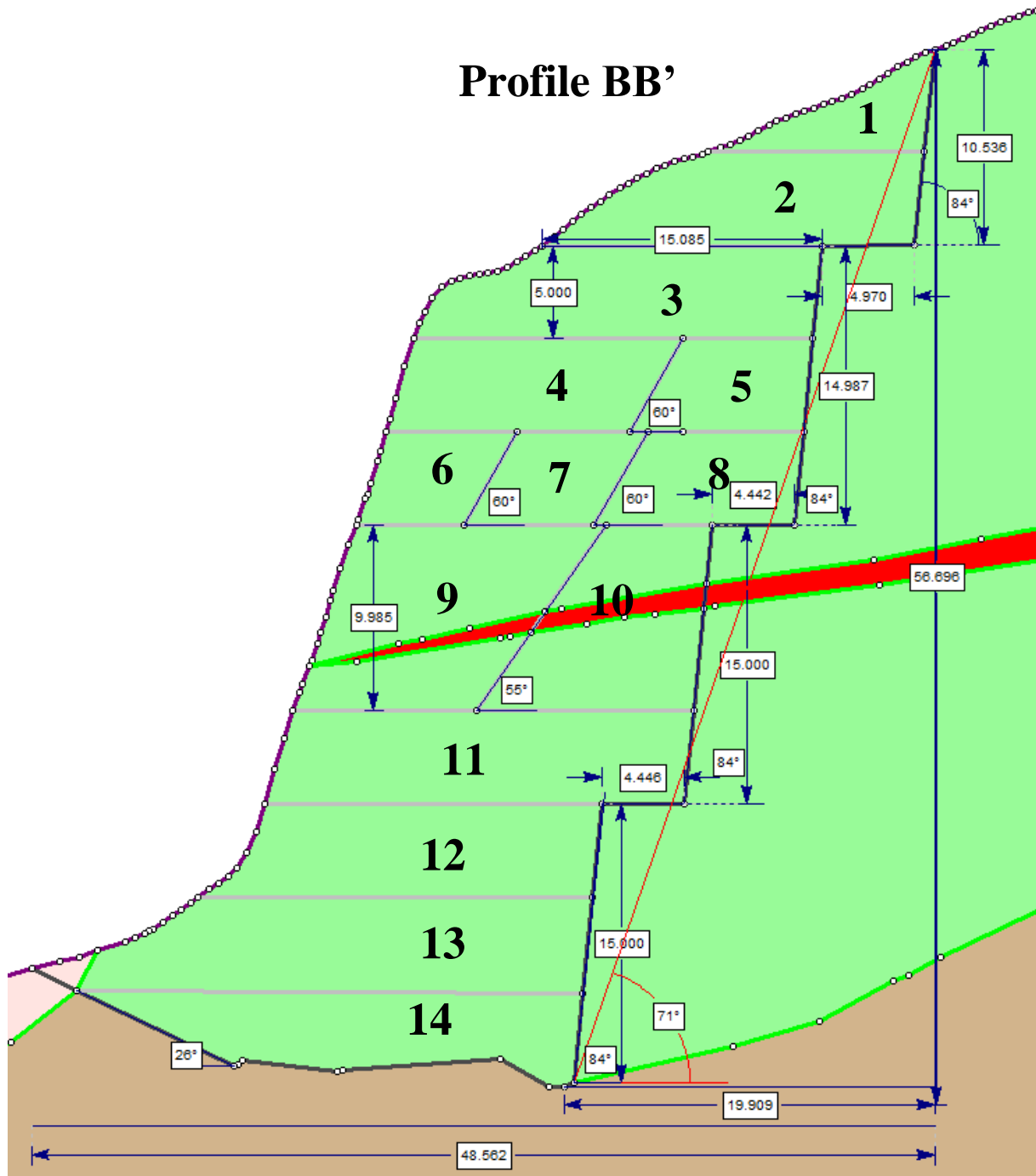


Figure 6.15: Excavation sequence for profile BB'. The excavation area is 1065 m<sup>2</sup> and the excavation perimeter is 176 m.

## Profile CC'

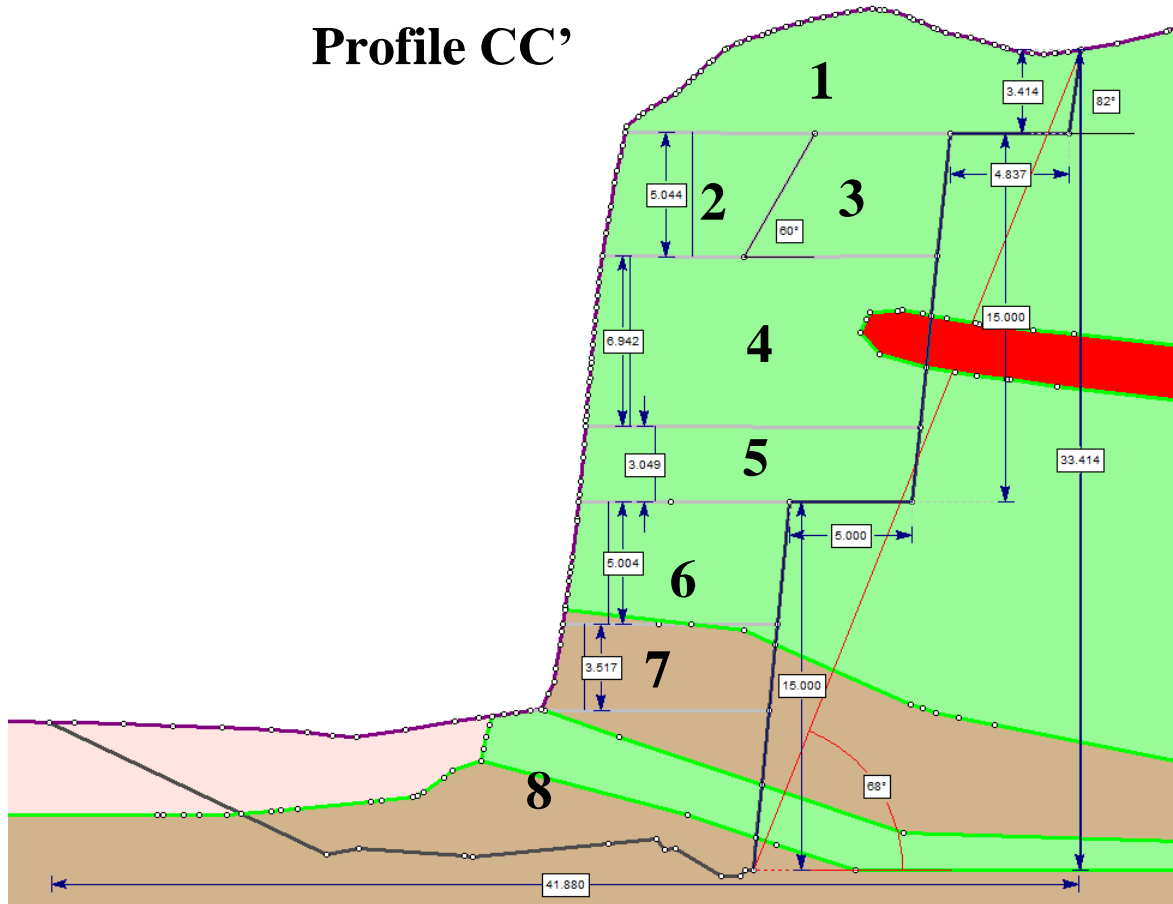


Figure 6.16: Excavation sequence for profile CC'. The excavation area is 471 m<sup>2</sup> and the excavation perimeter is 138 m<sup>2</sup>.

### 6.3.6 Sensitivity analysis

The results from the sensitivity analysis of the different parameters influence on the slope stability are presented in Table 6.8. The critical shear strength reduction factor (CSR<sub>F</sub>) and maximum total displacement were registered for each model. The maximum shear strain was also registered during the modelling but there was no evident trend. For instance, in the testing of profile CC', 7 of 11 models gave the same maximum shear strain of 0.00222, and the other models gave very similar results. Thus, it is not reported. Combinations of the discontinuities were also modelled but the general trend was that the models would not converge (which mean no CSR<sub>F</sub>) even though the tolerance and maximum number of iterations were adjusted. This is likely due to the steep angles of the slopes combined with small unstable wedges and blocks created near the surface.

The general trend from the results shows that CSRFB is lowest for profile AA' and highest for profile CC'. The implementation of groundwater increased the CSRFB for all profiles which is expected. However, for profile AA' the model with the higher groundwater table resulted in a higher value of CSRFB which is unexpected. When earthquake was introduced as a parameter too, CSRFB became highest for the normal groundwater table, which is to be expected. J2 and J4 were the most destabilizing joints (isolated) for profile AA', both resulted in CSRFB < 1.5. The model with J2 also resulted in the highest maximum displacement (1.89 cm) of all the tested models. J1 tested for profile AA' resulted in a significantly higher CSRFB than the raw model (base model). The spacing is very tight and the friction along all the joints planes can be considered stabilizing in RS2 when it is evaluated isolated. Earthquake tested isolated also resulted in a higher CSRFB than the raw model for profile AA'. None of the discontinuity sets from profile BB' did stand out. For profile CC' J4 was the discontinuity sets which resulted in the lowest CSRFB.

The total displacement and CSRFB for the different models are also shown in Figure 6.17, 6.18, 6.19, 6.20, and 6.21.

Table 6.8: Results from sensitivity analysis for the different parameters effect on the stability of the road cut.

State	Profile AA'		Profile BB'		Profile CC'	
	Max. total displacement [cm]	CSRFB	Max. total displacement [cm]	CSRFB	Max. total displacement [cm]	CSRFB
Raw	0.765	1.96	0.431	2.13	0.184	2.73
Groundwater (normal)	0.622	1.85	0.248	1.99	0.144	2.42
Groundwater (high)	0.699	1.90	-	-	-	-
Earthquake	0.916	2.00	0.346	1.97	0.185	2.58
Groundwater (normal) + earthquake	0.800	1.86	0.414	1.99	0.227	2.60
Groundwater (high) + earthquake	0.550	1.70	-	-	-	-
J1	1.16	2.38	0.658	2.12	0.243	2.62
J2	1.89	1.19	0.212	1.90	0.153	2.34
J3	0.445	1.75	0.184	1.92	0.119	2.34
J4	0.324	1.37	0.700	1.85	0.127	1.80
J5	0.303	1.72	0.284	1.87	0.0469	2.21
J6	0.856	1.95	0.551	1.83	0.238	2.70
J7	1.010	2.01	0.357	2.06	0.210	2.82
J1 + J3	-	-	0.0205	1.43	-	-
J2 + J3	-	-	0.0957	1.60	-	-



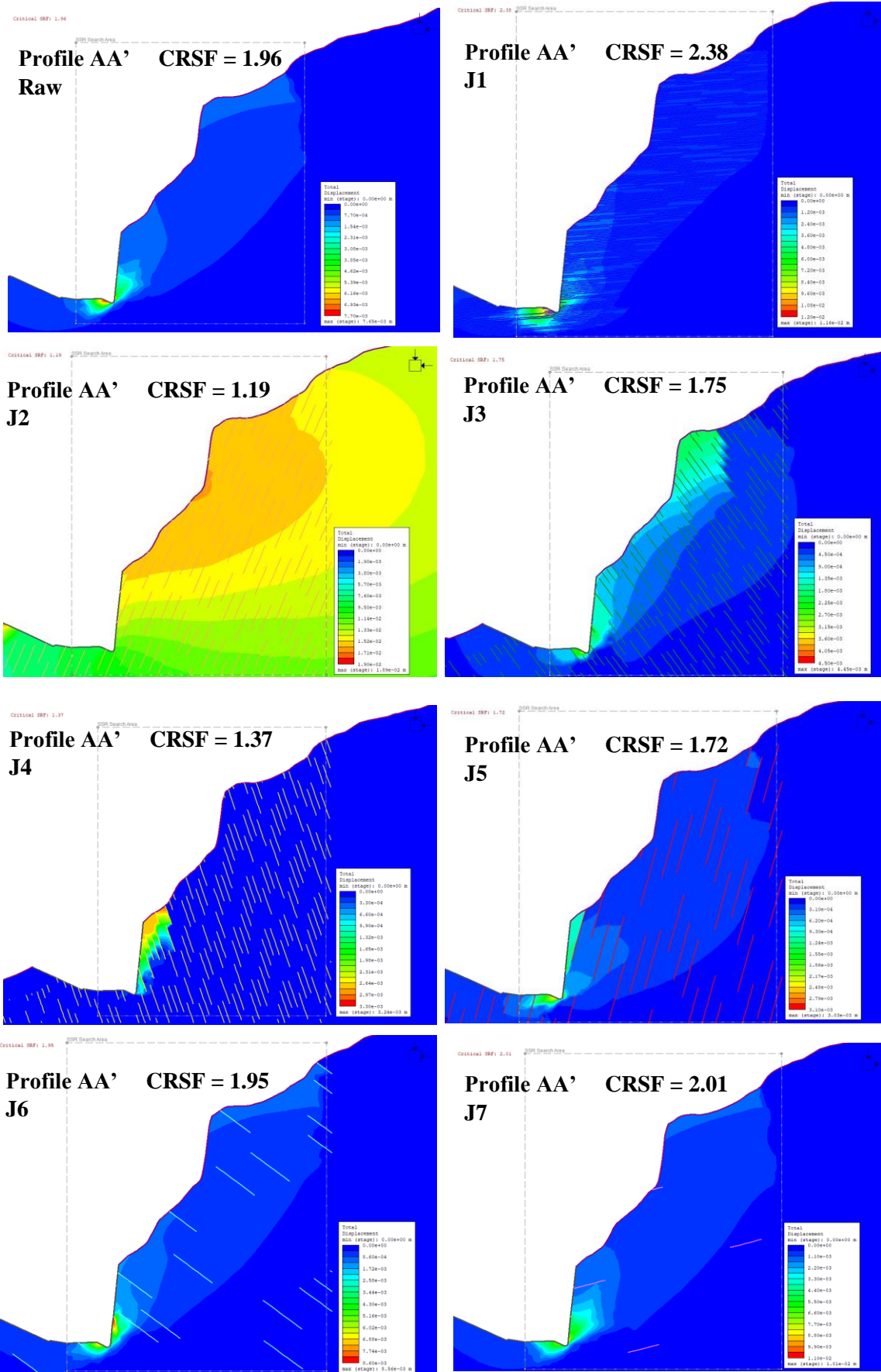


Figure 6.17: The influence on CRSF for profile AA by the different discontinuity sets.

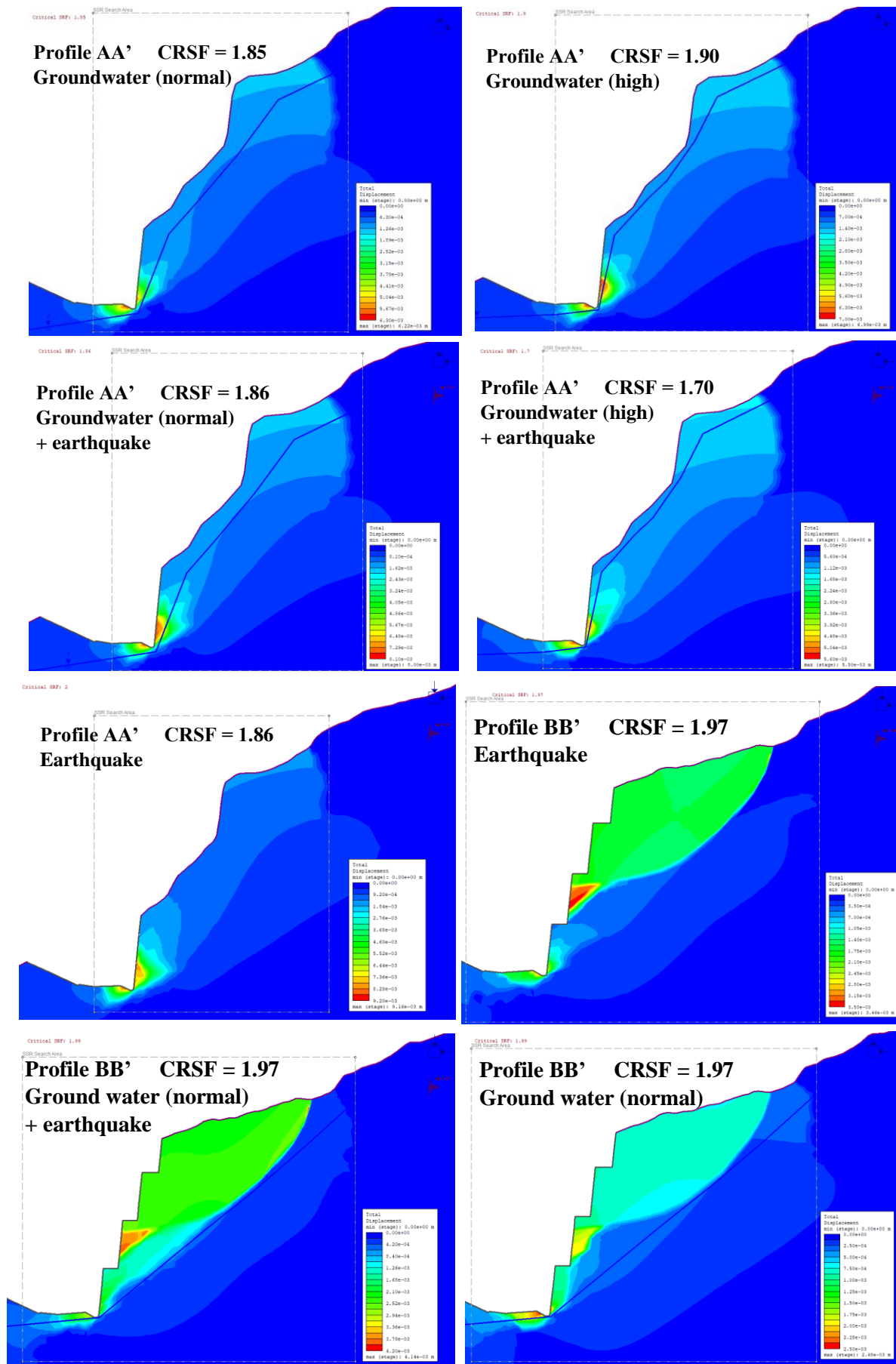


Figure 6.18: Groundwater and seismic event by earthquake effect on CRSF for profile AA' and BB'.

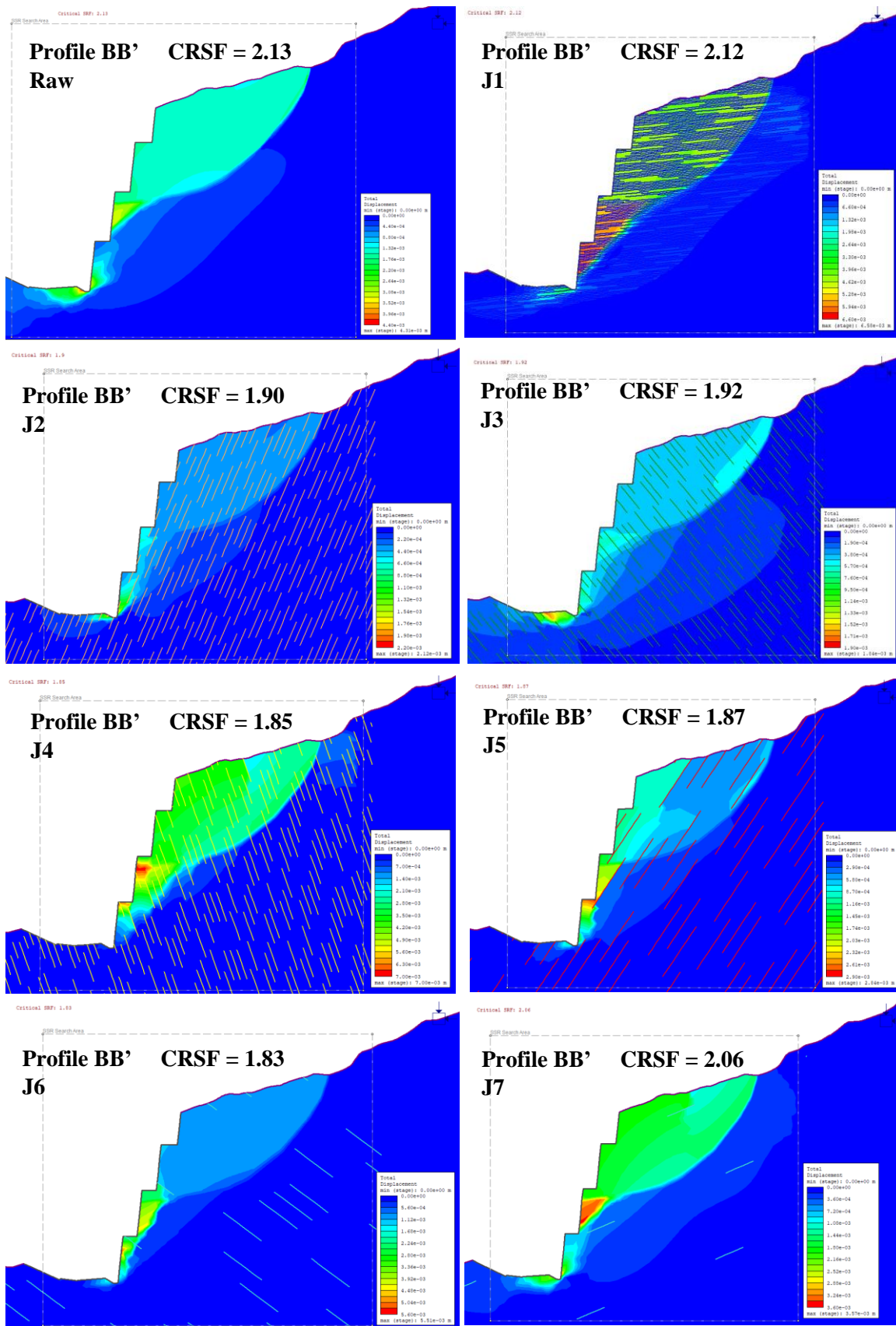


Figure 6.19: The influence on CRSF for profile AA' by the different discontinuity sets.

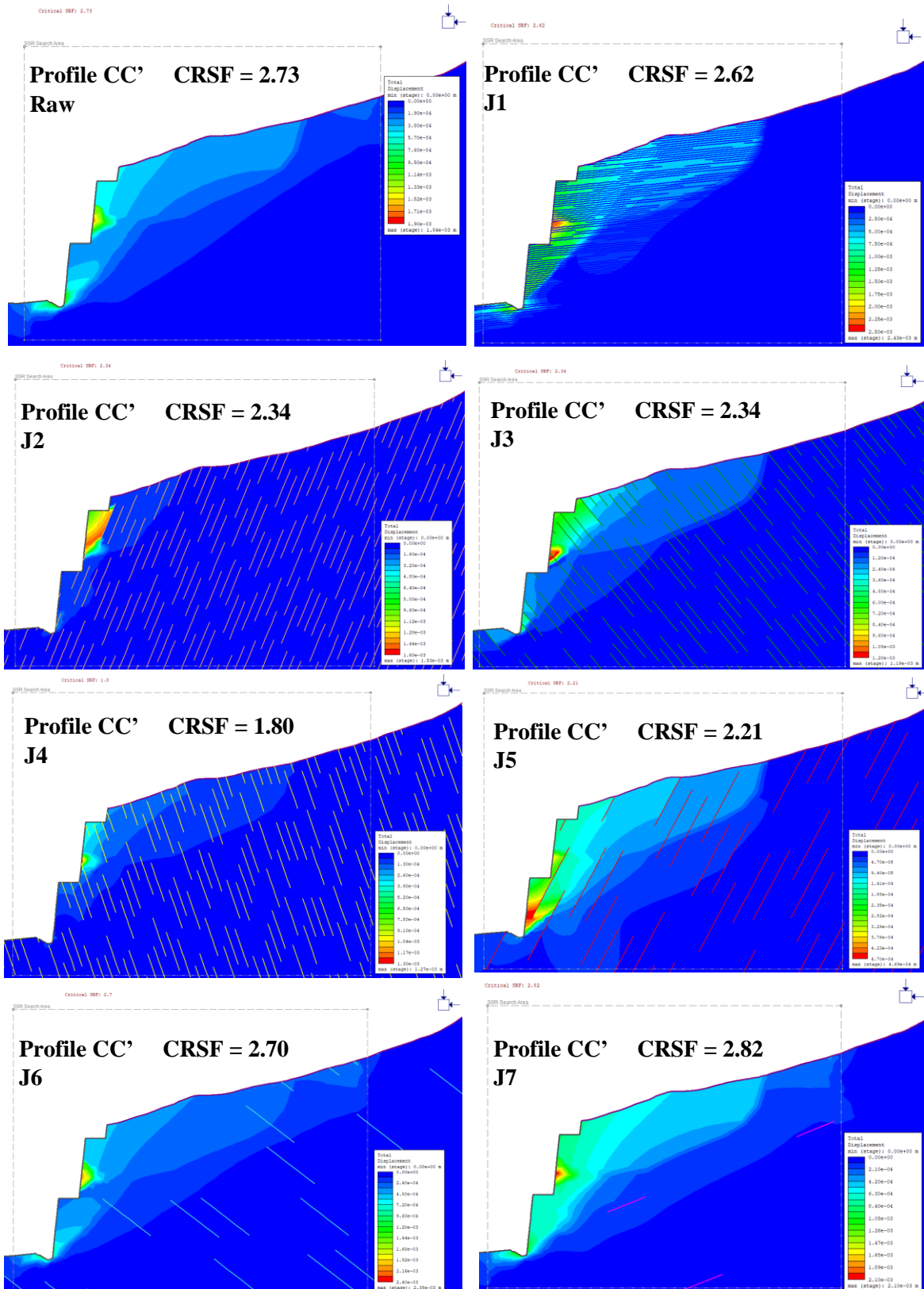


Figure 6.20: The influence on CRSF for profile AA' by the different discontinuity sets.

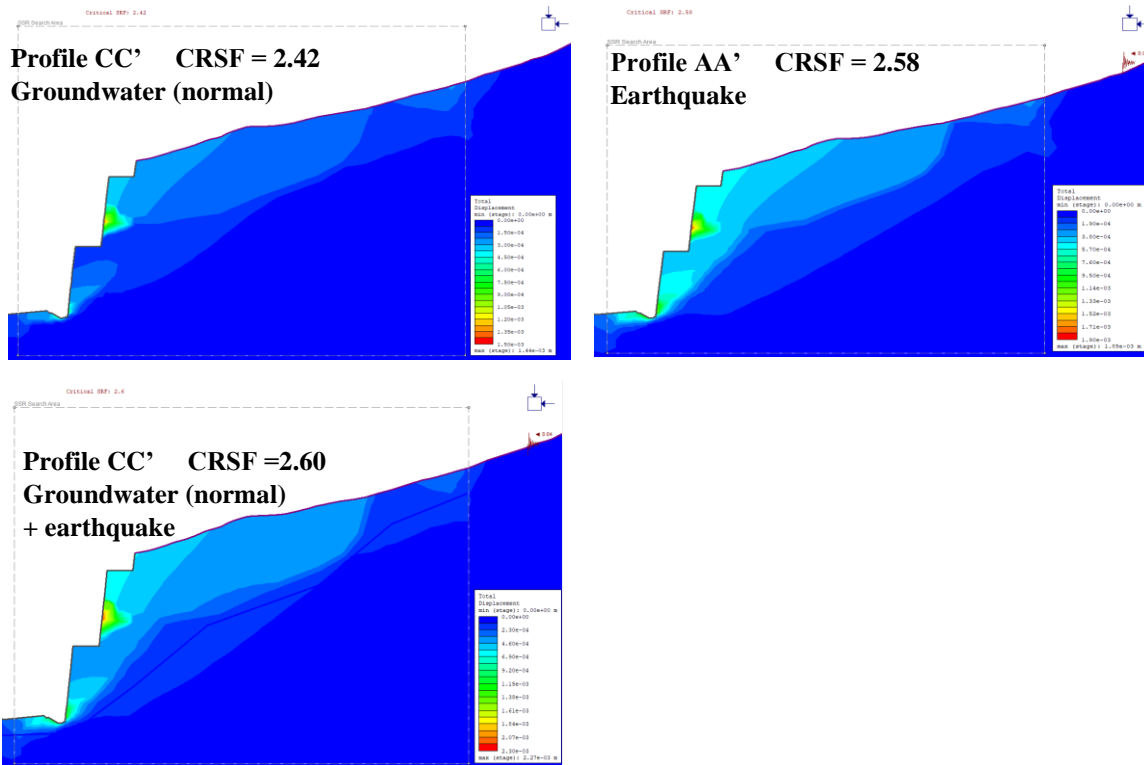


Figure 6.21: Groundwater and seismic event by earthquake effect on CRSF for profile AA' and BB'.

### 6.3.7 Stability measures

The stability measures installed for the road cut differs some for profile AA' compared to profile BB' and CC'. At profile AA' a combination of spilingbolts and CT-bolts were sufficient to acheive a CRSF > 1.5. However, at profile BB' and CC' cable bolts were nessarcy to secure and stabilize the crushed zone. Plain strand cables with standard values given RS2 were used, as illustrated in Table 6.10. However, de-bonded cable bolts could also be a good option to as they allow for more deformation to occur. The high stiffness of cable bolts is one of their main disadvantages (Li, 2018).

Table 6.9: Cable parameters.

Parameter	Plain strand cable	Unit
Borehole diamter	48	mm
Cable diamter	19	mm
Cable modulus	200000	MPa
Cable peak	0.1	MN
Out-of-plane spacing	1.5	M
Water cement ratio	0.35	-

Bolts of the the type CT-bolt M20 have been used for most of the walls. CT-bolts are often installed for subsea tunnels due its double corrosion protection and long lifetime (VIK Ørsta, 2022). They can be delivered with a length up to 8 m but only 6 m long bolts have been used as lengths longer than this are hard to handle during installation (Stefanussen, 2017). Bolts of the the type spillingbolt Ø32 have been used in the floor and is delivied at lengths of 6 or 8 m. They are typically used at tunnelopenings and tunnel portals to secure poor rock masses. These are also double corrosion protected (Pretec, 2016). Spilling bolts of 6 and 8 m have been used, as it is considered easier to install bolts in the floor compared to the walls. Furthermore, bolts of 12 m have also been installed at some of the excavation stages for profile BB' and CC'. They are for simplisitc reasons modelled as spilling bolts (which does not exist at that length) but are meant to represent Ischebeck self drilling rock anchors which are threaded. This means coupling of addional bars are possible (Ischebeck Titan, 2021). The rock bolts parameters are listed in Table 6.10.

Table 6.10: Rock bolt parameters.

<b>Parameter</b>	<b>CT-bolt M20</b>	<b>Spilingbolt Ø32</b>	<b>Unit</b>
Bolt diameter	20	32	mm
Bolt modulus, E	200000	200000	MPa
Tensile capacity	0.188	0.482	MN
Residual tensile capacity	0.157	0.402	MN
Out-of-plane spacing	1.5	1.5	m

Geosynthetics was installed at the crushed zone and for the surround rock mass. It is typically installed for reinforcement and stabilization of soils but can also be used for weak rock masses. However, extensive grouting of the crushed zone at the intersections of the road cut is likely the best possible method to stabilize it long term. It should also be combined with the installation of weep drains in the surrounding road cut face. It should be noted that grouting of weakness zones in RS2 is hard to model, thus the mentioned alternative was used. Furthermore, it was only installed for profile BB' as bolts were sufficient to secure the weakness zone in profile CC'. A standard type of geosynthetics listed in RS2 was used, called ACEGrid GG 1000\_I, and the parameters for it are shown in Table 6.11. Different types of shotcretes (both regular and reinforced) were also tested but were not sufficient to stabilize the crushed zone.

Table 6.11: Geosynthetics (reinforcement) parameters.

<b>Parameter</b>	<b>ACEGrid GG 1000_I</b>	<b>Unit</b>
Tensiel modulus	6.15385	MN/m
Ultimate tensile strength	1	MN/m
Long term design strength	0.635	MN/m

Clean up of the road cut during construction is also an important stability measure. Furthermore, ice nets and wire meshing will also be important to install to reduce icing, flaking, ravelling, and rock fall (Nicholson & Hencher, 1997). At some sections reinforced concrete may be used to secure smaller section with weak rock mass. Extensive protection measures should also be installed from around profile 16200-16500 as the natural rock slope is very steep ( $\sim 80^\circ$  some places) there. The overhanging cliffs and terrain are potential release areas for rock fall, soil and snow avalanches, as seen by the steepness and susceptibility maps found in Appendix E. NPRA (2018) states that a road cut should be built in such a way that there is no risk of rock or ice fall on the road. It should also be constructed such that new cleaning and implementation of stabilization measures are not needed within the first 20 years.

The installation plan for the stability measures at the different excavation stages for the profiles are presented in Table 6.12 and Table 6.13. The excavation stages and the corresponding installation stages for the stability measures are also illustrated in the RS2 models which can be found in Appendix N.

The angle of the bolts are set to be roughly  $30\text{-}50^\circ$  to the planes of weakness (NPRA, 2020). This is primarily done regarding the foliation and the crushed zone. However, at some sections this was not possible, but lower intersection angles were still strived for. This was particularly important for the cable bolts that intersected the crushed zone. If they had been installed close to normal the crushed zone they would have little stabilizing effects. Cable bolts have high tensile capacity but does not handle shear movements too well.

Table 6.12: Stability measures installed at the different excavation stages for profile CC'.

Stage	Stability measure	Description
<i>Profile CC'</i>		
0	3 x cable bolt, L = 20 m, c/c = 3 m, $-50^\circ$ HP, <b>P</b>	Above the road cut, 1 of the cable bolts will only be installed temporary
1	2 x CT-bolt, L = 6 m, c/c = 3 m, $-20^\circ$ HP, <b>P</b> 2 x cable bolt, L = 18 m, c/c = 1 m, $-40^\circ$ HP, <b>P</b> 2 x Ischebeck anchor*, L = 12 m, c/c = 2 m, $-70^\circ$ HP, <b>P</b>	
2	3 x spilingbolt, L = 8 m, c/c = 2 m, $-50^\circ$ HP, <b>P</b>	
3	3 x CT-bolt, L = 6 m, c/c = 1.5 m, $-20^\circ$ HP, <b>P</b> 1 x spillingbolt, L = 8 m, $-60^\circ$ HP, <b>P</b>	Installed at the wall in the direction of the crushed zone
4	7 x CT-bolt, L = 6 m, c/c = 1 m, $-20^\circ$ HP, <b>P</b>	
5	2 x CT-bolt, L = 6 m, c/c = 2 m, $-20^\circ$ HP, <b>P</b>	
6	3 x CT-bolt, L = 6 m, c/c = 2 m, $-20^\circ$ HP, <b>P</b>	
7	2 x CT-bolt, L = 6 m, c/c = 2 m, $0^\circ$ HP, <b>P</b>	
8	4 x CT-bolt, L = 6 m, c/c = 1.5 m, $0^\circ$ HP, <b>P</b>	

L = length, c/c = centre/centre in-plane spacing, HP = from horizontal plane, **P** = permanent rock support, **T** = temporary rock support, Ischebeck anchor\* is modelled as spiling bolts in RS2.

Table 6.13: Stability measures installed at the different excavation stages for profile AA' and BB'.

Stage	Stability measure	Description
<b>Profile AA'</b>		
0	2 x spilingbolt, L = 6 m, c/c = 5 m, +10° HP, <b>P</b> 2 x CT-bolt, L = 3 m, c/c = 4m, -20° HP, <b>P</b>	Installed in terrain above the road cut First bolt at the top of the road cut
1	2 x CT-bolt, L = 6 m, c/c = 3 m, 0° HP, <b>P</b> 3 x CT-bolt, L = 3 m, c/c = 3 m, -20° HP, <b>P</b>	
2	3 x CT-bolt, L = 6 m, c/c = 3 m, 0° HP, <b>P</b> 3 x CT-bolt, L = 3 m, c/c = 3 m, -20° HP, <b>P</b>	
3	3 x CT-bolt, L = 6 m, c/c = 3 m, 0° HP, <b>P</b> 3 x CT-bolt, L = 3 m, c/c = 3 m, -20° HP, <b>P</b> 2 x CT-bolt, L = 6 m, c/c = 2 m, -20° HP, <b>P</b>	At the bottom of road cut
<b>Profile BB'</b>		
0	5 x spilingbolt, L = 8 m, c/c = 4 m, -30° HP, <b>P</b> 2 x spilingbolt, L = 6, c/c = 1 m, -20° HP, <b>T</b>	Installed in terrain above the road cut  At the sliding surface (65 masl. ) which is likely the crushed zone
1	2 x CT-bolt, L = 6 m, c/c = 3 m, +20° HP, <b>P</b>	
2	2 x CT-bolt, L = 6 m, c/c = 3 m, +20° HP, <b>P</b> 3 x cable bolt, L = 30 m, c/c = 2m, -30° HP, <b>P</b>	Installed in the direction of the crushed zone
3	2 x CT-bolt, L = 6 m, c/c = 3 m, -20° HP, <b>P</b> 2 x cable bolts, L = 30 m, c/c = 30 m, -25° HP, <b>T</b>	
4	3 x Ischebeck anchor*, L = 12 m, c/c = 1.5 m, -60° HP, <b>T</b>	
5	2 x CT-bolt, L = 6 m, c/c = 3 m, -20° HP, <b>P</b> 2 x cable bolt, L = 25 m, c/c = 2 m, -20° HP, <b>P</b> 3 x Ischebeck anchor*, L = 12 m, c/c = 1.5m, -60° HP, <b>T</b> 3 x Ischebeck anchor* , L = 12 m, c/c = 1.5m, -50° HP, <b>T</b>	1 of the Ischebeck anchos will be located at final slope face, and will be permanent rock support
6	4 x spilingbolt, L = 8 m, c/c = 1.5 m, -60° HP, <b>T</b>	
7	4 x spilingbolt, L = 8 m, c/c = 2 m, -50° HP, <b>T</b>	
8	3 x spilingbolt, L = 8 m, c/c = 2 m, -40° HP, <b>T</b> 5 x spilingbolt, L = 8m, c/c = 1 m, -30° HP, <b>P</b>	
9	-	Excavation through the first section of the crushed zone
10	8 x CT-bolt, L = 6 m, c/c = 1 m, -20° HP, <b>P</b> Geosyntetecics	
11	3 x CT-bolt, L = 6 m, c/c = 2 m, -20° HP, <b>P</b>	
12	3 x CT-bolt, L = 6 m, c/c = 2 m, -20° HP, <b>P</b>	
13	2 x CT-bolt, L = 6 m, c/c = 2 m, -20° HP, <b>P</b>	
14	3 x CT-bolt, L = 6 m, c/c = 2 m, -20° HP, <b>P</b> 1 x CT-bolt, L = 1m, 20° HP, <b>P</b>	Near the bottom of the road cut

L = length, c/c = centre/centre in-plane spacing, HP = from horizontal plane, **P** = permanent rock support, **T** = temporary rock support, Ischebeck anchor\* is modelled as spilingbolt in RS2.



### 6.3.8 Results

Profile AA' was tested with the discontinuity sets J1, J2, J4, and J5 which was the most representative based on the earlier investigations done in Subsection 5.3.2. Furthermore, the lowest variant of groundwater table was used (normal case), and groundwater was included for profile BB' and CC' too. Profile BB' was tested with the combination of J1, J2, J3, J5, and J6. J4 was not included as it is variation of J3. J7 was also ignored as it did not destabilize the slope and had very low dominance (high spacing and low persistence). The combination of J1, J2, J3, and J5 were tested for profile CC'. J6 was not included as it was mainly observed near the area which profile BB' intersects. All the models also included horizontal loading from seismic events (earthquake) in the final stage.

The results show that 1004 joint elements and 161 mesh elements yielded at  $CSRF = 1.61$  for profile AA'. The yielded joints elements are represented as red/orange lines in Figure 6.22 (a). Furthermore, the concentration of the yielding is in the toe and lower part the road cut. The total displacement is almost equal at the entire slope face, as seen in Figure 6.22 (b).

For profile BB' 877 mesh elements and 3641 joint elements yielded  $CSRF = 1.8$ . The entire crushed zone yielded along with high concentration of yielding in the toe of the road cut, as illustrated in Figure 6.23 (b). The total displacement is also the highest in toe, but it evident that failure occurs along J5 (red line) which are steep dipping out of the slope, as seen in Figure 6.23 (a).

The results from profile CC' has similarities with profile BB', high concentration of yielding in the toe and the entire crushed zone. 775 mesh elements and 1567 joint elements yielded at  $CSRF = 2.33$  (Figure 6.24 (b)). The total displacement was more similar in values along the road cut face for profile CC' compared to profile BB'. However, the total displacement is also in this case defined by J4 as possible failure surface.

Evaluation of maximum shear strain for the profiles gave no indications of instabilities or useful information, as the shear strain was almost uniform throughout the entire models. This is likely a result the stability measures which reduces the shear in rock body and also effects the natural failure boundary for the slope.

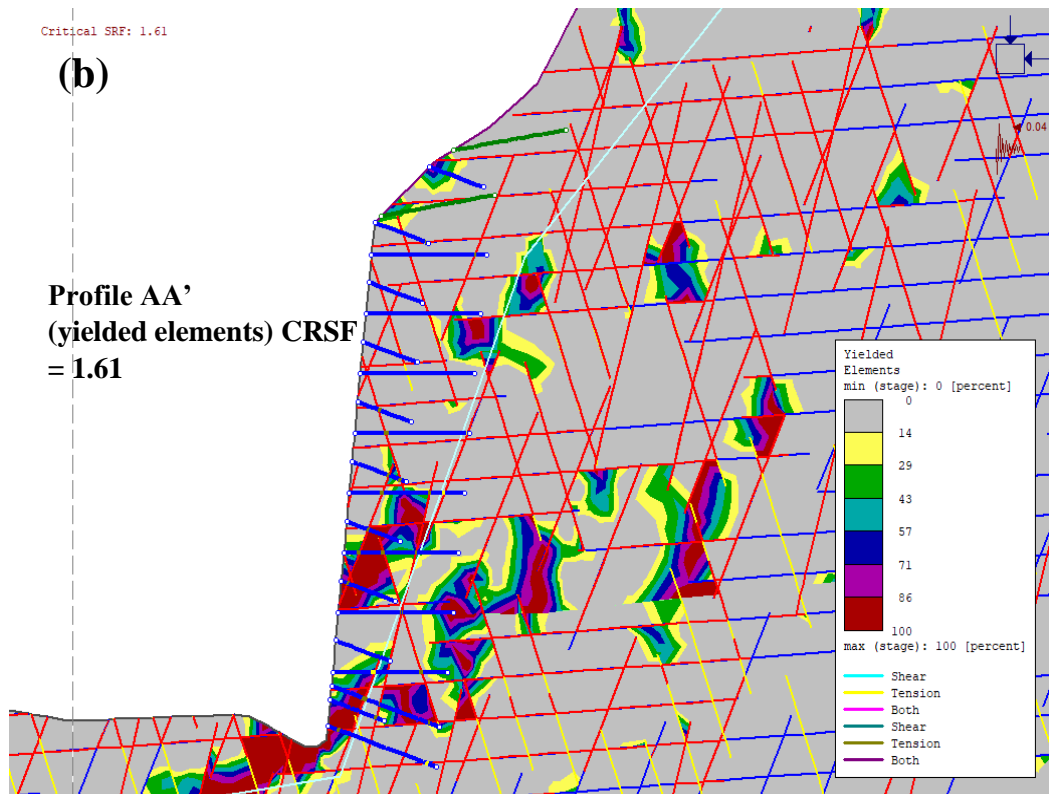
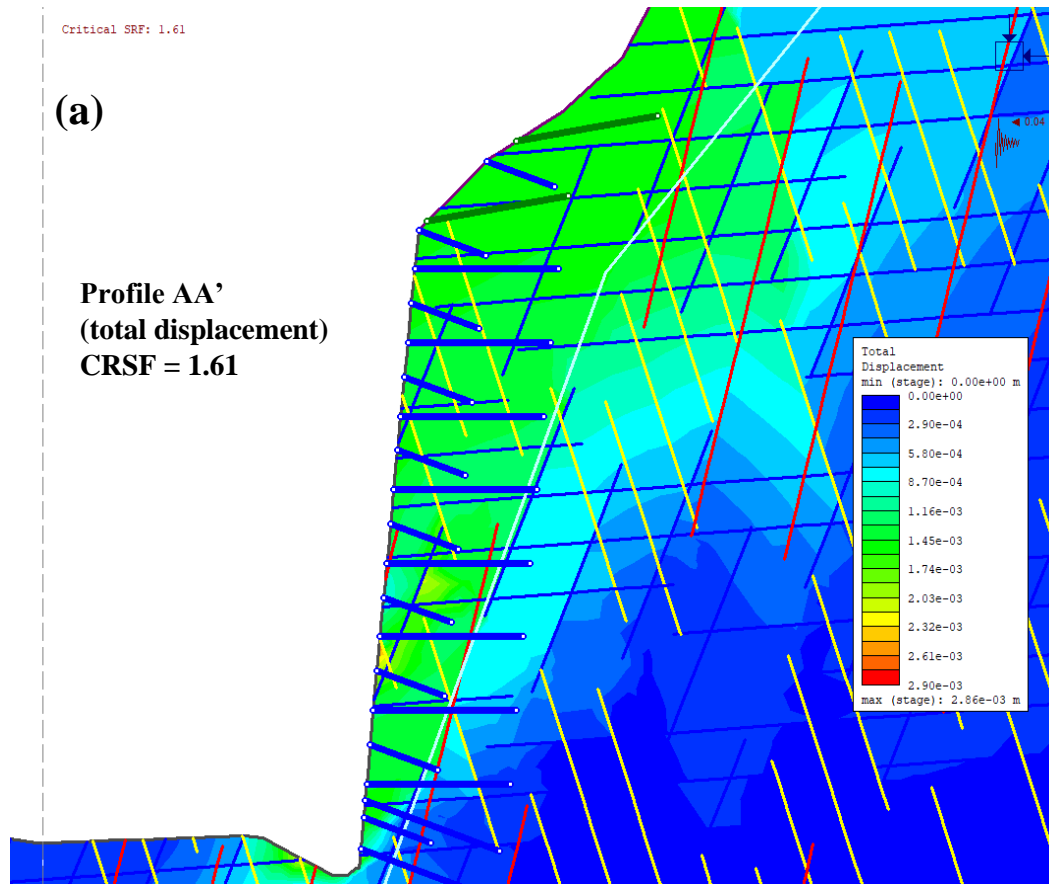


Figure 6.22: Results from profile AA'; (a) total displacement; and (b) yielded elements.

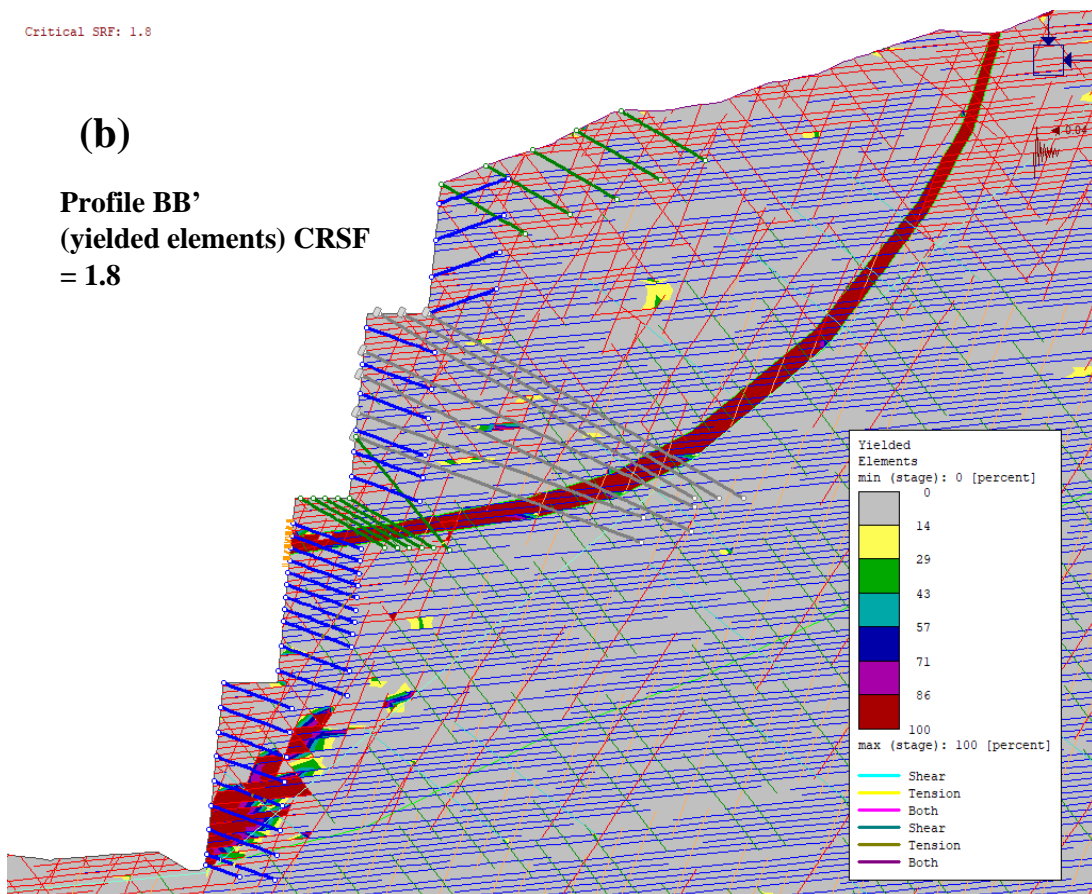
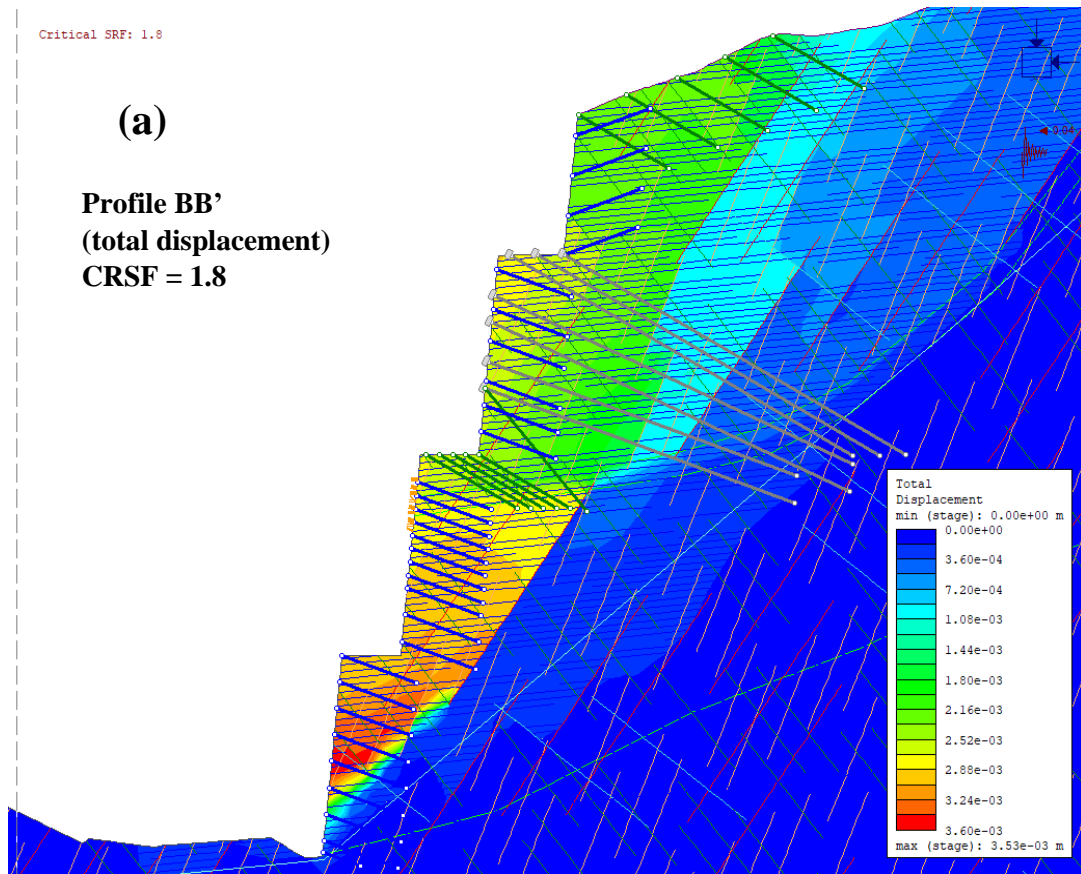


Figure 6.23: Results from profile BB'; (a) total displacement; and (b) yielded elements.

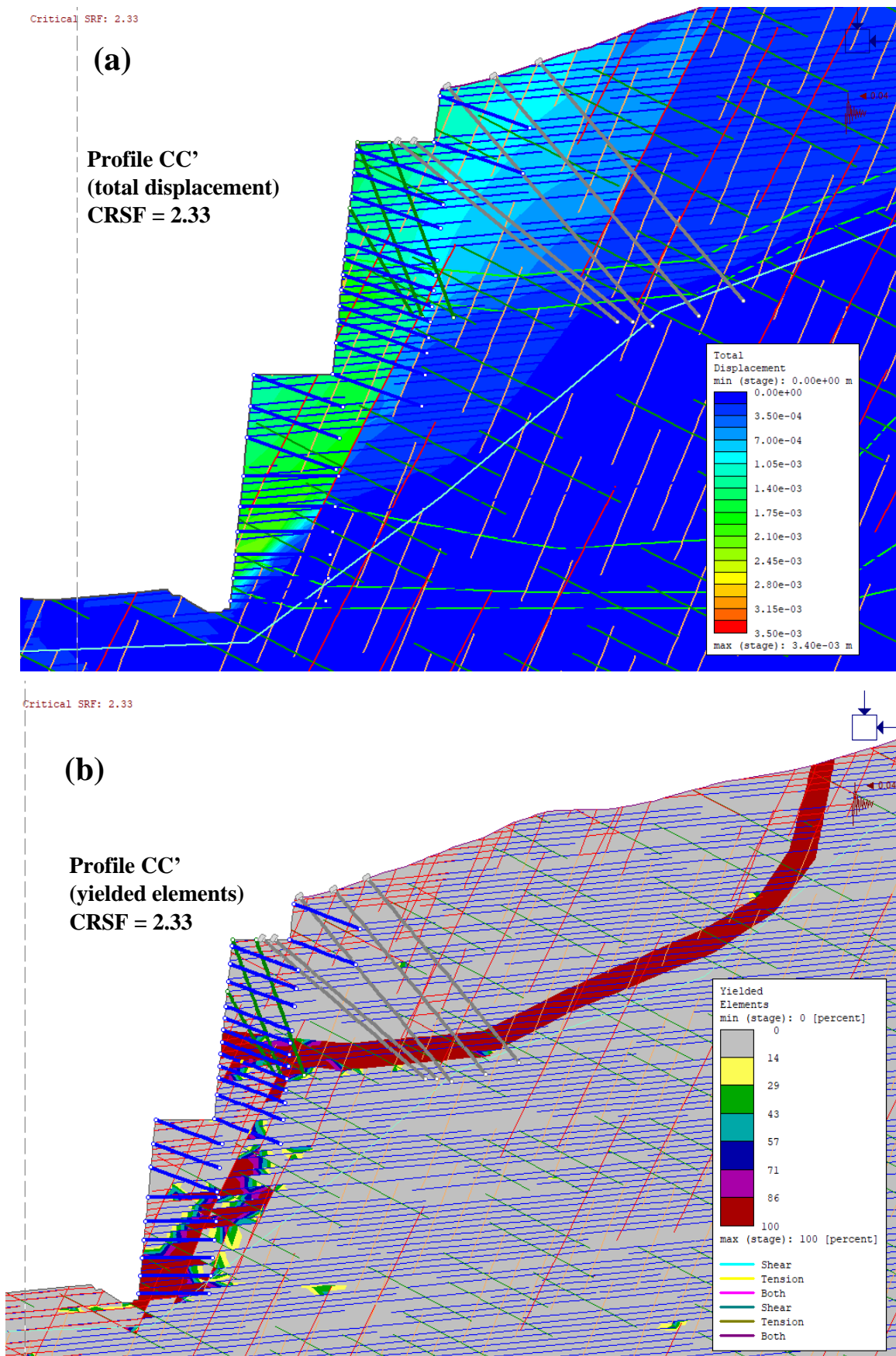


Figure 6.24: Results from profile CC'; (a) total displacement; and (b) yielded elements.

# 7 Discussions

This chapter will present a brief discussion of some relevant topics.

## 7.1 Evaluation of discontinuity sets

Different methods have been used to evaluate the discontinuity sets in the project area. The author has evaluated them based on the use of DSE (from point clouds) and orientation measurements from cores while Multiconsult Norge AS (2019a) has evaluated them from field mapping of the study area. The results from the different methods are presented in Table 7.1. The different discontinuity sets are sorted to be aligned with the discontinuity sets mapped with DSE from the current road cut. There are some clear trends in the mapped discontinuities. The foliation L mapped by Multiconsult corresponds with the foliation J1 mapped in DSE (current road). J2 for DSE (construction road) is likely the foliation too. Its dip direction is orientated more north, but the orientation of the foliation is likely affected by the terrain surface. The orientation of foliation is likely to be orientated almost parallel to the slope face. This is due to the rocks sedimentary origin with deposition events creating the foliation. This is likely as it is J3, J4, and J6 for DSE (current road cut) have similar orientations and could be classified as a single discontinuity set.

Table 7.1: Different methods used to evaluate the discontinuity sets at the project area. The orientation is dip dir./dip.

DSE (current road cut)	DSE (construction road)	Field mapping (profile 16100 – 16500)	Field mapping (profile 16600)	Core logging
J1	254°/35°	L	160-240°/ 25-55°	J1 198°/17°
J2	269°/68°	J2	310°/44°	C 265°/40-70°
J3	141°/64°	J3	135°/71°	3M 251°/82°
J4	106°/72°	J5	101°/90°	B 100-140°/55-80°
J5	356°/88°	J1	343°/71°	A 300-330°/60-85°
J6	076°/39°	J4	058°/74°	2M 352°/88°
J7	193°/61°			

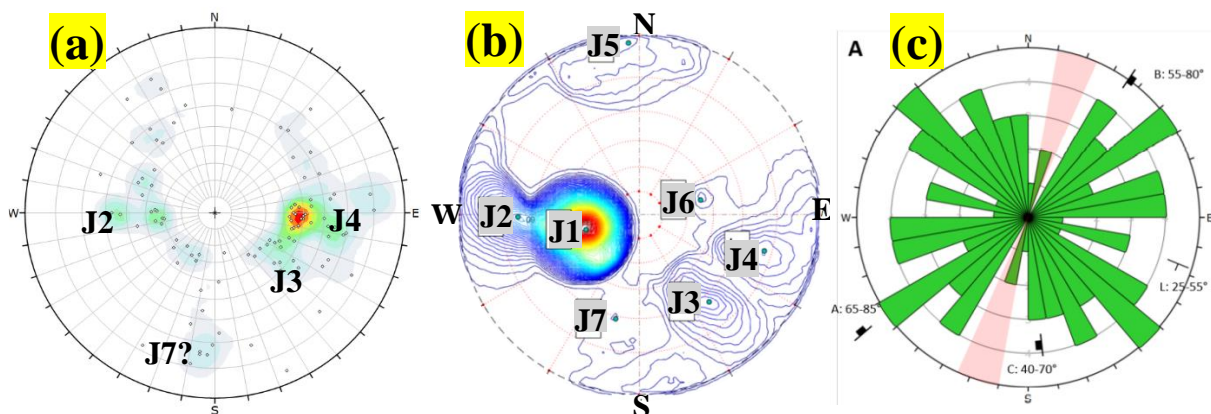


Figure 7.1: (a) Core logging with reduced bedding dominance filter turned on; (b) DSE from the current road cut; and (c) field mapping from Multiconsult Norge AS (2019a)

## 7.2 Uncertainties in the stability assessment

There are two types of uncertainty: epistemic and aleatory. Epistemic uncertainty is related to the lack of fundamental knowledge. In the context of engineering geology this is often related to the rock mass conditions. However, epistemic uncertainty can be reduced by extensive and systematic site/ground investigations. It was also be reduced during the construction itself as more information is gathered. On the other side, aleatory uncertainty is more related to chance, and is more inherently difficult to reduce. An example of this can be predicting when an earthquake will occur or the variability in fracture density. Both aleatory and epistemic uncertainties are unavoidable in any rock engineering project. They will both be reduced when the construction or excavation proceeds (Wyllie, 2018).

Wyllie (2018) lists six important factors that should be considered for stability assessments in engineering geology. They are particularly relevant for numerical modelling:

1. Representative stress-strain relations, and behaviour from peak to residual strengths
2. Anisotropy
3. Variable pore pressure distributions
4. Heterogeneity from variation of material properties with depth, layers and/or discontinuities
5. Influence of virgin rock stresses (in situ stresses)
6. Staging excavation sequence

(1) The rock types are assumed to be elastic-brittle. However, there are some uncertainties around the crushed zone. It has been modelled as a continuous rock mass but, it is possible it is discontinuities and connected by rock bridges. From the core logging it was also evident that were some significant variations in RQD and JRC values for crushed zone at the different boreholes. This means that modelled crushed zone can be either over or underrepresented in terms strength etc. The Poisson's ratio was set to 0.313 for both the metagreywacke and the weak metagreywacke (representing the crushed zone) but the latter could probably be adjusted.

(2) Anisotropy was not modelled directly into the material properties in RS2. The metagreywacke was classified as highly anisotropic from the laboratory investigations. However, it assumed that the overall anisotropy of the rock body is represented through the different discontinuity sets. Introducing the anisotropy directly as a material property would probably be difficult in the case of the folded and complex geology at the road cut. It is also high likelihood that it would only result in a misrepresentation for the overall rock body.

(3) Groundwater measurements have not been done, and the assumed groundwater table for the different profiles are highly uncertain. They are however set based on the basic concept from the literature and fields observations done by Multiconsult Norge AS previously. However, it is possible (and probably likely) that it deviates from the reality.

- (4) Heterogeneity in the material properties due to depth, layers, and discontinuities were integrated into the models in RS2 to some degree. The crushed zone was modelled as its own material, and the material boundaries close to boreholes is probably a decent representation of reality. However, the material boundaries further away highly uncertain.
- (5) The virgin stresses were ignored, and it was assumed only gravitational stresses. This was done due to the lack of relevant measurements in the area. This is likely a misrepresentation of reality as the planned road cut will be excavated into the bottom of the Svartløftberga (the ridge there). The major horizontal stress is likely orientated NE-SW which is parallel to the direction of the ridge.
- (6) Staging effects from the excavation sequence were also ignored. It was assumed that any stress relief and displacement will occur before stability measures are installed or a new excavation stage is started. Staging effects is often more important for open mine slopes due to removal of more overburden.

### **7.3 Stability assessments**

The utilized methods to perform the stability assessments for the planned road cut covers the overall (total) and detail (local) stability of the final slope configuration.

The kinematic analysis gave a good indication of the detail stability for planned road cut. It was evident that block toppling is the most likely failure mechanism, with 40.60%, 39.73%, and 38.07% critical intersections from the base plane of profile AA', BB', and CC' respectively. The slope angle is quite steep, and the foliation (J1) is with the mean orientation of  $198^{\circ}/17^{\circ}$  (dip dir./dip) means the intersection between the foliation and slope face may define potential blocks prone to toppling. Furthermore, the wedge sliding was also prominent as a failure mechanism for the profiles. The percentage of critical intersections was 17.06% for profile AA', 14.51% for profile BB', and 12.03% for profile CC'. All which are quite high. The percentage of planar sliding as failure mechanics is also quite high with 10.70% for profile AA', 9.83% for profile BB', 8.97% for profile CC'. It is likely that the intersection of either J2 or J5 with the foliation, will result in potential unstable wedges or blocks. Figure 7.2 illustrates the intersection of J3 (green), J5 (red), and J6 (dark) at the planned road cut near profile BB' and CC'. It gives an indication of possible wedges or block that can occur during the excavation phase.

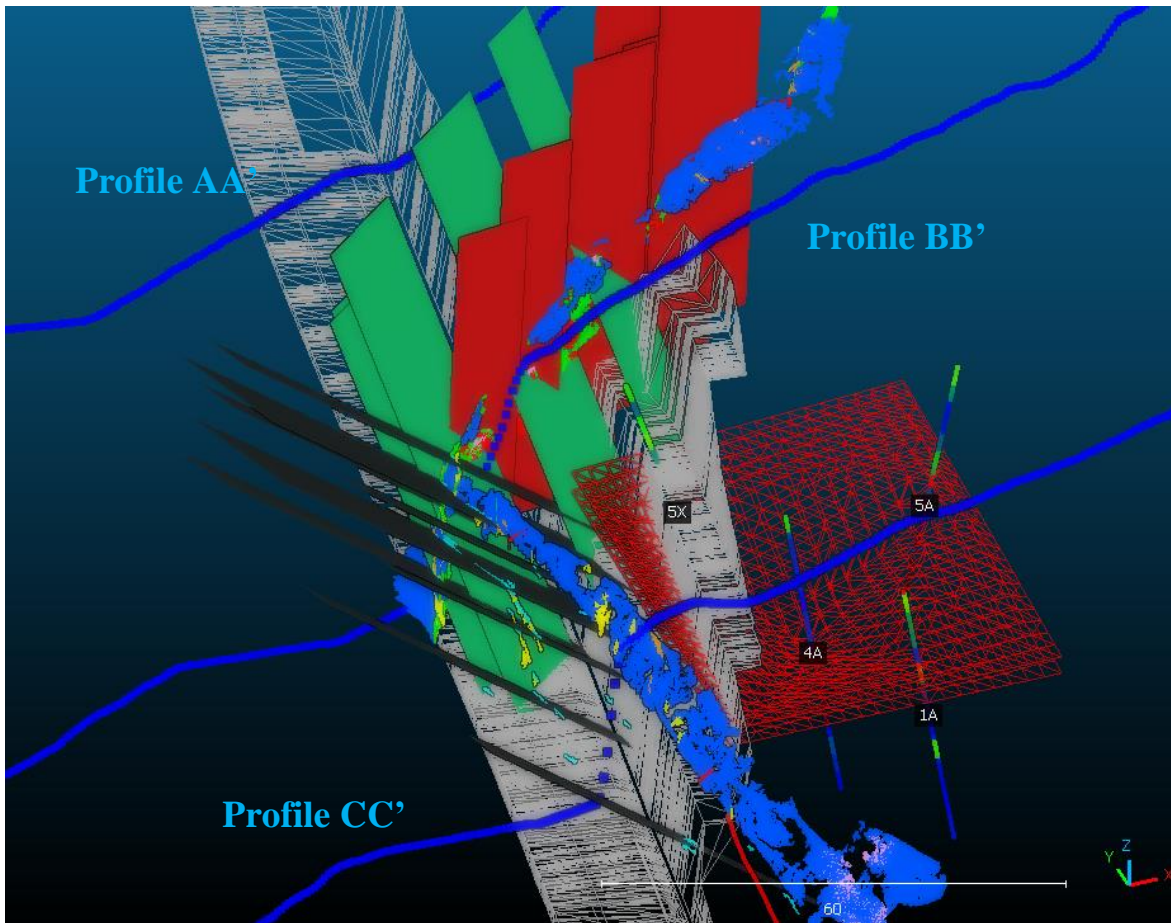


Figure 7.2: 3D model in CloudCompare with extrapolated planes for J3, J5, and J6. Illustrated potential blocks or wedges close to profile AA'.

The results from Q-slope suggested that the steepest stable slope angle  $\beta$  for the overall slope was  $66.0-67.4^\circ$ . However, both profile BB' and CC' exceed it, and have overall slope angles of  $71^\circ$  and  $68^\circ$  respectively. This is likely not a problem as Q-slope is an empirical method and meant to be used in the preliminary stages of a stability evaluation or as a supplementary method to more advanced methods such as numerical modelling. Q-slope is also sufficient for open pit slopes which do not require any stability measures. Thus, it was also used to evaluate the reinforcement slope angles for the intermediate benches at profile BB' and CC'.

The total stability for profile AA', BB', and CC' were evaluated in RS2 with and without support. The final design for all profiles resulted in CRSF above 1.5. It was calculated to be 1.61 for profile AA', 1.80 for profile BB', and 2.33 profile CC'. Further, adjustment to design could be done but the presented designs should be sufficient based on the extensive modelling.

Q-slope was also used to assess the reinforcement free angle of intermediate benches during the excavation.



## 7.4 Evaluation of used methods

RS2 was used as a software for the numerical modelling of this project. However, it turned out that the integration of multiple discontinuity sets in the models were problematic. RS2 which utilizes FEM, discretizes all the joints and their intersections. This results in a very dense mesh which means complex models and extensive computational time. Some of the models would not even run, and the entire program would shut down. This also explained why the literature was very scarce for modelling of excavated rock slopes which are heavily jointed. The models were simplified by defining a material boundary just outside the SSR search area, as described in Subsection 6.3.1. Joints were only assigned within that area and not whole area. The models with only one discontinuity set introduced converged most of the times. However, the difficulties started when two or more discontinuity sets were introduced. In most of the cases small wedges/blocks was created near the surface by the intersecting discontinuities. This would then cause the models to not being able to converge, thus the calculations were not able find a CSRF. An example of a non-converging model is illustrated in Figure 7.3.

The jointed rock mass was easier to handle in the second stage of the numerical modelling when stability measures were introduces. The bolts would secure the rock mass (as intended) but also make the model being able to converge. In some instances, particularly for profile AA' which located steep terrain with an overhanging cliff (up to 80°) above the planned road cut, wedges/blocks were created in the slope above the road cut. The profiles are intended to evaluate the stability of the planned road cut and not parts of the model far away. The best solution to problem was to ungroup the joints. Then manually inspect the joints for potential unstable wedges/block and remove the joints that defined them.

RS2 also supports XFEM (extended finite element method) which is essence means that the FEM mesh does not need to track the joints paths, and the mesh is assigned separately to the joints. It was tested but did not work any better than FEM in this case. UDEC which is a DEM (distinct-element method) would probably work well for a project like this. It was planned to be used but was not done due to time constrains.

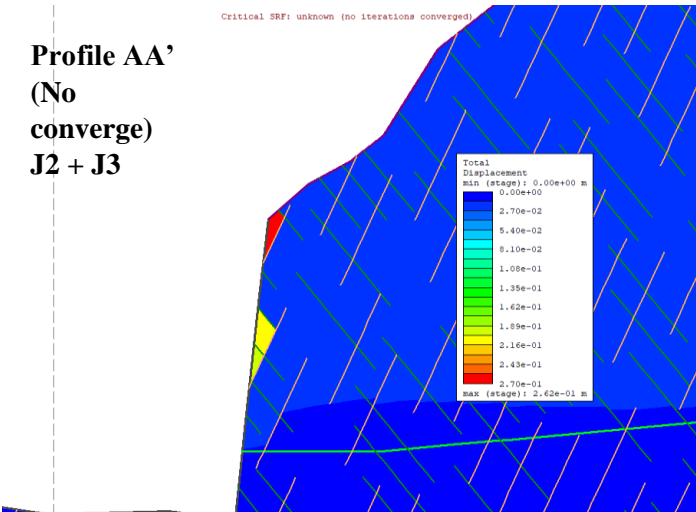


Figure 7.3: Model with J2 and J3 tested for profile AA'. The model did not converge at it is evident that the small wedges/blocks near the surface was the problem.

## 8 Conclusions and recommendations

This chapter will summarize the main findings for this thesis and give further recommendations.

### 8.1 Main findings

In this MSc thesis selected stability assessment methods have been used to evaluate the planned road cut at Hommelvik which is part of the E6 Ranheim – Værnes highway project. Geological mapping, laboratory investigations of rock mechanical and shear strength properties, core logging, and numerical modelling have been performed to evaluate the stability and establish reliable models. Furthermore, it has been important to perform a comprehensive assessment of the discontinuities and evaluate any potential weakness zones which might influence the stability of the road cut. The main findings are as follows:

- The steepest stable slope angle  $\beta$  for the overall slope of is calculated to be 66.0-67.4° from Q-slope. This is slightly lower than 71° and 68° which profile BB' and CC' are designed for respectively.
- Kinematic analysis shows that block toppling is the most likely failure mechanism to occur for section between profile BB' and CC'. The percentage of critical intersection for wedge failure is also quite high.
- Numerical modelling of slopes in jointed rock masses in RS2 is time consuming and requires the user to identify potential unstable small wedges and blocks before running the models. The joints defining the wedge or block must then be removed manually.
- Discontinuity Set Extractor (DSE) was utilized to semi-automatically extract discontinuities from points clouds. There are four main discontinuities sets and seven different discontinuities around the current road, given the different local variations of them are included.
- Semi-automatic extract of discontinuities reduces personal bias when defining the discontinuities, increases accessibility to discontinuities which would be out of reach in the field, achieves a quantitative weighting of the dominance of the different discontinuity sets, and allows for mapping of discontinuities over larger areas. It is less time intensive compared to manual field mapping and makes visualization of the discontinuities easier compared to pol or rosette pots (and regular pictures).

- The discontinuity sets from DSE can be integrated into 3D environment such as CloudCompare. This means other 3D data formats which are often used to represent the geometry of the excavation or road can be evaluated with along it.
- A crushed zone located under the current road cut and intersecting all the four boreholes was identified during the core logging. It was measured to be 0.5-3.0 m thick and with RDQ-values between 0-28. The geometry of it was extrapolated from Slide3, and it was evaluated against a potential sliding plane observed at profile 16160 which is parallel to the foliation, a depression located around 20-30 m east for borehole 5A, and a discontinuity (contained some crushed rock mass) observed at the southern part of the current road which was assumed to be the crushed zone. These surfaces were aligned to assess the geometry and extent of the crushed zone. The 3D models showed that it will likely daylight (intersect) the planned road cut at around 25 m above the trench bottom and stretch for around 50 m along the entire section of the bench at sub-horizontal angle. A rough estimation of the volume encapsulated by the crushed zone was calculated to be around 150 000 m<sup>3</sup>. It should be noted that it is possible that evaluated crushed zone is in fact two or more crushed zones which intersected boreholes with similar orientations. This could indicate that they are also connected to the depressions located further east in the terrain as all these depressions have similar form. However, a single continuous crushed zone was assumed as the worst-case scenario. If a slope configuration with implemented stability measures is stable in that scenario, it will be likely be stable for the real conditions which may be better.
- The depth the crushed zone combined with its likely curved geometry makes it difficult to secure and stabilize by bolts (or cable bolts). It is likely curved at an angle which makes securing it from the top of the terrain have reduced effect. It will likely be easier to secure it after the first few stages of excavation (total depth around 10 m) as 30 m long cable bolts can be installed there. Bolts and cable bolts should be installed at roughly 30-50° to the planes of weakness for maximum effect. However, any stabilization measures installed from the ground surface pre-excavation would intersect the crushed zone at high angle. Bolts are made to handle a lot of tensile stress but not too much shear stress. The crushed zone can be secured to some degree from the current road cut. However, it is uncertain if it is sufficient as only small part of it will be secured.
- The excavation sequence of profile BB' and CC' will be very complex and challenging.

## 8.2 Suggestions for further work

1. Develop a 3D model and perform slope stability analysis. Slide3 can be a good alternative as it is compatible with Slide2
2. Evaluate key blocks and wedges identified in CloudCompare with Swedge (Rocscience) for detail stability.
3. Carry out a more detailed stability analysis for northern part of the planned road cut (past profile AA').
4. Carry out drilling to identify and further evaluate the geometry of the crushed zone(s). This should be done close to the location of borehole 5A, but the trend of the borehole should be eastward. This should be done to check if the crushed zone is indeed connected to the closest lineament (depression) or if is more deep seated with a gentler angle. It is also possible that mapped crushed zone is more complex.
5. Perform groundwater measurements for Svartløftberga and further check for carbonate rich metagreywacke which can be indicative of potential karst. Test especially the depression located at profile 16160 (between profile AA' and BB').
6. Perform in-situ rock stress measurements such as 3D overcoring. FLAC3D can also be a good option for numerical modelling in 3D of a topographic stresses.

## References

- Aagaard, B. (1981). Ingeniørgeologiske forundersøkelser for E6 i tunnel ved Malvik, Rapport 6834.03. In: Trondheim: A/S Geoteam.
- Abdulai, M., & Sharifzadeh, M. (2019). Uncertainty and reliability analysis of open pit rock slopes: a critical review of methods of analysis. *Geotechnical and Geological Engineering*, 37(3), 1223-1247.
- Abdulai, M., & Sharifzadeh, M. (2021). Probability Methods for Stability Design of Open Pit Rock Slopes: An Overview. *Geosciences*, 11(8), 319.
- Alejano, L., Muralha, J., Ulusay, R., Li, C. C., Pérez-Rey, I., Karakul, H., Chryssanthakis, P., & Aydan, Ö. (2018). ISRM suggested method for determining the basic friction angle of planar rock surfaces by means of tilt tests. *Rock Mechanics and Rock Engineering*, 51(12), 3853-3859.
- Bandis, S., Lumsden, A., & Barton, N. (1981). Experimental studies of scale effects on the shear behaviour of rock joints. *International Journal of Rock Mechanics and Mining Sciences & Geomechanics Abstracts*,
- Bar, N., & Barton, N. (2017). The Q-slope method for rock slope engineering. *Rock Mechanics and Rock Engineering*, 50(12), 3307-3322.
- Bar, N., & Barton, N. (2018). Rock slope design using Q-slope and geophysical survey data. *Periodica Polytechnica Civil Engineering*, 62(4), 893-900.
- Bar, N., Barton, N., & Ryan, C. (2016). Application of the Q-slope method to highly weathered and saprolitic rocks in Far North Queensland. ISRM International Symposium-EUROCK 2016,
- Barla, G. (2016). Applications of numerical methods in tunnelling and underground excavations: Recent trends. ISRM International Symposium-EUROCK 2016,
- Barton, N. (1972). A model study of rock-joint deformation. *International Journal of Rock Mechanics and Mining Sciences & Geomechanics Abstracts*,
- Barton, N. (1973). Review of a new shear-strength criterion for rock joints. *Engineering Geology*, 7(4), 287-332. [https://doi.org/10.1016/0013-7952\(73\)90013-6](https://doi.org/10.1016/0013-7952(73)90013-6)
- Barton, N. (1974). A review of the shear strength of filled discontinuities in rock. *Norwegian Geotechnical Institute Publication*(105).
- Barton, N. (1978). Suggested methods for the quantitative description of discontinuities in rock masses: International Society for Rock Mechanics. *Int J Rock Mech Min Sci Geomech Abstr*, 15, 319-368.
- Barton, N. (2002). Some new Q-value correlations to assist in site characterisation and tunnel design. *International Journal of Rock Mechanics and Mining Sciences*, 39(2), 185-216. [https://doi.org/10.1016/s1365-1609\(02\)00011-4](https://doi.org/10.1016/s1365-1609(02)00011-4)
- Barton, N. (2007). Fracture-induced seismic anisotropy when shearing is involved in production from fractured reservoirs. *Journal of Seismic Exploration*, 16(2), 115.
- Barton, N., & Bandis, S. (1982). Effects of block size on the shear behaviour of jointed rock. 23rd US Symp on rock mechanics. *Berkeley, CA*, 739-760.
- Barton, N., & Bandis, S. (1990). Review of predictive capabilities of JRC-JCS model in engineering practice. Rock Joints-Proceeding of a regional conference of the International Society for Rock Mechanics. *Leon*.
- Barton, N., & Bar, N. (2015). Introducing the Q-slope Method and its Intended use Within Civil and Mining Engineering Projects. ISRM Regional Symposium - EUROCK 2015,

- Barton, N., & Choubey, V. (1977). The shear strength of rock joints in theory and practice. *Rock mechanics*, 10(1), 1-54. <https://doi.org/10.1007/BF01261801>
- Barton, N., Lien, R., & Lunde, J. (1974). Engineering classification of rock masses for the design of tunnel support. *Rock mechanics*, 6(4), 189-236.
- Beavis, F. (1985). Rock weathering. *Engineering Geology*. Blackwell Scientific, Melbourne.
- Belyadi, H., Fathi, E., & Belyadi, F. (2019). *Hydraulic fracturing in unconventional reservoirs: theories, operations, and economic analysis*. Gulf Professional Publishing.
- Bemis, S. P., Micklethwaite, S., Turner, D., James, M. R., Akciz, S., Thiele, S. T., & Bangash, H. A. (2014). Ground-based and UAV-Based photogrammetry: A multi-scale, high-resolution mapping tool for structural geology and paleoseismology. *Journal of Structural Geology*, 69, 163-178. <https://doi.org/https://doi.org/10.1016/j.jsg.2014.10.007>
- Bieniawski, Z. (1973). Engineering classification of jointed rock masses. *Civil Engineering= Siviele Ingenieurswese*, 1973(12), 335-343.
- Bieniawski, Z. (1993). Classification of rock masses for engineering: the RMR system and future trends. In *Rock Testing and Site Characterization* (pp. 553-573). Elsevier.
- Bieniawski, Z., & Bernede, M. (1979). Suggested methods for determining the uniaxial compressive strength and deformability of rock materials: Part 1. Suggested method for determining deformability of rock materials in uniaxial compression. *International Journal of Rock Mechanics and Mining Sciences & Geomechanics Abstracts*,
- Bieniawski, Z. T. (1978). Determining rock mass deformability: experience from case histories. *International Journal of Rock Mechanics and Mining Sciences & Geomechanics Abstracts*,
- Bieniawski, Z. T. (1984). Rock mechanics design in mining and tunneling.
- Bieniawski, Z. T. (1989). *Engineering rock mass classifications: a complete manual for engineers and geologists in mining, civil, and petroleum engineering*. John Wiley & Sons.
- Bjordal, H., Domaas, U., Holmøy, K. H., Moen, K., Farestveit, N., Ebeltoft, R. G., Nilsen, M. W., Larsen, J. O., & Frækaland, S. H. (2011). *Sikring av veger mot steinskred: Grunnlag for veiledning*. V. Oslo: Statens Vegvesen.
- Botsialas, K., Holmøy, K. H., & CardenasMorales, M. O. (2015). *Hazard zonation at the open pit mine Titania as – "old" and new methods for slope stability analysi* Fjellsprengningsteknikk, Bergmekanikk, Geoteknikk,
- Buyer, A., & Schubert, W. (2016). Extraction of discontinuity orientations in point clouds. ISRM International Symposium-EUROCK 2016,
- Cai, M., Kaiser, P., Tasaka, Y., & Minami, M. (2007). Determination of residual strength parameters of jointed rock masses using the GSI system. *International Journal of Rock Mechanics and Mining Sciences*, 44(2), 247-265.
- Call, R. D., & Savely, J. P. (1990). Open pit rock mechanics. *Surface mining*, 2, 860-882.
- Caltrans. (2020). Caltrans Geotechnical Manual. In: Office of Geotechnical Services.
- Caltrans. (2021). Caltrans Geotechnical Manual. In: Office of Geotechnical Services.
- Celada, B., & Bieniawski, Z. (2019). *Ground Characterization and Structural Analyses for Tunnel Design*. CRC Press.
- CEN. (2013). Eurocode 8: Design of structures for earthquake resistance-part 1 - general rules, seismic actions and rules for buildings. European Standard with Norwegian NA, NS-EN 1998-1:2004 + NA:2008. *Standards Norway/Comite' Europe'en de Normalisation*, 171.

- Chen, Z. (1995). Recent developments in slope stability analysis. 8th ISRM Congress,
- Cosgrove, J. W., & Hudson, J. A. (2016). *Structural geology and rock engineering*. World Scientific Publishing Company.
- Dannevig, P., & Harstveit, K. (2021). Klima i Norge. In *Store Norske Leksikon*.
- Deere, D. U. (1963). Technical description of rock cores for engineering purpose. *Felsmekanik und Ingenieurgeologie (Rock Mechanics and Engineering Geology)*, 1(1), 16-22.
- Deere, D. U., Hendron, A. J., Patton, F. D., & Cording, E. J. (1966). Design Of Surface And Near-Surface Construction In Rock. The 8th U.S. Symposium on Rock Mechanics (USRMS), New York.
- Deere, D. U., & Miller, R. (1966). *Engineering classification and index properties for intact rock*.
- Deng, K., & Chen, M. (2021). Blasting excavation and stability control technology for ultra-high steep rock slope of hydropower engineering in China: a review. *European Journal of Remote Sensing*, 54(sup2), 92-106.
- DFØ. (2022). *Nye Veier - pilot på BVP*. The Norwegian Agency for Public and Financial Management.
- Diederichs, M. S., Lato, M., Quinn, P., & Hammah, R. (2007). Shear strength reduction approach for slope stability analyses. 1st Canada-US Rock Mechanics Symposium,
- Duncan, J. M., & Goodman, R. E. (1968). Finite element analysis of slopes in jointed rock.
- Eberhardt, E. (2003). Rock slope stability analysis—utilization of advanced numerical techniques. *Earth and Ocean sciences at UBC*, 41.
- Geonorge. (2016). *Høydedata NDH Malvik-Stjørdal 2pkt 2016*.
- Gilson. (2022). *Type L Schmidt Test Hammers*. Gilson Company inc. Retrieved 25/03/2022 from <https://www.globalgilson.com/schmidt-type-l-test-hammers>
- Gokceoglu, C., Sonmez, H., & Kayabasi, A. (2003). Predicting the deformation moduli of rock masses. *International Journal of Rock Mechanics and Mining Sciences*, 40(5), 701-710.
- Golodkovskaia, G. A., Krasilova, N. S., Ladygin, V. M., & Shaumian, L. V. (1975). Factors controlling solid rock strength. *Bulletin of the International Association of Engineering Geology*, 11(1), 65-69. <https://doi.org/10.1007/bf02635456>
- Goodman, R. E. (1993). *Engineering Geology: Rock in Engineering Construction*. Wiley. <https://books.google.no/books?id=AcFMrgEACAAJ>
- Griffith, A. A. (1921). VI. The phenomena of rupture and flow in solids. *Philosophical transactions of the royal society of london. Series A, containing papers of a mathematical or physical character*, 221(582-593), 163-198.
- Grimstad, E., & Barton, N. (1993). Updating the Q-System for NMT. *Proceedings of the International Symposium on Sprayed Concrete-Modern use of wet mix sprayed concrete for underground support, Fagemes, Oslo, Norwegian Concrete Association, 1993*, 46-66. <https://cir.nii.ac.jp/crid/1571417124873087616>
- Grøneng, G. (2010). Stability analyses of the Åknes rock slope, Western Norway [PhD Thesis].
- Gullikstad, J., & Rønsberg, G. (2019). *Informasjonsmøte: Reguleringsplan E6 - Malvik kommune* <https://www.malvik.kommune.no/getfile.php/4588141.1760.qnkbmsuint7bmm/Pres+Malvik.pdf>
- Hack, R. (2002). An evaluation of slope stability classification. ISRM International Symposium- EUROCK 2002,
- Hammah, R., Yacoub, T., Corkum, B., Wibowo, F., & Curran, J. (2007). Analysis of blocky rock slopes with finite element shear strength reduction analysis. 1st Canada-US Rock Mechanics Symposium,
- Hansen, T. H. (1988). Rock properties *Norwegian Soil and Rock Engineering Association*(5), 41-44.

- Hermanns, R. L., Oppikofer, T., Anda, E., Blikra, L., Böhme, M., Bunkholt, H., Crosta, G., Dahle, H., Devoli, G., & Fischer, L. (2012). Recommended hazard and risk classification system for large unstable rock slopes in Norway. *NGU rapport*, 0800-3416.
- Hestnes, E. (1980). *Evaluation of slide risk*. N. G. Institute.
- Hoek, E. (1994). Strength of rock and rock masse. *International Society for Rock Mechanics News Journal*, 2(2), 4-16.
- Hoek, E. (2007). Practical rock engineering. 2007. *Online. ed. Rocscience*.
- Hoek, E., & Brown, E. T. (1980). Underground Excavations in Rock. *London: Institution of Mining and Metallurgy*, 137.
- Hoek, E., & Brown, E. T. (1997). Practical estimates of rock mass strength. *International Journal of Rock Mechanics and Mining Sciences*, 34(8), 1165-1186.  
[https://doi.org/https://doi.org/10.1016/S1365-1609\(97\)80069-X](https://doi.org/https://doi.org/10.1016/S1365-1609(97)80069-X)
- Hoek, E., & Brown, E. T. (2019). The Hoek–Brown failure criterion and GSI – 2018 edition. *Journal of Rock Mechanics and Geotechnical Engineering*, 11(3), 445-463.  
<https://doi.org/10.1016/j.jrmge.2018.08.001>
- Hoek, E., Carranza-Torres, C., & Corkum, B. (2002). Hoek-Brown failure criterion-2002 edition. *Proceedings of NARMS-Tac*, 1(1), 267-273.
- Hoek, E., Carter, T., & Diederichs, M. (2013). Quantification of the geological strength index chart. 47th US rock mechanics/geomechanics symposium,
- Hoek, E., & Diederichs, M. S. (2006). Empirical estimation of rock mass modulus. *International Journal of Rock Mechanics and Mining Sciences*, 43(2), 203-215.
- Hoek, E., Hutchinson, J., Kalenchuk, K., & Diederichs, M. (2009). Influence of in situ stress on open pit slope design. *Guidelines for open pit slope stability*.
- Huber, M. (2013). *Soil variability and its consequences in geotechnical engineering*. Inst. f. Geotechnik.
- Hudson, J. A., & Harrison, J. P. (2000). *Engineering rock mechanics: an introduction to the principles*. Elsevier.
- Hungr, O., Leroueil, S., & Picarelli, L. (2014). The Varnes classification of landslide types, an update. *Landslides*, 11(2), 167-194. <https://doi.org/10.1007/s10346-013-0436-y>
- Hunt, R. E. (2005). *Geotechnical engineering investigation handbook*. Crc Press.
- IDSR. (2002). *Living with risk: A global review of disaster reduction initiatives Preliminary version*. U. N. Publications. [http://inis.iaea.org/search/search.aspx?orig\\_q=RN:33048155](http://inis.iaea.org/search/search.aspx?orig_q=RN:33048155)
- Ischebeck Titan. (2021). Rock Bolts Brochure. In.
- ISRM. (1975). Terminology. *International Society for Rock Mechanics*.
- ISRM. (1978a). Suggested methods for determining sound velocity. *Int J Rock Mech Min Sci Geomech Abstr*, 15, 53-58.
- ISRM. (1978b). Suggested methods for determining tensile strength of rock materials. *Int J Rock Mech Min Sci Geomech Abstr*, 15(3), 99-103.
- ISRM. (1978c). Suggested methods for determining the strength of rock material in triaxial compression. *Int J Rock Mech Min Sci Geomech Abstr*, 15(2), 47-51.
- ISRM. (1978d). Suggested methods for the quantitative description of discontinuities in rock masses. *Int J Rock Mech Min Sci Geomech Abstr*, 15(6), 319-368.
- ISRM. (1981). Rock characterization, testing and monitoring. 211.
- ISRM. (1985). Suggested method for determining point load strength. *International Journal of Rock Mechanics and Mining Sciences & Geomechanics Abstracts*,



- Jaeger, J. C., Cook, N. G., & Zimmerman, R. (2009). *Fundamentals of rock mechanics*. John Wiley & Sons.
- Jing, L. (2003). A review of techniques, advances and outstanding issues in numerical modelling for rock mechanics and rock engineering. *International Journal of Rock Mechanics and Mining Sciences*, 40(3), 283-353.
- Kliche, C. A. (2018). *Rock slope stability: 2nd edition*. Society for Mining, Metallurgy & Exploration.
- Köken, E., Özarslan, A., & Bacak, G. (2016). Weathering effects on physical properties and material behaviour of granodiorite rocks. ISRM International Symposium-EUROCK 2016,
- Laubscher, D., & Jakubec, J. (2001). The MRMR rock mass classification for jointed rock masses. *Underground Mining Methods: Engineering Fundamentals and International Case Studies*, WA Hustrulid and RL Bullock (eds) Society of Mining Metallurgy and Exploration, SMME, 475-481.
- Lauffer, H. (1958). Gebirgsklassifizierung für den Stollenbau. *Geologie und Bauwesen*, 24(1), 46-51. <https://cir.nii.ac.jp/crid/1571135649588464896>
- Li, A. (2021). Dips Webinar - New features, Applications and Case Studies
- Li, C. C. (2018). *Rock Mechanics: Compendium TGB4210 - Rock and Soil Mechanics, Basic Course*. Department of Geoscience and Petroleum (IGP), Norwegian University of Science and Technology (NTNU).
- Li, Q. M. (2001). Strain energy density failure criterion. *International Journal of Solids and Structures*, 38(38-39), 6997-7013.
- Liu, S., Shao, L., & Li, H. (2015). Slope stability analysis using the limit equilibrium method and two finite element methods. *Computers and Geotechnics*, 63, 291-298.
- Lutro, O. (2005). Berggrunnskart Stjørdal 16211. 1: 50.000. *Norges geologiske undersøkelse, Trondheim*.
- Løset, F. (2006). Norges tunnelgeologi. *Norges Geotekniske Institutt (NGI)*.
- Marinos, P., & Hoek, E. (2001). Estimating the geotechnical properties of heterogeneous rock masses such as flysch. *Bulletin of Engineering Geology and the Environment*, 60(2), 85-92. <https://doi.org/10.1007/s100640000090>
- Marinos, P. G., Marinos, V., & Hoek, E. (2007). THE GEOLOGICAL STRENGTH INDEX (GSI): A CHARACTERIZATION TOOL. Proceedings of the international workshop on rock mass classification in underground mining,
- MET. (2021). *Ny normal i klimaforskningen*. The Norwegian Meteorological Institute. <https://www.met.no/vaer-og-klima/ny-normal-i-klimaforskningen>
- MET. (2022). *Hommelvik - Historikk*.
- Mohammed Al-Bared, M. A., Abdullah, R. A., Mohd Yunus, N. Z., Mohd Amin, M. F., & Awang, H. (2015). ROCK SLOPE ASSESSMENT USING KINEMATIC AND NUMERICAL ANALYSES. *Jurnal Teknologi*, 77(11). <https://doi.org/10.11113/jt.v77.6421>
- Multiconsult Norge AS. (2019a). *E6RV-MUL-GE-RPT-CAH13-0005 - Ingeniørgeologisk rapport for reguleringsplan – Dagsone Stavsjøfjelltunnelen-Værnes*. T. Multiconsult.
- Multiconsult Norge AS. (2019b). *E6RV-MUL-GT-RPT-CA#00-0001 -Datarapport grunnundersøkelser: E6 Ranheim - Værnes*. T. Multiconsult.
- Multiconsult Norge AS. (2019c). *E6RV-MUL-ZP-RPT-CA#00-0013 - Hommelvikparsellen i Malvik*

- kommune. Sammenligning av  
dagsone- og tunnelalternativet. . T. Multiconsult.
- Multiconsult Norge AS. (2020). *E6RV-MUL-GE-MEM-CA#00-0006 - Ingeniørgeologisk vurdering: Tunnelalternativ eller dagsonealternativ gjennom Hommelvik*. T. Multiconsult.
- NBG. (2011). Versjon 1 - Veileder for bruk av Eurokode 7 til bergteknisk prosjektering. In: Norsk Bergmekanikkgruppe.
- Newcomen, W., & Dick, G. (2016). An update to the strain-based approach to pit wall failure prediction, and a justification for slope monitoring. *Journal of the Southern African Institute of Mining and Metallurgy*, 116(5), 379-385.
- Nguyen, H., Bui, X.-N., & Moayed, H. (2019). A comparison of advanced computational models and experimental techniques in predicting blast-induced ground vibration in open-pit coal mine. *Acta Geophysica*, 67(4), 1025-1037.
- Nicholson, D. T., & Hencher, S. (1997). Assessing the potential for deterioration of engineered rock slopes. Proceedings of the IAEG symposium, Athens,
- Nilsen, B. (1979). *Stabilitet av høye fjellskjæringer [PhD Thesis]*. NTH.
- Nilsen, B. (2000). New trends in rock slope stability analyses. *Bulletin of Engineering Geology and the Environment*, 58(3), 173-178. <https://doi.org/10.1007/s100640050072>
- Nilsen, B. (2016). *Ingeniørgeologi-berg grunnkurskompendium*. Norges teknisk-naturvitenskapelige universitet, Institutt for geologi og bergteknikk.
- Nilsen, B. (2017). Rock slope stability analysis according to Eurocode 7, discussion of some dilemmas with particular focus on limit equilibrium analysis. *Bulletin of Engineering Geology and the Environment*, 76(4), 1229-1236.
- Nilsen, B., & Palmström, A. (2000). Engineering geology and rock engineering. *Norwegian Group for Rock Mechanics, Oslo*.
- Norrish, N. I., & Wyllie, D. C. (1996). Landslides: Investigation and Mitigation. Chapter 15-Rock slope stability analysis. *Transportation Research Board Special Report(247)*.
- NPRA. (2018). *Manual N200 Road Construction*. Norwegian Public Road Administration.
- NPRA. (2020). *Manual V225 Rock cuts*. Norwegian Public Road Administration.
- NVE. (2022). *NVE Atlas*. Norwegian Water Resources and Energy Directorate
- Nye Veier. (2021). *Regionrådet for Trondheimsregionen*
- Palmström, A. (1995). *RMI-a rock mass characterization system for rock engineering purposes [PhD thesis]*. na.
- Palmström, A. (2005). Measurements of and correlations between block size and rock quality designation (RQD). *Tunnelling and Underground Space Technology*, 20(4), 362-377.
- Palmström, A. (2019). *GLOSSARY OF TERMS IN ENGINEERING GEOLOGY AND ROCK MECHANICS*. RockMass AS. Retrieved June 2022 from
- Palmström, A. (2022). *Joints and Jointing*. RockMass AS. Retrieved June 2022 from <https://rockmass.net/joints-and-jointing/>
- Palmström, A., & Stille, H. (2015). *Rock Engineering, Second edition*. ICE Publishing.
- Pantelidis, L. (2009). Rock slope stability assessment through rock mass classification systems. *International Journal of Rock Mechanics and Mining Sciences*, 46(2), 315-325. <https://doi.org/10.1016/j.ijrmms.2008.06.003>
- Panthee, S., Singh, P., Kainthola, A., Das, R., & Singh, T. (2018). Comparative study of the deformation modulus of rock mass. *Bulletin of Engineering Geology and the Environment*, 77(2), 751-760.

- Panthi, K. K. (2006). Analysis of engineering geological uncertainties related to tunnelling in Himalayan rock mass conditions [PhD Thesis].
- Panthi, K. K. (2022). Boundary conditions in RS2 (April 8th, 2022). In.
- Patton, F. D. (1966). Multiple modes of shear failure in rock. 1st ISRM Congress, Pretec. (2016). Product data sheet: Spilingbolt Ø32.
- Rahardjo, H., Aung, K., Leong, E. C., & Rezaur, R. (2004). Characteristics of residual soils in Singapore as formed by weathering. *Engineering Geology*, 73(1-2), 157-169.
- Read, J., & Stacey, P. (2009). Guidelines for open pit slope design.
- Read, S. A. L., Perrin, N. D., & Richards, L. R. (1999). Applicability of the Hoek-Brown failure criterion to New Zealand greywacke rocks. 9th ISRM Congress, Paris.
- Riquelme, A., Cano, M., Tomás, R., & Abellan, A. (2017). Identification of Rock Slope Discontinuity Sets from Laser Scanner and Photogrammetric Point Clouds: A Comparative Analysis. *Procedia Engineering*, 191, 838-845. <https://doi.org/10.1016/j.proeng.2017.05.251>
- Riquelme, A. J., Abellán, A., & Tomás, R. (2015). Discontinuity spacing analysis in rock masses using 3D point clouds. *Engineering Geology*, 195, 185-195.
- Riquelme, A. J., Abellán, A., Tomás, R., & Jaboyedoff, M. (2014). A new approach for semi-automatic rock mass joints recognition from 3D point clouds. *Computers & Geosciences*, 68, 38-52. <https://doi.org/https://doi.org/10.1016/j.cageo.2014.03.014>
- Riquelme, A. J., Tomás, R., & Abellán, A. (2016). Characterization of rock slopes through slope mass rating using 3D point clouds. *International Journal of Rock Mechanics and Mining Sciences*, 84, 165-176.
- Robertson, A. (1988). Estimating weak rock strength. Proceedings of the SME annual meeting, Phoenix,
- Rocscience. (2022). *Documentation and Theory Overview*.
- Romana, M. (1985). New adjustment ratings for application of Bieniawski classification to slopes. Proceedings of the international symposium on role of rock mechanics Zacatecas, Mexico.
- Romana, M. (1995). The geomechanical classification SMR for slope correction. 8th ISRM Congress, Tokyo.
- Rutqvist, J., & Stephansson, O. (2003). The role of hydrochemical coupling in fractured rock engineering. *Hydrogeology Journal*, 11, 7-40. <https://doi.org/10.1007/s10040-002-0241-5>
- Sadoglu, E. (2015). Numerical analysis of centrally and eccentrically loaded strip footing on geotextile-reinforced sand. *Geosynthetics International*, 22, 225-234. <https://doi.org/10.1680/gein.15.00007>
- Selby, M. (1980). A rock mass strength classification for geomorphic purposes: with tests from Antarctica and New Zealand. *Zeitschrift für Geomorphologie*, 31-51.
- Serafim, J. L., & Pereira, J. P. (1983). Considerations on the geomechanical classification of Bieniawski: experience from case histories. Proceedings of symposium on engineering geology and under-ground openings, Lisbon, Portugal.
- Siddique, T., Pradhan, S. P., Vishal, V., & Singh, T. (2020). Applicability of Q-slope Method in the Himalayan Road Cut Rock Slopes and Its Comparison with CSMR. *Rock Mechanics and Rock Engineering*, 53(10), 4509-4522.
- Simonsen, A., & Li, C. C. (2019). Updated in situ rock stresses in Norway based on recent estimations and measurements. *Rock Mechanics for Natural Resources and Infrastructure Development*.
- Singh, A. (2004). FRHI-: a system to evaluate and mitigate rockfall hazard in stable rock excavations. *Journal of the Institution of Engineers. India. Civil Engineering Division*, 85(mai), 62-75.

- Singh, P., Wasnik, A., Kainthola, A., Sazid, M., & Singh, T. (2013). The stability of road cut cliff face along SH-121: a case study. *Natural hazards*, 68(2), 497-507.
- Singh, R. N., & Gahrooee, D. R. (1989). Application of rock mass weakening coefficient for stability assessment of slopes in heavily jointed rock mass. *International Journal of Surface Mining, Reclamation and Environment*, 3(4), 207-219. <https://doi.org/10.1080/09208118908944277>
- SINTEF. (2022). *Rock Mechanics Properties - Laboratory testing of samples from E6 Ranheim-Vearnes, Hommelvik - Report 22010BM*
- Soeters, R., & Van Westen, C. (1996). Slope instability recognition, analysis and zonation. *Landslides: investigation and mitigation*, 247, 129-177.
- Sowers, G. F., & Royster, D. L. (1978). Field investigation. *Special report*, 176, 81-111.
- StandardNorge. (2016). Eurocode: Basis of structural design NS-EN 1990:2002+A1:2005+NA:2016. 1 (2016-05-01). In.
- StandardNorge. (2020). Eurocode 7 — Geotechnical design - Part 1: General rules NS-EN 1997-1:2004+A1:2013+ NA:2020. 2004-11 (2020-12-18). In.
- Stead, D., & Havaej, M. (2016). Characterisation of open pit slopes: Toward an integrated remote sensing-numerical modelling approach. In *Rock Mechanics and Rock Engineering: From the Past to the Future*. Taylor & Francis Group.
- Stefanussen, W. (2017). *Bolttyper og funksjoner*. N. Bergmekanikkgruppe.
- Stimpson, B. (1981). A suggested technique for determining the basic friction angle of rock surfaces using core. *International Journal of Rock Mechanics and Mining Sciences & Geomechanics Abstracts*, 18(1), 63-65. [https://doi.org/https://doi.org/10.1016/0148-9062\(81\)90266-7](https://doi.org/https://doi.org/10.1016/0148-9062(81)90266-7)
- Stocker, T. F., Qin, D., Plattner, G.-K., Tignor, M. M., Allen, S. K., Boschung, J., Nauels, A., Xia, Y., Bex, V., & Midgley, P. M. (2013). Climate Change 2013: The physical science basis. contribution of working group I to the fifth assessment report of IPCC the intergovernmental panel on climate change. *Cambridge University Press*.
- Sullivan, T. D. (2013, 25-27 September). *Global slope performance index Slope Stability 2013: Proceedings of the 2013 International Symposium on Slope Stability in Open Pit Mining and Civil Engineering*, Brisbane. [https://papers.acg.uwa.edu.au/p/1308\\_0.4\\_Sullivan/](https://papers.acg.uwa.edu.au/p/1308_0.4_Sullivan/)
- Terzaghi, K. (1946). Rock defects and loads on tunnel supports. *Rock tunnelling with steel supports*(25).
- Terzaghi, R. D. (1965). Sources of error in joint surveys. *Geotechnique*, 15(3), 287-304.
- Torske, T. (1965). Geology of the Mostadmarka and Selbustrand area, Trøndelag.
- Turner, A. K., & Schuster, R. L. (2012). Rockfall : characterization and control. Transport Research Board of the National academies,
- Varnes, D. J. (1978). Slope movement types and processes. *Special report*, 176, 11-33.
- VIK Ørsta. (2022). CT-bolt M20. In.
- Westoby, M. J., Brasington, J., Glasser, N. F., Hambrey, M. J., & Reynolds, J. M. (2012). 'Structure-from-Motion' photogrammetry: A low-cost, effective tool for geoscience applications. *Geomorphology*, 179, 300-314. <https://doi.org/https://doi.org/10.1016/j.geomorph.2012.08.021>
- Wickham, G. E., Tiedemann, H. R., & Skinner, E. H. (1972). Support determinations based on geologic predictions. N Am Rapid Excav & Tunnelling Conf Proc,

- Wieczorek, G. F. (1996). Landslides: investigation and mitigation. Chapter 4-Landslide triggering mechanisms. *Transportation Research Board Special Report*(247).
- Wyllie, D. C. (2018). *Rock Slope Engineering: Civil Applications, Fifth Edition*. CRC Press.
- Wyllie, D. C., & Mah, C. (2004). *Rock slope engineering*. CRC Press.
- Zhang, L. (2010). Estimating the Strength of Jointed Rock Masses. *Rock Mechanics and Rock Engineering*, 43(4), 391-402. <https://doi.org/10.1007/s00603-009-0065-x>
- Zhang, L., & Einstein, H. H. (2004). Using RQD to estimate the deformation modulus of rock masses. *International Journal of Rock Mechanics and Mining Sciences*, 41(2), 337-341. [https://doi.org/10.1016/s1365-1609\(03\)00100-x](https://doi.org/10.1016/s1365-1609(03)00100-x)
- Zuidam, R. v. (1986). *Aerial photo-interpretation in terrain analysis and geomorphologic mapping*.

# Appendix A Ground investigations

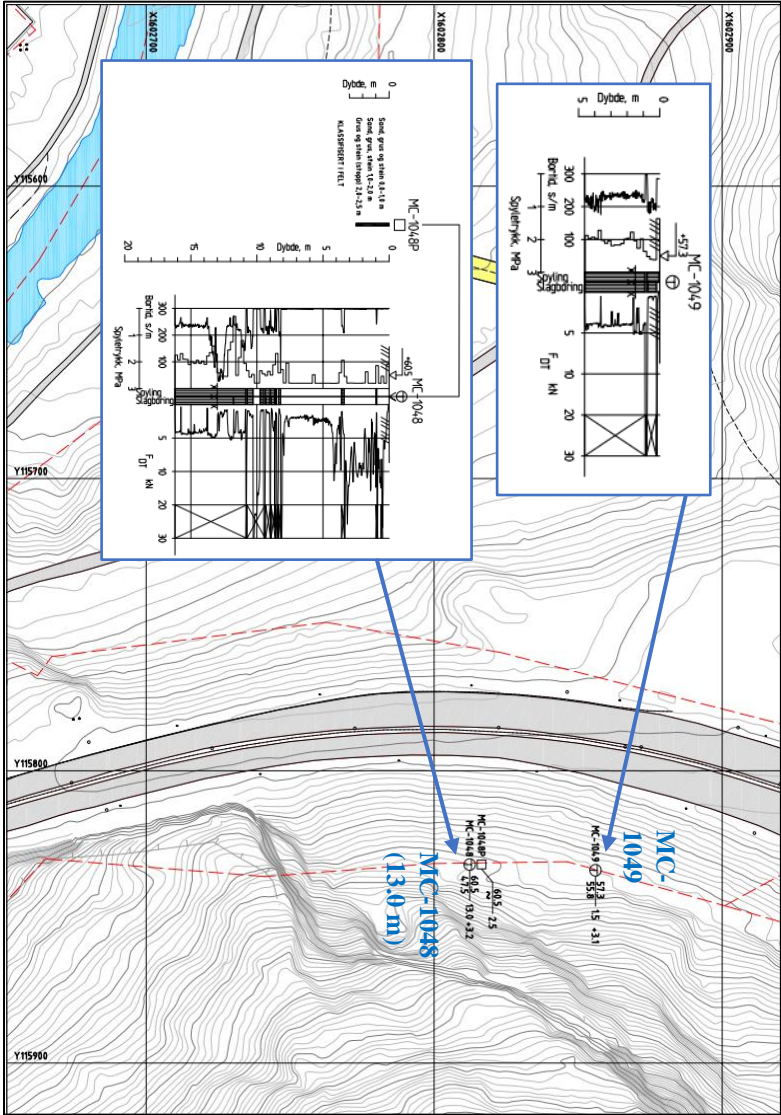


Figure A.1: Cone penetration testing (CPT) north of the current rock cut at Hommelvik. The depth to bedrock was 1.5 m for test MC-1049 and 13.0 m for test MC-1048 (blue text on figure). The results from the CPT are included too. Modified after Multiconsult Norge AS (2019b).

No.   Beskrivelse					
Kunde		Acciona Construction SA NUF			
Prosjekt		E6 Ranheim - Værnes			
Byggherren		Borplan			
Del -		Del - 7			
Status		Konstr./oppdr.	Konstr./oppdr.	Geoteknisk	RGS
10207634		ANT1	QNT1	AT1	00
10207634		RIG-TEG-001.7		1:1000	
www.multiconsult.no					

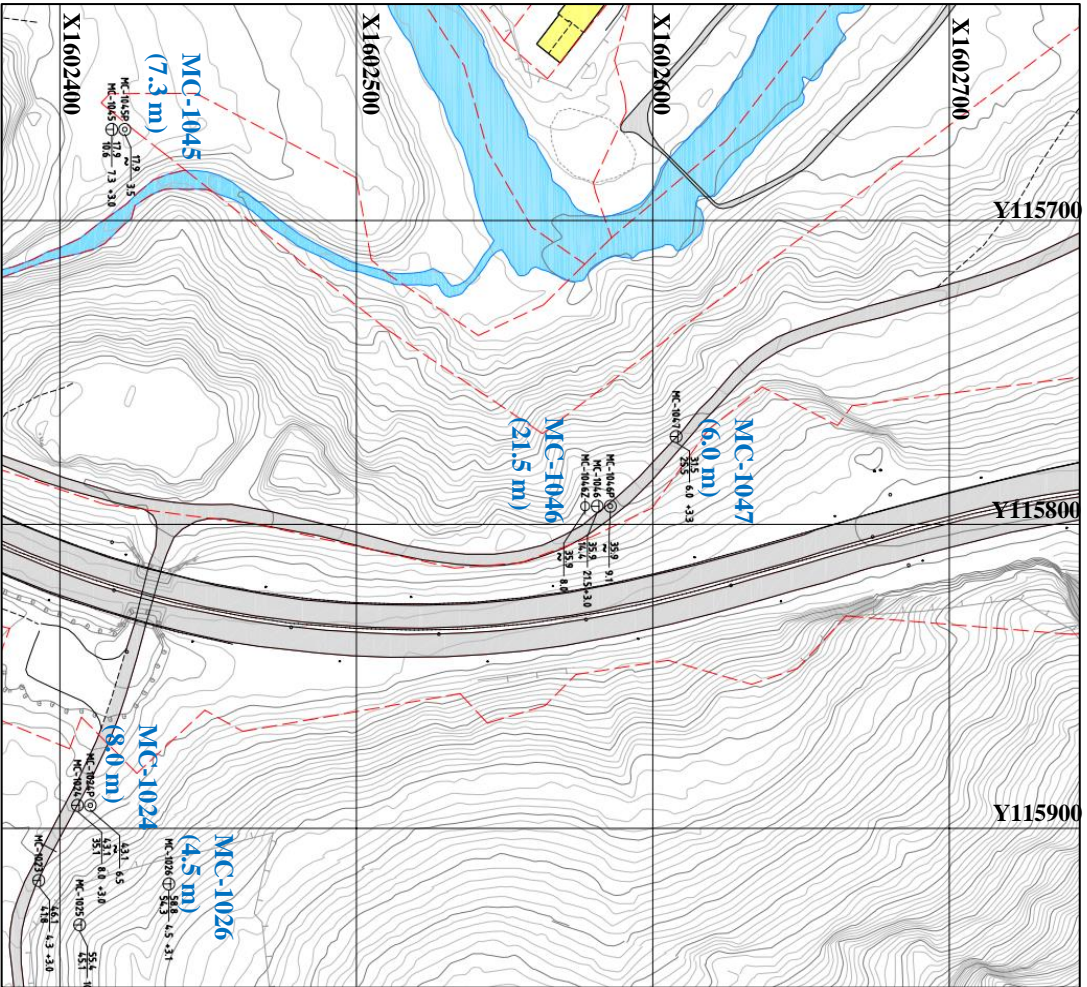


Figure A.2: Cone penetration testing (CPT) SW and SE of the current rock cut at Hommelvik. The most relevant CPT tests for the planned rock cut are highlighted in blue text with depth to bedrock in perentes. Modified after Multiconsult Norge AS (2019b)

<p>01 Nye Borplan, MC-1045 - MC-1047</p> <p>02 Bishovika</p>				
<p>2012/2018 JHM GJRT 305</p> <p>Dato</p>				
<p>Acciona Construction SA NUF</p> <p>E6 Ranheim-Værnes</p>				
<p>Borplan</p> <p>Del-5</p>				
<p>Formål/tilfellest: 1:1000</p> <p>Date: 30.11.2018</p>				
<p>Formål/tilfellest: 1:1000</p>				
<p>Multiconsult</p> <p>www.multiconsult.no</p>				
State	Signatur	Kontroll	Godkjent	Revis
10207634	RIG-TEG-001.5	JHM	GJRT	01

# Appendix B Plan and profile drawings

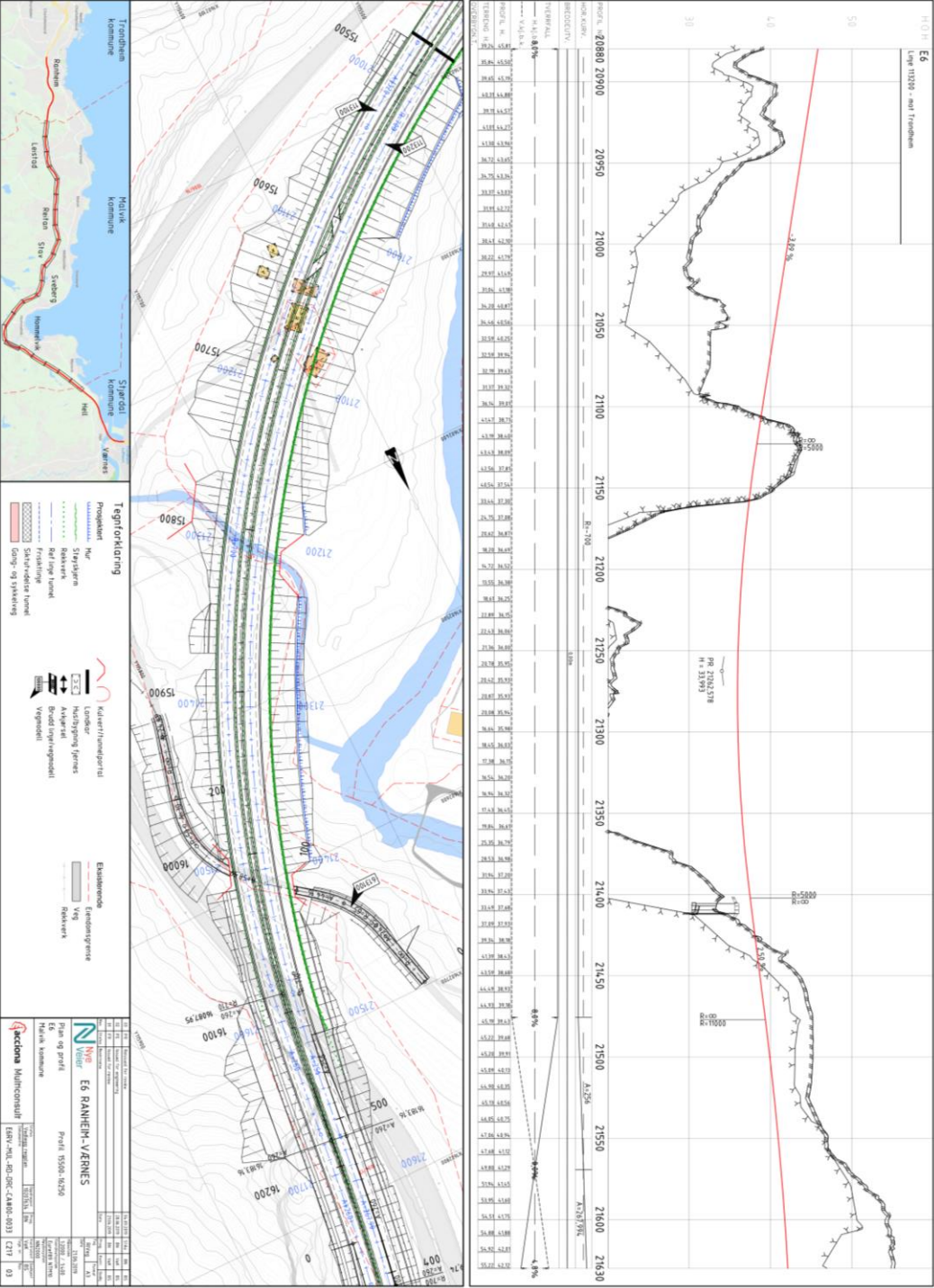


Figure B.1: Plan and profile drawings for profile 15500-16260 (Multiconsult Norge AS, 2019c).



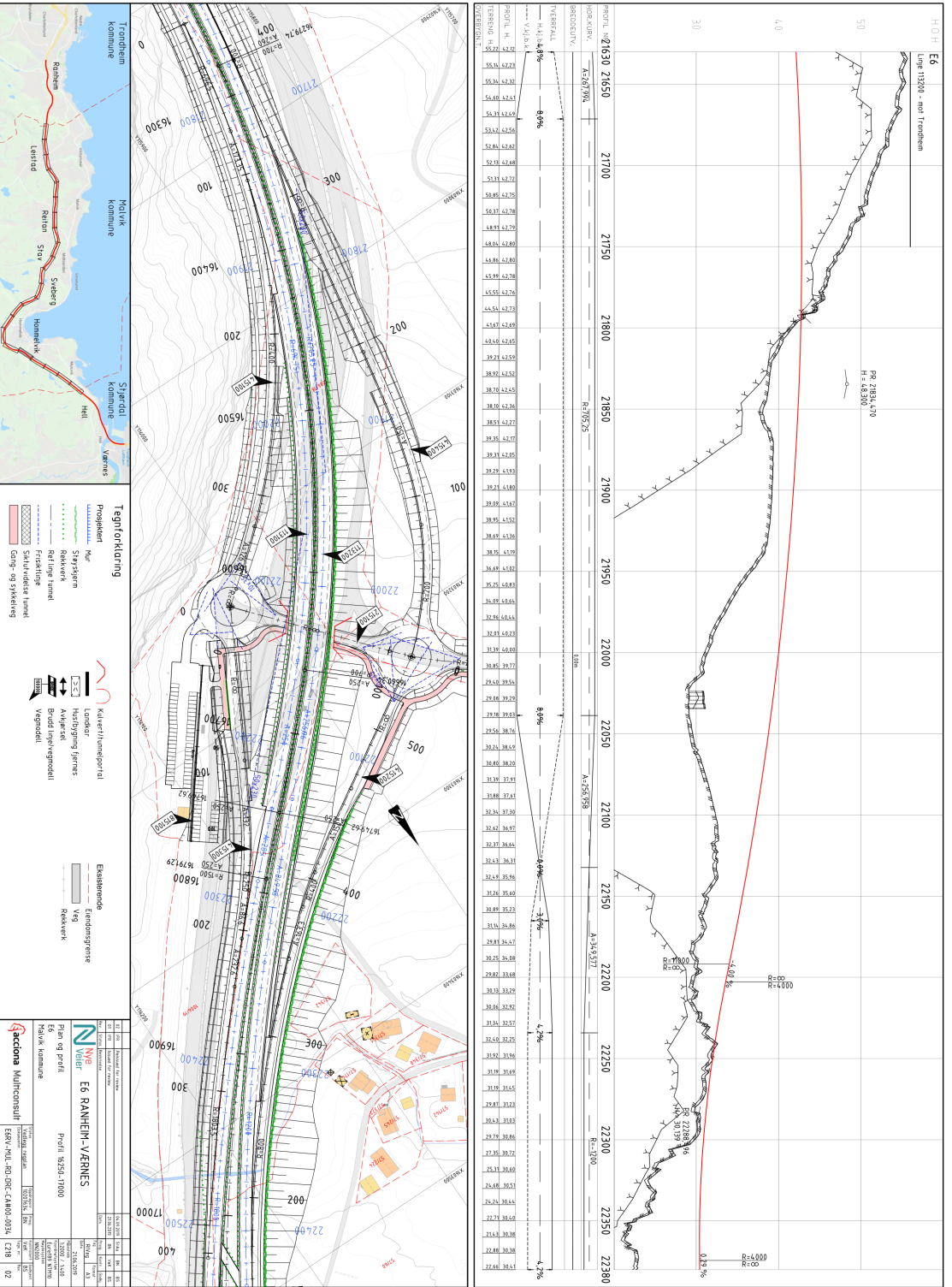


Figure B.2: Plan and profile drawings for profile 16260-17000 (Multiconsult Norge AS, 2019c).

# Appendix C Uniaxial compressive strength test results

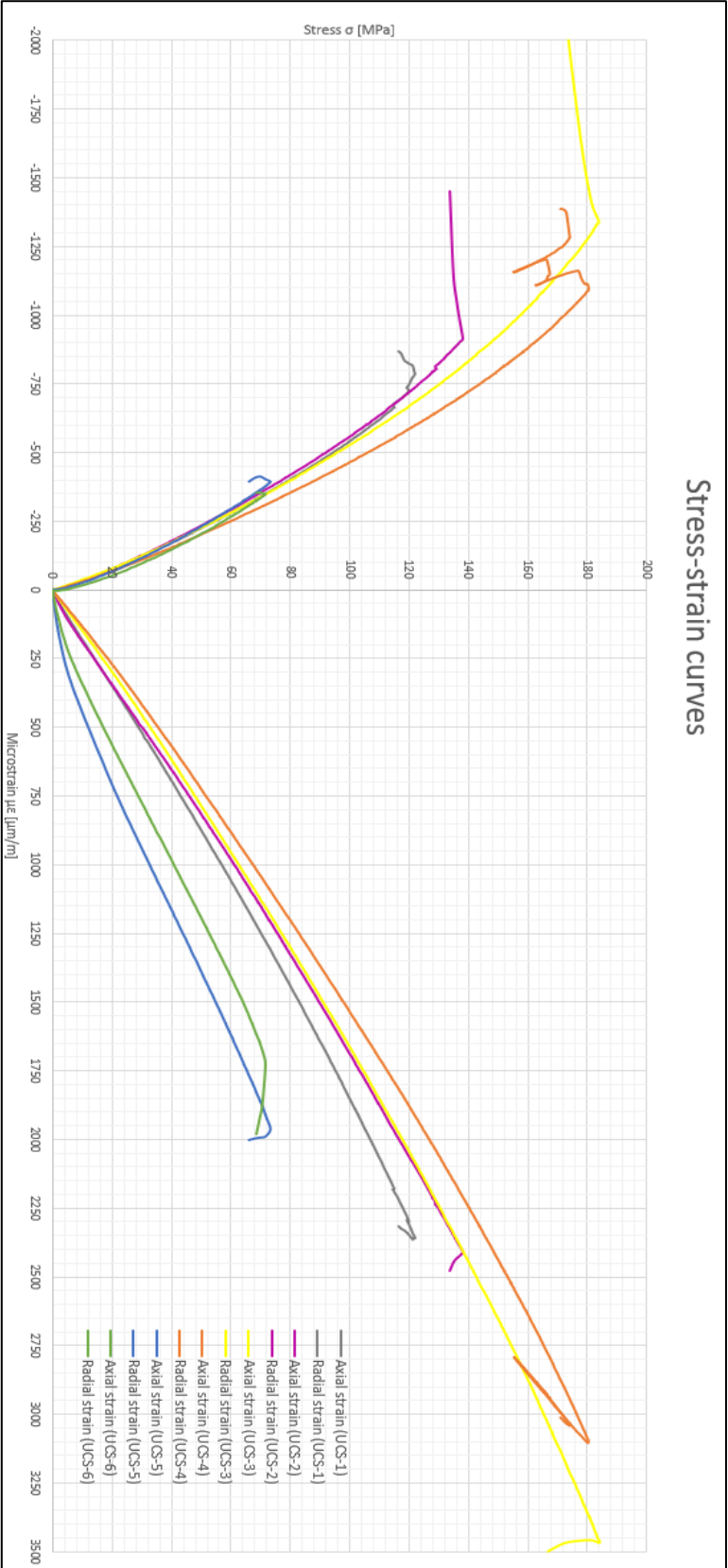


Figure C.1: Stress-strain curves from uniaxial compression tests of metagreywacke.

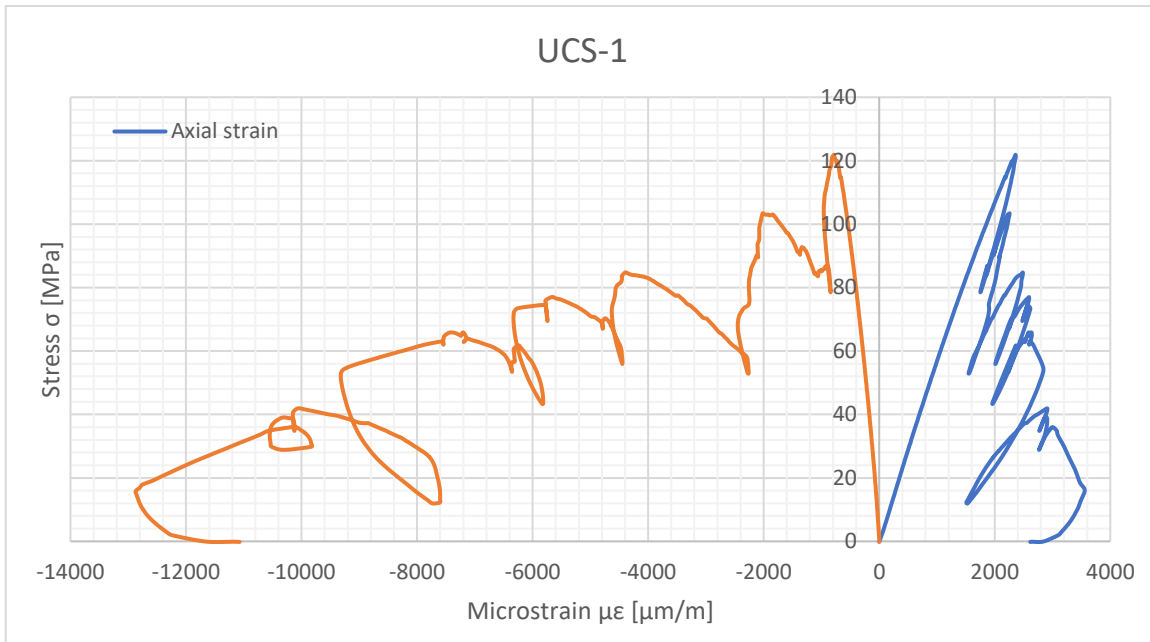


Figure C.2: Stress-strain curves for sample UCS-1

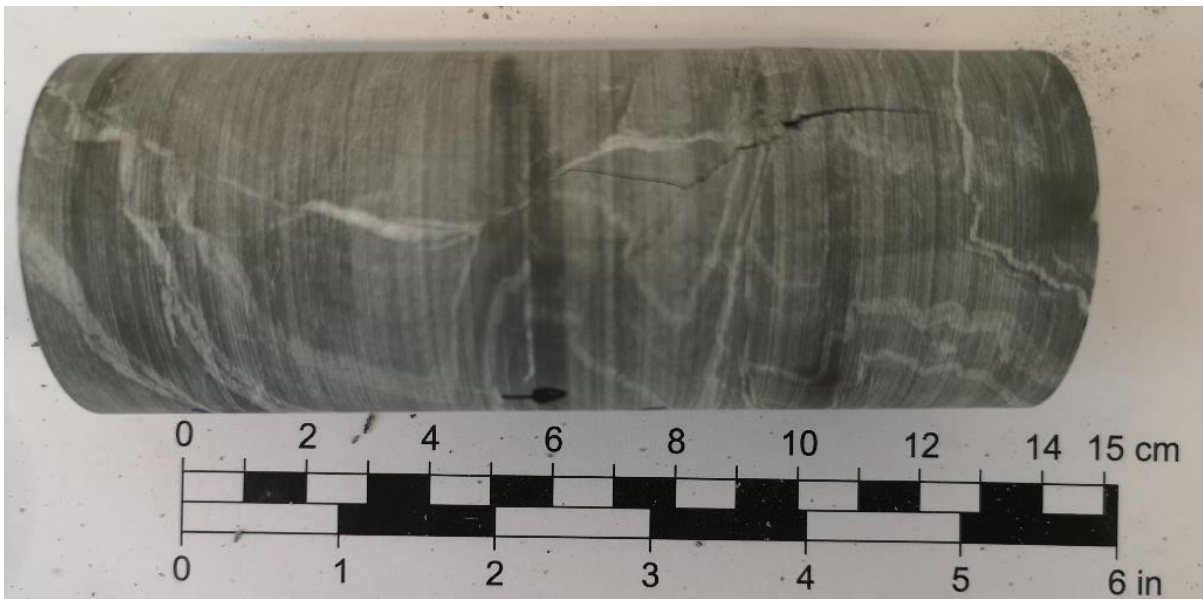
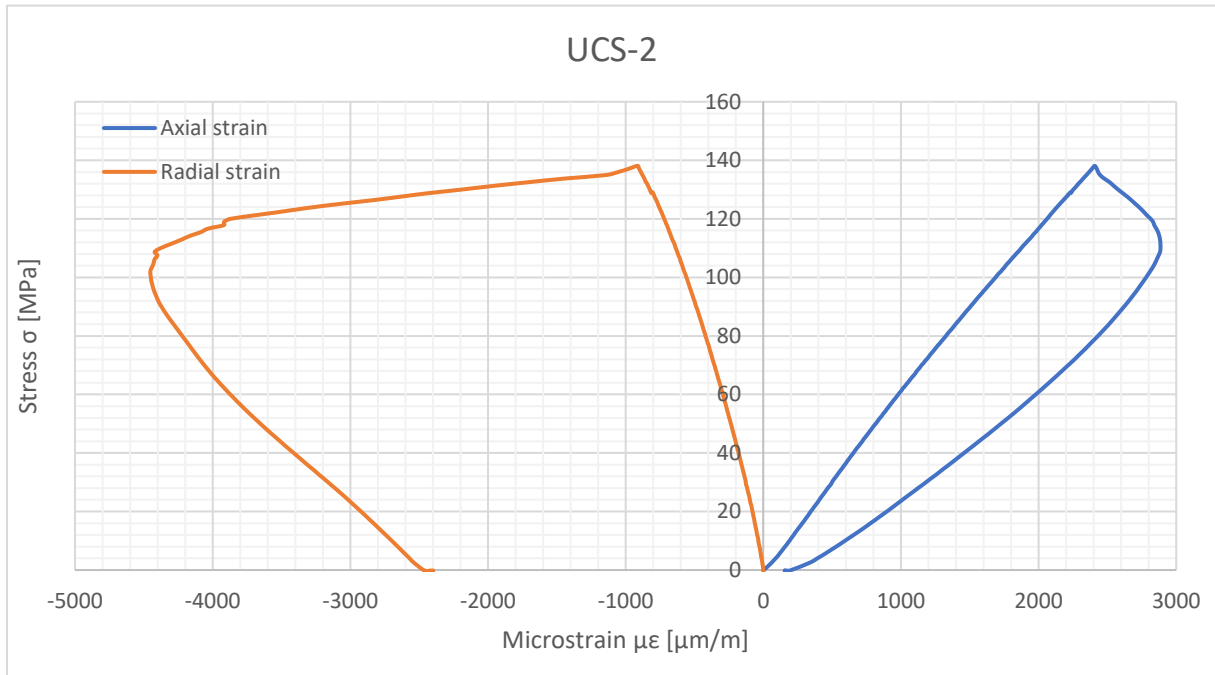


Figure C.3: Stress-strain curves for sample UCS-2.

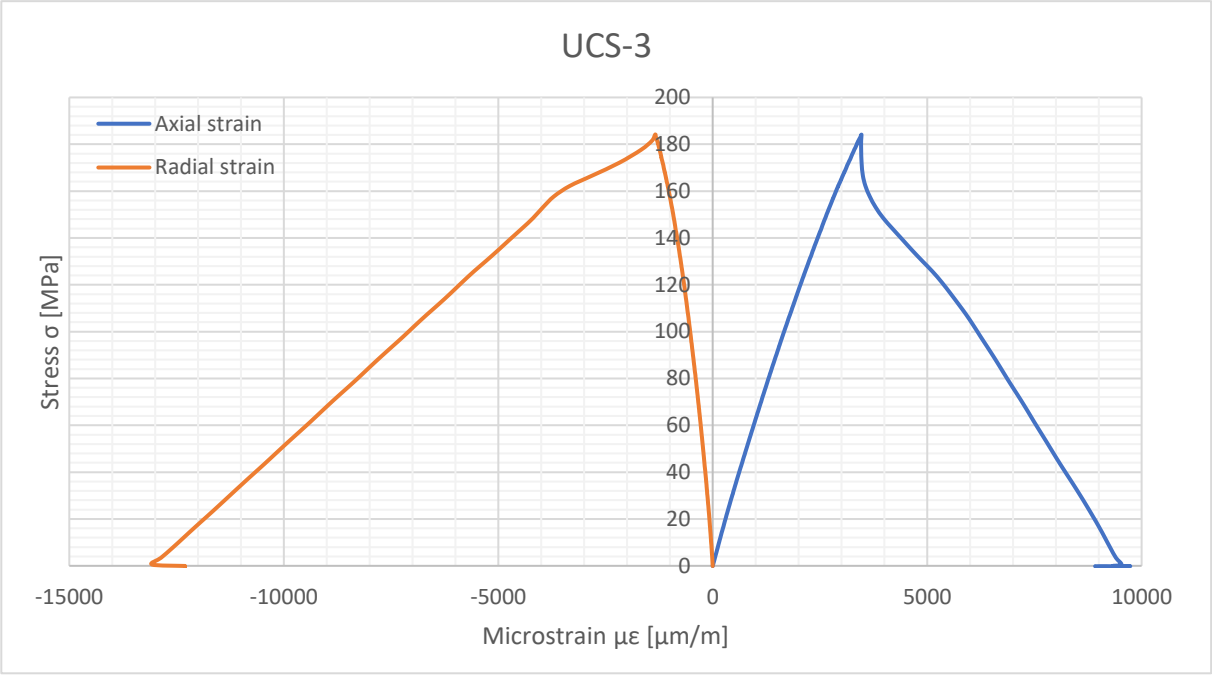


Figure C.4: Stress-strain curves for sample UCS-3.

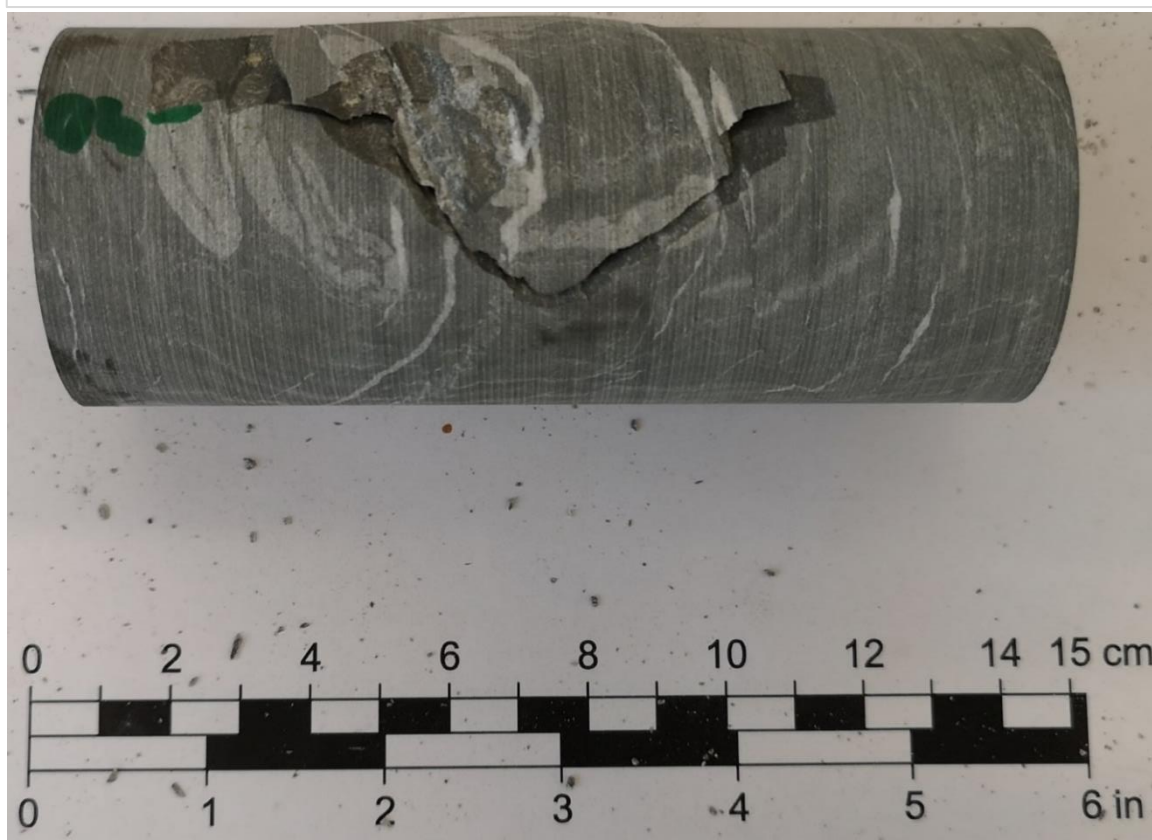
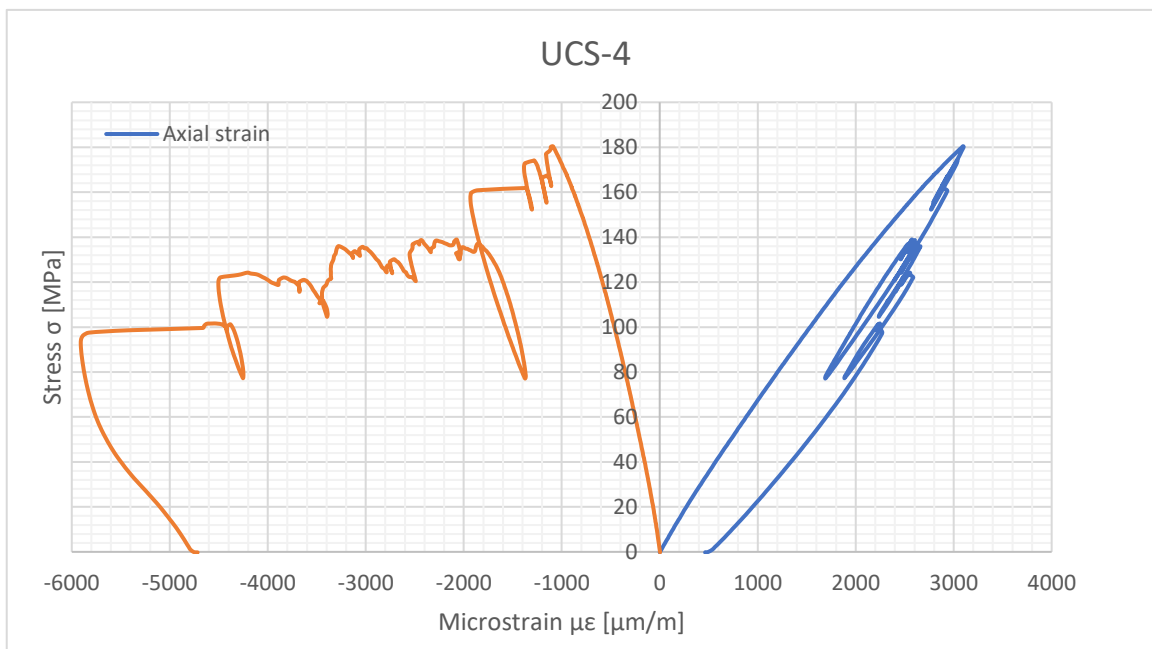


Figure C.5: Stress-strain curves for sample UCS-4.

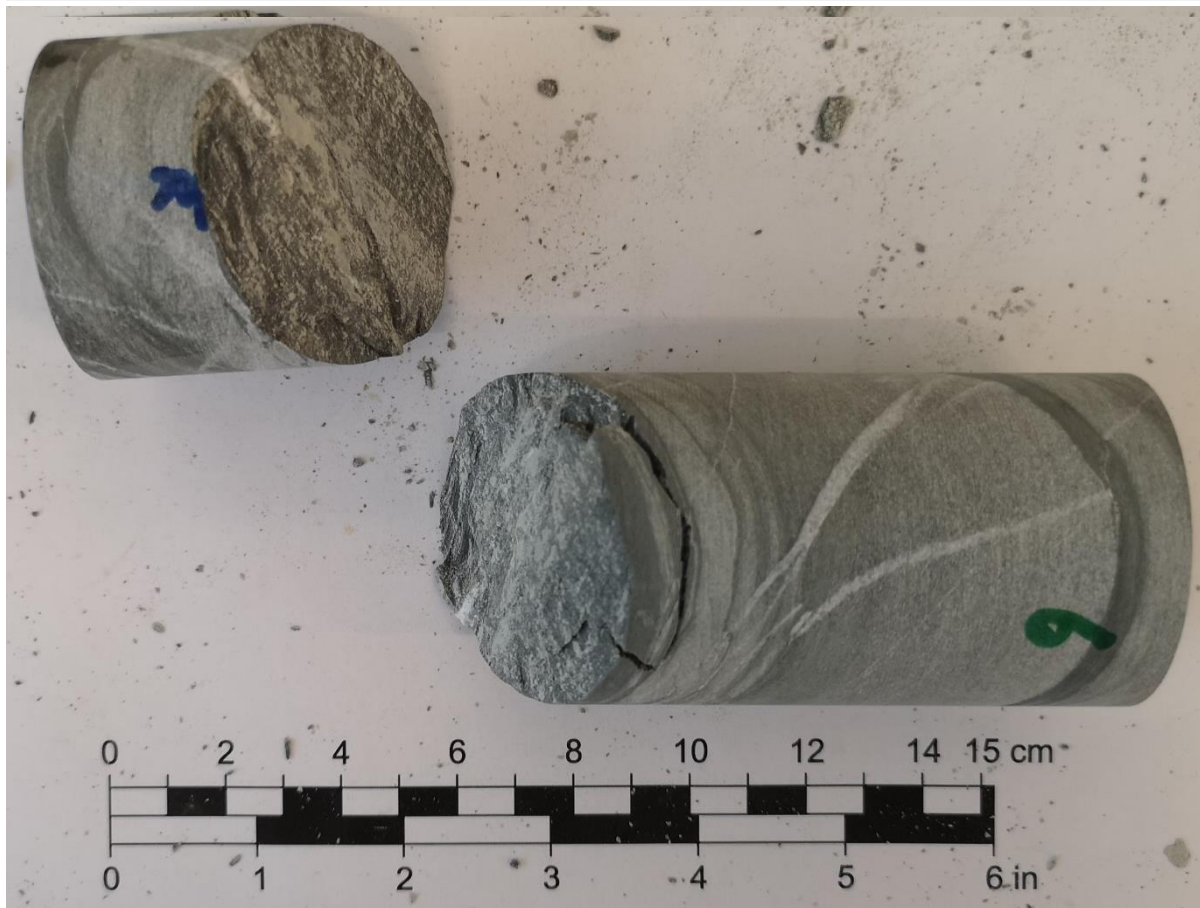
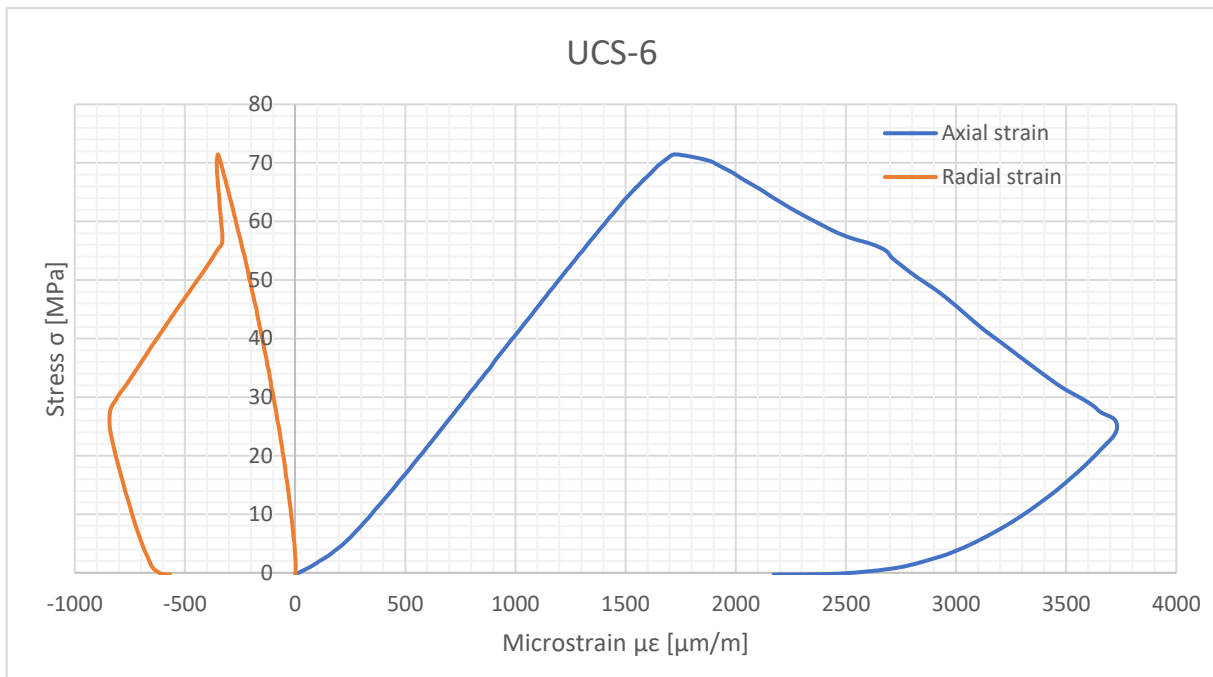


Figure C.7: Stress-strain curves for sample UCS-6.

## Appendix D Point load test results

Test date:	10.02.2022 and 17.02.2022									
Water saturation:	Assumed dry (water-% unspecified)									
Test ID	Type	W [mm]	D [mm]	De <sup>2</sup> [mm <sup>2</sup> ]	Hydraulic pressure [MPa]	Load [kN]	Is [MPa]	F	Is (50) [MPa]	Comment
1	Diametral		49.86	2486.02	8.74	8.43	3.39	1.00	<del>3.39</del>	
2	Diametral		49.86	2486.02	7.06	6.81	2.74	1.00	2.74	
3	Diametral		50.42	2542.18	6.76	6.52	2.57	1.00	<del>2.58</del>	
4	Diametral		50.42	2542.18	12.82	12.37	4.87	1.00	<del>4.88</del>	
5	Diametral		50.42	2542.18	2.62	2.53	0.99	1.00	<del>1.00</del>	
<b>Mean</b>									2.74	
<b>SD</b>									1.41	
<b>CV</b>									51.4%	
<hr/>										
A-1	Axial	49.97	15.66	996.35	6.58	6.35	6.37	0.81	<del>5.18</del>	
A-2	Axial	50.45	14.09	905.07	8.98	8.67	9.57	0.80	7.62	
A-3	Axial	50.01	22.44	1428.86	6.36	6.14	4.30	0.88	3.79	Invalid failure
A-4	Axial	50.51	16.73	1075.93	9.66	9.32	8.66	0.83	7.17	
A-5	Axial	49.9	21.16	1344.39	14.98	14.46	10.75	0.87	9.35	
A-6	Axial	49.91	19.6	1245.53	15.3	14.76	11.85	0.85	<del>10.13</del>	
A-7	Axial	49.91	19.31	1227.10	14.78	14.26	11.62	0.85	9.90	
A-8	Axial	50.48	21.86	1405.01	5.64	5.44	3.87	0.88	3.40	Invalid failure
A-9	Axial	49.91	21.57	1370.72	16.78	16.19	11.81	0.87	<del>10.32</del>	
A-10	Axial	50.52	24.9	1601.67	9.62	9.28	5.80	0.90	5.24	Invalid failure
A-11	Axial	50.41	22.04	1414.62	9.76	9.42	6.66	0.88	<del>5.86</del>	
<b>Mean</b>									8.51	
<b>SD</b>									2.02	
<b>CV</b>									23.7%	
									<b>Ia (50)</b>	<b>3.109</b>

Figure D.1: Results from point load tests.

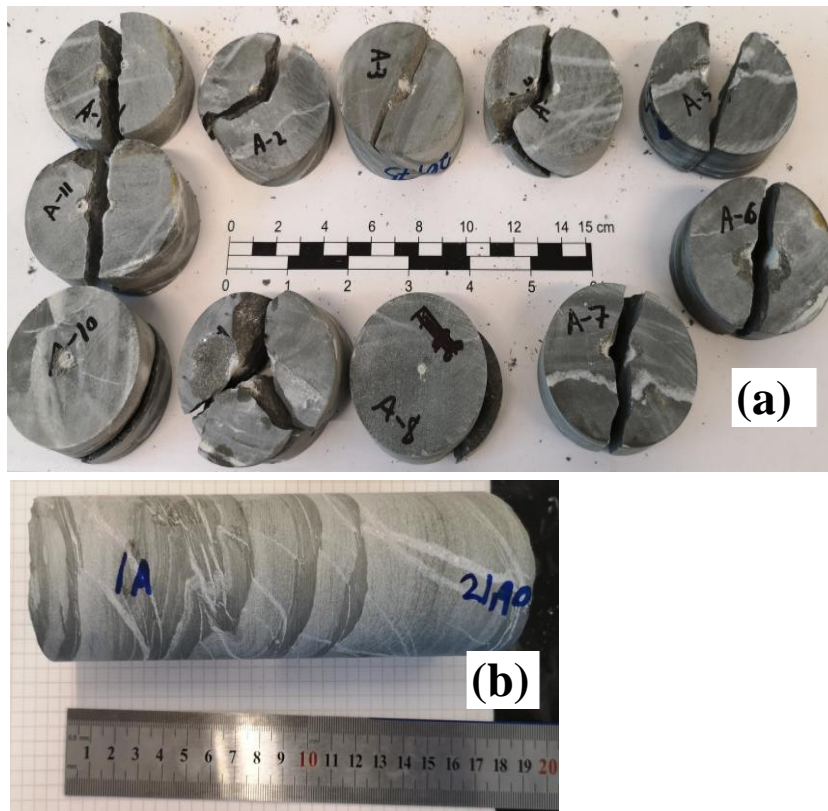


Figure D.2: Test material post-failure; (a) axial testing; and (b) pre-test for diametral.



# Appendix E Steepness and susceptibility maps for Hommelvik

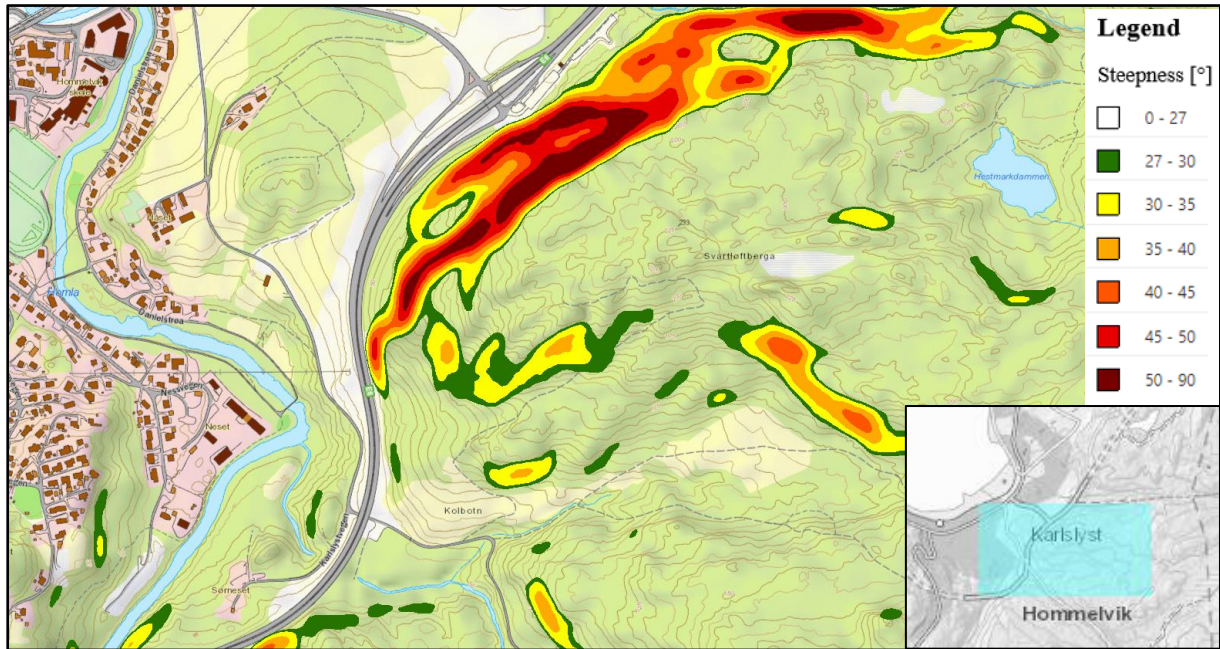


Figure E.1: Steepness map for snow avalanche (NVE, 2022)

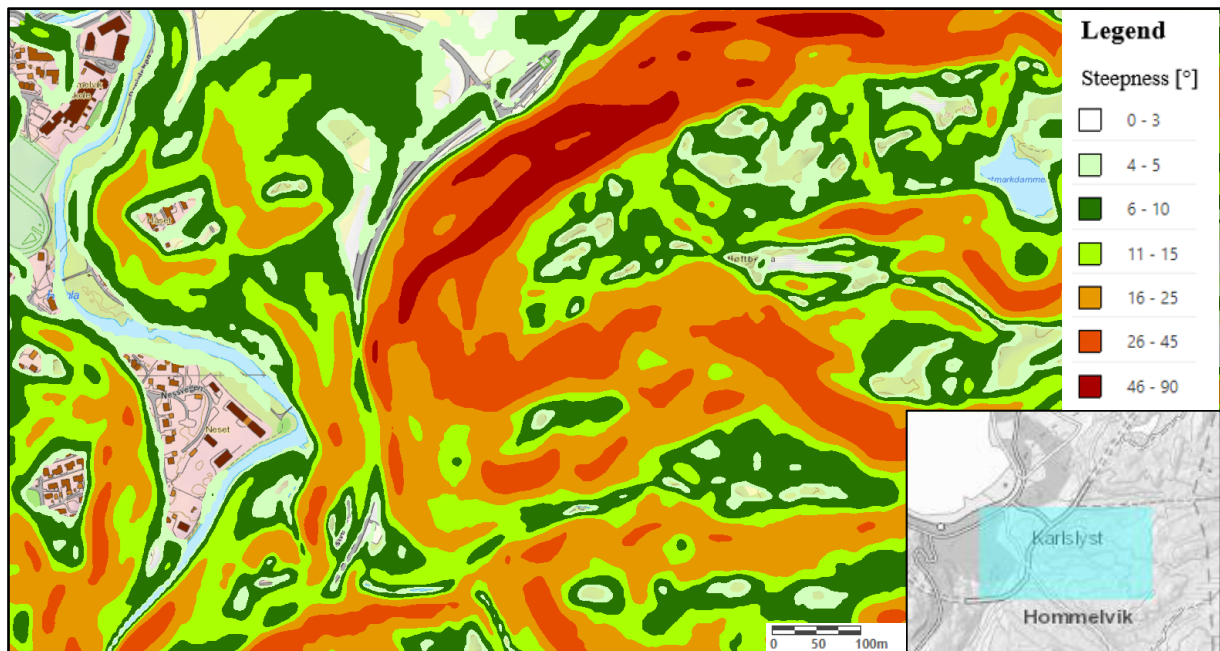


Figure E.2: Steepness map for soil avalanche (NVE, 2022)

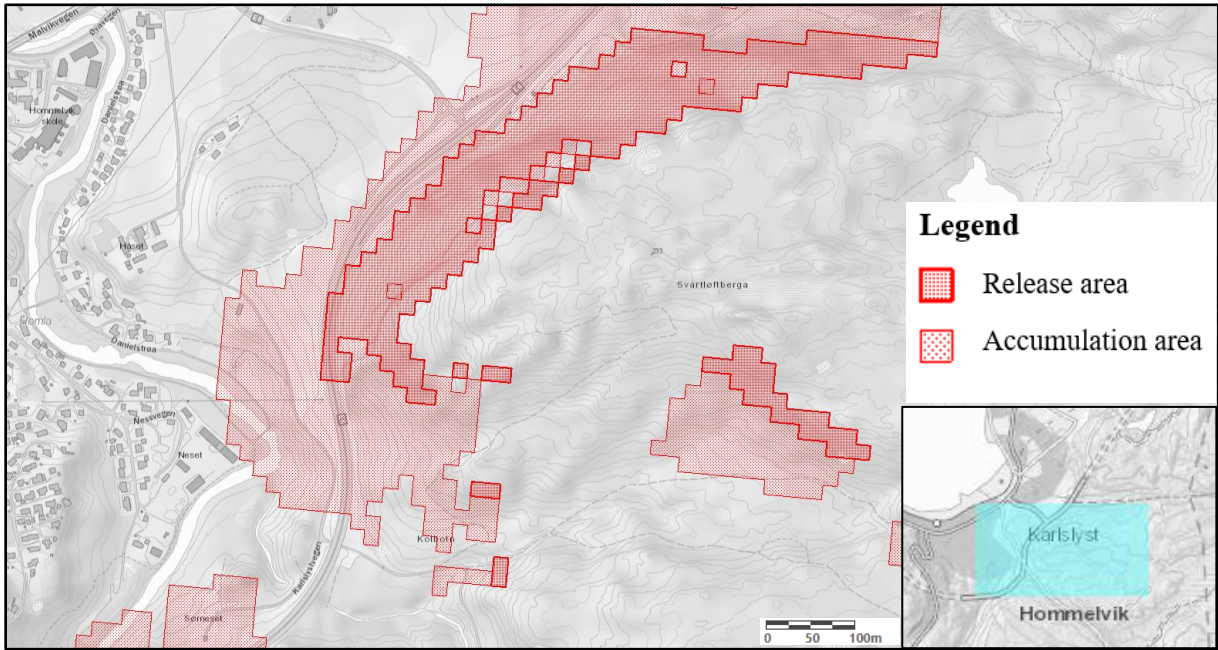


Figure E.3: Susceptibility map for snow avalanche (NVE, 2022)

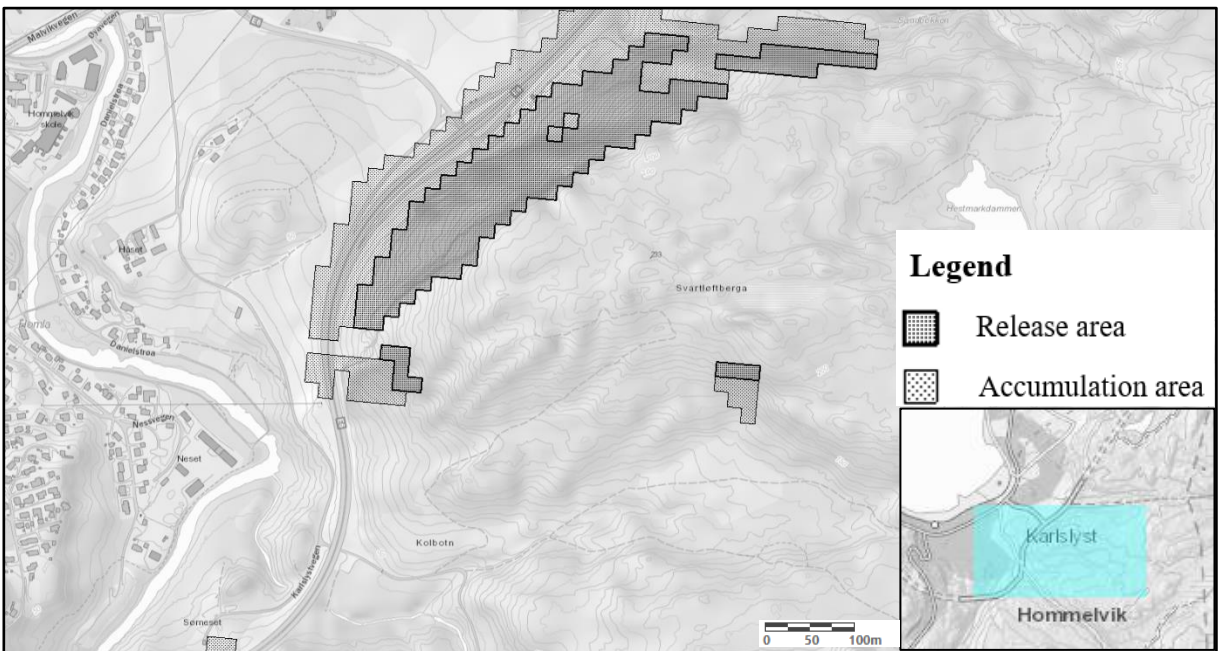


Figure E.4: Susceptibility map for rock fall (NVE, 2022)

## Appendix F Core logging



Figure F.1: Surface conditions at boreholes 1A, 4A, and 5A (from left to right). Drilling of boreholes 5X was not started at the time of inspection.



Figure F.2: Equipment used for drilling by Besab AB.

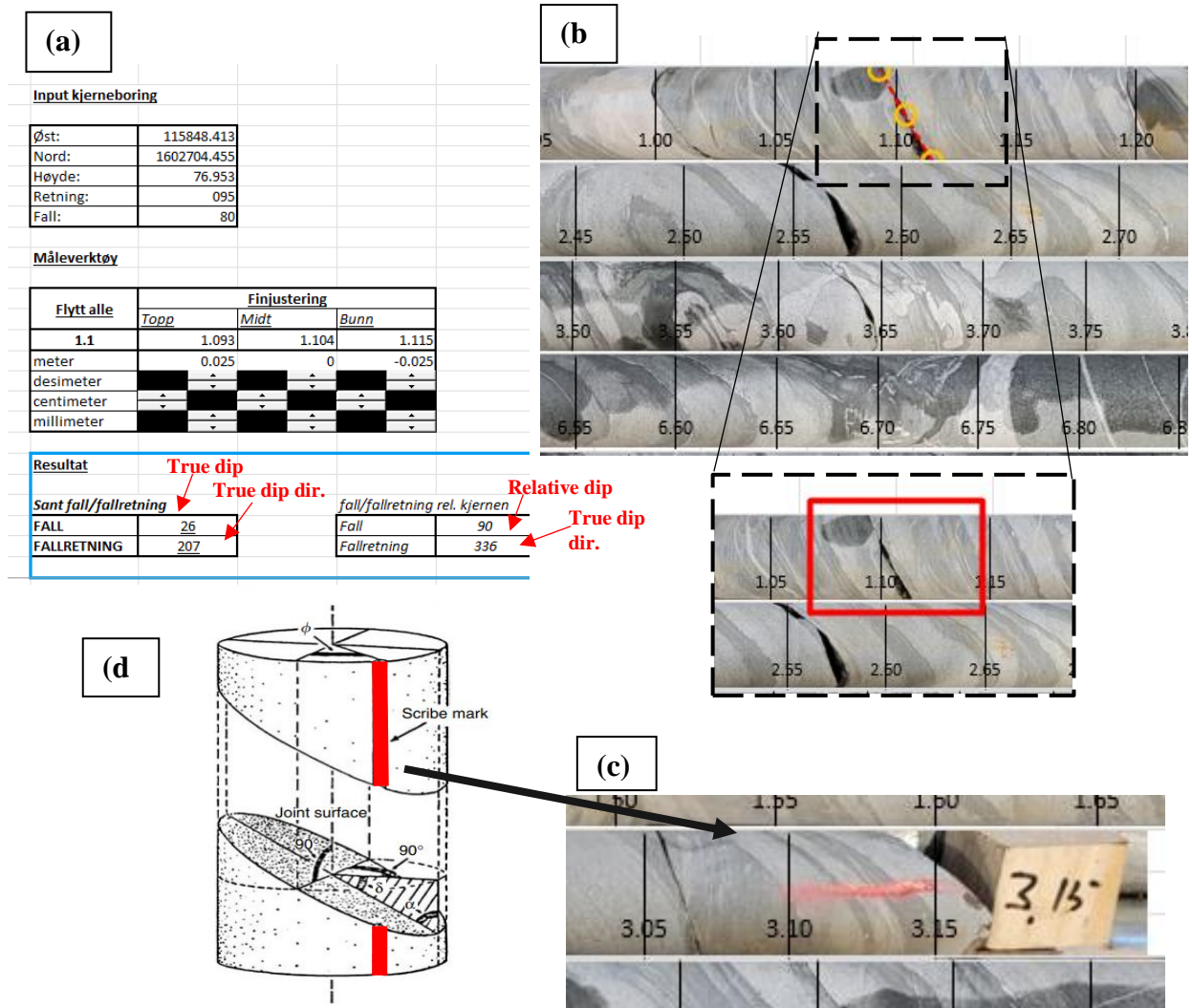


Figure F.3: Measurement of joint orientations. (a) Control panel in excel to fit curves on the cores. (b) Curve fitted on a joint with orientation of 26/207 (dip/dip direction). (c) Scribe mark used to orientate the cores. (d) Illustration of a joint intersecting an orientated core. Modified after Hunt (2005)

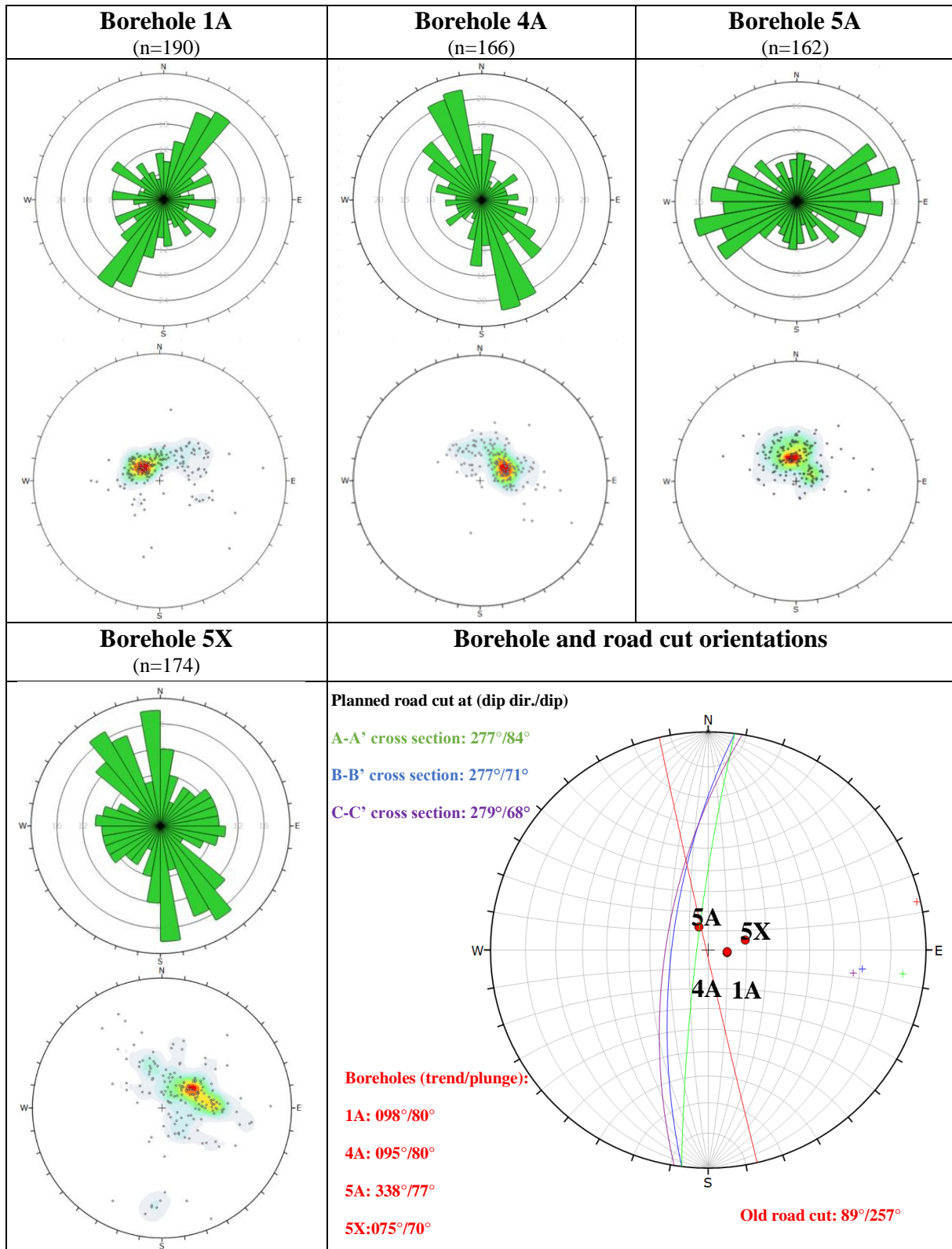


Figure F.4: Pol plots and rosette plots for the boreholes (with no weighting from  $f_i$ ).

# Appendix G Borehole 1A

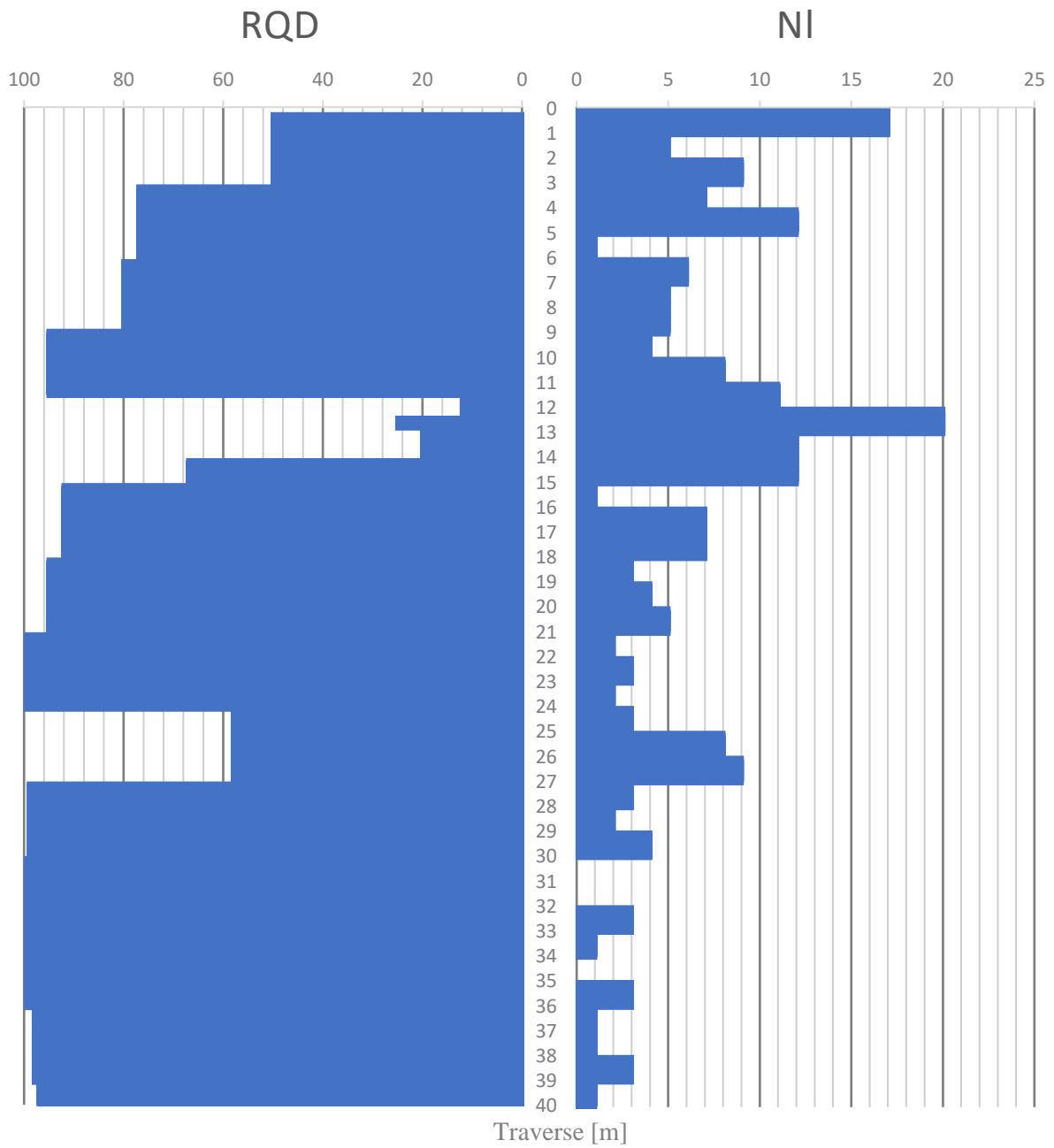


Figure G.1: RQD and NI (joint frequency per meter) for borehole 1A.



**1A - Box 1 (0-6 m)**

Nl (m)	17 (0-1)	5 (1-2)	9 (2-3)	7 (3-4)	12 (4-5)	1 (5-6)
RQD (m)	0 (0-0.2)		50 (0.2-3.1)		77 (3.1-6.0)	

Assumed rock type: Metagreywacke (0-6.0 m)

**1A - Box 2 (6-11 m)**

Nl (m)	6 (6-7)	5 (7-8)	5 (8-9)	4 (9-10)	8 (10-11)
RQD (m)	77 (6.0-6.1)		80 (6.1-8.9)		95 (8.9-11.0)

Assumed rock type: Metagreywacke (6.0-11.0 m)



**1A - Box 3 (11-15 m)**

Nl (m)	11 (11-12)	20 (12-13)	12 (13-14)	12 (14-15)
RQD (m)	95 (11.0-11.5)	12 (11.5-12.4)	25 (12.4-12.8)	20 (12.8-14.1) 67 (14.1-15.0)

Assumed rock type: Metagreywacke (11.0-15.0 m)



**1A - Box 4 (15-20 m)**

Nl (m)	1 (15-16)	7 (16-17)	7 (17-18)	3 (18-19)	4 (19-20)
RQD (m)	67 (15.0-15.1)	92 (15.1-18.1)	95 (18.1-20.0)		

Assumed rock type: Metagreywacke (15.0-20.0 m)





**1A - Box 5 (20-26 m)**

Nl (m)	5 (20-21)	2 (21-22)	3 (22-23)	2 (23-24)	3 (24-25)	8 (25-26)
RQD (m)	95 (20.0-21.1)		100 (21.1-24.1)		58 (24.1-26.0)	

Assumed rock type: Metagreywacke (20.0-26.0 m)

Comments:

Rock samples for rock mechanical investigations (21.20-21.90 m)



**1A - Box 6 (26-32 m)**

Nl (m)	9 (26-27)	3 (27-28)	2 (28-29)	4 (29-30)	0 (30-31)	0 (31-32)
RQD (m)	58 (26.0-27.1)		99 (27.1-30.1)		100 (30.1-32.0)	

Assumed rock type: Metagreywacke (26.0-26.1 m), polymictic conglomerate (26.1-32.0 m)



1A - Box 7 (32-37 m)						1A - Box 8 (37-40.65 m)				
Nl (m)	3 (32-33)	1 (33-34)	0 (34-35)	3 (35-36)	1 (36-37)	Nl (m)	1 (37-38)	3 (38-39)	1 (39-40)	4 (40-40.65)
RQD (m)	100 (32.0-36.1)		98 (36.1-37.0)			RQD (m)	98 (37.0-39.1)		97 (39.1-40.65)	
Assumed rock type: Polymictic conglomerate (32.0-37.0 m)						Assumed rock type: Polymictic conglomerate (37.0-40.65 m)				

Table G.1: Joint orientation measurements from borehole 1A.

<b>Borehole 1A</b>						
Joint nr.	Traverse [m]	True dip [°]	True dip direction [°]	Relative dip [°]	Relative dip direction [°]	fi-factor
1	0.44	32	049	60	207	1
2	0.47	37	036	66	216	1
3	0.52	26	039	68	204	1
4	0.60	29	028	72	208	1
5	0.75	28	054	61	202	1
6	0.88	46	226	71	323	1
7	1.07	29	164	70	152	1
8	1.17	22	119	59	171	1.5
9	1.28	30	118	53	168	1.5
10	1.38	12	124	69	174	1
11	1.80	5	199	81	175	1
12	2.04	15	123	66	173	1
13	2.13	18	126	65	171	1
14	2.29	22	122	60	170	1
15	2.59	15	123	66	173	1
16	2.76	19	150	69	164	1
17	2.85	29	105	51	175	1.5
18	2.95	30	210	88	333	1
19	3.12	32	131	54	159	1.5
20	3.36	31	127	54	162	1.5
21	3.48	33	126	53	161	1.5
22	3.54	32	123	52	163	1.5
23	3.65	21	157	70	161	1
24	3.81	28	114	53	171	1.5
25	4.01	26	102	54	178	1.5
26	4.07	27	102	53	178	1.5
27	4.11	20	107	60	177	1
28	4.19	37	091	43	186	1.5
29	4.21	31	084	50	189	1.5
30	4.25	32	078	51	193	1.5
31	4.38	35	082	46	192	1.5
32	4.50	19	187	80	161	1
33	4.60	45	080	39	201	1.5
34	4.69	11	092	69	181	1
35	4.90	12	124	69	174	1
36	5.25	13	207	84	168	1
37	5.74	53	089	28	196	3.5
38	5.98	20	234	86	347	1
39	6.11	24	230	83	342	1
40	6.16	14	081	66	185	1
41	6.49	25	091	55	183	1.5
42	6.63	27	102	53	178	1.5
43	6.70	27	096	54	181	1.5
44	6.80	25	100	55	179	1.5
45	6.86	23	103	57	178	1.5
46	7.18	27	096	54	181	1.5
47	7.23	21	084	60	186	1
48	7.48	17	115	64	174	1
49	7.81	30	124	54	164	1.5
50	8.13	27	124	57	167	1.5
51	8.29	33	110	48	171	1.5
52	8.55	31	130	54	160	1.5
53	8.65	19	159	71	162	1
54	8.93	29	102	51	178	1.5
55	9.67	22	141	64	163	1
56	9.94	28	122	55	167	1.5
57	10.08	28	139	60	159	1
58	10.26	25	138	62	162	1
59	10.47	16	125	66	172	1
60	10.49	21	112	60	174	1
61	10.64	20	133	64	168	1
62	10.74	21	170	74	159	1
63	11.01	21	133	63	167	1
64	11.11	28	142	61	158	1
65	11.28	20	145	67	164	1
66	11.36	30	132	56	160	1.5
67	11.48	16	151	71	167	1

68	11.56	14	115	66	176	1
69	11.62	79	263	25	324	3.5
70	11.72	23	127	60	168	1
71	11.85	28	125	56	165	1.5
72	11.95	22	157	69	160	1
73	11.99	23	172	75	157	1
74	12.01	25	148	65	159	1
75	12.05	31	127	54	162	1.5
76	12.12	24	131	61	165	1
77	12.19	25	158	69	157	1
78	12.21	22	179	77	158	1
79	12.39	39	297	63	013	1
80	12.42	41	294	60	012	1
81	12.54	46	281	54	002	1.5
82	12.58	45	289	56	009	1.5
83	12.67	48	290	53	011	1.5
84	12.74	32	296	69	010	1
85	12.80	36	297	66	012	1
86	12.86	44	231	70	327	1
87	12.90	37	229	75	332	1
88	12.96	46	244	62	333	1
89	13.03	43	243	65	334	1
90	13.15	31	276	69	359	1
91	13.24	26	268	74	355	1
92	13.31	41	260	61	347	1
93	13.35	47	112	35	162	1.5
94	13.39	36	264	65	351	1
95	13.44	57	090	24	197	3.5
96	13.57	38	218	80	327	1
97	13.76	46	240	64	331	1
98	13.77	59	189	85	121	1
99	13.85	40	256	63	344	1
100	13.92	35	254	68	345	1
101	13.95	36	253	67	344	1
102	14.02	63	012	82	243	1
103	14.02	24	248	64	338	1
104	14.16	21	055	65	196	1
105	14.20	22	039	69	200	1
106	12.27	22	114	59	173	1.5
107	14.55	13	127	68	173	1
108	14.74	13	133	69	172	1
109	14.75	15	123	66	173	1
110	14.84	56	007	85	236	1
111	15.04	61	249	48	326	1.5
112	15.09	17	117	64	174	1
113	15.93	66	293	37	024	1.5
114	16.22	13	118	68	175	1
115	16.34	16	175	77	164	1
116	16.37	14	210	86	167	1
117	16.47	14	187	80	165	1
118	16.53	19	181	78	161	1
119	16.78	23	138	63	163	1
120	17.04	22	121	61	171	1
121	17.50	18	145	69	167	1
122	17.54	10	110	70	178	1
123	17.87	20	191	81	160	1
124	17.91	16	135	68	170	1
125	18.05	12	108	68	178	1
126	18.10	26	113	55	172	1.5
127	18.16	12	343	86	191	1
128	18.77	24	093	56	182	1.5
129	19.00	17	109	63	177	1
130	19.53	25	091	55	183	1.5
131	19.53	75	314	44	055	1.5
132	19.90	15	152	72	168	1
133	20.11	33	100	47	179	1.5
134	20.28	20	141	66	165	1
135	20.48	18	145	68	165	1
136	20.61	15	183	79	164	1
137	20.78	20	167	73	160	1
138	20.93	24	183	79	155	1
139	21.11	15	152	72	168	1

140	21.26	22	122	60	170	1
141	21.49	20	125	62	170	1
142	21.80	15	152	17	168	3.5
143	22.10	10	155	75	171	1
144	23.40	25	119	57	170	1.5
145	23.65	20	119	62	172	1
146	24.11	16	156	72	165	1
147	23.16	27	201	87	153	1
148	24.59	33	216	84	331	1
149	24.86	26	210	90	156	1
150	25.03	11	193	81	169	1
151	25.33	19	127	64	170	1
152	25.41	31	188	81	148	1
153	25.64	15	157	73	167	1
154	25.74	28	244	77	344	1
155	25.86	40	227	75	329	1
156	25.90	38	218	80	327	1
157	26.08	48	240	63	329	1
158	26.20	47	237	65	327	1
159	26.33	9	127	72	175	1
160	26.47	41	218	79	324	1
161	26.52	30	208	89	332	1
162	26.67	29	186	80	151	1
163	26.87	24	175	76	156	1
164	27.11	26	172	74	154	1
165	27.32	24	195	84	156	1
166	29.20	31	140	58	156	1.5
167	29.92	14	115	66	175	1
168	29.96	29	131	56	161	1.5
169	30.11	23	185	80	156	1
170	31.58	24	238	81	344	1
171	32.08	20	197	84	160	1
172	32.26	28	171	73	152	1
173	32.53	30	210	88	333	1
174	32.92	29	109	59	175	1.5
175	33.10	27	231	81	340	1
176	33.87	30	256	73	349	1
177	34.46	26	234	81	342	1
178	35.29	40	229	74	330	1
179	35.75	22	201	86	158	1
180	35.85	29	222	84	336	1
181	36.10	19	187	80	161	1
182	37.59	29	225	83	337	1
183	37.97	15	163	74	165	1
184	38.55	42	218	78	323	1
185	38.80	26	183	79	153	1
186	38.82	34	213	85	330	1
187	39.10	26	260	79	353	1
188	39.86	34	309	71	028	1
189	40.27	38	233	73	333	1
190	40.44	23	219	88	340	1

# Appendix H Borehole 4A

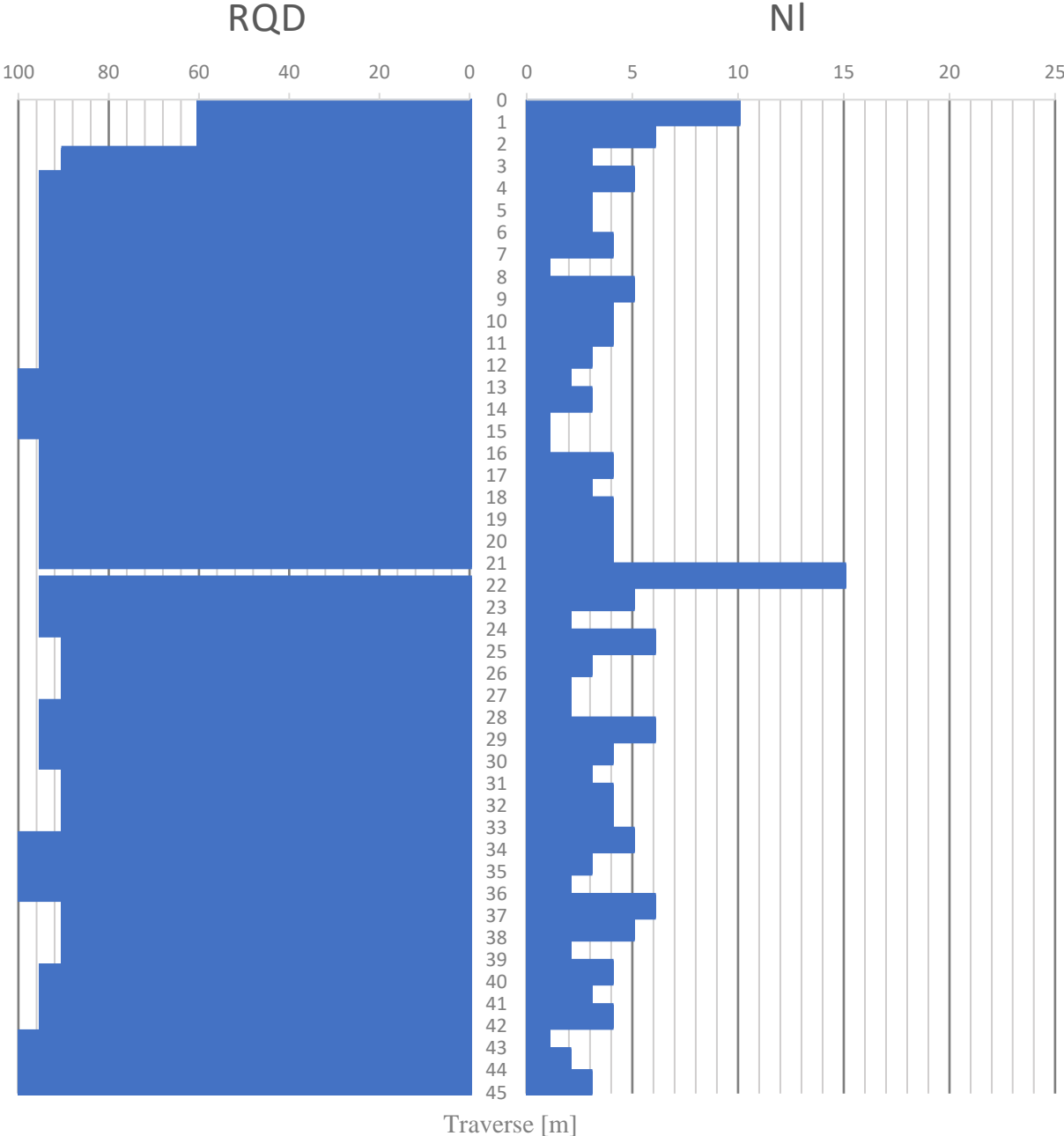


Figure H.1: RQD and NI (joint frequency per meter) for borehole 4A.



4A - Box 1 (0-5 m)						4A - Box 2 (5-11 m)						
Nl (m)	10 (0-1)	6 (1-2)	3 (2-3)	5 (3-4)	3 (4-5)	Nl (m)	3 (5-6)	4 (6-7)	1 (7-8)	5 (8-9)	4 (9-10)	4 (10-11)
RQD (m)	60 (0-2.1)		90 (2.1-3-2)		95 (3.2-5.0)	RQD (m)	95 (5.0-11.0)					
Assumed rock type: Metagreywacke (0-5.0 m)						Assumed rock type: Metagreywacke (5.0-11.0 m)						



**4A - Box 3 (11-16 m)**

Nl (m)	3 (11-12)	2 (12-13)	3 (13-14)	1 (14-15)	1 (15-16)
RQD (m)	95 (11.0-12.2)		100 (12.2-15.2)	95 (15.2-16.0)	

Assumed rock type: Metagreywacke (11.0-16.0 m)

**4A - Box 4 (16-21 m)**

Nl (m)	4 (16-17)	3 (17-18)	4 (18-19)	4 (19-20)	4 (20-21)
RQD (m)	95 (16.0-21.0)				

Assumed rock type: Metagreywacke (16.0-22.0 m)





**4A - Box 5 (21-26 m)**

Nl (m)	15 (21-22)	5 (22-23)	2 (23-24)	6 (24-25)	3 (25-26)
RQD (m)	95 (21.0-21.1)	0 (21.1-21.6)	95 (21.6-24.2)	90 (24.2-26.0)	

Assumed rock type: Metagreywacke (22.0-26.0 m)

Comments:

Rock sample for rock mechanical investigations (23.15-23.5 m)



**4A - Box 6 (26-32 m)**

Nl (m)	2 (26-27)	2 (27-28)	6 (28-29)	4 (29-30)	3 (30-31)	4 (31-32)
RQD (m)	90 (26.0-27.2)		95 (27.2-30.2)		90 (30.2-32.0)	

Assumed rock type: Metagreywacke (26.0-32.0 m)

Comments:

Rock sample for rock mechanical investigations (26.15-26.75 m)



**4A - Box 7 (32-38 m)**

**4A - Box 8 (38-42 m)**

Nl (m)	4 (32-33)	5 (33-34)	3 (34-35)	2 (35-36)	6 (36-37)	5 (37-38)	Nl (m)	2 (38-39)	4 (39-40)	3 (40-41)	4 (41-42)
RQD (m)	90 (32.0-33.2)		100 (33.2-36.2)		90 (36.2-38.0)		RQD (m)	90 (38.0-39.2)		95 (39.2-42.0)	
<u>Assumed rock type:</u> Metagreywacke (32.0-38.0 m)							<u>Assumed rock type:</u> Metagreywacke (38.0-38.9 m), polymictic conglomerate (38.9-39.0 m), metagreywacke (39.0-39.2 m), polymictic conglomerate (39.2-39.3 m), metagreywacke (39.3-40.5 m), polymictic conglomerate (40.5-42.0 m)				
<u>Jointing:</u>							<u>Jointing:</u>				
<u>Comments:</u>							<u>Comments:</u>				



**4A - Box 9 (42-45.15 m)**

NI (m)	1 (42-43)	2 (43-44)	3 (44-45)
RQD (m)	95 (42.0-42.2)	100 (42.2-45.15)	
<p><u>Assumed rock type:</u> Polymictic conglomerate (40.5-43.3 m), metagreywacke (43.3-45.15 m)</p> <p><u>Comments:</u></p> <p>Rock samples for rock mechanical investigations (42.15-42.65 m)</p>			

Table H. 1: Joint orientation measurements from borehole 4A.

<b>Borehole 4A</b>						
Joint nr.	Traverse [m]	True dip [°]	True dip direction [°]	Relative dip [°]	Relative dip direction [°]	fi-factor
1	0.65	46	257	57	344	1.5
2	0.86	22	285	81	157	1
3	0.91	23	223	86	342	1
4	1.00	48	251	57	339	1.5
5	1.10	26	207	90	336	1
6	1.12	31	245	73	344	1
7	1.44	39	143	57	146	1.5
8	1.68	31	172	75	149	1
9	1.78	35	174	75	144	1
10	1.86	28	195	86	153	1
11	1.94	31	137	58	156	1.5
12	2.01	31	157	67	151	1
13	2.04	30	149	64	153	1
14	2.10	41	181	80	139	1
15	2.57	33	161	69	148	1
16	2.90	36	182	80	143	1
17	3.06	23	223	86	342	1
18	3.15	44	198	88	317	1
19	3.64	33	144	60	152	1
20	4.21	30	189	83	150	1
21	4.44	30	150	61	144	1
22	5.25	37	128	50	154	1.5
23	5.40	77	295	30	041	1.5
24	6.12	38	239	69	337	1
25	6.14	43	246	63	338	1
26	6.33	38	136	53	150	1.5
27	6.96	27	248	76	348	1
28	7.38	54	276	46	001	1.5
29	7.89	45	255	58	343	1.5
30	8.15	22	111	59	173	1.5
31	8.56	24	281	77	002	1
32	8.96	23	169	75	157	1
33	9.21	21	227	86	344	1
34	9.41	29	216	85	335	1
35	9.68	18	227	88	347	1
36	10.10	29	216	85	335	1
37	10.17	26	164	72	154	1
38	10.72	22	131	62	165	1
39	10.93	54	262	48	345	1.5
40	11.57	12	144	72	171	1
41	11.71	21	205	88	160	1
42	12.72	28	280	72	002	1
43	13.38	20	255	81	353	1
44	13.53	13	248	89	354	1
45	13.72	9	124	72	175	1
46	13.94	13	109	67	177	1
47	14.91	26	241	78	345	1
48	15.15	6	345	82	186	1
49	15.28	26	257	76	352	1
50	15.68	17	147	70	165	1
51	16.06	26	249	77	349	1
52	16.14	35	249	69	344	1
53	16.35	32	171	68	358	1
54	16.64	32	169	73	147	1
55	16.81	49	274	51	359	1.5
56	17.01	41	272	59	358	1.5
57	17.31	27	263	73	354	1
58	17.94	16	153	72	165	1
59	18.10	21	138	65	164	1
60	18.15	30	279	70	002	1
61	18.53	15	226	90	349	1
62	18.95	24	269	77	358	1
63	19.10	19	257	82	354	1
64	19.30	27	268	73	357	1
65	19.60	25	178	78	154	1
66	19.88	21	223	87	343	1
67	19.99	30	225	81	337	1

68	20.12	27	201	88	154	1
69	20.28	27	211	88	336	1
70	20.50	24	247	79	349	1
71	20.54	23	252	79	351	1
72	20.60	28	244	76	345	1
73	20.92	27	277	73	001	1
74	20.99	25	267	75	357	1
75	21.13	26	265	74	355	1
76	21.15	13	270	87	359	1
77	21.24	14	261	87	357	1
78	21.33	32	261	69	352	1
79	21.46	13	270	87	359	1
80	21.58	38	278	63	002	1
81	21.94	61	221	65	309	1
82	22.17	40	202	87	322	1
83	22.36	37	258	65	349	1
84	22.58	21	236	83	347	1
85	22.98	34	195	87	147	1
86	23.49	43	212	80	322	1
87	23.69	44	171	73	136	1
88	23.83	16	271	84	359	1
89	24.14	21	259	80	354	1
90	24.29	46	010	79	227	1
91	24.55	22	253	80	352	1
92	24.69	36	171	64	358	1
93	25.18	25	254	77	351	1
94	25.31	29	286	71	006	1
95	25.85	33	285	67	061	1
96	26.50	55	308	54	033	1.5
97	26.72	21	269	79	358	1
98	27.15	25	288	75	006	1
99	27.82	43	298	60	018	1
100	28.08	26	249	77	349	1
101	28.18	24	255	78	352	1
102	28.60	21	227	86	344	1
103	28.84	23	243	80	348	1
104	28.91	29	240	76	343	1
105	28.93	27	231	80	341	1
106	29.38	33	199	89	148	1
107	29.57	7	146	75	174	1
108	29.64	35	254	68	348	1
109	29.99	31	234	76	339	1
110	30.15	30	256	71	350	1
111	30.71	35	201	89	327	1
112	31.03	48	279	52	003	1.5
113	31.44	39	254	64	345	1
114	31.51	32	251	71	347	1
115	31.70	35	218	80	331	1
116	31.88	25	254	77	351	1
117	32.19	16	250	85	353	1
118	32.36	41	217	78	325	1
119	32.64	43	259	59	348	1.5
120	32.89	31	240	75	342	1
121	33.00	32	248	72	345	1
122	33.09	26	234	80	343	1
123	33.15	27	234	79	342	1
124	33.58	26	238	79	344	1
125	33.75	31	225	80	336	1
126	33.87	26	221	85	339	1
127	34.06	29	213	86	334	1
128	34.26	29	247	75	347	1
129	34.38	23	219	87	341	1
130	34.98	65	277	35	003	1.5
131	35.37	50	312	61	032	1
132	36.16	34	186	82	146	1
133	36.23	37	194	87	143	1
134	36.48	21	219	88	342	1
135	36.70	31	202	90	151	1
136	36.88	38	215	80	327	1
137	36.98	51	194	89	310	1
138	37.25	19	212	89	163	1
139	37.30	27	234	79	342	1

140	37.47	32	217	83	333	1
141	37.73	28	228	80	339	1
142	37.90	32	257	69	350	1
143	37.99	43	242	64	335	1
144	38.60	39	246	66	340	1
145	38.83	38	147	59	146	1.5
146	39.15	34	148	62	150	1
147	39.32	16	153	72	165	1
148	39.38	27	282	73	003	1
149	39.30	16	271	84	359	1
150	40.19	28	159	69	153	1
151	40.90	29	240	76	343	1
152	41.25	16	209	87	165	1
153	41.54	33	223	80	334	1
154	41.74	28	195	86	153	1
155	42.01	40	114	43	162	1.5
156	42.15	24	259	77	353	1
157	42.92	23	182	80	156	1
158	43.25	26	224	84	340	1
159	43.51	20	272	80	359	1
160	43.84	19	246	83	351	1
161	44.14	22	248	80	350	1
162	44.34	17	243	85	351	1
163	44.51	26	252	76	350	1
164	44.81	26	221	85	339	1
165	45.06	13	179	79	167	1
166	45.12	25	199	87	155	1

# Appendix I Borehole 5A

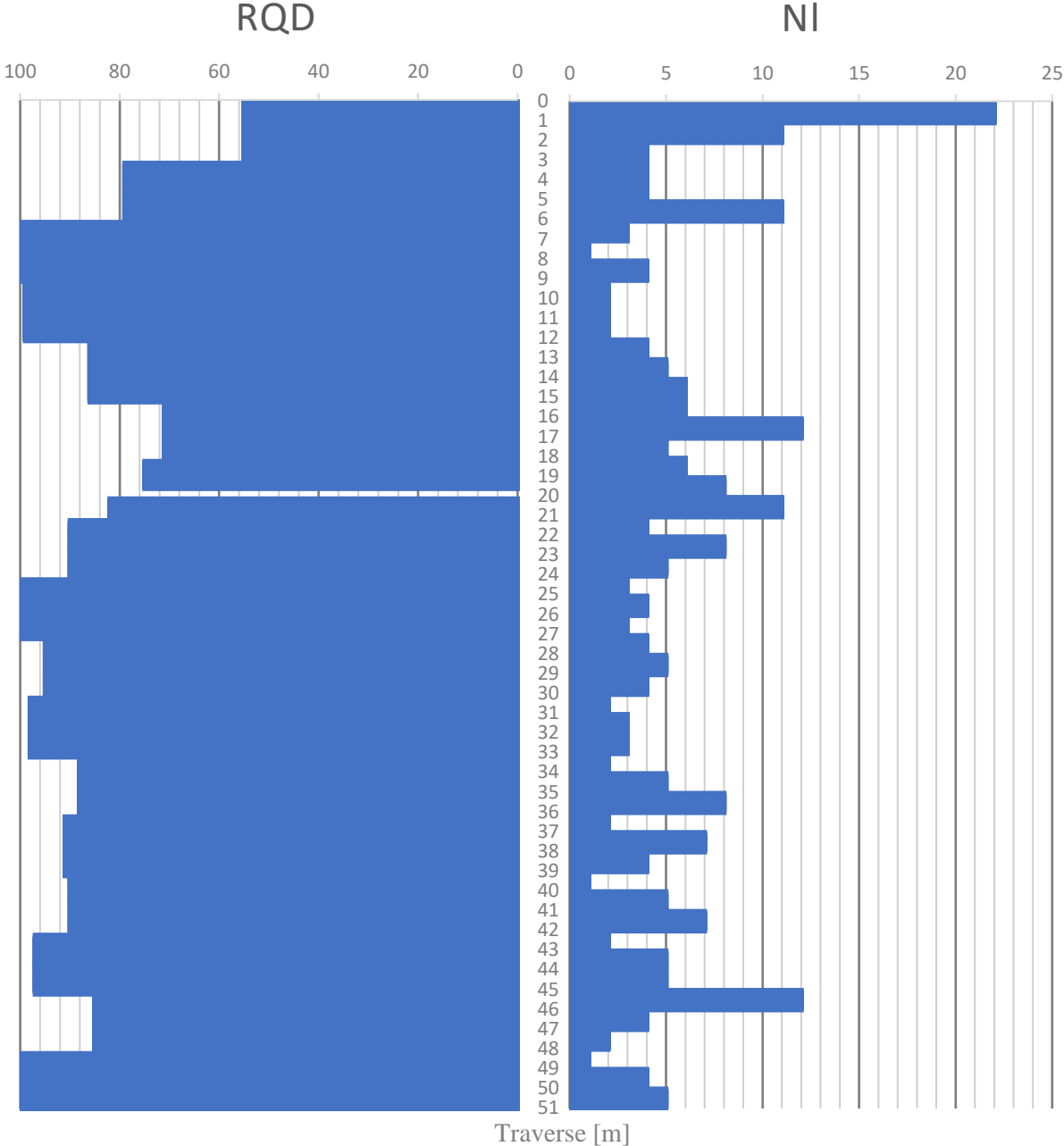


Figure I.1: RQD and NI (joint frequency per meter) fore borehole 5A.



5A - Box 1 (0-6 m)							5A - Box 2 (6-12 m)						
NI (m)	22 (0-1)	11 (1-2)	4 (2-3)	4 (3-4)	4 (4-5)	11 (5-6)	NI (m)	3 (6-7)	1 (7-8)	4 (8-9)	2 (9-10)	2 (10-11)	2 (11-12)
RQD (m)	55 (0-3.1)			79 (3.1-6.0)			RQD (m)	79 (6.0-6.1)		100 (6.1-9.1)		99 (9.1-12.0)	
Assumed rock type: Metagreywacke (0-6.0 m)							Assumed rock type: Metagreywacke (6.0-10.1 m), polymictic conglomerate (10.1-11.2 m), metagreywacke (11.2-12.0 m)						





**5A - Box 3 (12-18 m)**

**5A - Box 4 (18-22 m)**

NI (m)	4 (12-13)	5 (13-14)	6 (14-15)	6 (15-16)	12 (16-17)	5 (17-18)	NI (m)	6 (18-19)	8 (19-20)	11 (20-21)	4 (21-22)	
RQD (m)	99 (12.0-12.1)		86 (12.1-15.2)		71 (15.2-18.0)		RQD (m)	71 (18.0-18.2)	75 (18.2-19.6)	0 (19.6-20.1)	82 (20.1-21.2)	90 (21.2-22.0)

Assumed rock type: Metagreywacke (12.0-18.0 m)

Assumed rock type: Metagreywacke (18.0-22.0 m)

Comments:

Rock sample for rock mechanical investigations (17.35-17.95 m)



**5A - Box 5 (22-27 m)**

NI (m)	8 (22-23)	5 (23-24)	3 (24-25)	4 (25-26)	3 (26-27)
RQD (m)	90 (22.0-24.2)		100 (24.2-27.0)		

Assumed rock type: Metagreywacke (22.0-27.0 m)

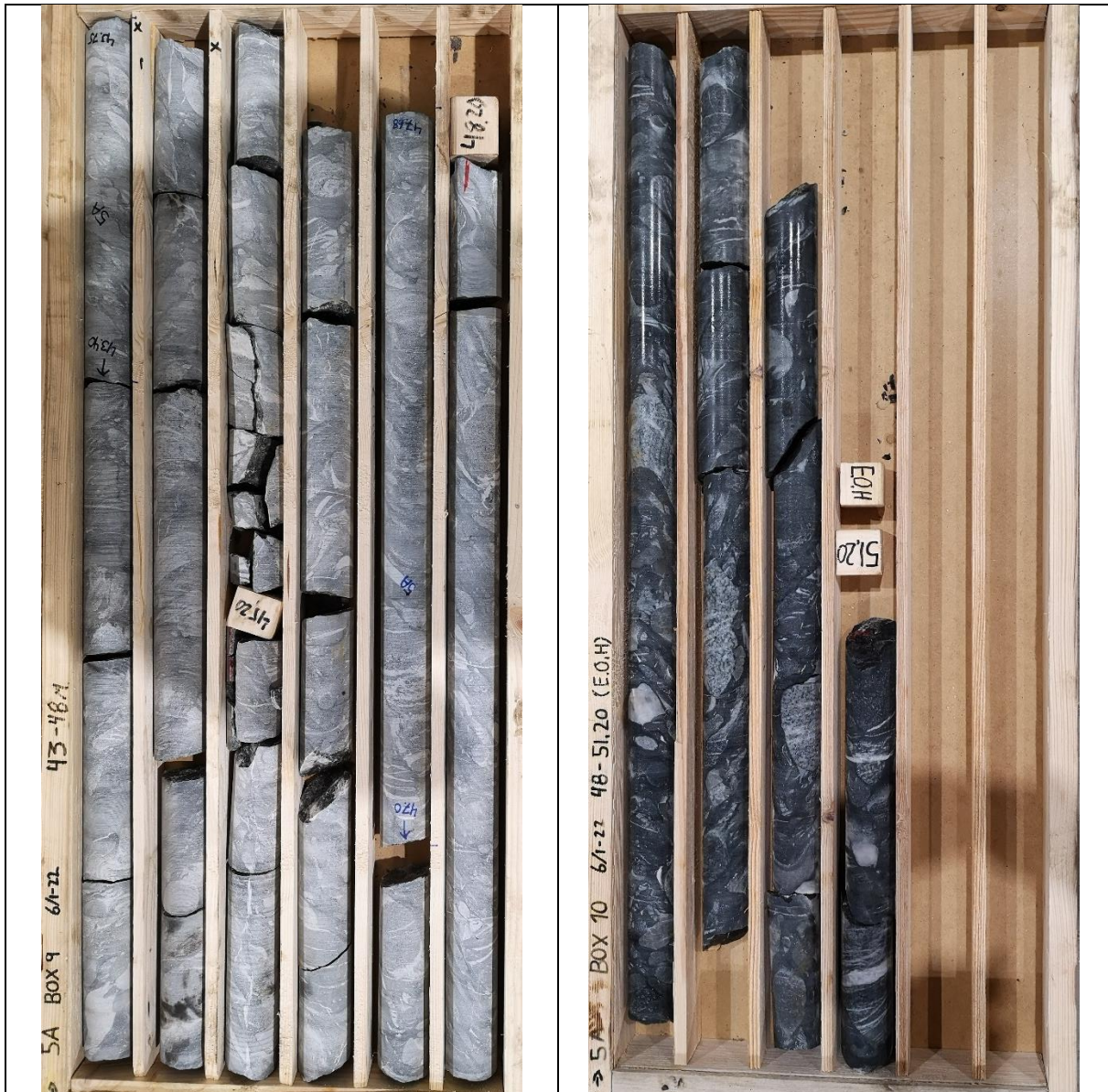
**5A - Box 6 (27-32 m)**

NI (m)	4 (27-28)	5 (28-29)	4 (29-30)	2 (30-31)	3 (31-32)
RQD (m)	100 (27.0-27.2)		95 (27.2-30.2)		98 (30.2-32.0)

Assumed rock type: Metagreywacke (27.0-30.0 m), polymictic conglomerate (30.0-32.0 m)



5A - Box 7 (32-37 m)						5A - Box 8 (37-43 m)						
NI (m)	3 (32-33)	2 (33-34)	5 (34-35)	8 (35-36)	2 (36-37)	NI (m)	7 (37-38)	4 (38-39)	1 (39-40)	5 (40-41)	7 (41-42)	2 (42-43)
RQD (m)	98 (32.0-33.2)		88 (33.2-36.2)		91 (36.2-37.0)	RQD (m)	91 (37.0-39.2)		90 (39.2-42.2)		97 (42.2-43.0)	
Assumed rock type: Metagreywacke (32.0-37.0 m)						Assumed rock type: Polymictic conglomerate (37.0-37.1 m), metagreywacke (37.1-37.9 m), polymictic conglomerate (37.9-43.0 m)						
						<u>Comments:</u>						



5A - Box 9 (43-48 m)						5A - Box 10 (48-51.20 m)			
NI (m)	5 (43-44)	5 (44-45)	12 (45-46)	4 (46-47)	2 (47-48)	NI (m)	1 (48-49)	4 (49-50)	5 (50-51)
RQD (m)	97 (43.0-45.2)		85 (45.2-48.0)			RQD (m)	85 (48.0-48.2)		100 (48.2-51.20)
Assumed rock type: Metagreywacke (43.0-48.0 m)						Assumed rock type: Metagreywacke (48.0-51.20 m)			
<u>Comments:</u> Rock samples for rock mechanical investigations (43.40-43.75 m and 47.0-47.68 m)									

Table I. 1: Joint orientation measurements from borehole 5A.

Borehole 5A						
Joint nr.	Traverse [m]	True dip [°]	True dip direction [°]	Relative dip [°]	Relative dip direction [°]	fi-factor
1	6.50	32	109	82	336	1
2	7.06	29	144	74	353	1
3	7.43	65	109	61	309	1
4	7.95	31	196	78	019	1
5	8.20	16	261	74	197	1
6	8.64	65	261	73	248	1
7	8.76	23	170	81	005	1
8	8.90	20	186	85	009	1
9	9.12	6	242	78	186	1
10	9.65	13	240	83	212	1
11	10.42	27	238	83	207	1
12	10.61	10	225	81	189	1
13	11.13	26	201	83	018	1
14	11.14	28	204	84	020	1
15	11.50	42	137	63	144	1
16	11.62	37	131	70	343	1
17	12.09	60	131	51	329	1.5
18	12.37	43	104	77	326	1
19	12.82	27	287	61	204	1
20	13.04	22	192	84	012	1
21	13.21	25	169	79	005	1
22	13.49	15	229	82	195	1
23	13.64	15	270	72	195	1
24	13.78	17	227	83	196	1
25	14.21	25	142	79	353	1
26	14.28	34	156	69	359	1
27	14.41	23	141	81	353	1
28	14.73	35	127	73	342	1
29	14.81	40	132	67	342	1
30	14.90	36	138	70	348	1
31	15.20	26	126	81	347	1
32	15.46	20	151	83	358	1
33	15.63	19	162	84	001	1
34	15.72	34	160	69	001	1
35	15.91	27	180	78	010	1
36	15.96	31	193	77	018	1
37	16.12	37	174	68	010	1
38	16.44	42	150	62	354	1
39	16.65	26	176	78	008	1
40	17.06	33	172	71	008	1
41	17.24	33	158	70	360	1
42	17.36	37	179	69	013	1
43	17.66	44	138	62	344	1
44	17.96	24	189	82	012	1
45	18.09	36	182	70	150	1
46	18.20	35	202	78	024	1
47	18.33	32	148	71	354	1
48	18.56	35	197	75	022	1
49	18.58	33	202	79	023	1
50	18.89	46	163	57	005	1.5
51	19.09	36	192	73	020	1
52	19.20	36	176	69	011	1
53	19.26	53	142	52	343	1.5
54	19.37	39	236	87	218	1
55	19.43	33	223	88	029	1
56	19.90	34	092	88	329	1
57	19.93	38	175	67	011	1
58	20.04	45	183	62	020	1
59	20.12	43	180	63	017	1
60	20.15	42	181	64	017	1
61	20.30	49	201	67	034	1
62	20.36	30	207	83	023	1
63	20.42	36	178	70	012	1
64	20.51	37	114	76	334	1
65	20.70	42	161	61	002	1

66	20.81	46	155	57	358	1.5
67	20.99	40	150	64	354	1
68	21.04	41	156	62	359	1
69	21.20	40	158	63	360	1
70	21.45	23	111	87	343	1
71	22.23	42	179	63	016	1
72	22.34	10	225	81	189	1
73	22.46	20	165	83	002	1
74	22.58	31	158	82	360	1
75	22.93	46	158	57	360	1.5
76	23.00	33	131	74	345	1
77	23.10	24	060	75	155	1
78	23.14	28	146	75	354	1
79	23.74	33	114	79	337	1
80	24.01	22	115	87	345	1
81	24.20	23	141	81	353	1
82	24.50	16	111	88	169	1
83	24.90	31	166	72	005	1
84	25.14	36	204	78	026	1
85	25.59	12	152	89	179	1
86	25.82	19	229	83	198	1
87	26.14	8	206	82	186	1
88	26.77	17	239	80	197	1
89	26.93	13	132	89	174	1
90	27.20	30	083	86	151	1
91	27.23	35	093	87	328	1
92	28.01	29	149	74	355	1
93	28.14	35	171	69	008	1
94	28.34	28	195	80	017	1
95	28.71	46	201	69	032	1
96	28.91	29	198	80	019	1
97	29.16	16	253	76	197	1
98	29.78	43	126	66	336	1
99	30.13	15	242	79	196	1
100	30.20	26	228	87	205	1
101	30.49	19	169	84	003	1
102	31.24	7	167	84	181	1
103	31.45	36	140	69	349	1
104	31.52	22	158	81	360	1
105	32.37	22	161	82	001	1
106	32.63	11	119	85	173	1
107	32.89	26	251	77	207	1
108	33.20	20	175	84	006	1
109	33.83	26	247	79	209	1
110	34.41	62	277	59	245	1.5
111	34.62	23	146	81	355	1
112	35.16	19	265	72	199	1
113	35.61	21	187	84	010	1
114	35.70	19	219	87	197	1
115	35.75	19	262	73	200	1
116	35.93	20	200	88	013	1
117	36.18	19	190	87	010	1
118	36.20	18	225	85	197	1
119	37.10	54	248	82	234	1
120	37.21	39	206	76	029	1
121	37.77	24	266	71	205	1
122	38.24	38	195	73	023	1
123	38.39	29	261	73	209	1
124	39.15	15	270	72	195	1
125	39.20	26	171	78	006	1
126	40.13	21	167	82	003	1
127	40.56	38	144	67	351	1
128	40.75	23	149	80	357	1
129	40.89	19	169	84	003	1
130	41.10	22	205	88	016	1
131	41.39	15	250	77	196	1
132	41.52	17	239	80	197	1
133	41.60	9	285	71	188	1
134	41.88	18	184	87	008	1
135	41.94	16	349	62	177	1
136	42.13	17	348	60	177	1
137	42.85	22	158	81	360	1

138	43.28	23	128	83	349	1
139	43.49	20	093	86	162	1
140	43.82	15	186	90	187	1
141	44.10	20	141	84	354	1
142	44.45	11	094	82	170	1
143	44.64	15	288	68	192	1
144	44.78	14	325	63	183	1
145	44.97	19	162	84	001	1
146	45.42	24	189	82	012	1
147	45.57	29	186	77	013	1
148	46.08	23	167	80	003	1
149	36.35	22	124	84	348	1
150	46.52	4	043	75	077	1
151	47.37	6	327	71	181	1
152	48.07	20	165	83	002	1
153	48.20	10	257	76	190	1
154	49.12	44	219	80	038	1
155	49.58	24	247	79	205	1
156	49.78	17	182	88	007	1
157	49.99	16	277	70	195	1
158	50.13	25	182	80	010	1
159	50.33	35	194	74	021	1
160	50.55	60	217	71	052	1
161	50.81	49	234	88	047	1
162	50.97	45	282	57	224	1.5

# Appendix J Borehole 5X

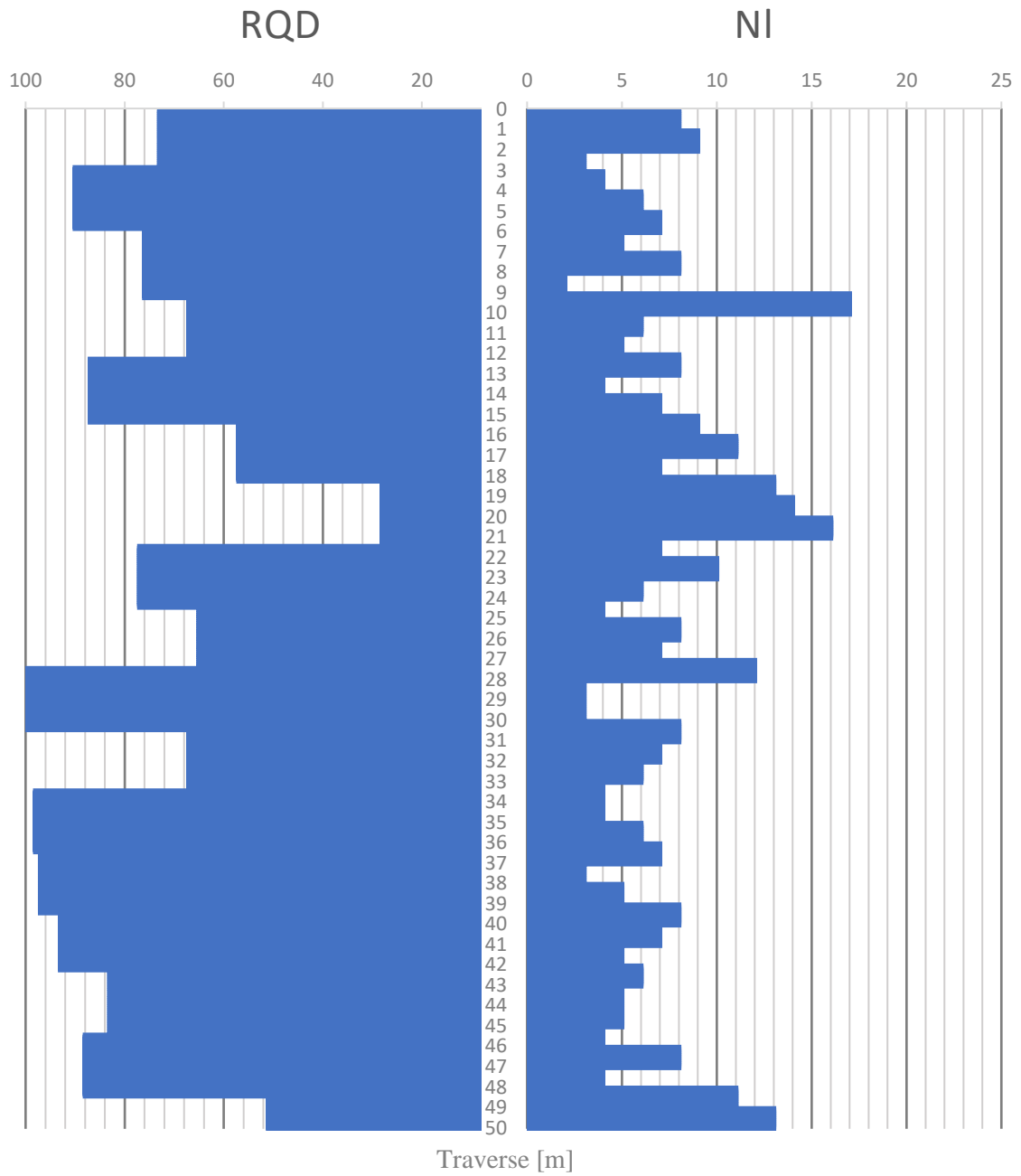
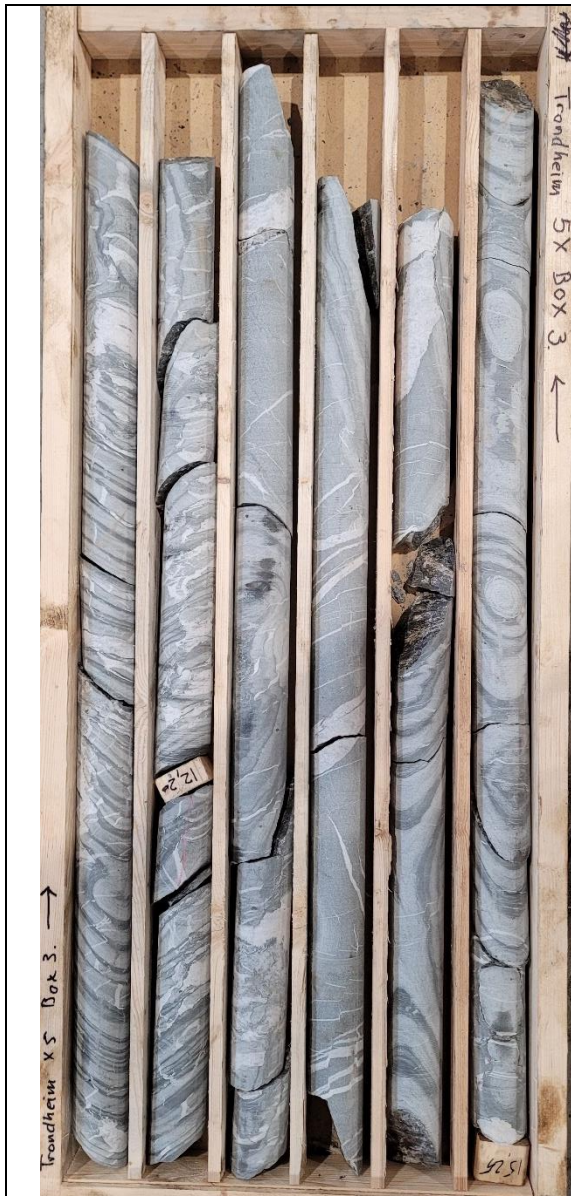


Figure J.1: RQD and NI (joint frequency per meter) for borehole 5X.

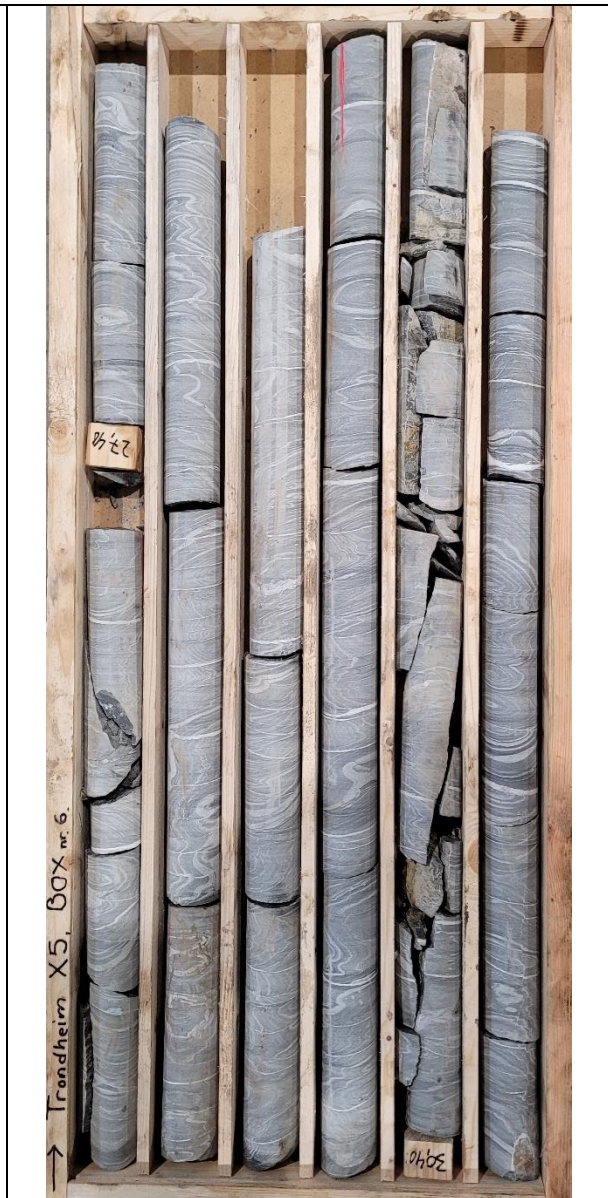




5X - Box 1 (0-5 m)						5X - Box 2 (5-11 m)						
Nl (m)	8 (0-1)	9 (1-2)	3 (2-3)	4 (3-4)	6 (4-5)	Nl (m)	7 (5-6)	5 (6-7)	8 (7-8)	2 (8-9)	17 (9-10)	6 (10-11)
RQD (m)	73 (0-2.8)		90 (2.8-5.0)			RQD (m)	90 (5.0-5.8)		76 (5.8-9.2)		67 (9.2-11.0)	
Assumed rock type: Metagreywacke (0-5.0 m)						Assumed rock type: Metagreywacke (5.0-11.0 m)						



5X - Box 3 (11-16 m)						5X - Box 4 (16-22 m)						
NI (m)	5 (11-12)	8 (12-13)	4 (13-14)	7 (14-15)	9 (15-16)	NI (m)	11 (16-17)	7 (17-18)	13 (18-19)	14 (19-20)	16 (20-21)	7 (21-22)
RQD (m)	67 (11.0-12.2)		87 (12.2-15.3)		57 (15.3-16.0)	RQD (m)	57 (16.0-18.2)		28 (18.2-21.4)		77 (21.4-22.0)	
Assumed rock type: Metagreywacke (11.0-16.0 m)						Assumed rock type: Metagreywacke (16.0-21.0 m)						



5X - Box 5 (22-27 m)						5X - Box 6 (27-32 m)					
NI (m)	10 (22-23)	6 (23-24)	4 (24-25)	8 (25-26)	7 (26-27)	NI (m)	12 (27-28)	3 (28-29)	3 (29-30)	8 (30-31)	7 (31-32)
RQD (m)	77 (22.0-24.4)		65 (24.4-27.0)			RQD (m)	65 (27.0-27.4)		100 (27.4-30.4)		67 (30.4-32.0)
Assumed rock type: Metagreywacke (21.0-27.0 m)						Assumed rock type: Metagreywacke (27.0-32.0 m)					



**5X - Box 7 (32-38 m)**

NI (m)	6 (32-33)	4 (33-34)	4 (34-35)	6 (35-36)	7 (36-37)	3 (37-38)
RQD (m)	67 (32.0-33.4)		98 (33.4-36.4)		97 (36.4-38.0)	

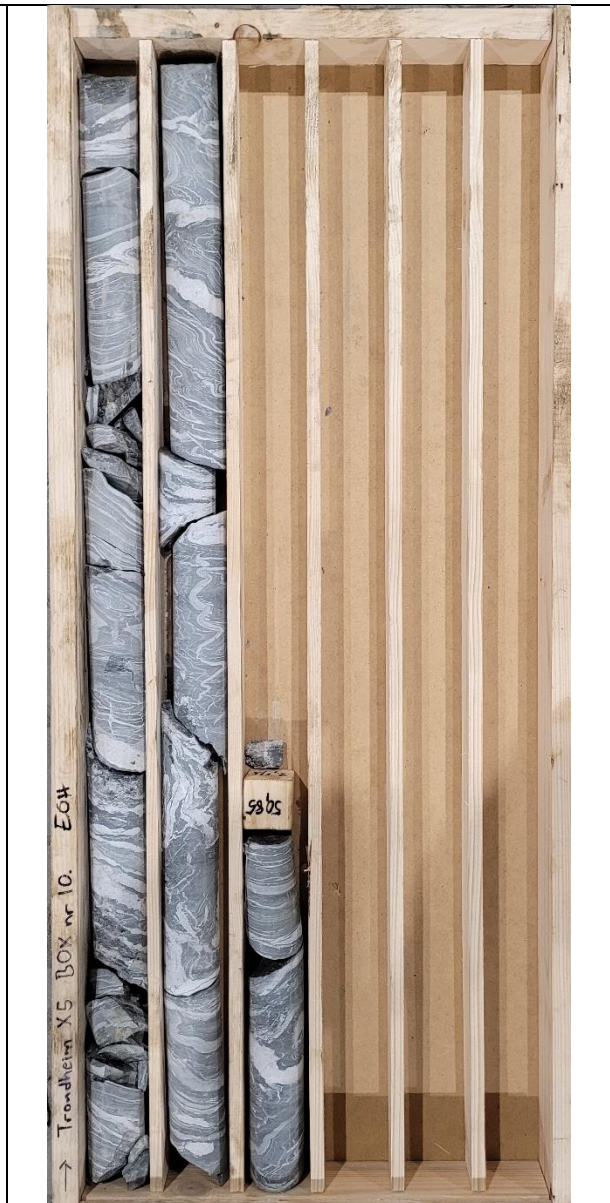
Assumed rock type: Metagreywacke (32.0-38.0 m)

**5X - Box 8 (38-44 m)**

NI (m)	5 (38-39)	8 (39-40)	7 (40-41)	5 (41-42)	6 (42-43)	5 (43-44)
RQD (m)	97 (38.0-39.4)		93 (39.4-42.4)		83 (42.4-44.0)	

Assumed rock type: Metagreywacke (38.0-44.0 m)

Comments:  
Rock sample for rock mechanical investigations (40.2-40.8 m and 41.10-41.55 m)



5X - Box 9 (44-49 m)						5X - Box 10 (49-50.85 m)	
Nl (m)	5 (44-45)	4 (45-46)	8 (46-47)	4 (47-48)	11 (48-49)	Nl (m)	13 (49-50)
RQD (m)	83 (44.0-45.4)	88 (45.4-48.4)	51 (48.4-49.0)			RQD (m)	51 (49.0-50.85)
Assumed rock type: Metagreywacke (44.0-49.0 m)						Assumed rock type: Metagreywacke (49.0-58.85 m)	

Table J. 1: Joint orientation measurements from borehole 5X.

Borehole 5X						
Joint nr.	Traverse [m]	True dip [°]	True dip direction [°]	Relative dip [°]	Relative dip direction [°]	fi-factor
1	0.07	12	187	75	169	1
2	0.32	41	257	69	001	1
3	0.42	32	272	79	009	1
4	0.45	29	271	82	008	1
5	0.54	14	286	89	12	1
6	0.83	24	286	89	12	1
7	0.95	26	326	81	205	1
8	1.10	48	266	63	009	1
9	1.67	42	264	68	007	1
10	1.82	26	305	88	207	1
11	2.05	44	276	69	016	1
12	2.49	35	286	79	018	1
13	3.03	32	264	79	005	1
14	3.77	29	289	86	016	1
15	4.00	30	230	82	348	1
16	4.32	45	270	67	011	1
17	4.36	42	261	68	005	1
18	4.54	24	224	89	348	1
19	4.58	65	297	61	044	1
20	4.91	50	189	86	316	1
21	5.11	30	194	86	154	1
22	5.31	47	308	80	037	1
23	5.59	41	202	83	328	1
24	5.85	52	302	72	037	1
25	6.36	70	279	46	032	1.5
26	6.56	50	272	62	015	1
27	6.85	19	297	84	192	1
28	6.92	37	270	75	009	1
29	7.54	60	273	53	020	1.5
30	7.80	77	155	76	199	1
31	8.50	16	355	68	197	1
32	8.80	11	317	76	190	1
33	9.27	72	157	77	105	1
34	9.38	63	263	47	010	1.5
35	9.54	71	001	69	257	1
36	9.61	34	267	77	007	1
37	9.91	47	171	81	133	1
38	10.22	62	165	81	117	1
39	11.17	53	190	84	313	1
40	11.40	38	171	78	141	1
41	11.50	40	202	84	329	1
42	12.12	51	199	79	319	1
43	12.02	28	182	80	153	1
44	12.46	36	174	79	144	1
45	12.59	50	144	61	126	1
46	12.73	46	264	65	007	1
47	13.31	31	159	70	147	1
48	14.00	46	271	66	012	1
49	14.50	56	156	72	121	1
50	15.26	8	221	77	175	1
51	15.61	42	269	10	069	6
52	15.79	34	247	77	355	1
53	16.12	35	164	73	143	1
54	16.20	40	170	78	139	1
55	16.25	40	151	66	137	1
56	16.37	43	158	71	134	1
57	16.44	37	125	50	143	1.5
58	16.56	43	154	68	133	1
59	16.68	46	116	41	135	1.5
60	16.81	30	230	82	348	1
61	17.10	22	129	58	159	1.5
62	17.30	19	195	80	163	1
63	17.32	33	161	71	145	1
64	17.50	37	164	74	141	1
65	17.61	34	117	47	150	1.5
66	17.68	26	161	70	153	1
67	17.93	43	166	76	136	1

68	18.12	15	191	77	167	1
69	18.17	78	028	46	273	1.5
70	18.32	18	248	88	178	1
71	18.86	32	200	90	154	1
72	19.02	29	221	86	334	1
73	19.11	35	318	88	211	1
74	19.16	36	302	84	026	1
75	19.23	27	317	84	204	1
76	19.28	18	321	78	197	1
77	19.45	39	243	71	352	1
78	19.57	51	225	66	335	1
79	19.66	18	248	88	178	1
80	19.73	32	322	85	210	1
81	19.84	25	347	71	207	1
82	20.06	25	333	77	205	1
83	20.12	50	274	63	017	1
84	20.23	17	311	80	195	1
85	20.34	24	197	84	160	1
86	20.70	41	357	67	224	1
87	20.92	62	237	51	339	1.5
88	21.40	33	186	84	149	1
89	20.09	42	261	68	005	1
90	21.12	43	273	69	013	1
91	22.31	33	245	78	354	1
92	22.47	54	234	59	340	1.5
93	22.70	14	178	74	165	1
94	23.24	27	163	72	152	1
95	23.31	28	199	87	157	1
96	23.35	43	235	70	345	1
97	24.16	45	251	65	357	1
98	24.32	14	178	74	165	1
99	25.02	30	248	80	357	1
100	25.04	8	231	78	177	1
101	25.57	74	006	66	261	1
102	25.62	46	244	65	351	1
103	25.81	40	235	73	347	1
104	26.14	22	102	51	168	1.5
105	26.62	17	140	64	162	1
106	26.88	17	140	64	162	1
107	26.96	75	143	65	097	1
108	27.12	17	231	85	173	1
109	27.18	57	198	75	313	1
110	27.40	32	253	78	359	1
111	27.94	29	246	81	355	1
112	28.28	29	246	81	355	1
113	29.05	37	231	76	345	1
114	30.60	23	186	79	158	1
115	30.66	75	003	68	261	1
116	30.89	66	358	71	250	1
117	31.06	79	009	63	266	1
118	31.27	35	230	78	345	1
119	31.38	34	247	77	355	1
120	31.86	8	312	74	187	1
121	32.00	35	261	75	003	1
122	32.16	31	211	87	339	1
123	32.31	14	215	81	171	1
124	32.49	26	234	85	351	1
125	32.64	23	212	88	164	1
126	33.12	31	240	80	352	1
127	33.26	28	236	83	351	1
128	33.40	29	221	86	344	1
129	33.84	27	020	57	207	1.5
130	34.05	31	021	55	210	1.5
131	34.24	26	223	88	347	1
132	34.85	23	228	89	350	1
133	35.28	80	269	33	026	1.5
134	35.98	36	229	77	344	1
135	36.05	39	238	73	349	1
136	36.41	27	135	59	153	1.5
137	36.52	56	304	72	041	1
138	36.82	38	228	76	343	1
139	36.95	33	249	78	357	1

140	37.86	21	236	90	353	1
141	38.65	38	251	72	358	1
142	39.40	9	240	79	178	1
143	39.50	44	266	65	009	1
144	39.78	51	271	61	015	1
145	40.06	59	143	61	115	1
146	40.58	21	258	89	001	1
147	40.73	37	246	73	354	1
148	41.07	30	253	80	359	1
149	41.53	27	245	83	355	1
150	41.95	30	257	80	001	1
151	42.17	36	232	77	347	1
152	42.40	15	227	83	173	1
153	42.57	30	237	81	351	1
154	43.61	75	006	65	262	1
155	43.78	28	233	84	350	1
156	44.73	46	264	65	007	1
157	45.40	27	193	84	156	1
158	46.33	73	345	84	254	1
159	46.45	26	226	87	348	1
160	46.65	35	268	76	008	1
161	46.74	45	311	83	036	1
162	46.97	27	327	80	206	1
163	47.43	38	266	72	007	1
164	47.94	54	221	65	330	1
165	48.00	54	266	57	010	1.5
166	48.22	25	219	89	345	1
167	48.40	43	266	67	008	1
168	48.66	86	336	83	083	1
169	48.86	63	282	53	030	1.5
170	48.91	44	261	66	005	1
171	49.10	74	222	48	316	1.5
172	49.27	26	284	87	012	1
173	49.53	16	209	81	169	1
174	49.96	69	280	47	031	1.5



# Appendix K GSI and disturbance factor charts







<p><b>GEOLOGICAL STRENGTH INDEX FOR JOINTED ROCKS (Hoek and Marinos, 2000)</b></p> <p>From the lithology, structure and surface conditions of the discontinuities, estimate the average value of GSI. Do not try to be too precise. Quoting a range from 33 to 37 is more realistic than stating that GSI = 35. Note that the table does not apply to structurally controlled failures. Where weak planar structural planes are present in an unfavourable orientation with respect to the excavation face, these will dominate the rock mass behaviour. The shear strength of surfaces in rocks that are prone to deterioration as a result of changes in moisture content will be reduced if water is present. When working with rocks in the fair to very poor categories, a shift to the right may be made for wet conditions. Water pressure is dealt with by effective stress analysis.</p>		<p><b>SURFACE CONDITIONS</b></p> <p><b>VERY GOOD</b> Very rough, fresh unweathered surfaces</p> <p><b>GOOD</b> Rough, slightly weathered, iron stained surfaces</p> <p><b>FAIR</b> Smooth, moderately weathered and altered surfaces</p> <p><b>POOR</b> Slackensided, highly weathered surfaces with compact coatings or fillings or angular fragments</p> <p><b>VERY POOR</b> Slackensided, highly weathered surfaces with soft clay coatings or fillings</p>				
<p><b>STRUCTURE</b></p>		<p><b>DECREASING SURFACE QUALITY</b> →</p>				
 <p><b>INTACT OR MASSIVE</b> - intact rock specimens or massive in situ rock with few widely spaced discontinuities</p>	90			N/A	N/A	
 <p><b>BLOCKY</b> - well interlocked undisturbed rock mass consisting of cubical blocks formed by three intersecting discontinuity sets</p>	80	70				
 <p><b>VERY BLOCKY</b>- interlocked, partially disturbed mass with multi-faceted angular blocks formed by 4 or more joint sets</p>		60	50			
 <p><b>BLOCKY/DISTURBED/SEAMY</b> - folded with angular blocks formed by many intersecting discontinuity sets. Persistence of bedding planes or schistosity</p>			40	30		
 <p><b>DISINTEGRATED</b> - poorly interlocked, heavily broken rock mass with mixture of angular and rounded rock pieces</p>				20		
 <p><b>LAMINATED/SHEARED</b> - Lack of blockiness due to close spacing of weak schistosity or shear planes</p>	N/A	N/A			10	

Figure K.1: Chart for estimating GSI values for blocky rock masses (Marinos et al., 2007).

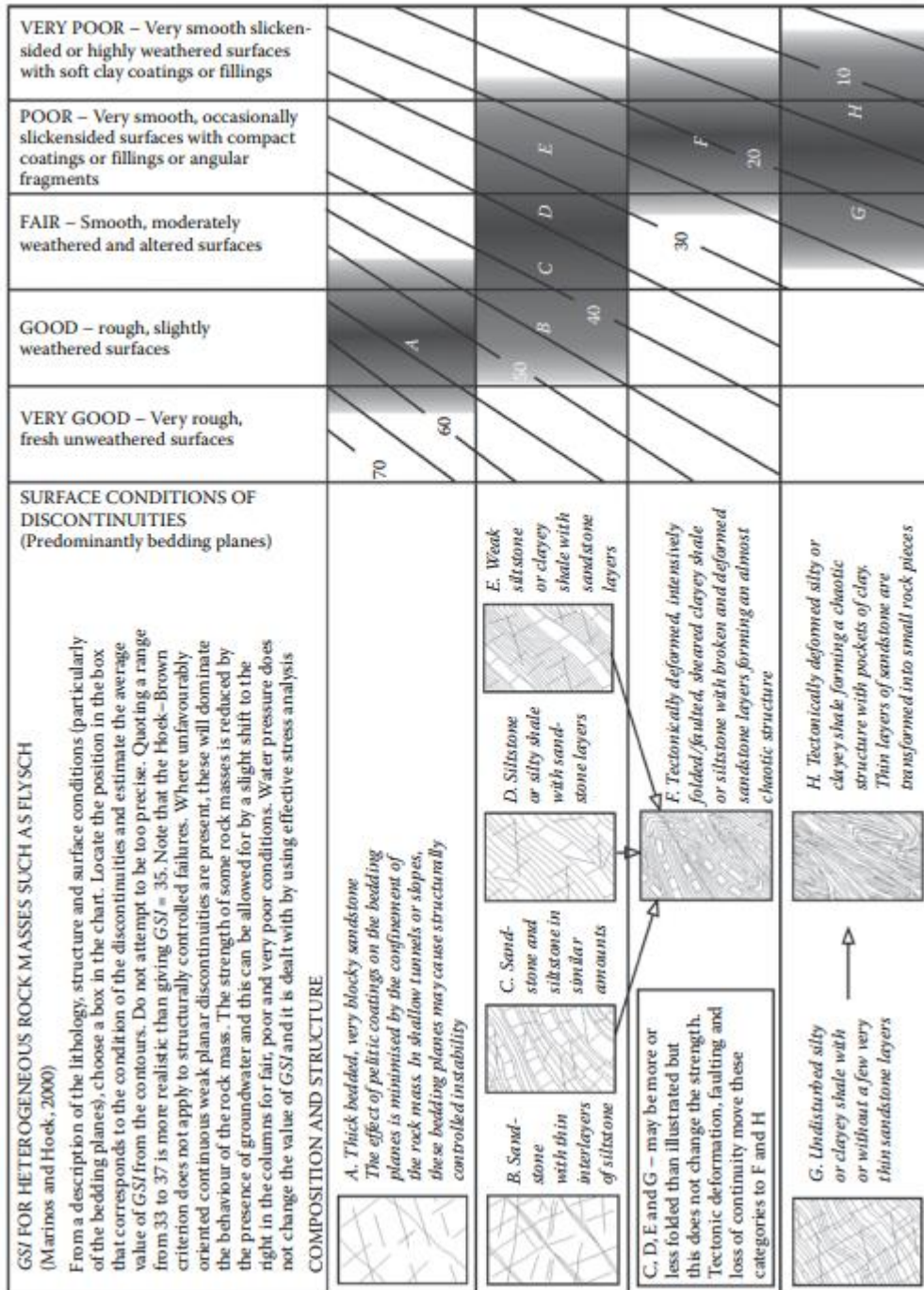







Figure K.2: Chart for estimating GSI values for heterogeneous rock masses (Wyllie, 2018).

Appearance of rock mass	Description of rock mass	Suggested value of D
	Excellent quality controlled blasting or excavation by Tunnel Boring Machine results in minimal disturbance to the confined rock mass surrounding a tunnel.	D = 0
	Mechanical or hand excavation in poor quality rock masses (no blasting) results in minimal disturbance to the surrounding rock mass.  Where squeezing problems result in significant floor heave, disturbance can be severe unless a temporary invert, as shown in the photograph, is placed.	D = 0  D = 0.5 No invert
	Very poor quality blasting in a hard rock tunnel results in severe local damage, extending 2 or 3 m, in the surrounding rock mass.	D = 0.8
	Small scale blasting in civil engineering slopes results in modest rock mass damage, particularly if controlled blasting is used as shown on the left hand side of the photograph. However, stress relief results in some disturbance.	D = 0.7 Good blasting  D = 1.0 Poor blasting
	Very large open pit mine slopes suffer significant disturbance due to heavy production blasting and also due to stress relief from overburden removal.  In some softer rocks excavation can be carried out by ripping and dozing and the degree of damage to the slopes is less.	D = 1.0 Production blasting  D = 0.7 Mechanical excavation

Small-scale blasting in civil engineering slopes results in modest rock mass damage when controlled blasting is used, as shown on the left-hand side of the photograph. Uncontrolled production blasting can result in significant damage to the rock face.

D = 0.5 for controlled presplit or smooth wall blasting with  
D = 1.0 for production blasting

Figure K.3: Guidelines for estimating disturbance factor D (from blasting damage and stress relaxation). Modified after Hoek (2007) and Hoek and Brown (2019).

## Appendix L Discontinuity sets from DSE

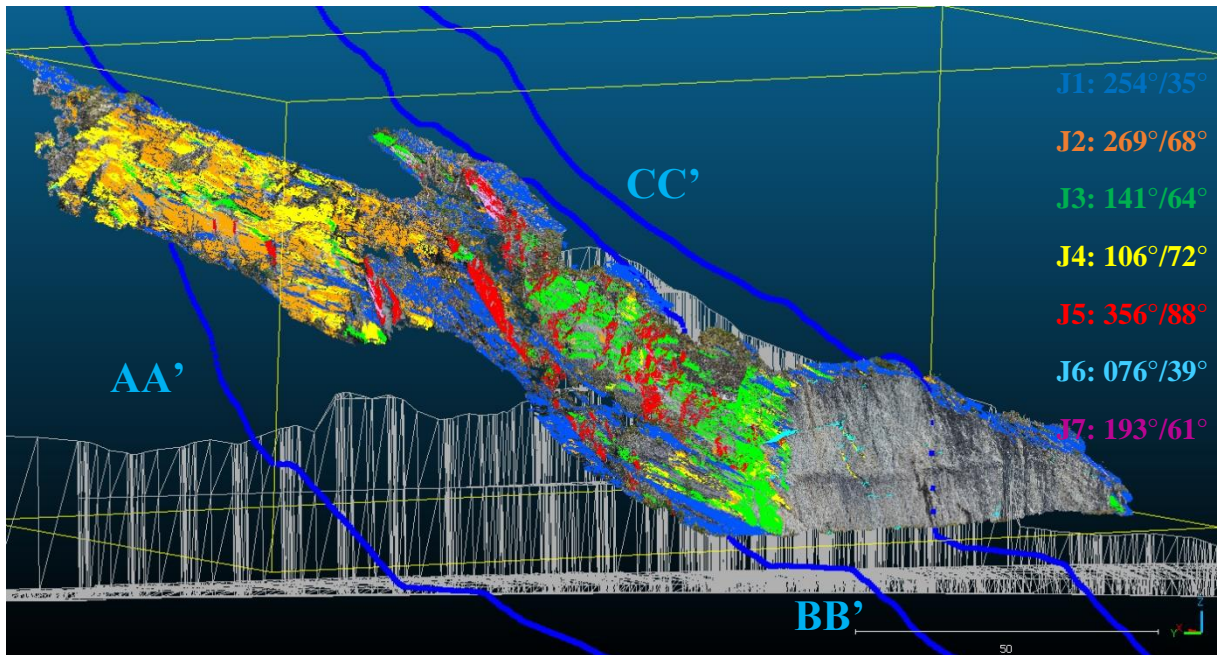


Figure L.1: Discontinuity sets (J1-J7) mapped with DSE from SfM point cloud at the current road cut. Dark blue lines indicate profile AA', BB', and CC'. Grey mesh is the planned road cut, deep blasting surface and trench bottom.

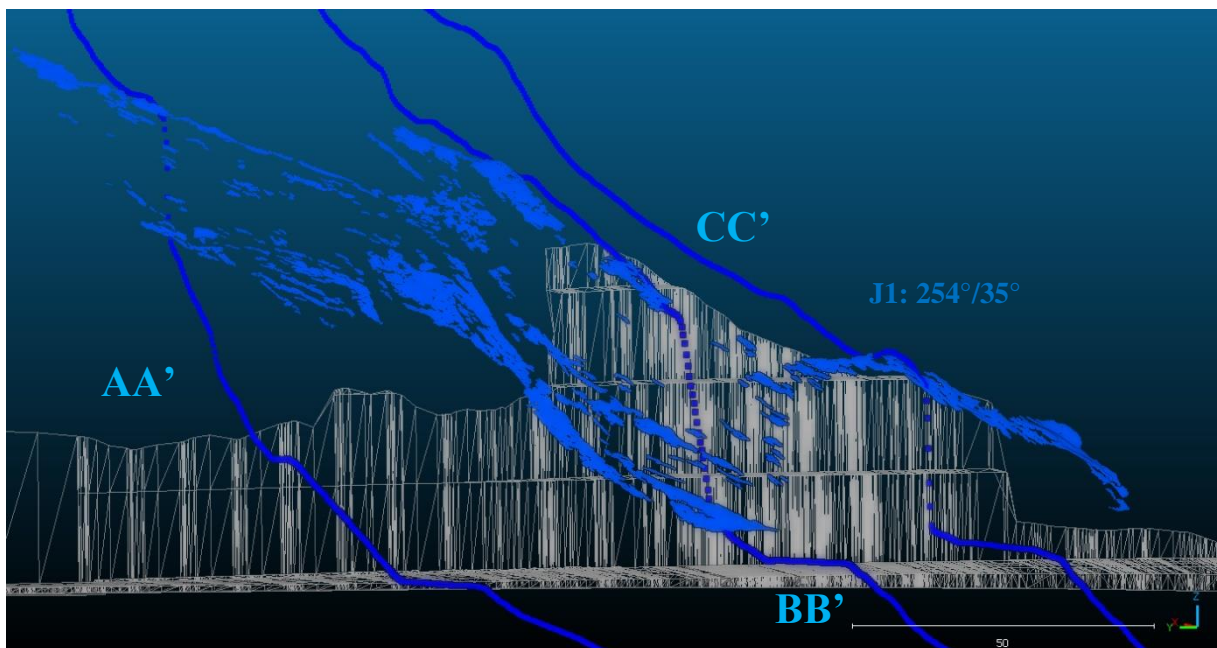


Figure L.2: Discontinuity set J1 (foliation) with profile AA', BB', and CC'. Dark blue lines indicate profile AA', BB', and CC'. Grey mesh is the planned road cut, deep blasting surface and trench bottom.

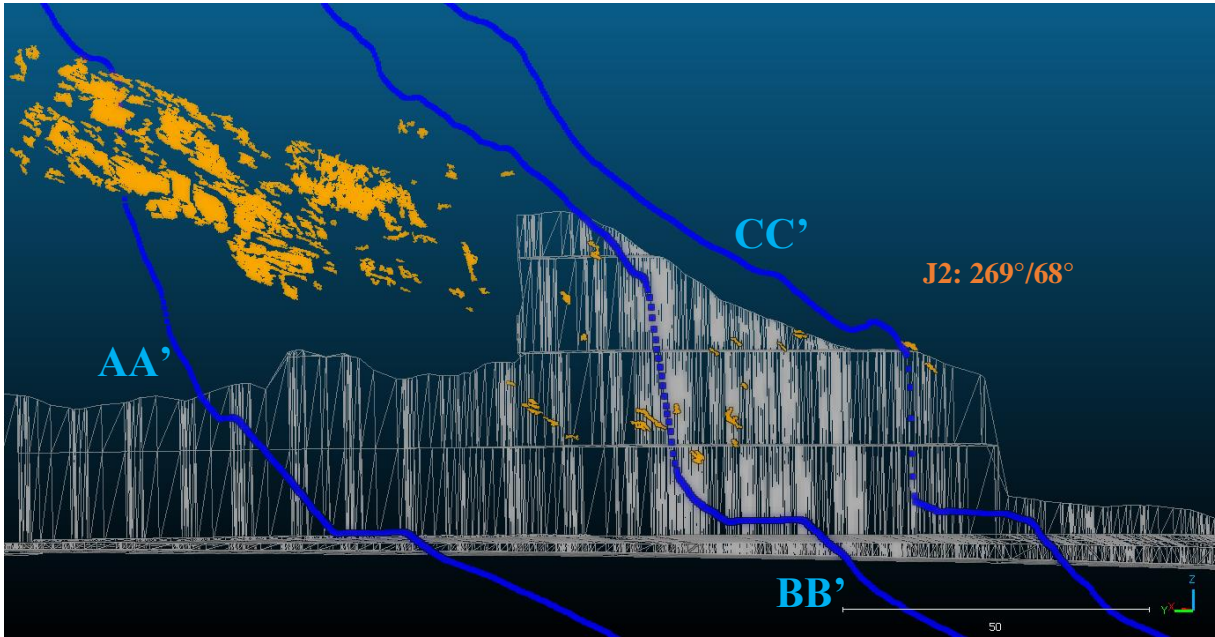


Figure L.4: Discontinuity set J2 with profile AA', BB', and CC'. Dark blue lines indicate profile AA', BB', and CC'. Grey mesh is the planned road cut, deep blasting surface and trench bottom.

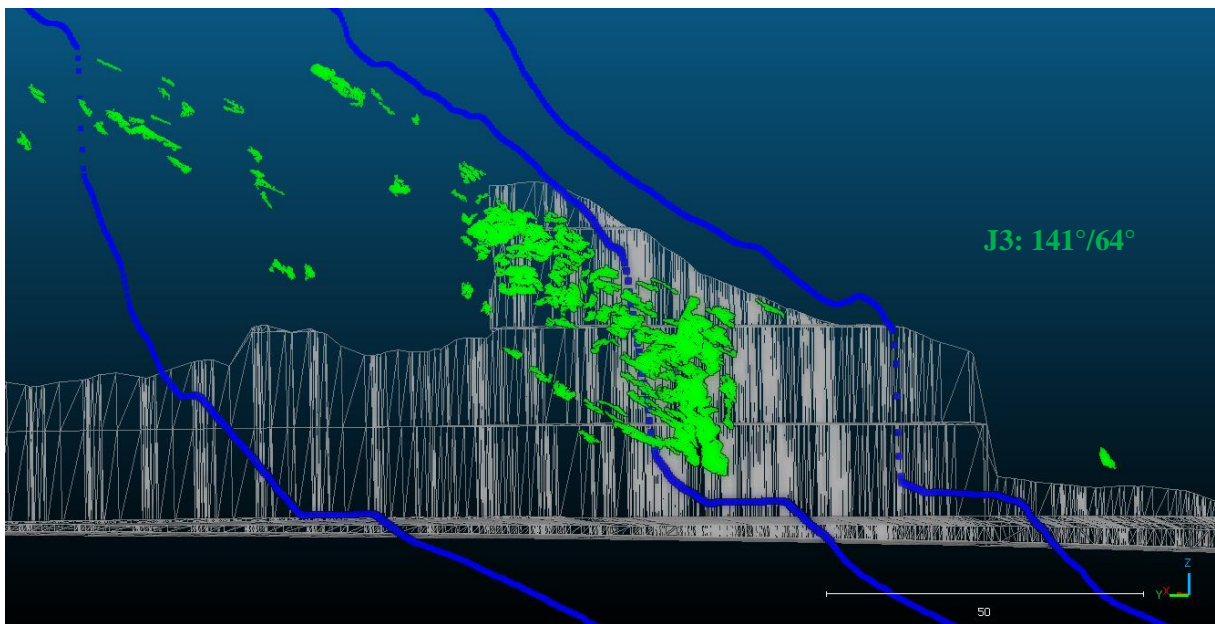


Figure L.3: Discontinuity set J3 with profile AA', BB', and CC'. Dark blue lines indicate profile AA', BB', and CC'. Grey mesh is the planned road cut, deep blasting surface and trench bottom.

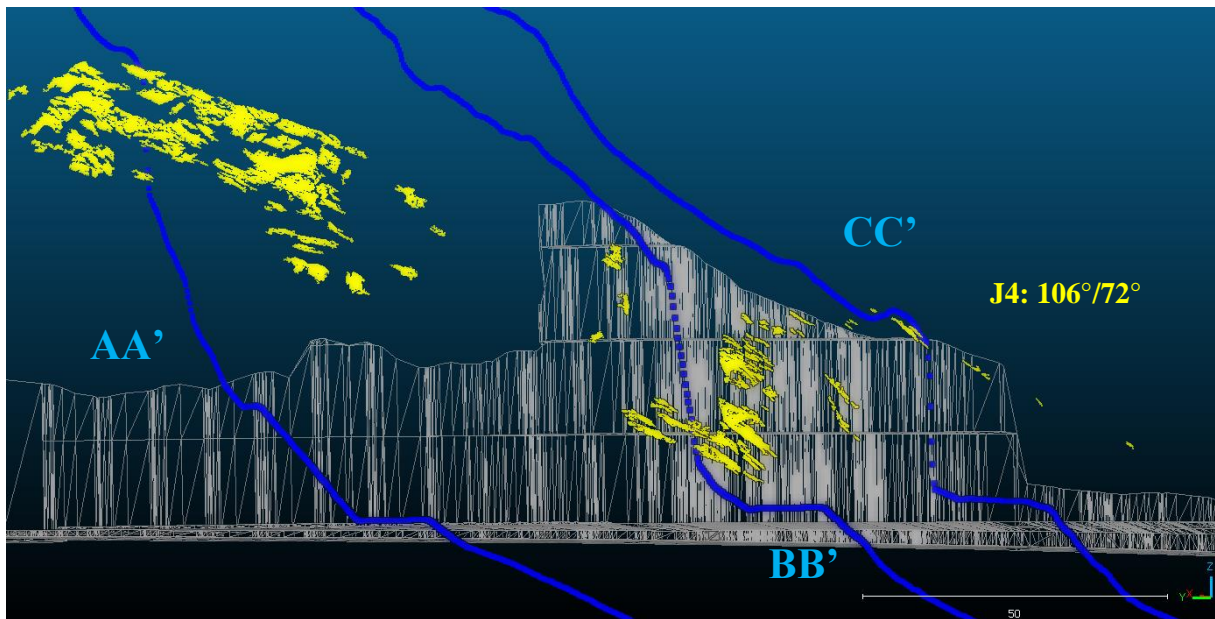


Figure L.5: Discontinuity set J4 with profile AA', BB', and CC'. Dark blue lines indicate profile AA', BB', and CC'. Grey mesh is the planned road cut, deep blasting surface and trench bottom.

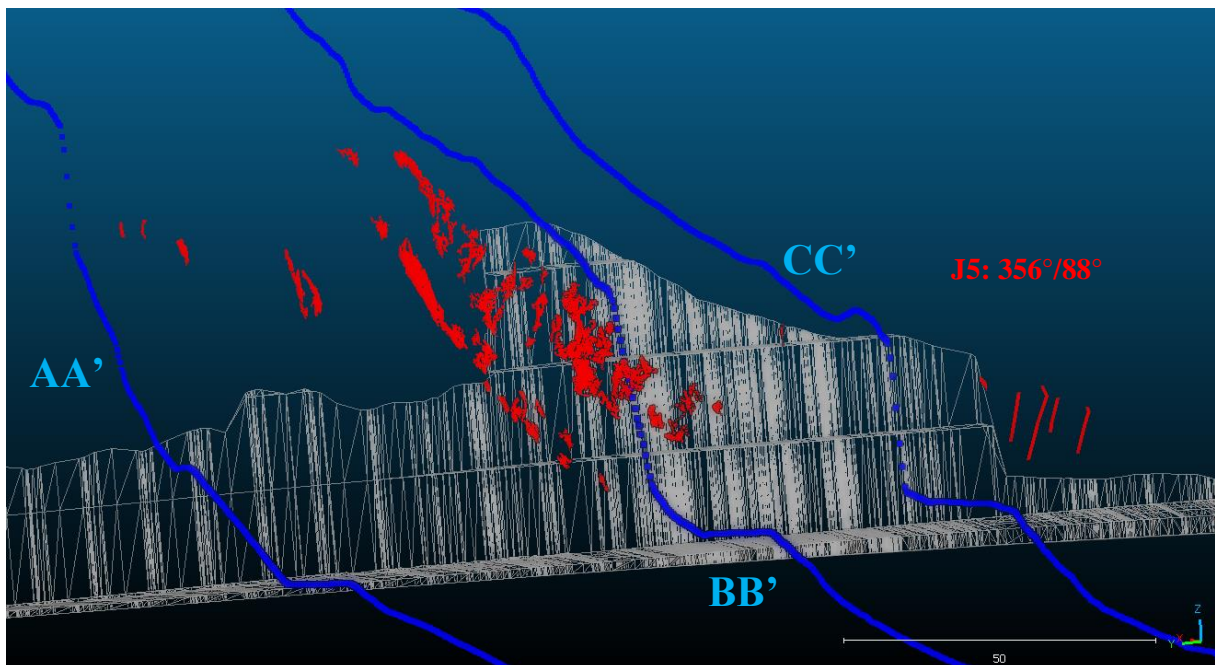


Figure L.6: Discontinuity set J5 with profile AA', BB', and CC'. Dark blue lines indicate profile AA', BB', and CC'. Grey mesh is the planned road cut, deep blasting surface and trench bottom. The four lines (discontinuities) to the right are mapped manually in CloudCompare as the surface area was too small for DSE to be detected.

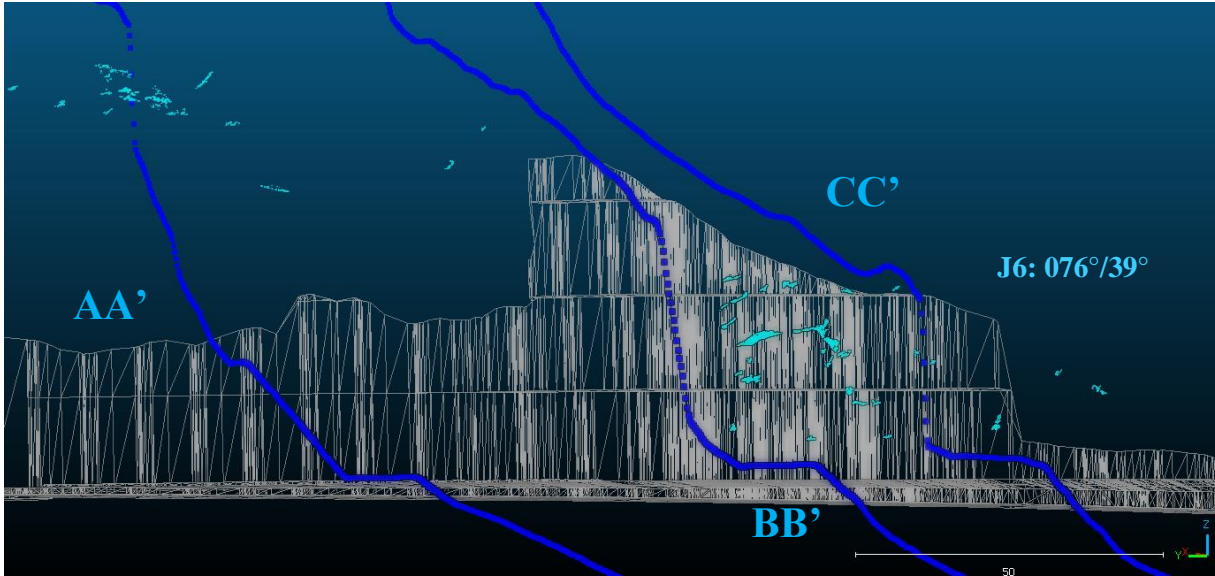


Figure 8.1: Discontinuity set J6 with profile AA', BB', and CC'. Dark blue lines indicate profile AA', BB', and CC'. Grey mesh is the planned road cut, deep blasting surface and trench bottom.

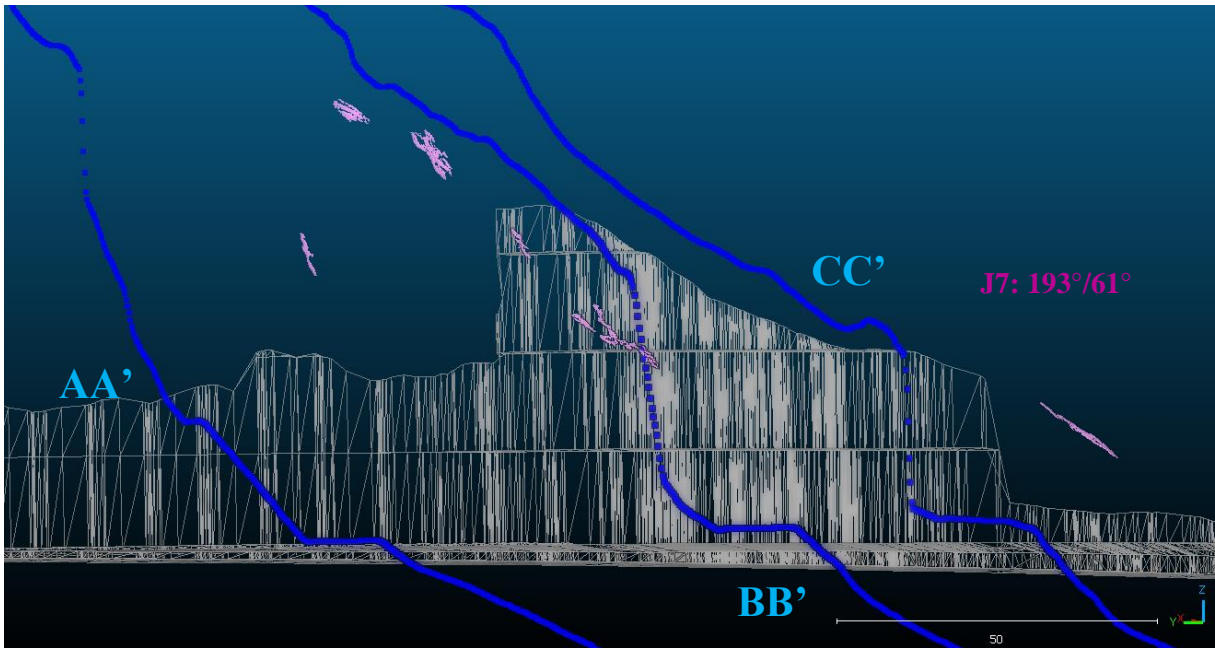


Figure L.7: Discontinuity set J7 with profile AA', BB', and CC'. Dark blue lines indicate profile AA', BB', and CC'. Grey mesh is the planned road cut, deep blasting surface and trench bottom.

# Appendix M Kinematic analysis

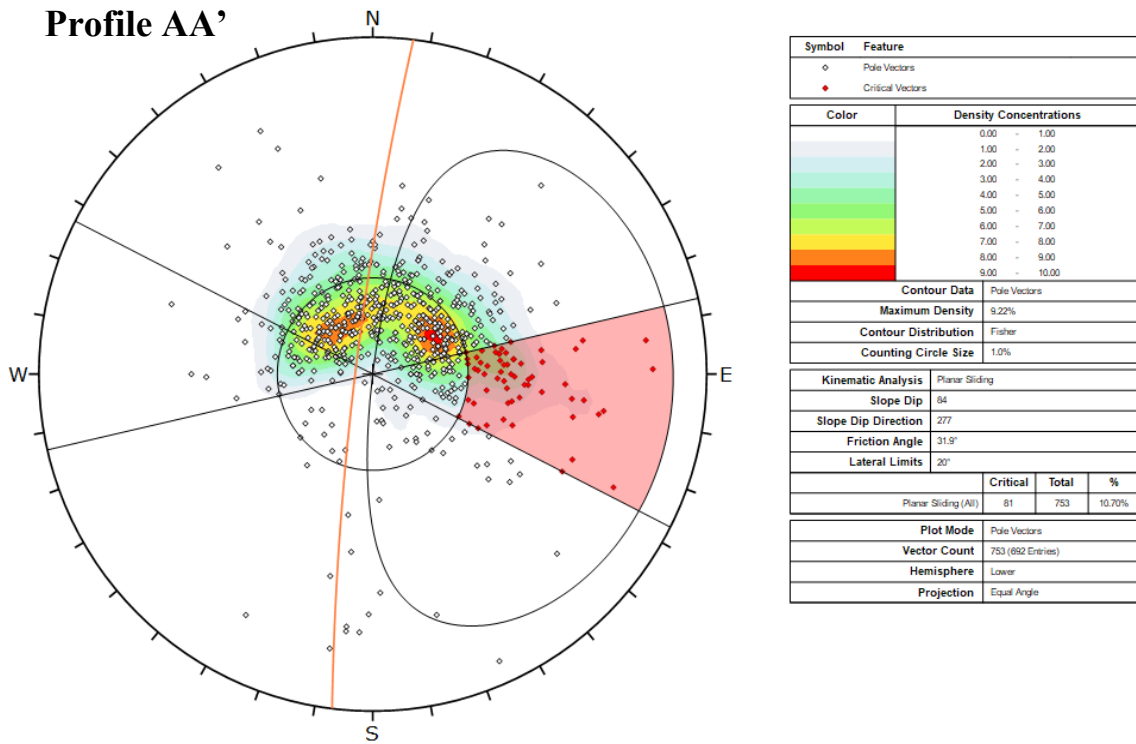


Figure M.1: Kinematic analysis for planar sliding (profile AA'). 10.70% of the poles are within the critical zone.

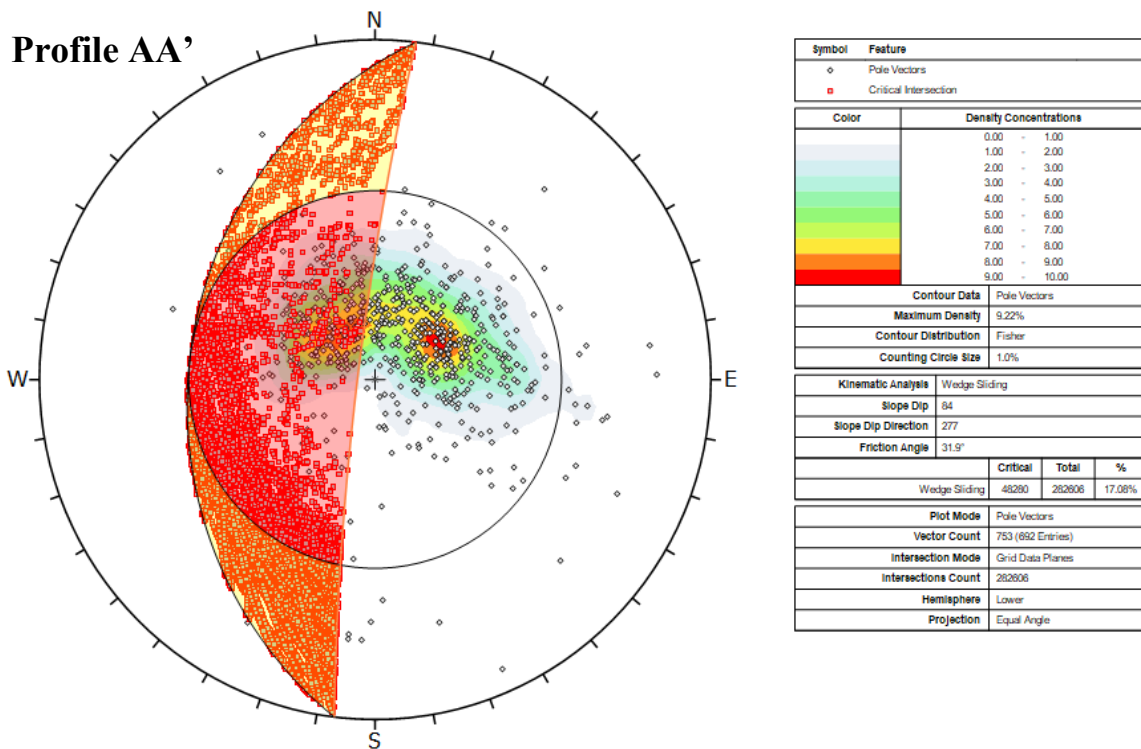
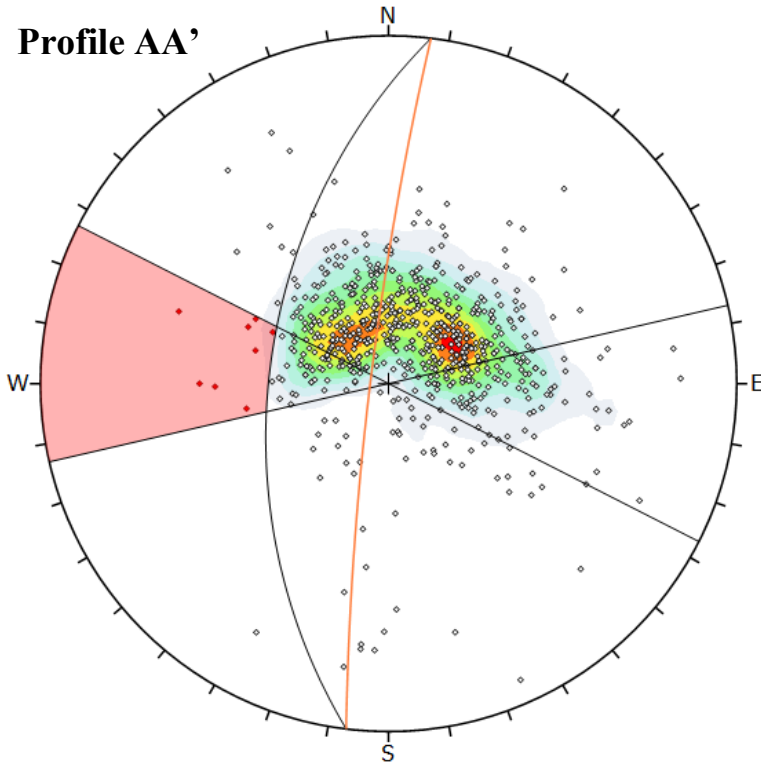


Figure M.2: Kinematic analysis for wedge sliding (profile AA'). 17.08% of the poles are within the critical zone.



### Profile AA'



Symbol	Feature
◊	Pole Vectors
•	Critical Vectors

Color	Density Concentrations
	0.00 - 1.00
	1.00 - 2.00
	2.00 - 3.00
	3.00 - 4.00
	4.00 - 5.00
	5.00 - 6.00
	6.00 - 7.00
	7.00 - 8.00
	8.00 - 9.00
	9.00 - 10.00

Contour Data		Pole Vectors
Maximum Density	9.22%	
Contour Distribution	Fisher	
Counting Circle Size	1.0%	

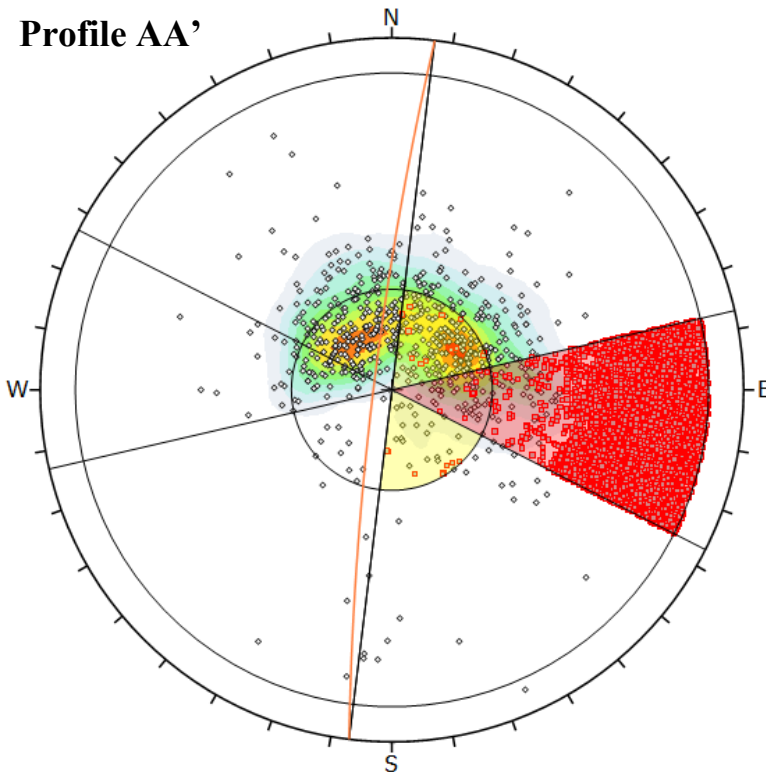
Kinematic Analysis		Flexural Topping		
Slope Dip	84			
Slope Dip Direction	277			
Friction Angle	31.9°			
Lateral Limits	20°			
		Critical	Total	%
Flexural Topping (All)	15	753		1.99%

Plot Mode		Pole Vectors
Vector Count	753 (892 Entries)	
Hemisphere	Lower	
Projection	Equal Angle	

Figure M.3: Kinematic analysis for flexural toppling (profile AA'). 1.99% of the poles are within the critical zone.

### Profile AA'



Symbol	Feature
◊	Pole Vectors
•	Critical Vectors
■	Critical Intersection

Color	Density Concentrations
	0.00 - 1.00
	1.00 - 2.00
	2.00 - 3.00
	3.00 - 4.00
	4.00 - 5.00
	5.00 - 6.00
	6.00 - 7.00
	7.00 - 8.00
	8.00 - 9.00
	9.00 - 10.00

Contour Data		Pole Vectors
Maximum Density	9.22%	
Contour Distribution	Fisher	
Counting Circle Size	1.0%	

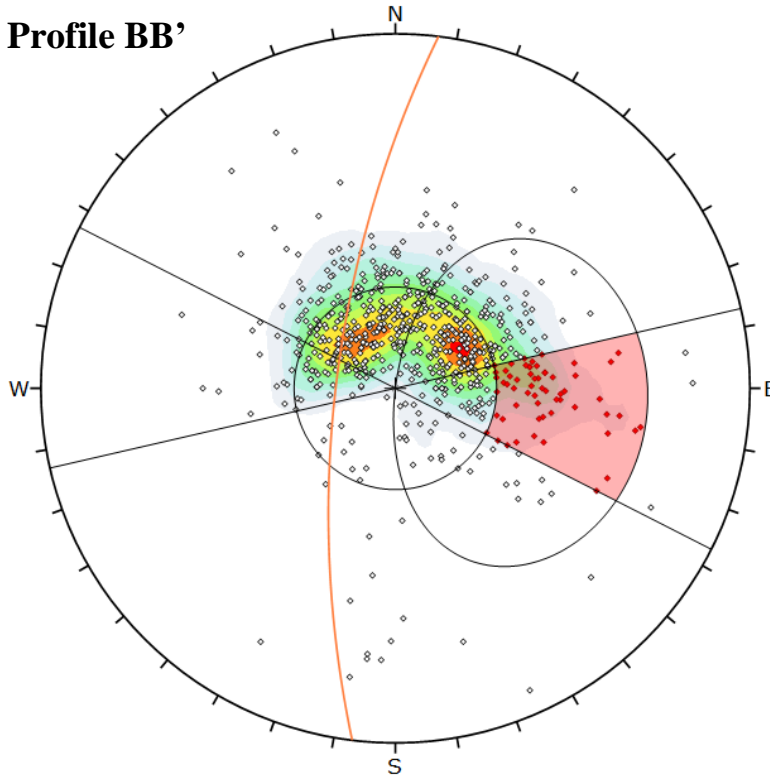
Kinematic Analysis		Direct Topping		
Slope Dip	84			
Slope Dip Direction	277			
Friction Angle	31.9°			
Lateral Limits	20°			
		Critical	Total	%
Direct Topping (Intersection)	16015	282606		5.67%
Oblique Topping (Intersection)	28	282606		0.01%
Base Plane (All)	306	753		40.60%

Plot Mode		Pole Vectors
Vector Count	753 (892 Entries)	
Intersection Mode	Grid Data Planes	
Intersections Count	282606	
Hemisphere	Lower	
Projection	Equal Angle	

Figure M.4: Kinematic analysis for block toppling (profile AA'). 5.67% of the intersections cause direct topping while 40.60% from the base plane are critical.

### Profile BB'



Symbol	Feature
◊	Pole Vectors
•	Critical Vectors

Color	Density Concentrations
	0.00 - 1.00
	1.00 - 2.00
	2.00 - 3.00
	3.00 - 4.00
	4.00 - 5.00
	5.00 - 6.00
	6.00 - 7.00
	7.00 - 8.00
	8.00 - 9.00
	9.00 - 10.00

<b>Contour Data</b>		Pole Vectors
<b>Maximum Density</b>		9.22%
<b>Contour Distribution</b>		Fisher
<b>Counting Circle Size</b>		1.0%

<b>Kinematic Analysis</b>	Planar Sliding
<b>Slope Dip</b>	71
<b>Slope Dip Direction</b>	277
<b>Friction Angle</b>	31.9°
<b>Lateral Limits</b>	20°

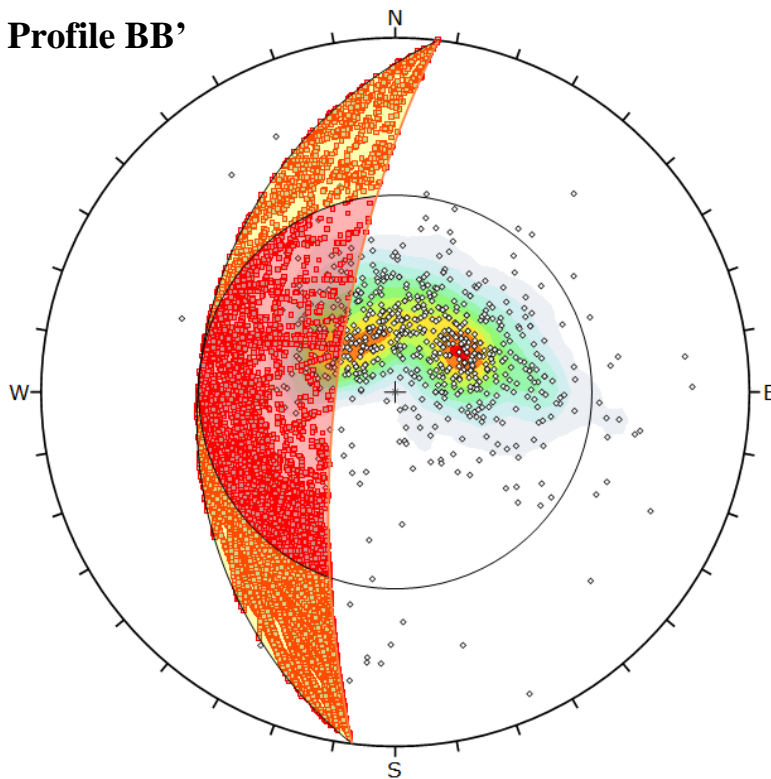
	Critical	Total	%
Planar Sliding (All)	74	753	9.83%

<b>Plot Mode</b>	Pole Vectors
<b>Vector Count</b>	753 (692 Entries)
<b>Hemisphere</b>	Lower
<b>Projection</b>	Equal Angle

Figure M.5: Kinematic analysis for planar sliding (profile BB'). 9.83% of the poles are within the critical zone.

### Profile BB'



Symbol	Feature
◊	Pole Vectors
■	Critical Intersection

Color	Density Concentrations
	0.00 - 1.00
	1.00 - 2.00
	2.00 - 3.00
	3.00 - 4.00
	4.00 - 5.00
	5.00 - 6.00
	6.00 - 7.00
	7.00 - 8.00
	8.00 - 9.00
	9.00 - 10.00

<b>Contour Data</b>		Pole Vectors
<b>Maximum Density</b>		9.22%
<b>Contour Distribution</b>		Fisher
<b>Counting Circle Size</b>		1.0%

<b>Kinematic Analysis</b>	Wedge Sliding
<b>Slope Dip</b>	71
<b>Slope Dip Direction</b>	277
<b>Friction Angle</b>	31.9°

	Critical	Total	%
Wedge Sliding	41001	282608	14.51%

<b>Plot Mode</b>	Pole Vectors
<b>Vector Count</b>	753 (692 Entries)
<b>Intersection Mode</b>	Grid Data Planes
<b>Intersections Count</b>	282608
<b>Hemisphere</b>	Lower
<b>Projection</b>	Equal Angle

Figure M.6: Kinematic analysis for wedge sliding (profile BB'). 14.51% of the poles are within the critical zone.

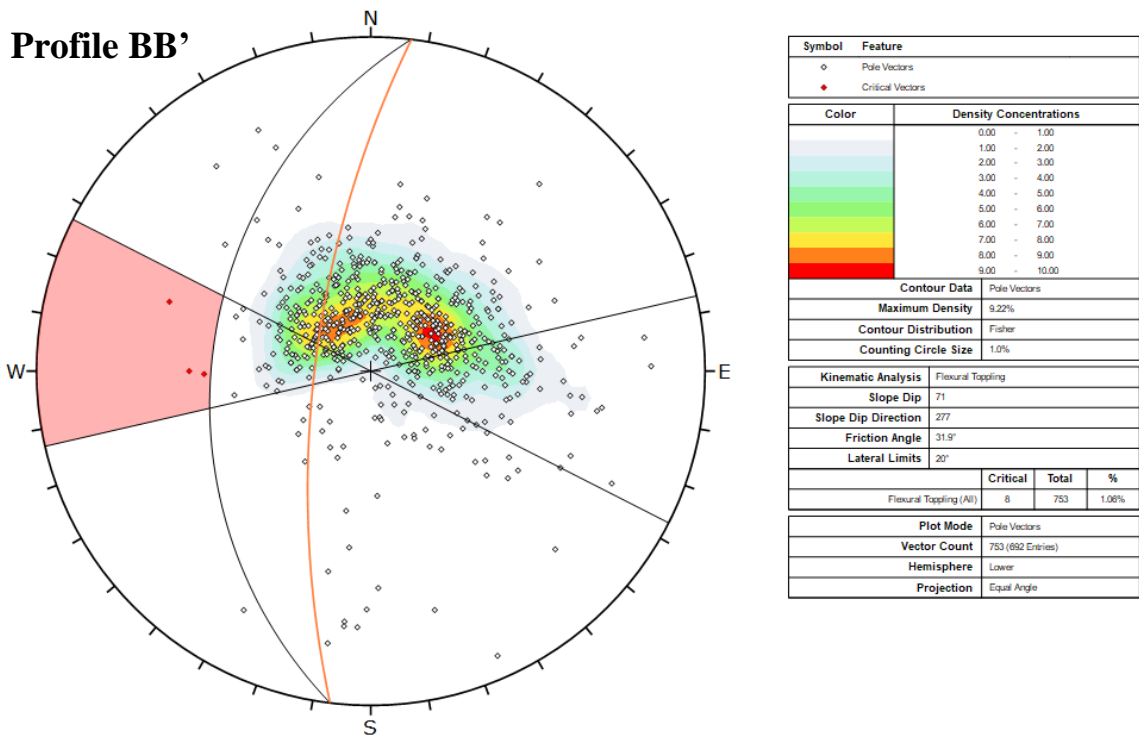


Figure M.7: Kinematic analysis for flexural toppling (profile BB'). 1.06% of the poles are within the critical zone.

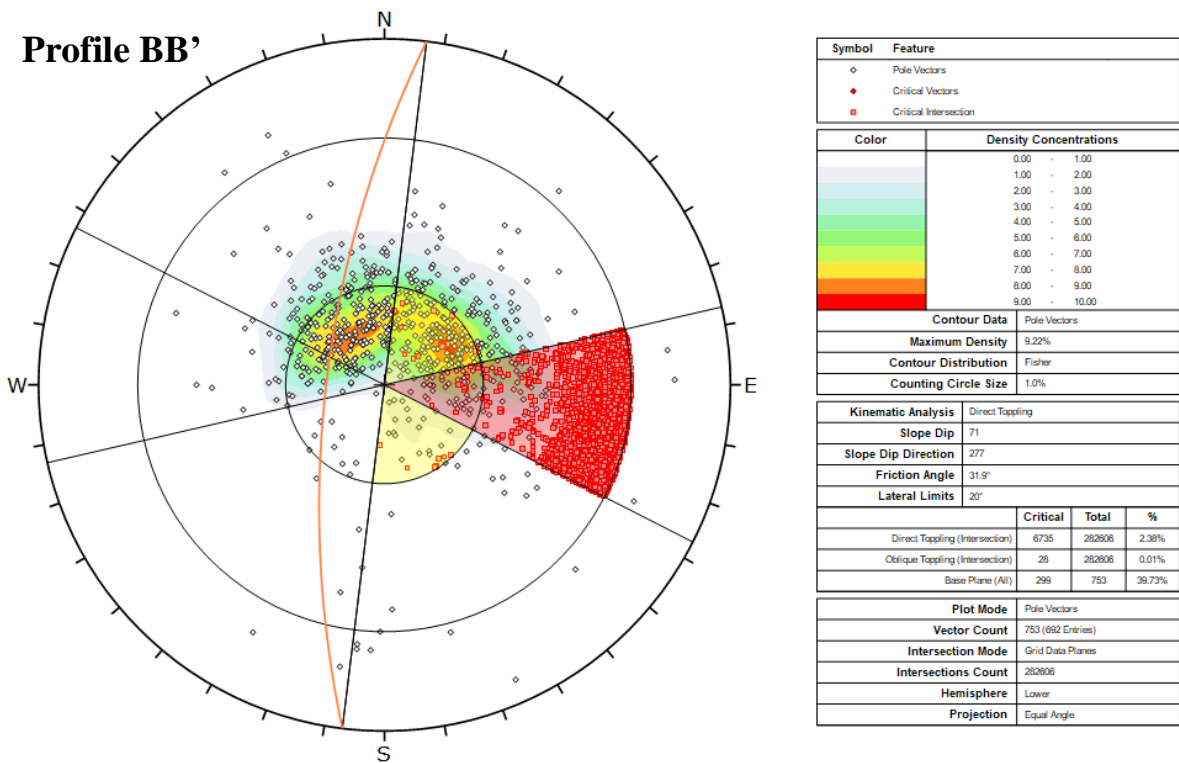
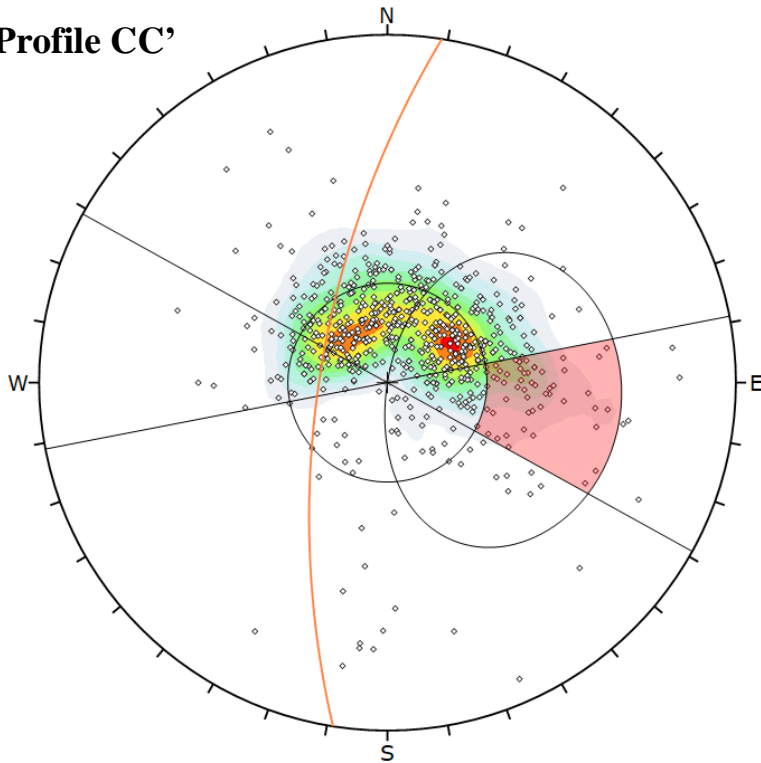


Figure M.8: Kinematic analysis for block toppling (profile BB'). 2.38% of the intersections can cause direct toppling while 39.73% of the intersections from the base plane are critical.

### Profile CC'



Symbol	Feature
◊	Pole Vectors

Color	Density Concentrations
	0.00 - 1.00
	1.00 - 2.00
	2.00 - 3.00
	3.00 - 4.00
	4.00 - 5.00
	5.00 - 6.00
	6.00 - 7.00
	7.00 - 8.00
	8.00 - 9.00
	9.00 - 10.00

Contour Data		Pole Vectors	
Maximum Density	9.22%		
Contour Distribution	Fisher		
Counting Circle Size	1.0%		

Kinematic Analysis		Planar Sliding	
Slope Dip	68		
Slope Dip Direction	279		
Friction Angle	31.9°		
Lateral Limits	20°		

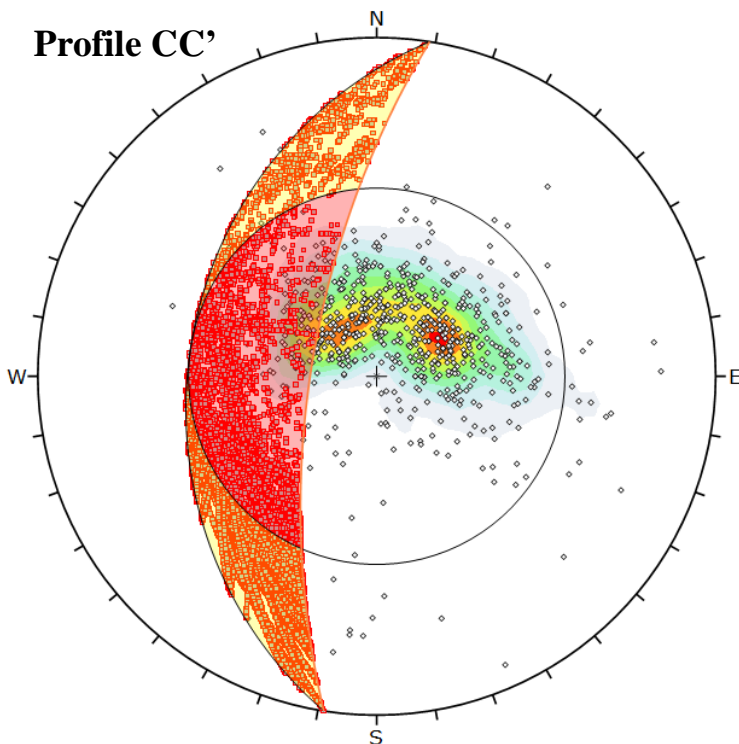
	Critical	Total	%
Planar Sliding (All)	68	753	8.97%

Plot Mode		Pole Vectors	
Vector Count	753 (692 Entries)		
Hemisphere	Lower		
Projection	Equal Angle		

Figure M.9: Kinematic analysis for planar sliding (profile CC'). 8.97% of the poles are within the critical zone.

### Profile CC'



Symbol	Feature
◊	Pole Vectors
■	Critical Intersection

Color	Density Concentrations
	0.00 - 1.00
	1.00 - 2.00
	2.00 - 3.00
	3.00 - 4.00
	4.00 - 5.00
	5.00 - 6.00
	6.00 - 7.00
	7.00 - 8.00
	8.00 - 9.00
	9.00 - 10.00

Contour Data		Pole Vectors	
Maximum Density	9.22%		
Contour Distribution	Fisher		
Counting Circle Size	1.0%		

Kinematic Analysis		Wedge Sliding	
Slope Dip	68		
Slope Dip Direction	279		
Friction Angle	31.9°		

	Critical	Total	%
Wedge Sliding	34006	282606	12.03%

Plot Mode		Pole Vectors	
Vector Count	753 (692 Entries)		
Intersection Mode	Grid Data Planes		
Intersections Count	282606		
Hemisphere	Lower		
Projection	Equal Angle		

Figure M.10: Kinematic analysis for wedge sliding (profile CC'). 12.03% of the poles are within the critical zone.

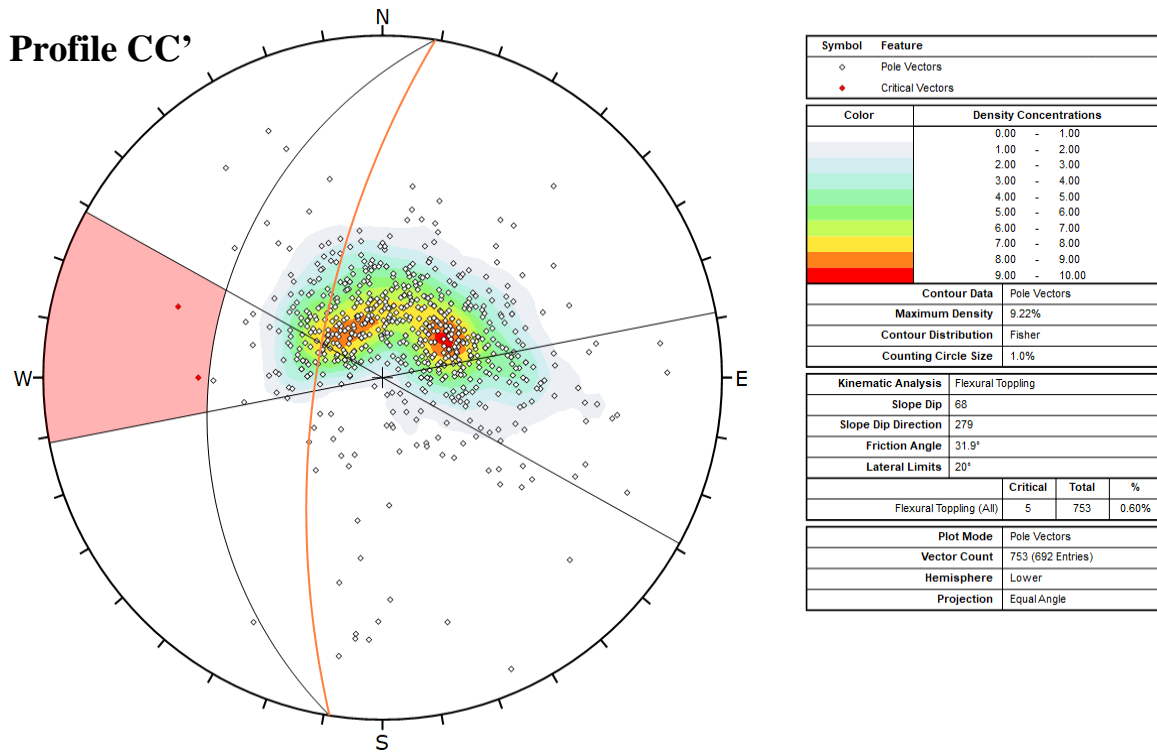


Figure M.11: Kinematic analysis for flexural toppling (profile CC'). 0.60% of the poles are within the critical zone.

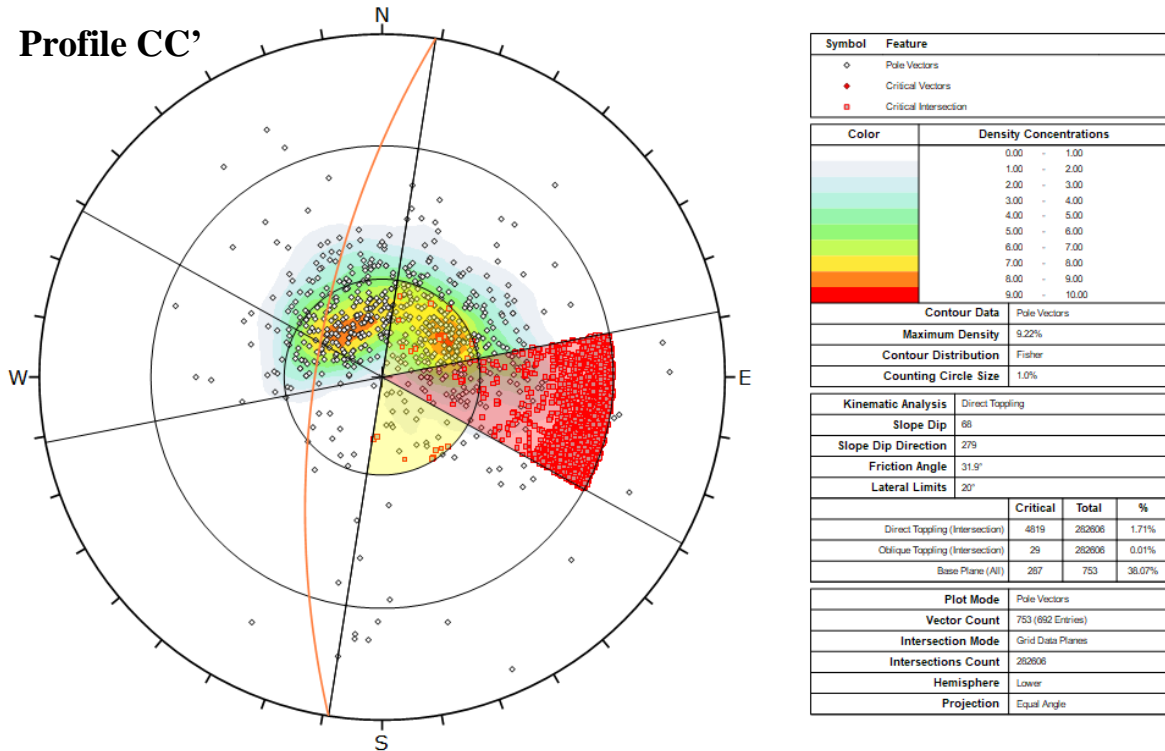


Figure M.12: Kinematic analysis for block toppling (profile CC'). 1.71% of the intersections can cause direct toppling while 38.07% of the intersections from the base plane are critical.

# Appendix N Sequence of excavation and installation of stability measures

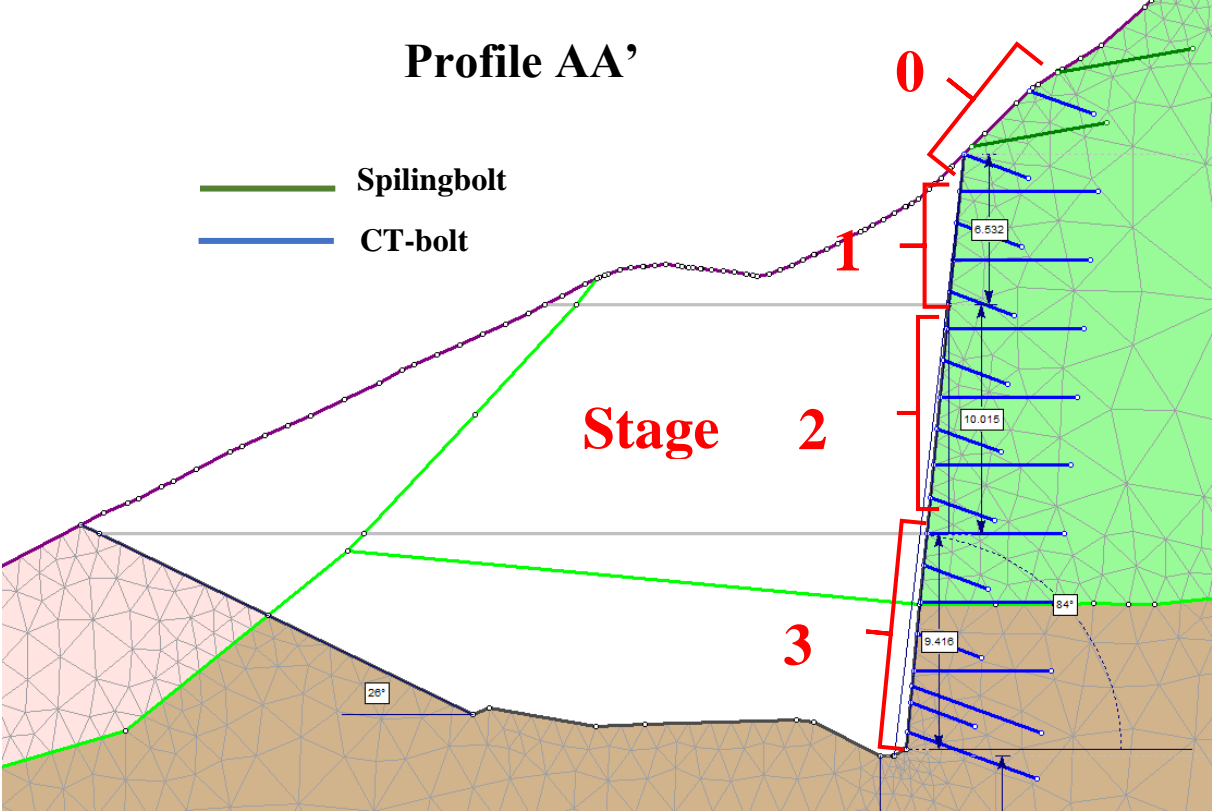


Figure N.1: Excavation stages and corresponding installation stages for the stability measures at profile AA'.

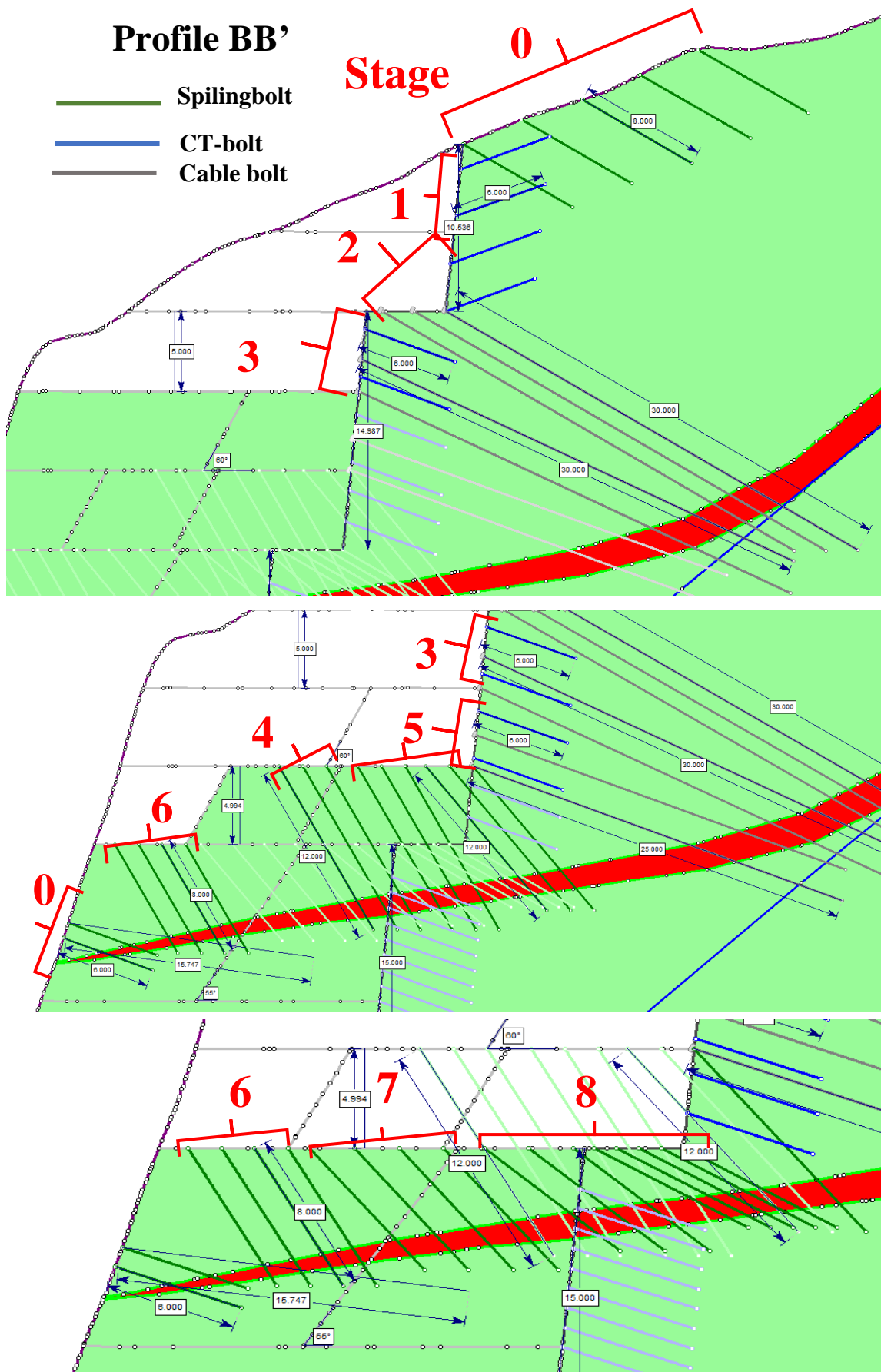


Figure N.2: Excavation stages and corresponding installation stages for the stability measures at profile BB'. Spiling bolts longer than 8 m are in reality Ischebeck self-drilling rock anchors [1/2].

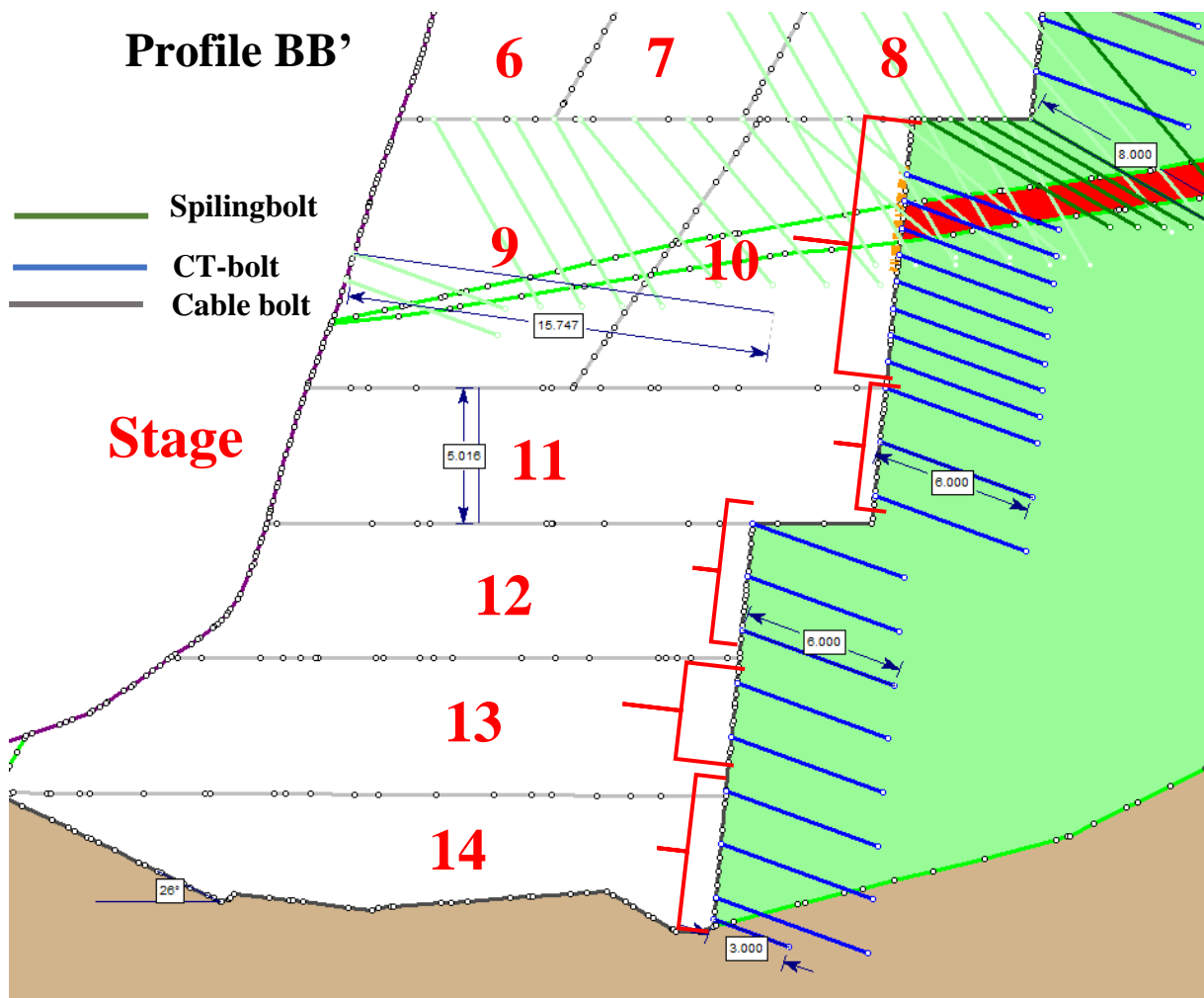


Figure N.3: Excavation stages and corresponding installation stages for the stability measures at profile BB'. Spiling bolts longer than 8 m are in reality Ischebeck self-drilling rock anchors [2/2].



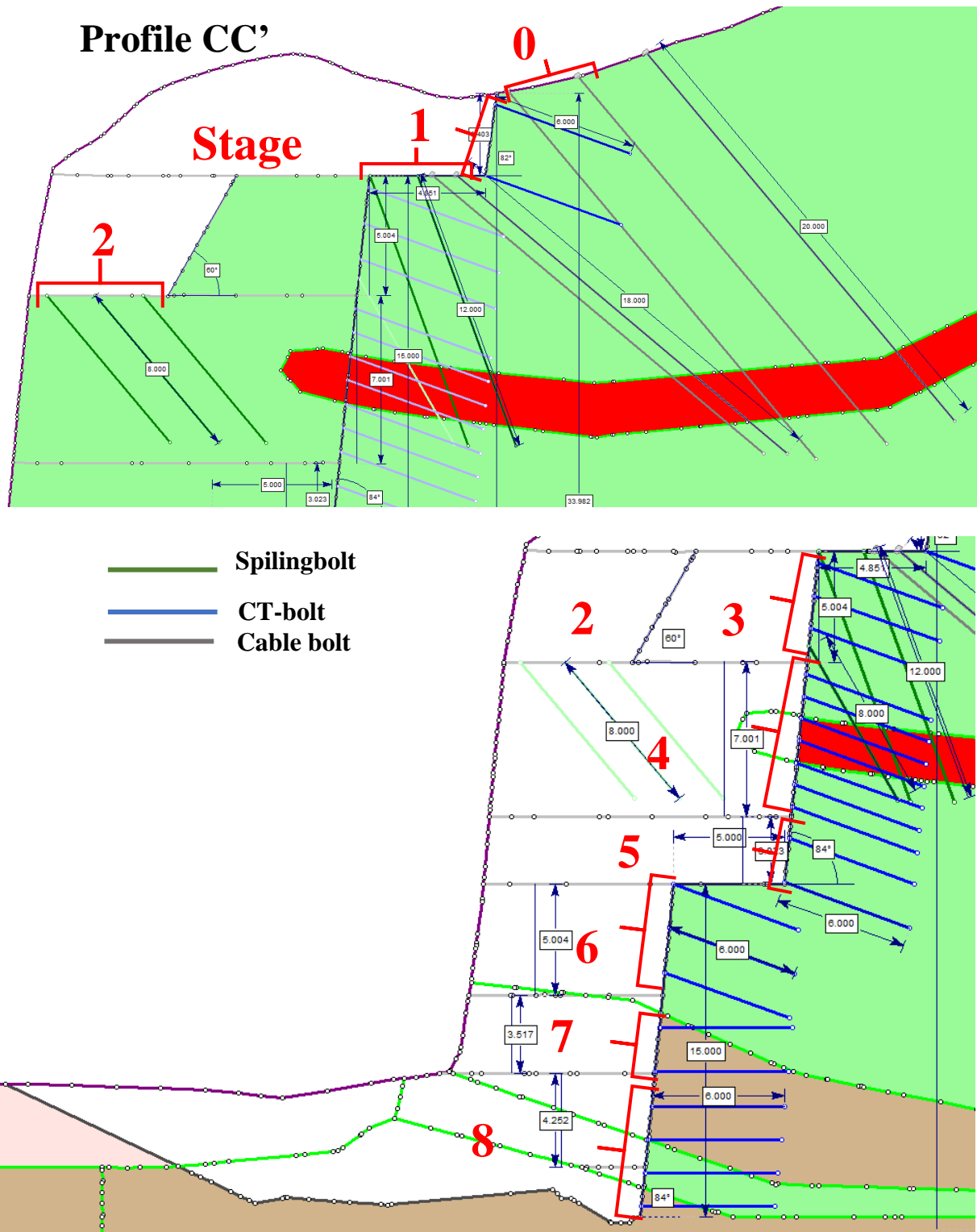


Figure N.4: Excavation stages and corresponding installation stages for the stability measures at profile BB'. Spiling bolts longer than 8 m are in reality Ischebeck self-drilling rock anchors. The crushed zone is likely stretching out even further, thus spiling bolts are installed at stage 2. If not, a potential sliding plane could be created during the excavation of stage 3 (in the floor) and resulting in a collapse.

